UNIVERSITY OF CALIFORNIA

Santa Barbara

Characterization of β-Hydroxyaspartate Siderophores: Structures, Biosyntheses, Coordination Chemistry, and Photoreactivity

A dissertation submitted in partial satisfaction of the

requirements for the degree Doctor of Philosophy

in Chemistry

by

Clifford Douglas Hardy

Committee in charge:

Professor Alison Butler, Chair

Professor Peter Ford

Professor Gabriel Ménard

Professor David Valentine

June 2020

The dissertation of Clifford Douglas Hardy is approved.

_____

Peter Ford

_____

Gabriel Ménard

_____

David Valentine

_____

Alison Butler, Committee Chair

June 2020

Characterization of β-Hydroxyaspartate Siderophores: Structures, Biosyntheses, Coordination Chemistry, and Photoreactivity

ACKNOWLEDGEMENTS

In January of 2020, I put together a six-month timeline to write my dissertation and finish all remaining experiments necessary to publish one more journal publication. But as often happens to the best laid plans of mice and men, halfway into that timeline I found myself scrambling to put samples into cold storage. UCSB had implemented a total shut down of research operations, and the state of California issued a stay at home order, in response to the COVID-19 crisis. Defending my dissertation through video conference, after 3 months of working from home, was certainly not how I envisioned the conclusion of my PhD education would play out. Despite this surreal ending, my time researching in the Butler group has been one of the most academically and personally fulfilling experiences of my life. This dissertation represents 5 years of hard work, work that I would have never been able to carry out without support from countless individuals.

I first would like to thank my advisor Professor Alison Butler. From the start, she has provided unconditional support and guidance, and I would not be the scientist I am today without it. The excellent culture and approach to science that Alison has cultivated in her research group allowed me to thrive, and I cannot imagine working with any other advisor. I would also like to thank my committee members Professor Peter Ford, Professor Gabriel Ménard, and Professor David Valentine, for their support and insight.

None of my research would be possible without the use of shared facilities at UCSB. I want to thank Dr. Hongjun Zhou for his expertise and insight into NMR spectroscopy, and his willingness to provide one-on-one assistance with custom experiment design. I especially wish to thank Dr. Rachel Behrens for her continual support and hard work maintaining the UPLC-

MS. This instrument was a critical tool in all of my projects, and her advice and help with troubleshooting and method development has been indispensable.

I am extremely thankful for my fellow group members, their camaraderie, and their scientific insight over the past 6 years. To Gregory Meier, Robert Lewis, Jeffrey Carmichael, Zachary Reitz, Aneta Jelowicki, Parker Stow, Christina Makris, Kalana Dulaney, and Jaewon Suk—each of you are excellent co-workers, and wonderful friends. I am proud of our positive, friendly, and collaborative group dynamic, and I hope and know it will continue into the future. I want to also thank all of my friends at UCSB outside of our research group, you have all played a role in making graduate school such a wonderful experience.

Lastly, I would like to thank my family. To my parents Jim and Bonnie, to my sister Alison, and the rest of my family—thank you for a lifetime of love and support. I never would have started this journey without you. Finally, thank you, Erika, for all the warmth, love, and support you have given me as I have navigated the end of my PhD.

VITA OF CLIFFORD DOUGLAS HARDY

June 2020

EDUCATION

Doctor of Philosophy in Chemistry, **June 2020**
University of California, Santa Barbara

Bachelor of Science in Chemistry, **May 2014**
University of Texas at Austin

PUBLICATIONS

Hardy, Clifford D.; Suk, J.; Butler, A. Characterizing and Modulating Photoreactivity of Fe(III)-β-Hydroxyaspartic Acid Siderophore Complexes. *In Preparation.*

Reitz, Z. L.; Hardy, Clifford D.; Suk, J.; Bouvet, J.; Butler, A. Genomic Analysis of Siderophore β-Hydroxylases Reveals Divergent Regio- and Stereocontrol and Expands the Condensation Domain Family. *Proc. Nat. Acad. Sci.* **2019**, *116*, 19805-19814 DOI: 10.1073/pnas.1903161116

Hardy, Clifford D.; Butler, A. On the Ambiguity of NRPS Structure Predictions: Four Bidentate Chelating Groups in the Siderophore Pacifibactin. *J. Nat. Prod.* **2019**, *82*, 990–997 DOI: 10.1021/acs.jnatprod.8b01073

Hardy, Clifford D.; Butler, A., β-Hydroxyaspartic acid in siderophores: biosynthesis and reactivity. *J. Biol. Inorg. Chem.* **2018**, *23*, 957-967 DOI: 10.1007/s00775-018-1584-2

Foster, L. M.; Worthen, A. J.; Foster, E. L.; Dong, J.; Roach, C. M.; Metaxas, A. E.; Hardy, Clifford D.; Larsen, E. S.; Bollinger, J. A.; Truskett, T. M.; Bielawski, C. W.; Johnston, K. P., High Interfacial Activity of Polymers "Grafted through" Functionalized Iron Oxide Nanoparticle Clusters. *Langmuir* **2014**, *30*, 10188-10196. DOI: 10.1021/la501445f

FELLOWSHIPS AND AWARDS

Outstanding Service to the Department, Department of Chemistry and Biochemistry, University of California, Santa Barbara. **2019**

Mellichamp Academic Initiative in Sustainability Fellowship, University of California, Santa Barbara. **2016**

CONFERENCES AND MEETINGS

"Probing the Photoreactions of Fe(III)-Siderophore Complexes Containing β-Hydroxyaspartic Acid" contributed poster presentation at the American Chemical Society National Meeting, San Diego, CA, August 25, **2019**

"Improving Throughput of Siderophore Discovery Through Genome Mining" contributed oral presentation at the Bioinorganic Chemistry Gordon Research Seminar, Ventura, CA, February 2, **2019**

"Coordination Chemistry and Photoreactivity of the New Siderophore Pacifibactin" contributed poster presentation at the Bioinorganic Chemistry Gordon Research Seminar, Ventura, CA, January 31, **2019**

"Coordination Chemistry and Photoreactivity of the Genome Mined Siderophore Pacifibactin" contributed oral presentation at the Southern California Bioinorganic Chemistry Meeting, California Institute of Technology, Pasadena, CA, December 8, **2018**

"Photoreactive Marine Siderophore From *Alcanivorax pacificus*" contributed poster presentation at the American Chemical Society National Meeting, New Orleans, LA, March 18, **2018**

"*Alcanivorax pacificus* Synthesizes a Photoreactive Siderophore With Unique Iron-Binding Properties" contributed poster presentation at the Southern California Bioinorganic Chemistry Meeting, University of California, Irvine, December 2, **2017**

"Investigating Iron Acquisition in a Hydrocarbon-Degrading Marine Bacterium Through Genome Mining" invited poster presentation at the Renewable Carbon Workshop, University of California, Santa Barbara, September 21, **2016**

"Investigating Marine Bacterial Siderophores Through Bioinformatics Approaches" contributed poster presentation at the University of California Symposium for Chemical Sciences, Lake Arrowhead, CA, March 22, **2016**

"Solution Routes to Tungsten Sulfide Nanoparticles" contributed poster presentation at the American Chemical Society National Meeting, New Orleans, LA, April 7, **2013**

TEACHING EXPERIENCE

Teaching Assistant: Advanced Analytical, Physical, and Inorganic Laboratory, University of California, Santa Barbara, **2015-2016, 2020**

Teaching Assistant: General Chemistry Laboratory, University of California, Santa Barbara, **2014-2015**

ABSTRACT

Characterization of β-Hydroxyaspartate Siderophores: Structures, Biosyntheses, Coordination Chemistry, and Photoreactivity

by

Clifford Douglas Hardy

Nearly all bacteria require iron to function. Bio-available iron is quite limited in many environments, however. To grow and thrive under iron-limited conditions, bacteria have evolved multiple iron-acquisition strategies. One such strategy is the production of siderophores, small molecule Fe(III)-chelating ligands synthesized by bacteria and exported into the environment. Siderophores bind to environmental Fe(III), and the subsequent metal-ligand complex is recognized by receptors on the surface of the bacterium, whereupon the complex is brought back into the cell, and the iron released for utilization by the microbe. This work is focused on investigations into the structures, biosyntheses, coordination chemistry, and photochemistry of siderophores containing the Fe(III)-binding functional group β-hydroxyaspartate.

Reported herein is the characterization of the new siderophore pacifibactin, predicted through a genome mining approach. Pacifibactin is unusual in that it contains four bidentate metal binding sites, including two β-OHAsp functional groups, and Fe(III), Ga(III), and Zr(IV)

coordination chemistry of the ligand is discussed. All β-OHAsp siderophores are photoreactive when complexed to Fe(III), and the photoreactivity of Fe(III)-pacifibactin is reported.

Siderophores containing β-OHAsp are biosynthesized by nonribosomal peptide synthetases (NRPSs), large multi-modular enzymes that assemble peptidic natural products. Two distinct strategies for aspartyl β-hydroxylation in NRPS biosynthesis have evolved—one strategy involves β-hydroxylation by discrete hydroxylase enzymes (termed $T\beta H_{Asp}$), the other involves hydroxylase domains with NRPS enzymes (termed $I\beta H_{Asp}$). A recent phylogenetic analysis of genes encoding these hydroxylase enzymes and NRPSs containing hydroxylase domains uncovered a striking pattern between phylogeny and the stereoselectivity of the hydroxylases. In this work, three known siderophores (delftibactin, pyoverdine GB-1, and histicorrugatin) are stereochemically characterized for the first time, and the stereochemistry of another siderophore (cupriachelin) is revised. This wealth of new characterization supports and strengthens the known association between phylogeny and stereoselectivity, making it a powerful tool for enhancing structural predictions of NRPS natural products.

Lastly, this work details extensive investigations of siderophore photochemistry. The Fe(III) complexes of two β-OHAsp siderophores, pacifibactin and cupriachelin, are known to be photoreactive, and photoproducts of each complex are known. Reported herein is the structural characterization of several new photoproducts of both Fe(III)-pacifibactin and Fe(III)-cupriachelin, differing significantly from the previously known photoproducts. The relative abundances of photoproducts observed at differing time points of irradiation are also described, the first example of a time-dependent analysis of Fe(III)-siderophore photoreactivity. Together these results support a mechanistic hypothesis of successive photolytic decarboxylation events driving Fe(III)-siderophore photoreactions.

TABLE OF CONTENTS

1. Microbial Iron Acquisition Through Siderophores 1

1.1. Environmental Scarcity of Iron and Role of Siderophores 1

1.2. Siderophore Structural Motifs and Fe(III) Binding Sites 2

1.2.1. Catechol Binding Groups 2

1.2.2. Hydroxamate and Diazeniumdiolate Binding Groups 4

1.2.3. α-Hydroxycarboxylate Binding Groups 6

1.2.3.1. Citrate and α-Ketoglutarate Binding Groups 6

1.2.3.1. β-Hydroxyaspartate Binding Groups 7

1.3. Fe(III)-Siderophore Complex Stability and Chirality 10

1.4. Photoreactivity of Fe(III)-Siderophore Complexes 11

1.4.1. Photoreactivity of Fe(III) Complexes of Citrate Siderophores 11

1.4.2. Photoreactivity of Fe(III) Complexes of β-Hydroxyaspartate Siderophores 12

1.4.3. Mechanistic Insights of Siderophore Photoreactivity from Synthetic Studies 14

1.4.4. Biological Considerations of Fe(III)-Siderophore Photoreactivity 17

1.5. Microbial Biosynthesis of Siderophores 18

1.5.1. Biosyntheses Mediated by Non-Ribosomal Peptide Synthetases .. 18

1.5.1.1. Siderophore Biosynthesis by Iterative NRPSs 20

1.5.1.2. Hybrid NRPS/PKS Biosynthesis 22

1.5.1.3. Aspartyl β-Hydroxylases Involved in NRPS Siderophore Biosyntheses 23

1.5.1.4. Genome Mining for NRPS Biosynthesis Pathways 27
1.5.2. Biosyntheses Mediated by NRPS-Independent Synthetases 27
1.6. Siderophore Transport and Iron Release 29
1.6.1. Siderophore Export 29
1.6.2. Uptake of Fe(III)-Siderophore Complexes and Release of Iron 30
1.7. Conclusions 33
1.8. References 35
2. Characterization of the New Siderophore Pacifibactin and its Biosynthetic Gene Cluster in *Alcanivorax pacificus* 49
2.1. Introduction 49
2.2. Experimental 50
2.2.1. General Experimental Procedures 50
2.2.2. Genome Mining and Gene Cluster Annotation 51
2.2.3. Bacterial Growth and Siderophore Isolation 51
2.2.4. Amino Acid Analysis 52
2.2.5. Fe(III) Titration of Pacifibactin 53
2.2.6. Photolysis of Pacifibactin 54
2.2.7. Preparation of Ga(III)-Pacifibactin 54
2.2.8. Exchange of Zr(IV) Between Pacifibactin and Desferrioxamine B 54
2.3. Results and Interpretation 55
2.3.1. Putative Siderophore Biosynthetic Gene Cluster Identified Through Genome Mining 55

2.3.2. Isolation and Structural Characterization of Pacifibactin 57

2.3.3. Characterization of Structural Variants of Pacifibactin 68

2.3.4. Fe(III) Titration of Pacifibactin 74

2.3.5. Photolysis of Fe(III)-Pacifibactin 75

2.3.6. Characterization of Ga(III)-Pacifibactin 76

2.3.7. Zr(IV) Exchange Between Pacifibactin and Desferrioxamine B ... 81

2.4. Discussion 83

2.5. References 85

3. Stereochemical Characterization of β-Hydroxyaspartate Siderophores 89

3.1. Introduction 89

3.2. Experimental 91

3.2.1. Bacterial Strains and Growth 91

3.2.2. Siderophore Isolation 92

3.2.3. Amino Acid Analysis 93

3.3. Results and Interpretation 94

3.3.1. Isolation and Characterization of Alterobactin A from *P. luteoviolacea* DSM-6061 94

3.3.2. Isolation and Stereochemical Characterization of Delftibactin 98

3.3.3. Isolation and Stereochemical Characterization of Pyoverdine GB-1 102

3.3.4. Isolation and Stereochemical Characterization of Histicorrugatin 106

3.4. Discussion 109

3.5. References 111

4. Structural Revision of the Siderophore Cupriachelin, and Characterization of New Cupriachelin Variants 114

4.1. Introduction 114

4.2. Experimental 115

4.2.1. Culturing of *Cupriavidus necator* H16 115

4.2.2. Isolation and Characterization of Cupriachelins 115

4.2.3. Amino Acid Analysis 116

4.3. Results and Interpretation 116

4.3.1. Isolation and Stereochemical Characterization of Cupriachelin 116

4.3.2. Characterization of Cupriachelin Fatty Acid Variants 120

4.3.3. Characterization of Cupriachelin C-Terminal Residue Variants 127

4.4. Discussion 133

4.5. References 135

5. Characterizing and Modulating Photoreactivity of Fe(III)-β-Hydroxyaspartic Acid Siderophore Complexes 137

5.1. Introduction 137

5.2. Experimental 139

5.2.1. Isolation of Pacifibactin from *Alcanivorax pacificus* W11-5 139

5.2.2. Isolation of Cupriachelin from *Cupriavidus necator* H16 140

5.2.3. Preparation of Fe(III)-Siderophore Reaction Mixtures 141

5.2.4. Photolysis Conditions 141

5.2.5. UPLC-ESIMS and ESIMS/MS Analysis of Photoreactions 142

5.3. Results and Interpretation 142

5.3.1. Characterization of New Pacifibactin Photoproducts 142

5.3.2. Characterization of New Cupriachelin Photoproducts 151

5.3.3. Shifts in Photoproduct Abundance Over Time 157

5.3.4. Changes in Photoproduct Abundance from Addition of Phenanthroline 165

5.4. Discussion 168

5.5. References 171

LIST OF FIGURES

Figure 1.1 Schematic of siderophore-mediated iron acquisition 2

Figure 1.2 Tris-catecholate siderophores 3

Figure 1.3 Examples of hydroxamate-containing siderophores 5

Figure 1.4 The siderophore gramibactin of *Paraburkholderia graminis* 6

Figure 1.5 Examples of siderophores containing citrate and α-ketoglutarate functional groups 7

Figure 1.6 Selection of siderophores containing β-hydroxyaspartate.....9

Figure 1.7 Possible stereocenters around the iron center of a typical hexadentate Fe(III)-siderophore complex containing three bidentate metal binding sites 11

Figure 1.8 Photoreactions of Fe(III)-citrate siderophore complexes 12

Figure 1.9 Photoreactions of β-OHAsp Fe(III)-siderophore complexes 14

Figure 1.10 Synthetic metallo-α-hydroxy acid complexes. 15

Figure 1.11 Proposed photolysis reaction scheme of $[M_3(X\text{-}Sal\text{-}AHA)_3(\mu_3\text{-}OCH_3)]^-$ trimeric clusters, adapted from Grabo *et al*. 17

Figure 1.12 The core enzymatic domains in a NRPS protein.....20

Figure 1.13 Schematic of the iterative biosynthesis of enterobactin in *Escherichia coli* 21

Figure 1.14 Visualization of PKS-mediated Claisen condensation between a NRPS-recruited amino acid and a PKS-recruited substrate 22

Figure 1.15 Stereoisomers of β-OHAsp 23

Figure 1.16 Proposed mechanistic pathway for β-hydroxylation of thiolated L-Asp catalyzed by SyrP, adapted from the mechanism of substrate hydroxylation in non-heme Fe(II) αKG-dependent dioxygenases.....24

Figure 1.17 NRPS biosynthetic pathways for the siderophores taiwachelin (top) and serobactin (bottom).....26

Figure 1.18 Crystal structure of ferric enterobactin OMR protein FepA 31

Figure 2.1 Graphical representation of *pfb* gene cluster within the *Alcanivorax pacificus* genome; *pfb* gene cluster annotated with NRPS and PKS domains 56

Figure 2.2 HR-ESI-MS spectrum of pacifibactin, m/z 923.4081 $[M+H]^{1+}$ 58

Figure 2.3 ESI-MSMS spectrum of pacifibactin (m/z = 462.2, z = 2), with selected regions zoomed in for clarity 59

Figure 2.4 Structure of pacifibactin, with b/y peptide fragment masses 61

Figure 2.5 ^{1}H (500 MHz) NMR spectrum of pacifibactin (20 mg) in $(CD_3)_2SO$ 62

Figure 2.6 ^{1}H (500 MHz) NMR spectrum of pacifibactin (10 mg) in $(CD_3)_2SO$ previously dissolved in D_2O to eliminate signals from exchangeable protons.....62

Figure 2.7 ^{13}C (125 MHz) NMR spectrum of pacifibactin (20 mg) in $(CD_3)_2SO$ 63

Figure 2.8 ^{1}H-^{13}C HSQC (600 MHz) NMR spectrum of pacifibactin (20 mg) in $(CD_3)_2SO$..63

Figure 2.9 ^{1}H-^{1}H COSY (600 MHz) NMR spectrum of pacifibactin (20 mg) in $(CD_3)_2SO$...64

Figure 2.10 ^{1}H-^{13}C HMBC (600 MHz) NMR spectrum of pacifibactin (20 mg) in $(CD_3)_2SO$ 64

Figure 2.11 HPLC chromatograms of FDAA-derivatized pacifibactin hydrolysate and FDAA-derivatized pacifibactin hydrolysate co-injected with FDAA-derivatized amino acid standards 67

Figure 2.12 HPLC chromatograms of FDAA-derivatized pacifibactin hydrolysate from reductive hydrolysis with HI co-injected with FDAA-derivatized L-Orn and D-Orn standards 68

Figure 2.13 MSMS b/y fragmentation patterns for pacifibactin Ser (470.2 *m/z* $[M+2H]^{2+}$) and Gly (455.2 *m/z* $[M+2H]^{2+}$) variants 70

Figure 2.14 ESI-MS spectrum of pacifibactin variants from an L-Ser-amended culture of *A. pacificus* and from a Gly-amended culture of *A. pacificus*.....71

Figure 2.15 ESI-MSMS spectrum of pacifibactin-Ser (m/z = 470.2, z = 2), with selected region zoomed in for clarity 72

Figure 2.16 ESI-MSMS spectrum of pacifibactin-Gly (m/z = 455.2, z = 2), with selected region zoomed in for clarity 73

Figure 2.17 UV-visible absorption spectrum of 0.1 mM Fe(III)-pacifibactin in 100 mM MOPS buffer pH 7.1. Insert: spectrophotometric titration of apo pacifibactin 75

Figure 2.18 UV-visible absorbance spectra of 0.1 mM Fe(III)-pacifibactin in 100 mM MOPS buffer pH 7.1 subjected to 8 h of continuous photolysis with 450W UV mercury-arc lamp. Inset: structure of photoproduct detected by UPLC-ESI-MSMS (390.2 *m/z*, z = 1), with MSMS b/y fragmentation pattern 76

Figure 2.19 ^{1}H (500 MHz) NMR spectrum of Ga(III)-pacifibactin (10 mg) in D_2O 78

Figure 2.20 ^{13}C (125 MHz) NMR spectrum of Ga(III)-pacifibactin (10 mg) in D_2O 78

Figure 2.21 ^{1}H-^{1}H COSY (600 MHz) NMR spectrum of Ga(III)-pacifibactin (10 mg) in D_2O 79

Figure 2.22 ^{1}H-^{13}C HMBC (600 MHz) NMR spectrum of Ga(III)-pacifibactin (10 mg) in D_2O. 79

Figure 2.23 ^{1}H-^{13}C HMBC (600 MHz) NMR spectrum of Ga(III)-pacifibactin (10 mg) in 10% D_2O 80

Figure 2.24 ^{1}H (500 MHz) NMR spectrum of Ga(III)-pacifibactin (10 mg) in D_2O 80

Figure 2.25 Extracted ion chromatograms of apo pacifibactin and Zr(IV)-pacifibactin from a UPLC-ESIMS analysis of 0.1 mM pacifibactin and 0.1 mM $Zr(acac)_2$ after overnight incubation; Inset: ESI-MS spectrum of Zr(IV)-pacifibactin.....82

Figure 2.26 Extracted ion chromatograms of Zr(IV)-desferrioxamine B, Zr(IV)-pacifibactin, apo desferrioxamine B, and apo pacifibactin from UPLC-ESIMS analysis of 0.1 mM Zr(IV)-pacifibactin incubated with 0.1 mM apo DFOB for one hour 83

Figure 3.1 Phylogenetic tree of putative NRPS-associated β-hydroxylase-encoding genes ...90

Figure 3.2 Positive-ion mode ESI-MS spectrum of alterobactin A from *P. luteoviolacea* DSM 6061.....95

Figure 3.3 ESI-MSMS spectrum of alterobactin A 96

Figure 3.4 HPLC co-injection of FDAA-derivatized D,L-*threo*-β-OHAsp standard with derivatized alterobactin hydrolysate 97

Figure 3.5 Positive-ion mode ESI-MS spectrum of delftibactin isolated from *Delftia acidovorans* DSM 39 99

Figure 3.6 Extracted ion chromatograms of the FDAA-β-OHAsp molecular ion (402 m/z $[M+H]^+$) from UPLC-ESIMS analysis of FDAA-derivatized DL-*erythro*-β-OHAsp, DL-*threo*-β-OHAsp and delftibactin hydrolysate (HCl hydrolysis) 100

Figure 3.7 HPLC co-injections of FDAA-derivatized amino acid standards with delftibactin hydrolysate 101

Figure 3.8 Positive-ion mode ESI-MS spectrum of pyoverdine GB-1 isolated from *Pseudomonas putida* GB-1 103

Figure 3.9 Extracted ion chromatograms of the FDAA-β-OHAsp molecular ion (402 m/z $[M+H]^+$) from UPLC-ESIMS analysis of FDAA-derivatized DL-*erythro*-β-OHAsp, DL-*threo*-β-OHAsp and pyoverdine GB-1 hydrolysate (HCl hydrolysis) 104

Figure 3.10 HPLC co-injections of FDAA-derivatized amino acid standards with pyoverdine GB-1 hydrolysate (HCl hydrolysis) 106

Figure 3.11 Positive-ion mode ESI-MS spectrum of histicorrugatin isolated from *P. thivervalensis* DSM 13194 107

Figure 3.12 Extracted ion chromatograms of the FDAA-β-OHAsp molecular ion (402 m/z $[M+H]^+$) from UPLC-ESIMS analysis of FDAA-derivatized DL-*erythro*-β-OHAsp, DL-*threo*-β-OHAsp and histicorrugatin hydrolysate (DCl hydrolysis) 108

Figure 3.13 HPLC co-injections of FDAA-derivatized amino acid standards with histicorrugatin hydrolysate (HCl hydrolysis) 109

Figure 3.14 Phylogenetic tree of putative NRPS-associated β-hydroxylase-encoding genes labelled with the stereochemistry at the 3 carbon of the β-OHAsp residue associated with the hydroxylase with associations determined from the work presented in this chapter 110

Figure 4.1 Positive-ion mode ESI-MS spectrum of cupriachelin isolated from *Cupriavidus necator* H16 117

Figure 4.2 ESI-MSMS spectrum of cupriachelin 118

Figure 4.3 Extracted ion chromatograms of the FDAA-β-OHAsp molecular ions (402 m/z $[M+H]^+$, 803 m/z $[M+M+H]^+$) from UPLC-ESIMS analysis of FDAA-derivatized DL-*erythro*-β-OHAsp, DL-*threo*-β-OHAsp and cupriachelin hydrolysate (HCl hydrolysis), and co-injections of cupriachelin hydrolysate with each standard 119

Figure 4.4 Positive-ion mode ESI-MS spectrum of cupriachelin C8 121

Figure 4.5 ESI-MSMS spectrum of cupriachelin C8 122

Figure 4.6 Positive-ion mode ESI-MS spectrum of cupriachelin C12 123

Figure 4.7 ESI-MSMS spectrum of cupriachelin C12 124

Figure 4.8 Positive-ion mode ESI-MS spectrum of cupriachelin C11 125

Figure 4.9 ESI-MSMS spectrum of cupriachelin C11 126

Figure 4.10 Total ion chromatogram of *C. necator* culture supernatant extract injection on UPLC-ESI-MS, highlighting the peaks of m/z 762 and 790 closely eluting to cupriachelins C8 and C10, respectively 128

Figure 4.11 Positive-ion mode ESI-MS spectrum of cupriachelin C8a. The structure is depicted as a desaturation in the 3-hydroxybutyrate moiety, but this structure is speculative until further characterization is completed 129

Figure 4.12 Positive-ion mode ESI-MS spectrum of cupriachelin C10a. The structure is depicted as a desaturation in the 3-hydroxybutyrate moiety, but this structure is speculative until further characterization is completed 130

Figure 4.13 ESI-MSMS spectrum of cupriachelin C8a 131

Figure 4.14 ESI-MSMS spectrum of cupriachelin C10a 132

Figure 4.15 Phylogenetic tree of putative NRPS-associated β-hydroxylase-encoding genes labelled with the stereochemistry at the 3 carbon of the β-OHAsp residue associated with the hydroxylase with associations determined from this chapter and that presented in Chapter 3 134

Figure 5.1 Photoreactions and known photoproducts of Fe(III)-aerobactin and Fe(III)-aquachelin 138

Figure 5.2 Pacifibactin photoproducts identified by ESI-MS/MS 144

Figure 5.3 Positive-mode ESI-MS spectrum of pacifibactin photoproducts **1-3** molecular ions detected after 30 minutes of irradiation of 0.1 mM Fe(III)-pacifibactin in 25 mM MOPS buffer 145

Figure 5.4 Positive mode ESI-MS/MS spectrum of pacifibactin photoproduct **1**: 439 m/z, $[M+2H]^{2+}$ 146

Figure 5.5 Positive mode ESI-MS/MS spectrum of pacifibactin photoproduct **2**: 416 m/z, $[M+2H]^{2+}$ 147

Figure 5.6 Positive mode ESI-MS/MS spectrum of pacifibactin photoproduct **3**: 402 m/z, $[M+2H]^{2+}$ 148

Figure 5.7 Positive-mode ESI-MS spectrum of pacifibactin photoproduct **4** and backbone cleavage photoproduct molecular ions detected after 30 minutes of irradiation of 0.1 mM Fe(III)-pacifibactin in 25 mM MOPS buffer 149

Figure 5.8 Positive mode ESI-MS/MS spectrum of pacifibactin photoproduct **8**: 388 m/z, $[M+2H]^{2+}$ 150

Figure 5.9 Cupriachelin photoproducts identified by ESI-MS/MS 152

Figure 5.10 Positive-mode ESI-MS spectrum of cupriachelin photoproducts **5-10** molecular ions detected after 30 minutes of irradiation of 0.1 mM Fe(III)-cupriachelin in 25 mM MOPS buffer.....153

Figure 5.11 Positive mode ESI-MS/MS spectrum of cupriachelin photoproducts **5** and **6**: 762 m/z, $[M+H]^{+}$.....154

Figure 5.12 Positive mode ESI-MS/MS spectrum of cupriachelin photoproduct **7**: 716 m/z, $[M+H]^{+}$.....155

Figure 5.13 Positive mode ESI-MS/MS spectrum of cupriachelin photoproducts **8** and **9**: 688 m/z, $[M+H]^{+}$.....156

Figure 5.14 Positive mode ESI-MS/MS spectrum of cupriachelin photoproduct **10**: 688 m/z, $[M+H]^{+}$.....157

Figure 5.15 Extracted ion chromatograms of pacifibactin photoproducts **1-4** and backbone cleavage photoproduct from UPLC-ESIMS analysis of 0.1 mM Fe(III)-pacifibactin in 25 mM MOPS pH 7.2 after 10, 20, 30, 60, and 120 minutes of irradiation.....159

Figure 5.16 Putative N-terminal peptide backbone cleavage photoproducts identified from Fe(III)-cupriachelin photoreaction samples.....160

Figure 5.17 ESIMS/MS spectrum of 403 m/z molecular ion detected in Fe(III)-cupriachelin photoreactions. Fragmentation observed is consistent with a peptide backbone cleavage structure.....161

Figure 5.18 ESIMS/MS spectrum of 403 m/z molecular ion detected in Fe(III)-cupriachelin photoreactions. Fragmentation observed is consistent with a peptide backbone cleavage structure and loss of one equivalent of CO_2 from the β-OHAsp residue 162

Figure 5.19 Extracted ion chromatograms of cupriachelin photoproducts **5-10** and putative backbone cleavage photoproducts from UPLC-ESIMS analysis of 0.1 mM Fe(III)-cupriachelin in 25 mM MOPS pH 7.2 after 10, 20, 30, 60, and 120 minutes of irradiation .164

Figure 5.20 UV-visible absorbance spectrum of Fe(III)-cupriachelin (0.1 mM, 25 mM MOPS) in presence of 0.6 mM phenanthroline, before UV irradiation and after 1 h UV irradiation.....166

Figure 5.21 Extracted ion chromatograms of pacifibactin photoproducts **1-4** and backbone cleavage photoproduct from UPLC-ESIMS analysis of 0.1 mM Fe(III)-pacifibactin 0.6 mM phen after 3 h of irradiation 167

Figure 5.22 Extracted ion chromatograms of cupriachelin photoproducts **5-10** and backbone cleavage photoproducts from UPLC-ESIMS analysis of 0.1 mM Fe(III)-cupriachelin and 0.6 mM phen in 25 mM MOPS after 3 h of irradiation 168

LIST OF TABLES

Table 1.1 Proton-independent formation constants ($\log K_f$) and pFe measurements of selected hexadentate Fe(III)-siderophore complexes and that of Fe(III)-EDTA.....10

Table 2.1 Full annotation of the *pfb* gene cluster.....57

Table 2.2 NMR spectroscopic data (500 MHz, $(CD_3)_2SO$) for pacifibactin 65

Table 2.3 ^{13}C Chemical shifts of Ga(III)-pacifibactin (in D_2O) compared to apo pacifibactin 77

1. Microbial Iron Acquisition Through Siderophores

Sections of this chapter were published in: Hardy, C. D.; Butler, A. β-Hydroxyaspartic acid in siderophores: biosynthesis and reactivity. *J. Biol. Inorg. Chem.* **2018**, *23*, 957-967.

1.1. Environmental Scarcity of Iron and Role of Siderophores

Iron is a required nutrient for nearly all life, yet many microbes thrive in environments that lack iron in readily bio-available forms. Fe(III) forms insoluble ferric hydroxide species at aerobic physiological pH conditions, while bacteria require micromolar intracellular levels of iron.[1] The insolubility of Fe(III) is particularly striking in the oceans. Dissolved iron concentrations below 1 nM are observed in surface ocean waters.[2-4] Pathogenic bacteria also face severe iron limitations. In eukaryotic organisms, cellular Fe(III) is sequestered by storage proteins, transport proteins and iron-utilizing enzymes, preventing uptake of the iron by bacteria. To compensate for these environmental conditions, bacteria have evolved several systems to effectively scavenge iron. One strategy is the biosynthesis and export of siderophores, small molecule Fe(III) chelators that coordinate Fe(III) with exceptional affinity.[5-8] Siderophores are exported into the environment to scavenge Fe(III). Fe(III)-siderophore complexes are then recognized by specific outer membrane receptor proteins and brought into the cell through an active transport mechanism.

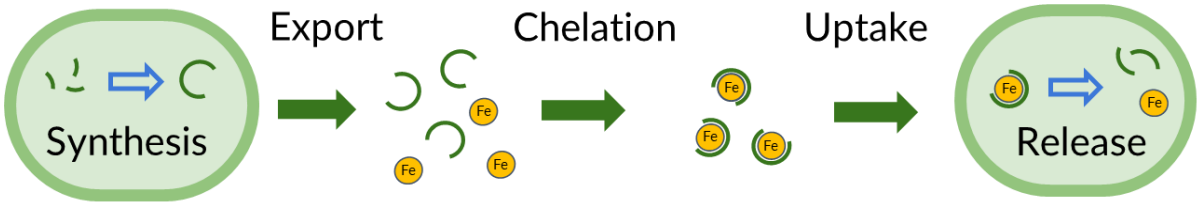

Figure 1.1. Schematic of siderophore-mediated iron acquisition. Siderophores are biosynthesized within the bacterial cell and exported into the extracellular environment, whereupon the ligands bind to Fe(III). The Fe(III)-siderophore complex is then recognized by an outer membrane receptor and brought back into the bacterium, and the iron is released for use in cellular processes.

1.2. Siderophore Structural Motifs and Fe(III) Binding Sites

Siderophores are an incredibly diverse class of secondary metabolites. Over 500 siderophores have been identified, nearly 300 of which have been structurally characterized.[8] Most siderophores provide hexadentate coordination of Fe(III) via hard donor groups, typically oxygen, yielding stable high spin Fe(III) complexes. Siderophores are typically classified by their component Fe(III) binding groups. Siderophores can contain one or multiple types of Fe(III) binding sites, the common classes of which are described herein.

1.2.1. Catechol Binding Groups

The catechol functional group provides bidentate Fe(III) coordination through the deprotonated hydroxy substituents of the benzyl ring. The well-studied siderophore enterobactin,[9] produced by *E. coli* and several other bacteria, contains three catechol groups derived from 2,3-dihydroxybenzoic acid (DHB), which is appended to L-serine. Three 2,3-DHB-L-Ser are cyclized to form a macrolactone backbone (Figure 1.2).

Several tris-catecholate siderophores structurally similar to enterobactin have been characterized. Salmochelin, produced by *Salmonella* species, some pathogenic *E. coli* strains, and some *Klebsiella* strains, is a glycosylated derivative of the 2,3-DHB-Ser cyclized trimer,

with two catechol moieties glycosylated at the 5 position (Figure 1.2).[10-12] This glycosylation is notable as it allows salmochelin to evade the mammalian protein siderocalin,[13] a protein which sequesters Fe(III)-enterobactin as part of the innate immune response.[14] The amphi-enterobactins are yet another example of an enterobactin derivative.[15] Amphi-enterobactin consists of three 2,3-DHB-Ser units and one L-Ser-fatty acid unit of varying length, cyclized to form a tetralactone core (Figure 1.2).

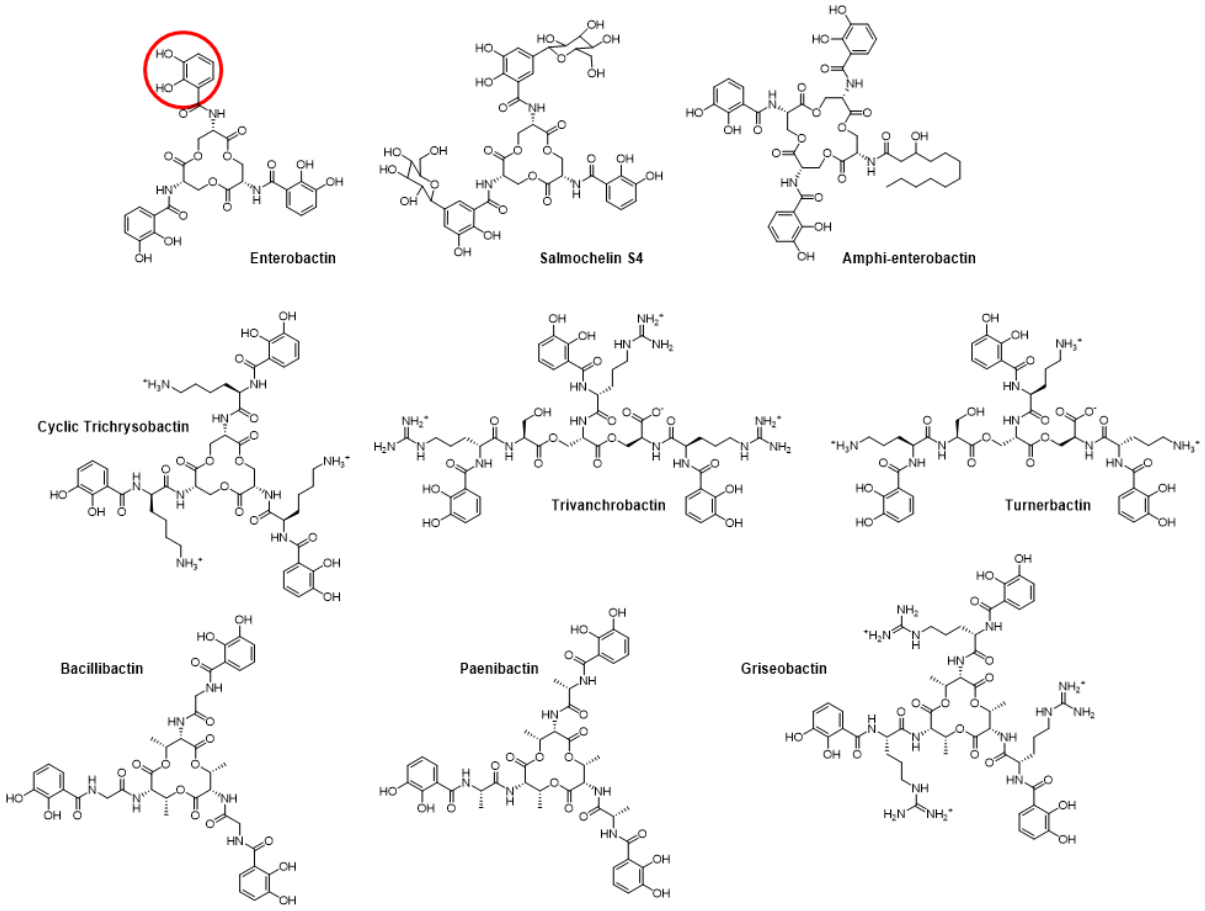

Figure 1.2. Tris-catecholate siderophores (catechol group circled).

Many tris-catecholate siderophores differ from enterobactin by the incorporation of an additional amino acid residue between DHB and Ser. In several examples, these "spacer" amino acid residues are cationic amino acids. Cyclic trichrysobactin of *Dickeya chrysanthemi*

is a trimer of 2,3-DHB-D-Lys-L-Ser, trivanchrobactin *Vibrio campbellii* DS40M4 is a trimer of 2,3-DHB-D-Arg-L-Ser, and turnerbactin of *Teredinibacter turnerae* T7901 is a trimer of 2,3-DHB-L-Orn-L-Ser (Figure 1.2).[16-18] Bacillibactin of *Bacilius subtillis* 168 incorporates a spacer Gly residue, but additionally differs from enterobactin by incorporating threonine in place of serine (Figure 1.2).[19] Similar to bacillibactin, paenibactin of *Paenibacillus elgii* B69 is a trimer of 2,3-DHB-L-Ala-L-Thr, and griseobactin of *Streptomyces* sp. 700974 is a trimer of 2,3-DHB-L-Arg-L-Thr (Figure 1.2).[20-21]

1.2.2. Hydroxamate and Diazeniumdiolate Binding Groups

Hydroxamates are functional groups consisting of a carbonyl bound to a N-hydroxy group that provide bidentate OO' Fe(III) coordination. One well-characterized group of hydroxamate siderophores are the desferrioxamines, produced by many microbes over a diversity of environments (Figure 1.3). Most notable of this family is desferrioxamine B, first isolated from *Streptomyces pilosus*, and long used as a therapeutic agent in humans to treat iron-overload.[22-23] Siderophores of the desferrioxamine family consist of succinic acid and monohydroxylated diamines, such as N-hydroxycadaverine, joined by amide bonds, either linearized or as a macrocycle. Most desferrioxamines provide hexadentate coordination of Fe(III) through three hydroxamate functionalities, but variants containing two or four hydroxamate functionalities are also known.[24-26]

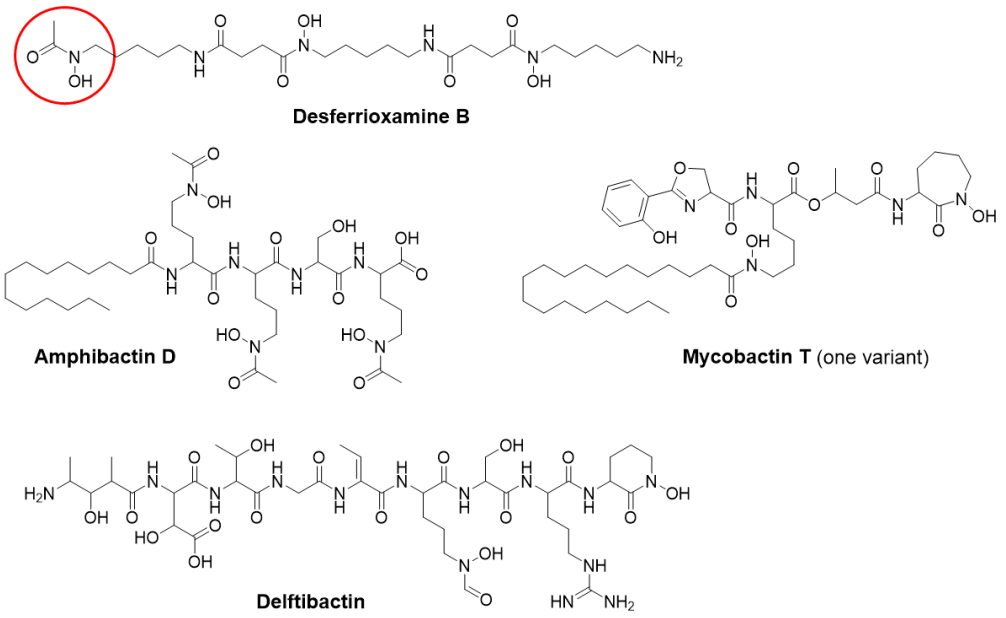

Figure 1.3. Examples of hydroxamate-containing siderophores (hydroxamate group circled).

Hydroxamates are also commonly found in peptidic siderophores, typically through hydroxylation and acylation of the side chain amine of ornithine, as in the amphibactins, produced by several *Vibrio* species and *Alcanivorax borkumensis* SK2 (Figure 1.3).[27-29] Hydroxamate moieties can also be formed from a carboxy terminus ornithine residue through N^5-hydroxylation and cyclization of the side chain with the carboxyl terminus, as observed in delftibactin of *Delftia acidovorans* (Figure 1.3).[30] N^5-hydroxylysine can function similarly, forming hydroxamates either through acylation or cyclization; both examples are present in the mycobactin siderophores of *Mycobacterium tuberculosis* and related species (Figure 1.3).[31]

The siderophore gramibactin of rhizosphere bacterium *Paraburkholderia graminis* C4D1M (Figure 1.4) has recently been reported to utilize diazeniumdiolate as an Fe(III) binding group.[32] The diazeniumdiolate functional group is structurally similar to, but distinct from, hydroxamate functional groups, consisting of an NO group bound to an N-hydroxy group. Genome screening of other plant-associated bacteria has identified several gene clusters

possibly encoding diazeniumdiolate-incorporating siderophore production, and has led to the structural characterization of several new siderophores.[33] Notably, diazeniumdiolate siderophores have been shown to release nitric oxide *in vitro* when incubated with plant root proteins, as well as *in planta*.[33]

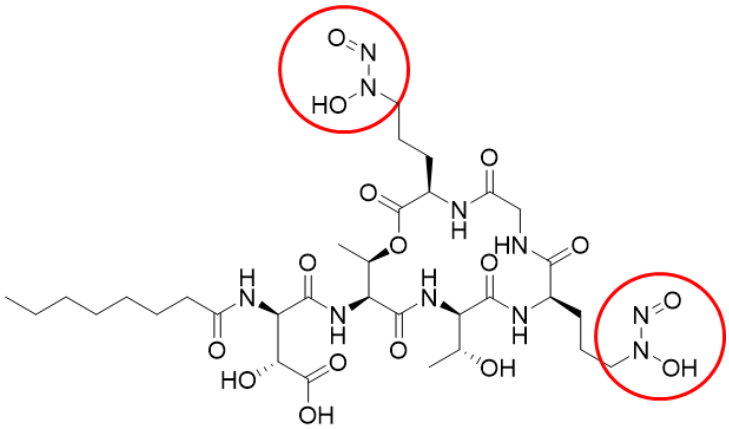

Figure 1.4. The siderophore gramibactin of *Paraburkholderia graminis* (diazeniumdiolate functional groups circled in red).

1.2.3. α-Hydroxycarboxylate Binding Groups

1.2.3.1. Citrate and α-Ketoglutarate Binding Groups

Citric acid is commonly incorporated into siderophore structures, providing bidentate OO' Fe(III) coordination through the α-hydroxycarboxylate functional group. Aerobactin, first isolated from opportunistic nosocomial pathogen *Klebsiella aerogenes* 62-1 (prev. known as *Aerobacter aerogenes*), coordinates iron through one citrate moiety and two hydroxamate functional groups (Figure 1.5).[34] Aerobactin biosynthesis genes have since been observed in several human pathogens, including in *Shigella* species, *Klebsiella pneumoniae,* and virulent *E. coli* strains.[35-37] Aerobactin production in these strains is often found to be a virulence factor.[35-36] Citric acid alone has also been reported to function as a siderophore in certain bacteria, with the diferric dicitrate complex taken up by outer membrane receptor FecA.[38]

Vibrioferrin, isolated from marine bacterium *Vibrio parahaemolyticus*, coordinates Fe(III) through both a citrate moiety as well as an α-hydroxy carboxylate group derived from cyclization of α-ketoglutaric acid (Figure 1.5).[39]

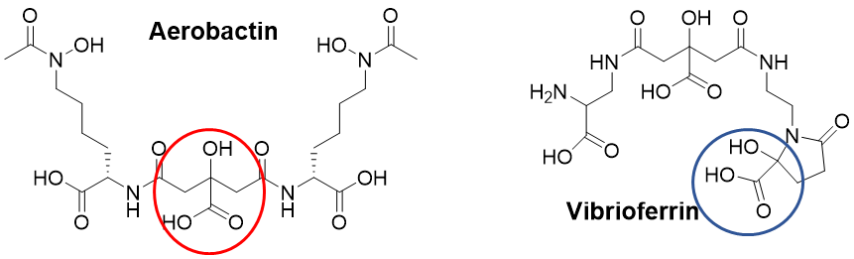

Figure 1.5. Examples of siderophores containing citrate (circled in red) and α-ketoglutarate (circled in blue) functional groups.

1.2.3.2. β-Hydroxyaspartate Binding Groups

β-Hydroxyaspartate functions as an Fe(III) binding group in an abundance of peptidic siderophores, providing bidentate coordination through the α-hydroxy carboxylate moiety, as observed with citrate functional groups. β-OHAsp was first reported as an Fe(III)-chelating group in a siderophore with the discovery of pseudobactin, a member of the pyoverdine siderophore family (Figure 1.6).[40-41] Since this discovery, many β-OHAsp siderophores have been isolated from marine bacteria, such as the alterobactins (Figure 1.6).[42] Many of the marine β-OHAsp siderophores are acylated at the N-terminus, including aquachelins,[27] marinobactins,[27] loihichelins,[43] and recently reported imaqobactin (Figure 1.6).[44] Acyl peptidic siderophores with β-OHAsp have also been isolated from terrestrial bacteria, including corrugatins,[45-47] serobactins,[48] variochelins,[49] taiwachelin,[50] crochelins,[51] and variobactins,[52] which are all produced by plant-associated and rhizosphere bacteria; cupriachelin, which is produced by a freshwater bacterium,[53] and sodachelins and halochelins which are produced by bacterial isolates from an alkaline saline lake (Figure 1.6).[54-56] Many examples of β-OHAsp

are not acylated, including many examples of pyoverdine siderophores incorporating β-OHAsp, the aforementioned alterobactins, malleobactins,[57-59] delftibactin,[30] vacidobactins,[52] acidobactins,[52] and pseudoalterobactins.[60]

β-OHAsp, unlike most amino acids, contains two chiral centers, at the α-carbon and the hydroxylated β-carbon. Most β-OHAsp siderophores contain either the L-*threo* (2S, 3S) or D-*threo* (2R, 3R) stereoisomer, but some examples containing the L-*erythro* (2S, 3R) isomer are known. To date, no siderophore incorporating a D-*erythro* (2R, 3S) β-OHAsp residue has been characterized. Several examples of pyoverdines[61-64] as well as the corrugatin siderophores[45-47] contain β-hydroxyhistine residues, which are known to function as bidentate metal chelators.[61] β-OHHis can form four stereoisomers in the same fashion as β-OHAsp, however to date only the L-*threo* residue has been observed in a siderophore structure.

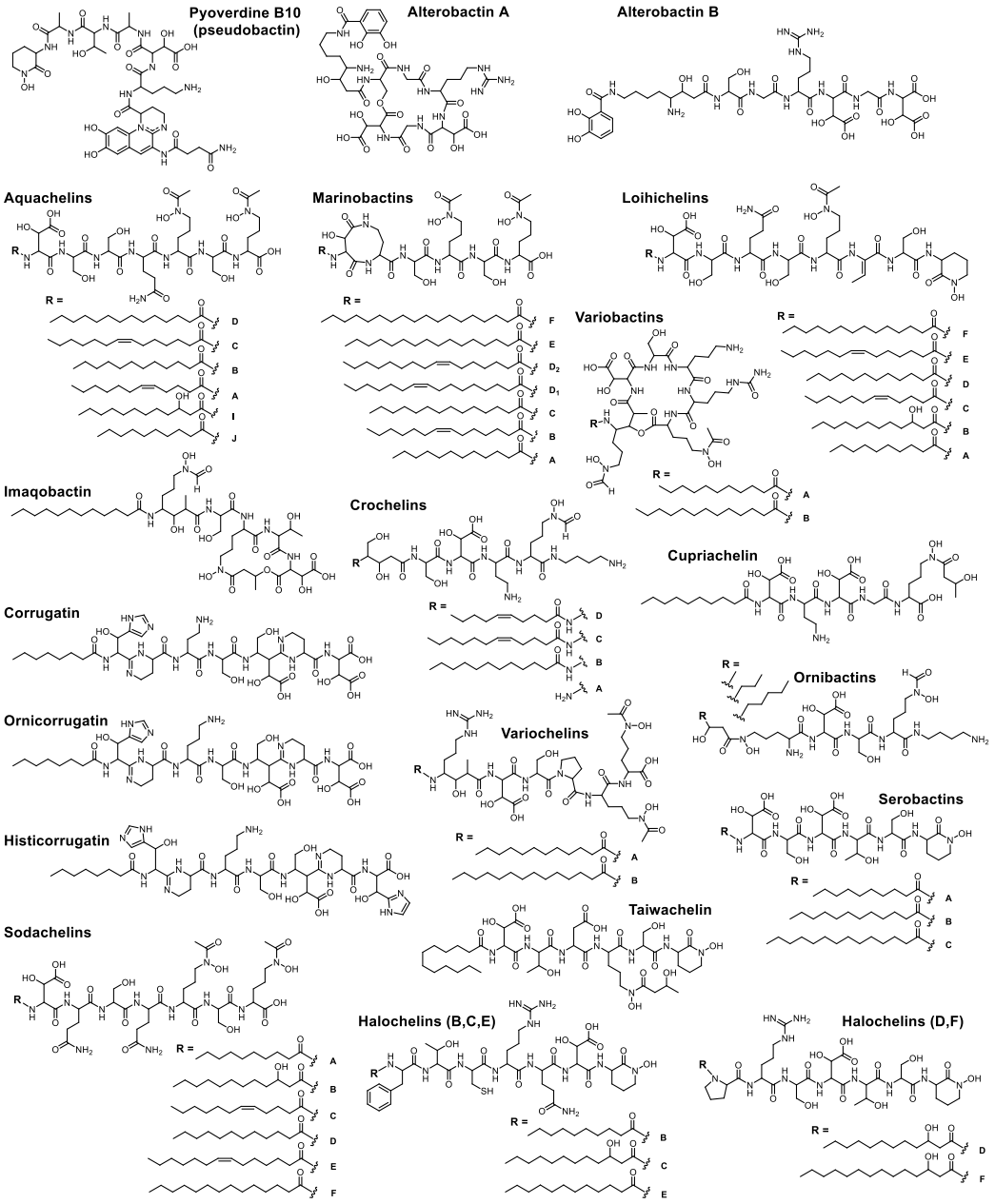

Figure 1.6. Selection of siderophores containing β-hydroxyaspartate. From top left: pyoverdine B10, also known as pseudobactin (*Pseudomonas* sp. B10);[40] alterobactins A and B (*Pseudoalteromonas luteoviolacea*);[42] aquachelins (*Halomonas aquamarina* DS40M3, *H. meridiana* str. HC4321C1);[27-28] marinobactins (*Marinobacter* sp. DS40M6, *M. nanhaiticus* D15-8w);[27, 65] variobactins (*Variovorax paradoxus* P4B);[52] loihichelins (*Halomonas* sp. LOB-5);[43] imaqobactin (*Variovorax* sp. RKJM285);[44] crochelins (*Azotobacter chroococcum*);[51] cupriachelin (*Cupriavidus necator* H16);[53] corrugatin (*Pseudomonas corrugata*);[47] ornicorrugatin (*Pseudomonas fluorescens* AF76);[46] histicorrugatin (*Pseudomonas thivervalensis* LMG 21626T);[45] variochelins (*Variovorax boronicumulans* BAM-48);[49] ornibactins (*Burkholderia cepacia* complex);[66-67] serobactins (*Herbaspirillum seropedicae* Z67);[48] taiwachelin (*Cupriavidus taiwanensis* LMG19424);[50] sodachelins (*Halomonas* sp. SL28);[54, 56] halochelins (*Halomonas* sp. SL01).[55]

1.3. Fe(III)-Siderophore Complex Stability and Chirality

The coordination chemistry properties of siderophores include a remarkable specificity for binding Fe(III), forming very thermodynamically stable complexes. The stability of an Fe(III)-siderophore complex is often represented by the proton-independent stability constant (K_f) defined for the reaction between a fully deprotonated ligand and Fe(III).[68] K_f measurements for Fe(III)-siderophore complexes are among the highest Fe(III) stability constants known.[69] To provide a more physiologically-relevant picture of complex stability, the pFe scale of Fe(III)-siderophore stability was developed. The pFe, or pM, term is usually defined as $-\log[Fe(H_2O)_6^{3+}]$ for $[Fe]_{total} = 10^{-6}$ M, [L] = 10^{-5} M, and pH 7.4.[70] A collection of siderophore stability constants is provided below (Table 1.1).

Table 1.1. Proton-independent formation constants ($\log K_f$) and pFe measurements of selected hexadentate Fe(III)-siderophore complexes and that of Fe(III)-EDTA.

Siderophore	$\log K_f$	pFe^{III}
Enterobactin[68]	49.0	34.3
Desferrioxamine B[71]	30.5	25
Marinobactin E[72]	31.8	25.8
Mycobactin J[70]	43.2	39.7
EDTA[73]	25.2	23.4

For siderophores that provide hexadentate Fe(III) coordination through three bidentate binding sites, the metal center of the Fe(III)-siderophore complex is chiral. Two enantiomers are possible: the right-handed (Δ) configuration and the left-handed (Λ) configuration (Figure 1.7). The chirality of the iron center is dependent on the overall structure and geometry of the ligand, and small perturbations in siderophore structure can alter this chirality. Fe(III)-

enterobactin is known to form the Δ configuration,[74] yet Fe(III)-bacillibactin forms the opposite Λ configuration, despite its similarity to the structure of enterobactin (Figure 1.2).[75] Cyclic trichrysobactin and trivanchrobactin each form the Δ configuration when bound to Fe(III).[16-17] This variation in chirality is relevant biologically, as stereoselectivity regarding the iron center in microbial Fe(III)-siderophore uptake is evident in multiple bacteria.[76-77]

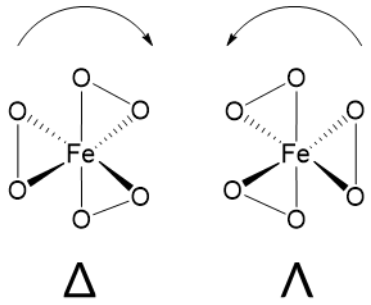

Figure 1.7. Possible stereocenters around the iron center of a typical hexadentate Fe(III)-siderophore complex containing three bidentate metal binding sites, the (Δ) configuration and the lambda (Λ) configuration.

1.4. Photoreactivity of Fe(III)-Siderophore Complexes

1.4.1. Photoreactivity of Fe(III) Complexes of Citrate Siderophores

Fe(III) complexes of citrate-containing siderophores are photochemically reactive,[78] as are Fe(III)-citrate complexes themselves.[79-80] In a $Fe(III)_2citrate_2$ complex, photon absorption into the Fe(III)-α-hydroxycarboxylate LMCT band, which is in the UV region, induces photoreduction of two equivalents of Fe(III) to Fe(II), coupled with decarboxylation and thus oxidation of one equivalent of citrate ligand to yield β-ketoglutaric acid (Figure 1.8a).[80] The 2:1 ratio of Fe(III) reduction to ligand oxidation is consistent with the two-electron decarboxylation of citrate. Fe(III)-aerobactin as well as other citrate-containing siderophores undergoes a photoinduced decarboxylation analogous to Fe(III)-citrate complexes, yielding a ketone/enol tautomer and Fe(II) (Figure 1.8b).[81-84] Fe(III) complexes of vibrioferrin undergo a

rapid photoinduced decarboxylation of the cyclized α-ketoglutarate group yielding Fe(II) and a photoproduct with the citrate group retained (Figure 1.8c).[85]

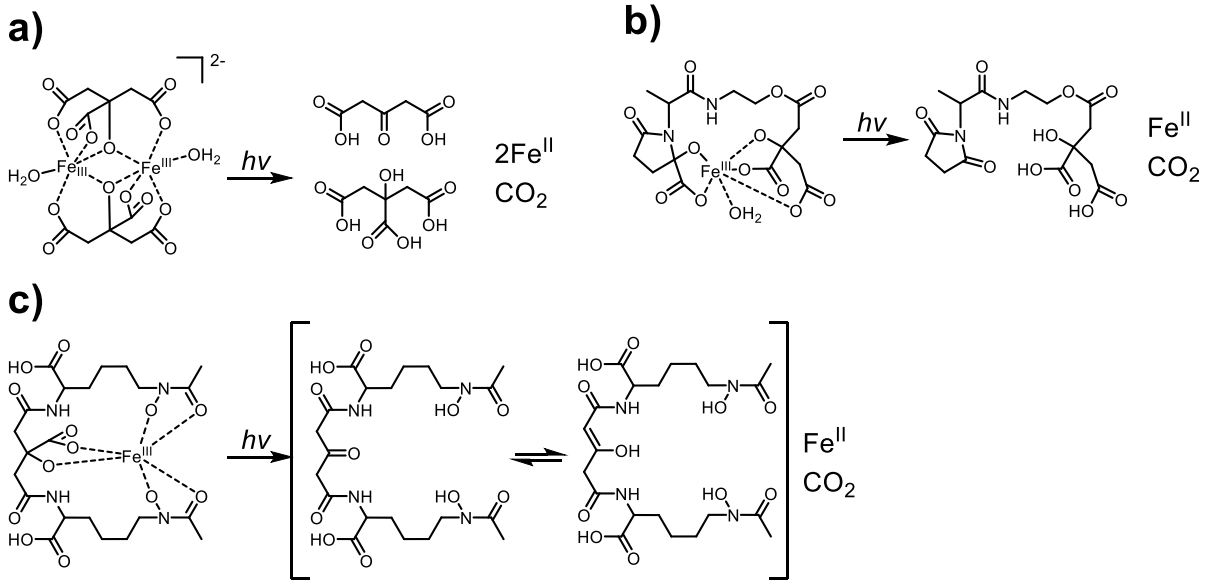

Figure 1.8. Photoreactions of Fe(III)-citrate siderophore complexes. a) Photoreaction of $Fe(III)_2citrate_2$. Two Fe(III) are reduced to Fe(II) while one citrate reacts to form β-ketoglutaric acid and CO_2 through an oxidative decarboxylation. Structure of complex adapted from X-ray crystallographic data by Shweky *et al*.[86] b) Photoreaction of Fe(III)-vibrioferrin. Decarboxylation of the cyclized α-ketoglutarate moiety occurs but the terminal citrate moiety remains intact.[85] c) Photoreaction of Fe(III)-aerobactin. Decarboxylation of the citrate moiety yields a ketone/enol tautomer photoproduct.[81]

1.4.2. Photoreactivity of Fe(III) Complexes of β-Hydroxyaspartate Siderophores

Photoreactivity of Fe(III) β-OHAsp siderophore complexes was first discovered with the aquachelins.[87] Fe(III)-aquachelin complexes exposed to natural sunlight exhibit an oxidative cleavage of the peptide backbone at the site of the β-OHAsp residue paired with Fe(III) reduction (Figure 1.9a), resulting in a hydrophilic peptide product that retains the two hydroxamate groups and coordinates Fe(III). The conditional stability constant for Fe(III) coordination by the product, $K_{FeL,Fe'}$ of $10^{11.5}$ M^{-1}, is somewhat less than the Fe(III) conditional stability constant of native aquachelin, $10^{12.2}$ M^{-1}.[87] The photoproducts of the citrate

siderophores aerobactin and petrobactin also coordinate Fe(III), with stability constants higher than that of the native siderophores.[81-82] Photolysis of Fe(III)-cupriachelin is only reported to generate a small hydrophilic peptidic product resulting from peptide backbone cleavage at the β-OHAsp residue of the C-terminal side (Figure 1.9b).[53] A fatty acid-containing photoproduct of Fe(III)-cupriachelin or a photoproduct resulting from cleavage at the β-OHAsp residue of the N-terminal side were not reported. Photolysis of Fe(III)-variochelin produces multiple photoproducts, including a hydrophobic fatty acid-containing fragment and a photoproduct with an intact backbone resulting from decarboxylation of the β-OHAsp residue (Figure 1.9c).[49]

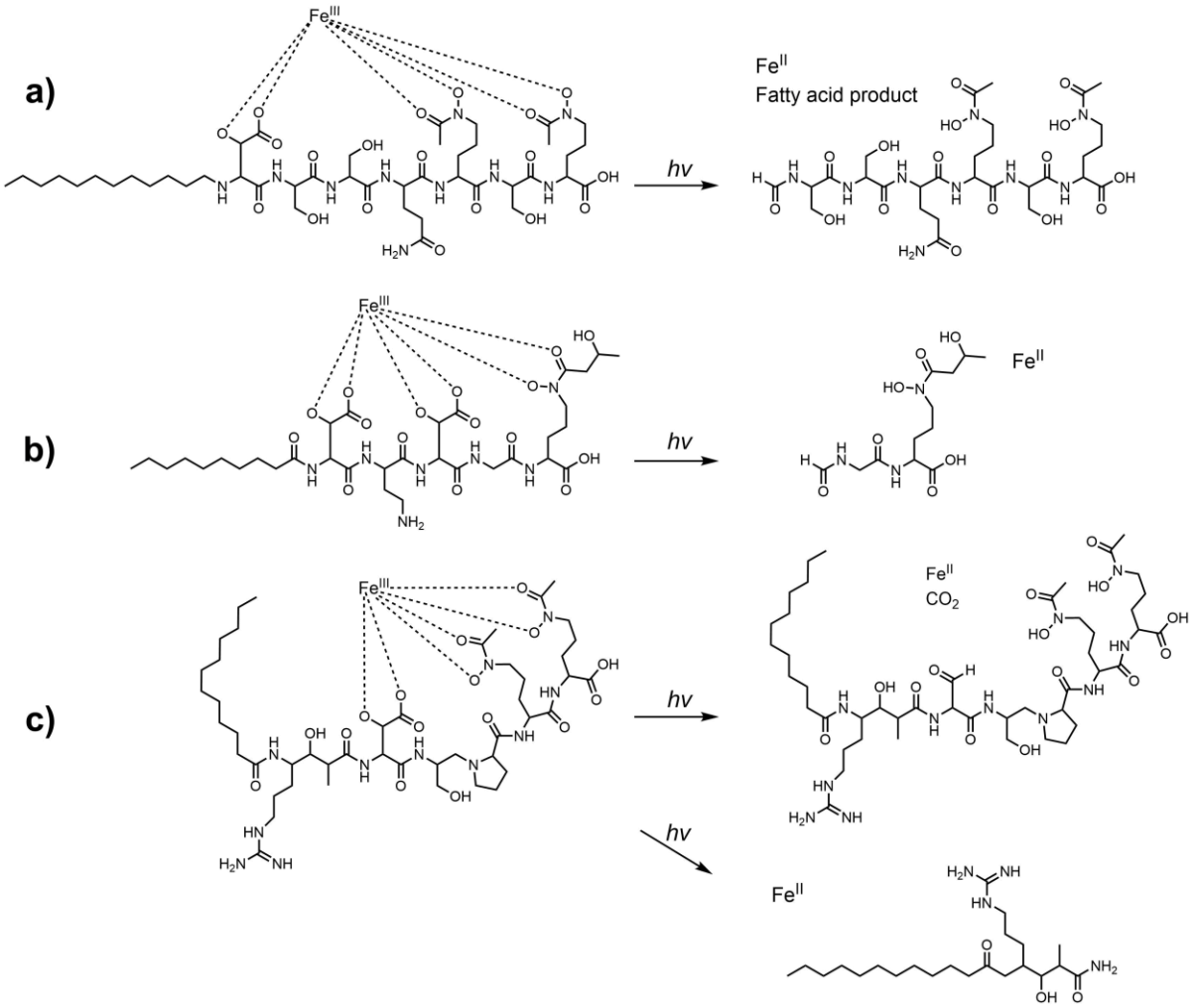

Figure 1.9. Photoreactions of β-OHAsp Fe(III)-siderophore complexes. a) Fe(III)-aquachelin, C-terminal photoproduct resulting from oxidative cleavage of the peptide backbone.[87] b) Fe(III)-cupriachelin, C-terminal photoproduct resulting from oxidative cleavage of the peptide backbone.[53] c) Fe(III)-variochelin, photoproduct with intact backbone resulting from oxidative decarboxylation of the β-OHAsp group and N-terminal photoproduct resulting from oxidative cleavage of the peptide backbone.[49]

1.4.3. Mechanistic Insights of Siderophore Photoreactivity from Synthetic Studies

While diferric dicitrate complexes exhibit a photolytic 2:1 Fe(III) reduction-to-ligand oxidation ratio, β-OHAsp siderophores coordinate Fe(III) in hexadentate mononuclear 1:1 complexes. Yet, these complexes are still readily photoreactive, producing one equivalent of Fe(II) per 2-electron oxidized siderophore photoproduct. Investigations of synthetic complexes

shed light on the mechanisms of the underlying Fe(III)-α-hydroxycarboxylate photochemical reactions and help explain this discrepancy. The trimeric cluster $[Fe(III)_3(X\text{-}Sal\text{-}AHA)_3(\mu_3\text{-}OCH_3)]^-$, where X-Sal-AHA is a tetradentate chelator consisting of an α-hydroxycarboxylate moiety appended to a salicylidene with varying phenolic ring substituents (Figure 1.10a),[88] undergoes a photoreaction yielding Fe(II) and an oxidized ligand photoproduct, the structure of which is dependent on the reaction conditions, as discussed below. Fe(III) reduction is coupled to ligand oxidation at a 2:1 ratio, measuring Fe(II) accumulation spectrophotometrically through bathophenanthroline disulfonate sequestration of Fe(II) and ligand oxidation by loss of circular dichroism spectroscopy signal from cleavage of the chiral α-carbon.[89] When the trimeric complex is prepared with Fe(III) and Ga(III), yielding mixed-ratio Fe(III)/Ga(III) clusters, the $FeGa_2$ cluster undergoes photolysis at the same rate as the Fe_3 clusters, with only the Ga_3 cluster proving resistant to photolysis. This result suggests that the reduction of two Fe(III) is not necessary for ligand oxidation to occur.[89]

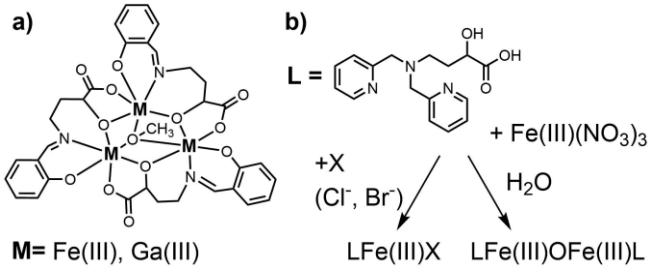

Figure 1.10. Synthetic metallo-α-hydroxy acid complexes. a) $[M_3(X\text{-}Sal\text{-}AHA)_3(\mu_3\text{-}OCH_3)]^-$ trimeric clusters, where X represents substituents on the phenolate rings: 5-NO_2, 3-5-diCl, 3-OCH_3, 3-5-di-*t*-Bu (for clarity, substituents not drawn).[88-89] b) Pyr-TPA-AHA complexes[90].

In photoreactions with a different set of clusters consisting of mono- and di-nuclear Fe(III)(Pyr-TPA-AHA) complexes, where Pyr-TPA-AHA is a tripodal amide chelate with two pyridyl groups and an α-hydroxycarboxylate moiety (Figure 1.10b), the stoichiometry of Fe(III) reduction to ligand oxidation is 2:1, while a 1:1 ratio is observed in mononuclear

complexes.[90] This difference in redox ratios is explained mechanistically through flash photolysis studies of related Fe(III)-carboxylate complexes, which indicate that the laser-triggered photolysis mechanism involves a long-lived Fe(II)-organic radical complex.[91] In a 2Fe(III) α-hydroxycarboxylate complex that radical is further oxidized by the second Fe(III), resulting in two Fe(II) and one two-electron oxidation product, as in $Fe(III)_2citrate_2$ complexes. In complexes with only one Fe(III) such as Fe(III)-β-OHAsp siderophore complexes, the extra electron likely reduces dioxygen or possibly solvent.[89, 92]

Mechanistic studies of these synthetic Fe(III) α-hydroxycarboxylate complexes[89, 92] can also explain the differences in photoproducts between citrate and β-OHAsp siderophore photoreactions. The $[Fe(III)_3(X\text{-}Sal\text{-}AHA)_3(\mu_3\text{-}OCH_3)]^-$ clusters under anaerobic conditions exhibit a photolytic decarboxylation of the β-OHAsp residue to form an aldehyde, cleaving the cluster and reducing Fe(III).[89] Under aerobic conditions a mass corresponding with further loss of CO from the anaerobic photoproduct is observed.[89] Both photoproducts are observed with addition of phenanthroline to the aerobic reaction, which slows air oxidation of photochemically-generated Fe(II).[89] When the clusters are irradiated under anaerobic conditions, then aerated and left in darkness, masses are observed corresponding to oxidation of an aldehyde to a carboxylate moiety, allowing for formation of a new Fe(III)-containing cluster.[89] These results together suggest a stepwise reaction sequence for photolysis dependent on light, Fe(III), and O_2 (Figure 1.11).[89] This proposed mechanism helps to explain the significantly different photoproducts observed from citrate and β-OHAsp Fe(III)-siderophore photoreactions. Initial light-driven decarboxylation of Fe(III)-siderophore complexes yields a ketone/enol tautomer moiety in citrate siderophores and an aldehyde moiety in β-OHAsp siderophores, and as aldehydes are more sensitive to oxidation than ketones, β-OHAsp Fe(III)-

siderophore complexes exhibit further photo-induced ligand breakdown. The proposed mechanism is supported by photoproducts of the Fe(III)-variochelin complex, which yields both a decarboxylation photoproduct and a backbone cleavage photoproduct (Figure 1.9c).[49]

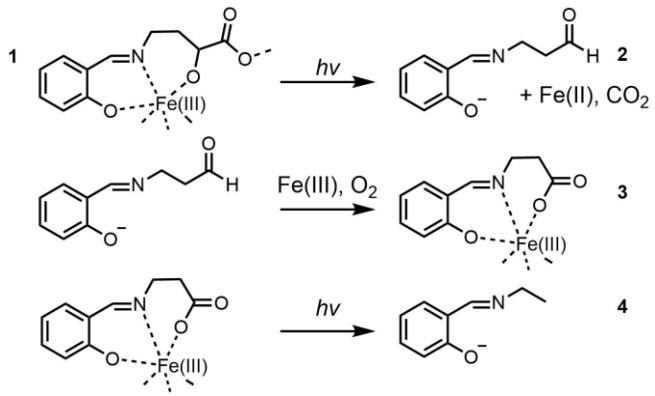

Figure 1.11. Proposed photolysis reaction scheme of $[M_3(X\text{-}Sal\text{-}AHA)_3(\mu_3\text{-}OCH_3)]^-$ trimeric clusters, adapted from Grabo *et al*.[89] Coordination mode of **3** to Fe(III) is not established crystallographically, thus coordination shown is based on known coordination mode of **1** to Fe(III).

1.4.4. *Biological Considerations of Fe(III)-Siderophore Photoreactivity*

The role of Fe(III)-siderophore photoreactivity in the biogeochemical cycling of iron in the oceans is of particular interest due to the abundance of β-OHAsp and citrate siderophores isolated from marine bacteria in the photic zone.[93-94] Fe(II) in oceanic surface waters undergoes diurnal cycles, with Fe(II) concentrations increasing during daylight hours.[95-97] Fe(III)-siderophore complex photoreactivity could partially contribute to this iron redox cycling, in light of the fact that greater than 99% of dissolved iron present in seawater is bound by strong organic ligands of comparable Fe(III) binding affinities to siderophores[2, 98] and the prevalence of biosynthetic genes encoding photoreactive siderophore production among microbes isolated from ocean environments.[99]

Because siderophore photoproducts can retain strong Fe(III) binding functionality, they may function as siderophores, promoting Fe(III) uptake. While this possibility has yet to be

studied with any β-OHAsp siderophore, the Fe(III)-bound photoproduct of aerobactin is taken up by the aerobactin producer *Vibrio sp.* DS40M5,[81] and petrobactin producers *Bacillus subtilis and B. cereus* can take up the Fe(III)-bound photoproduct of petrobactin.[14, 100] Fe(III)-siderophore complex photoreactivity has direct implications on iron uptake not only in the siderophore-producing bacteria, but also in other organisms. In ocean conditions, Fe(III) reduction is known to increase iron bioavailability to phytoplankton and stimulate growth,[93, 101] and indeed a natural planktonic assemblage is able to take up iron from photolyzed Fe(III)-aquachelin at levels comparable to uptake of inorganic iron supplementation, while native Fe(III)-aquachelin remains largely unavailable to phytoplankton.[87] Photolysis of Fe(III)-vibrioferrin promotes uptake of Fe(III) by the alga *Scrippsiella trochoida,* and alga-associated *Marinobacter* species which produce vibrioferrin, reflecting bacterial-algal symbiosis through siderophore-mediated photochemical cycling of Fe(III).[102] Fe(III) uptake is promoted despite the vibrioferrin photoproduct having no significant binding affinity towards Fe(III).[85]

1.5. Microbial Biosynthesis of Siderophores

1.5.1. Biosyntheses Mediated by Non-Ribosomal Peptide Synthetases

Many siderophores are biosynthesized by non-ribosomal peptide synthetases (NRPSs). An NRPS is a modular enzyme that synthesizes a peptide metabolite through an assembly line approach.[103-104] NRPS modules consist of discrete catalytic domains, each fulfilling distinct roles in the addition of a substrate, typically an amino acid, to the assembled product. An NRPS module must consist of at minimum an adenylation (A) domain, a thiolation (T) domain (often referred to as a peptidyl carrier protein, or PCP, domain), and a condensation (C) domain to incorporate a new residue (Figure 1.12).[104-105] The adenylation domain enforces selectivity of

the residue by admitting only the desired substrate for that step of metabolite formation, and catalyzes the reaction of the selected substrate with ATP to form the corresponding amino acyl-adenylate. The thiolation, or peptide carrier protein (PCP), domain reacts the formed amino acyl-adenylate with the terminal thiolate of the prosthetic 4'-phosphopantetheinyl arm bound to the domain, anchoring the substrate for further reactivity (Figure 1.12). The condensation domain catalyzes amide bond formation between two thiolation domain-bound substrates. Once all residues are incorporated, the complete product is passed to the thioesterase (TE) domain, where it is released from the assembly line for further tailoring and cellular export. NRPS domains responsible for epimerization of L to D-amino acids, and substrate modifications such as cyclization, N-methylation, N-formylation, oxidation, and reduction are often present within an NRPS protein.[105] External enzymes responsible for tailoring peptide resides before, during, and after chain elongation, are often co-located with NRPS genes in the biosynthetic gene cluster.[106]

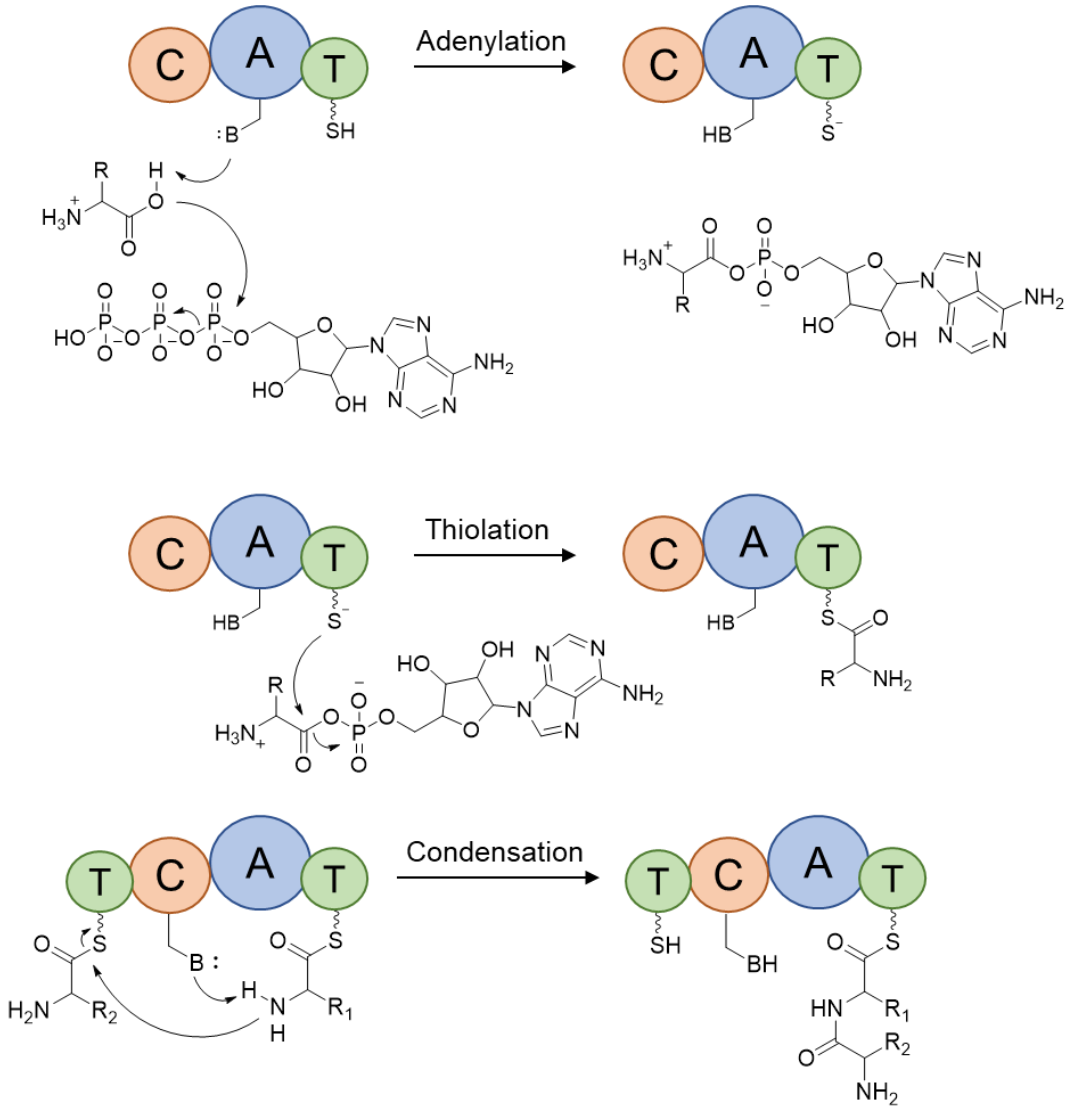

Figure 1.12. The core enzymatic domains in a NRPS protein: A − adenylation; T − thiolation; C − condensation.

1.5.1.1. Siderophore Biosynthesis by Iterative NRPSs

NRPS-directed biosynthesis generally passes from domain to domain, with the growing peptide interacting with each domain only once, often across multiple NRPS enzymes. Some siderophores, however, are biosynthesized through an iterative NRPS assembly, wherein a core set of NRPS domains add the same substrate to a growing peptide chain multiple times. Enterobactin is entirely assembled by the single one-module NRPS protein EntF, which

catalyzes amide bond formation between 2,3-dihydroxybezoic acid and L-Ser, as well as the ester linkages between three 2,3-DHB-L-Ser residues to form the intact cyclic tris-catecholate siderophore.[107] Other tris-catecholate siderophores are also synthesized through this iterative approach—for siderophores with a spacer amino acid between the macrolactone core and catechol arms (such as cyclic trichrysobactin and bacillibactin), a single module NRPS protein with two condensation domains is responsible for assembly of the 2,3-DHB-AA_1-AA_2 monomer, as well as condensation of the three monomers into the full trilactone siderophore.[108] In amphi-enterobactin biosynthesis, AebF functions as an analogue of EntF by forming 2,3-DHB-L-Ser and catalyzed ester bond linkage between 2,3-DHB-L-Ser subunits, but serves an additional biosynthetic role by catalyzing ester bond linkage between 2,3-DHB-L-Ser and acyl-L-Ser.[15] AebF thus fully forms the cyclic tetralactone structure of amphi-enterobactin through bifunctional substrate selectivity.

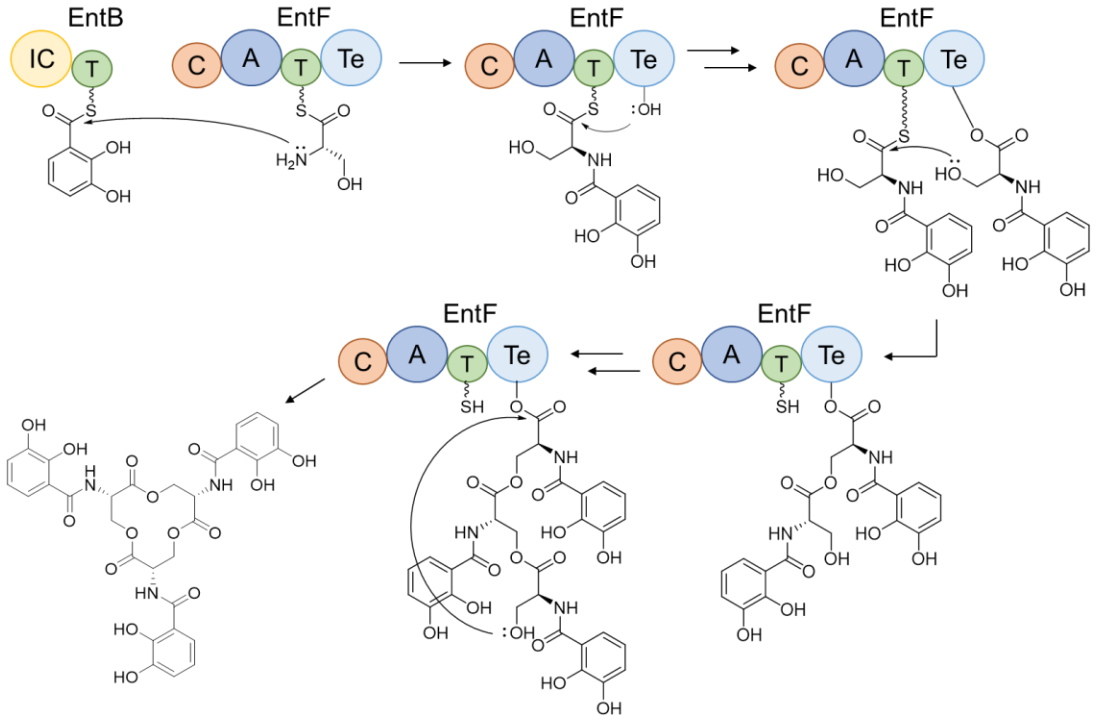

Figure 1.13. Schematic of the iterative biosynthesis of enterobactin in *Escherichia coli*. IC − isochorismatase; TE − thioesterase domain.

1.5.1.2. Hybrid NRPS/PKS biosynthesis

NRPS-directed biosyntheses can also interface with polyketide synthases (PKSs) to assemble a single product. Polyketide synthetases are a class of enzymes that synthesize natural products from acyl-CoA precursors through C-C bond formation.[109-110] PKSs are organized similarly to NRPSs, split into discrete catalytic domains each responsible for different steps in product formation. In the context of siderophore biosynthesis, PKS genes are co-located with NRPS genes and are directly involved in the assembly line. A peptide substrate is passed from an NRPS to a PKS; the ketoacyl synthase domain of the PKS then catalyzes decarboxylative Claisen condensation between the carboxylate functional group of the peptide and a PKS-recruited substrate (such as malonate) tethered to an aryl carrier protein domain of the PKS (Figure 1.14).[111] The elucidation of mycobactin biosynthesis in *Mycobacterium tuberculosis* first implicated polyketide synthases in the assembly of a siderophore.[112] PKSs MbtC and MbtD are responsible for the placement of a 3-hydroxybutyrate residue between two OHLys residues in mycobactin. During the biosynthesis of delftibactin by *Delftia acidovorans*, a methylmalonic acid residue is incorporated by a PKS, with one of two keto moieties reduced to a hydroxy functionality by ketoreductase domain within the PKS;[30] a methylmalonic acid residue is also incorporated during the biosynthesis of variochelin by *Variovorax boronicumulans*.[49]

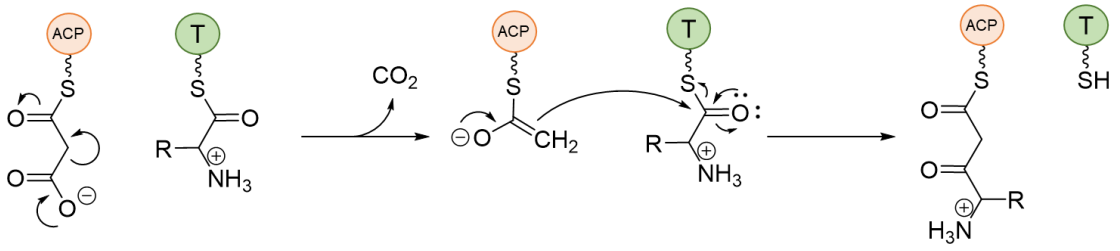

Figure 1.14. Visualization of PKS-mediated Claisen condensation between a NRPS-recruited amino acid and a PKS-recruited substrate (in this example, malonate). ACP − aryl carrier protein domain of a PKS; T − thiolation domain of an NRPS.

1.5.1.3. Aspartyl β-Hydroxylases Involved in NRPS Siderophore Biosyntheses

Aspartyl β-hydroxylases have been functionally characterized in only one bacterial species, despite the prevalence of β-OHAsp residues in siderophores, antibiotics, and phytotoxins.[113-119] Aspartyl β-hydroxylases SyrP and AspH from *Pseudomonas syringae* produce L-*threo* and L-*erythro* β-OHAsp, respectively (Figure 1.15).[120] SyrP hydroxylates L-Asp in the biosynthetic pathway of phytotoxin syringomycin E, while the specific substrate for AspH hydroxylation has not yet been identified.

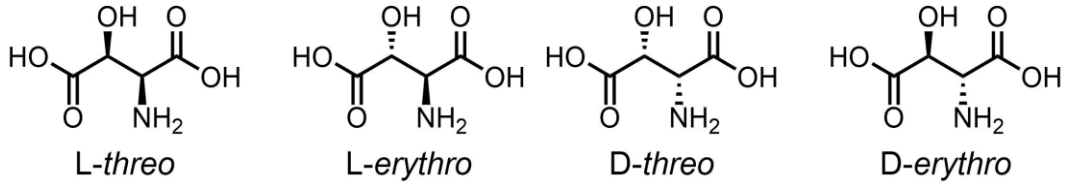

Figure 1.15. Stereoisomers of β-OHAsp. Only the D-*erythro* stereoisomer has yet to be observed in the structure of a siderophore

SyrP is homologous to the taurine hydroxylase TauD, a non-heme iron(II) α-ketoglutarate-dependent dioxygenase.[121] The TauD His_2-Asp facial triad responsible for Fe(II)-coordination[122-123] is conserved in SyrP, and *in vitro* reactions with the L-Asp substrate depend on α-ketoglutarate (αKG) for hydroxylation. Thus, SyrP and its homologues in siderophore biosynthetic pathways likely catalyze hydroxylation of L-Asp through a similar mechanism to TauD-catalyzed taurine hydroxylation. TauD reductively activates dioxygen by Fe(II)-αKG to yield an oxo-ferryl species that initiates Asp hydroxylation through hydrogen atom abstraction at the β-carbon, and subsequent Fe^{III}–OH attack on the resultant radical species (Figure 1.16).[124-126] This mechanistic pathway is conserved among the non-heme Fe(II), αKG-dependent dioxygenases.[127-131] Genes encoding putative discrete aspartyl β-hydroxylating enzymes homologous to αKG-dependent dioxygenases have been identified in the siderophore gene clusters of ornibactin,[132] cupriachelin,[53] serobactin,[48] pyoverdines from *Pseudomonas*

putida GB-1 and KT2240,[62, 133] and malleobactin,[57, 59] suggesting these hydroxylases are widespread in siderophore biosynthesis.

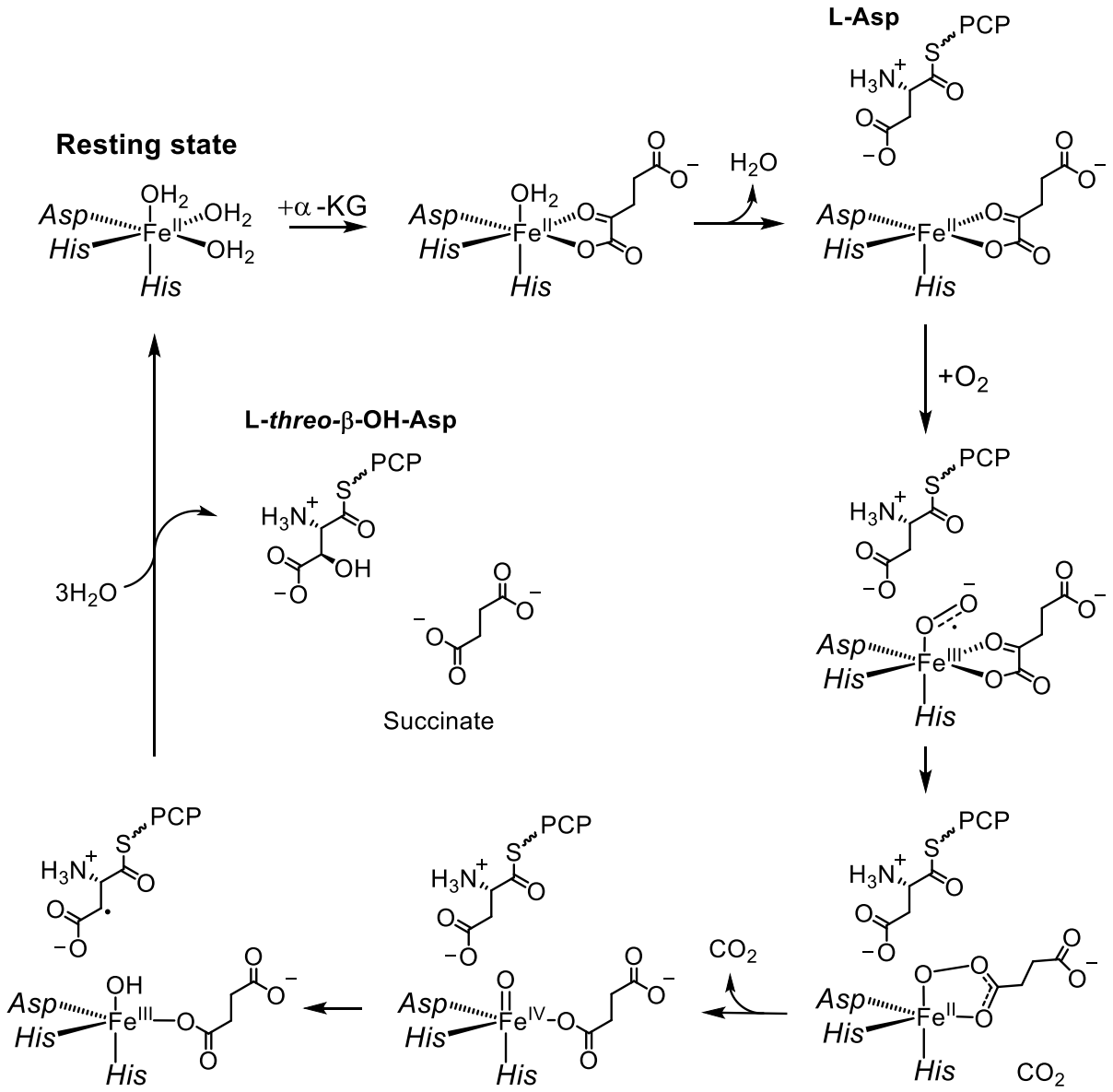

Figure 1.16. Proposed mechanistic pathway for β-hydroxylation of thiolated L-Asp catalyzed by SyrP, adapted from the mechanism of substrate hydroxylation in non-heme Fe(II) αKG-dependent dioxygenases.[124, 127, 130-131] L-Asp is drawn bound to the thiolation (PCP) domain of a NRPS, as experimental evidence indicates SyrP hydroxylates only PCP-bound L-Asp.[120] While β-hydroxylation of Asp is known to occur after tethering to the NRPS assembly line, it is not known if hydroxylation occurs before or after peptide bond formation.

A new type of NRPS domain with TauD-homology has been reported in the gene clusters of cupriachelin, taiwachelin, serobactin, and variochelin.[48-50, 53] These domains are always adjacent to L-Asp-selective adenylation domains in the NRPS and these Asp residues are always hydroxylated in the natural product. Cupriachelin and serobactin each contain two β-OHAsp residues, and each corresponding biosynthetic gene cluster encodes both a putative discrete aspartyl β-hydroxylating enzyme and putative aspartyl β-hydroxylating NRPS domain. While the functions of these enzymes and domains have yet to be characterized, it is possible that one Asp residue in each siderophore is hydroxylated by the NRPS domain, while the other Asp residue is hydroxylated by the discrete aspartyl β-hydroxylating enzyme. Taiwachelin and variochelin each contain only one β-OHAsp residue, which is expected to be hydroxylated by the NRPS aspartyl hydroxylating domain. Taiwachelin also has another Asp residue that remains un-hydroxylated. Moreover, neither gene cluster encodes a putative discrete aspartyl β-hydroxylating enzyme. The proposed biosynthetic pathways for taiwachelin and serobactin are shown in Figure 1.17 as examples.

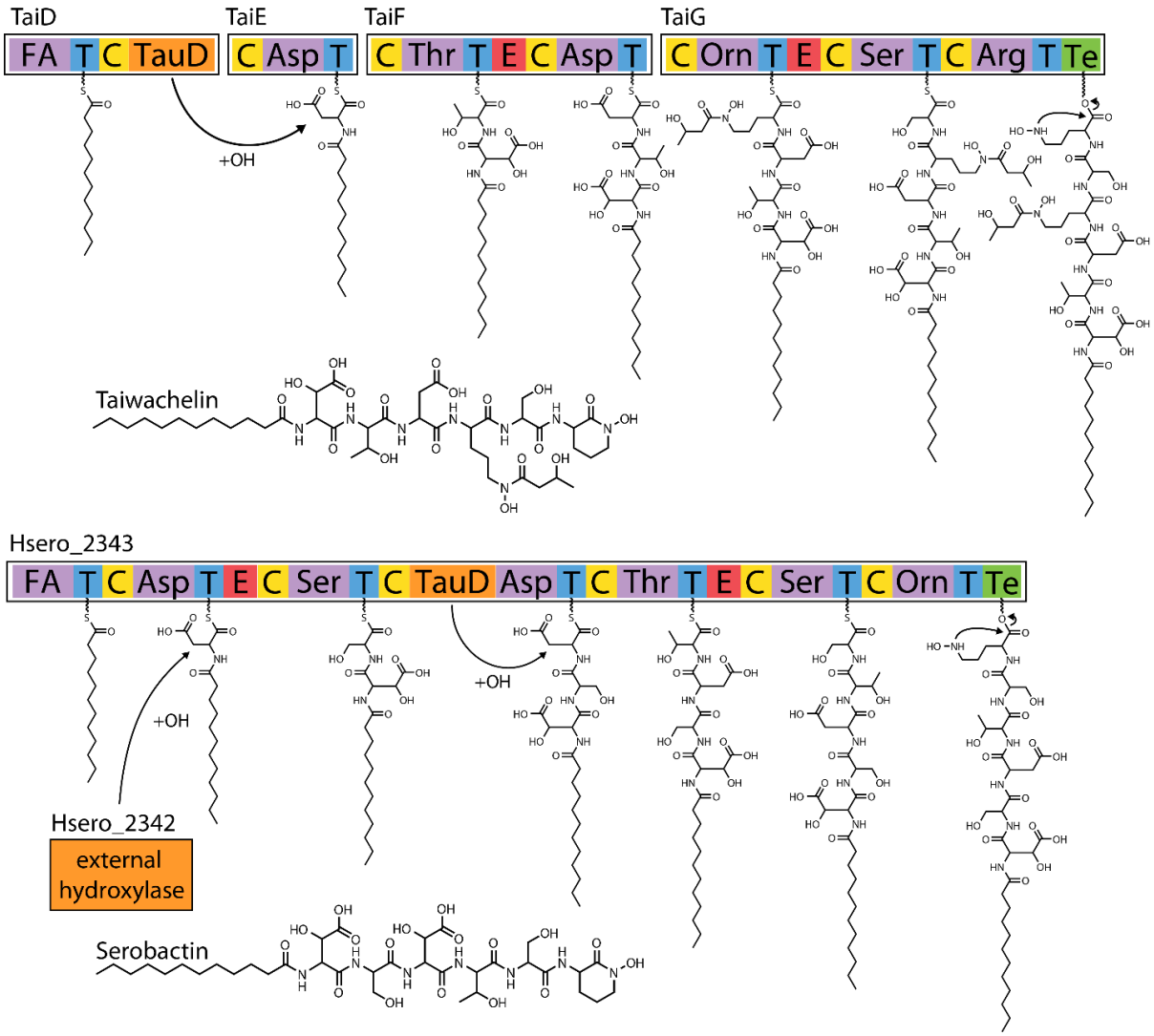

Figure 1.17. NRPS biosynthetic pathways for the siderophores taiwachelin (top) and serobactin (bottom). In taiwachelin, both β-OHAsp and native Asp residues are present. The gene cluster of taiwachelin encodes only one TauD-like domain within a NRPS protein, and encodes no external TauD homologue hydroxylases.[50] The serobactin gene cluster encodes both a TauD-homologous discrete enzyme and a TauD-homologous NRPS domain. Accordingly, the structure contains two β-OHAsp residues.[48] The zig-zag bonds represent the anchoring of each substrate to the thiolation domains or thioesterase domain. FA − fatty acid; C − condensation domain; E − epimerization domain; TE − thioesterase domain; TauD − Asp β-hydroxylating domain.

1.5.1.4. Genome Mining for NRPS Biosynthesis Pathways

In recent years genome mining has developed into an important tool to complement classical bioassay- and chemistry-driven natural product discovery, a development enabled by rapid expansion in the numbers and capabilities of bioinformatics tools for genomic analysis.[134-135] The straightforward architecture and co-linearity, conservation of core enzymatic features, and predictability of substrate specificities all help to make NRPS biosynthetic pathways ideal genome mining targets for the discovery of new siderophores and other natural products.[136] The most powerful tool for generation of NRPS product structural predictions is the substrate specificity of adenylation domains. Several tools have been developed to harness structure-function relationships correlating amino acid residues in the active site pocket of an adenylation domain with the corresponding substrate selectivity.[137-139] Building on this specificity prediction, software tools such as antiSMASH can identify NRPS clusters in a genome, map out and identify the component modules and domains, predict the substrates, and give a final set of possible metabolite structures.[140]

1.5.2. Biosyntheses Mediated by NRPS-Independent Synthetases

Many siderophores are synthesized by a separate class of enzymes, the NRPS-independent synthetases (NISs). NISs assemble siderophores through amide and ester bond formation between dicarboxylic acids and diamines or amino alcohols.[141] The biosynthesis of aerobactin in *E. coli* (structure of aerobactin, Figure 1.5) was the first NIS pathway elucidated, and served as the basis of characterizing further examples.[142-144] The aerobactin cluster consists of five genes, four of which are involved in aerobactin biosynthesis (*iucABCD*). Gene deletion and *in vitro* experiments determined that IucD and IucB are responsible for N^6 hydroxylation and N^6 acetylation of lysine, respectively.[143] IucA and IucC both catalyze amide bond formation

between the carboxy terminus of citric acid with the α-amine of N^6-acetyl-N^6-hydroxylysine, with IucA affecting the first condensation and IucC catalyzing the second condensation to yield aerobactin.[144]

Since the characterization of aerobactin biosynthesis, many more NIS pathways have been identified differing from the prototypical aerobactin pathway.[145-146] Petrobactin is a citrate-catecholate siderophore first isolated from *Marinobacter hydrocarbonoclasticus*[147-148] and later from the deadly human pathogen *Bacilius anthracis*.[149] Biosynthesis of petrobactin in *Bacilius anthracis* begins with amide bond formation between the carboxy terminus of citric acid and spermidine, catalyzed by AsbA. Subsequently, a second spermidine residue is condensed onto the other citric acid carboxy moiety by AsbB. The functions of AsbA and AsbB are thus analogous to that of IucA and IucC in aerobactin biosynthesis. Completing the assembly are the NRPS-like proteins AsbCDE, which respectively adenylate, tether, and condense 2 units of 3,4-dihydroxybenzoic acid onto the amide termini of the spermidine-citryl-spermidine intermediate.[150-152] Recently, the woodybactin siderophores have been isolated from marine bacterium *Shewanella woodyi*.[153] Woodybactins consist of one acyl-hydroxylysine residue appended to a carboxy terminus citric acid. Unlike aerobactin, the other terminus of citric acid is unmodified, leading to an asymmetric structure. The putative woodybactin biosynthetic gene cluster contains *swoA*, a homologue of *iucA*, but the only homologue of *iucC* in the *S. woodyi* genome resides 2.5 million base pairs downstream from the rest of the gene cluster. The apparent lack of IucC-like activity (stemming from the asymmetric structure) suggests the *iucC* homologue is non-functional or encodes an enzyme of entirely different function.

1.6. Siderophore Transport and Iron Release

1.6.1. Siderophore Export

Siderophores are delivered out of the cytoplasm and exported into the environment through active transport. Relatively few siderophore export pathways have been completely characterized, compared to the amount of biosynthesis and uptake pathways studied. One well understood system is the export of enterobactin in *E. coli*. Enterobactin is translocated across the inner membrane into the periplasm by EntS, an active efflux pump within the major facilitator superfamily of proteins.[154] From the periplasm, enterobactin is excreted into the environment through the outer membrane channel protein TolC, an exit channel shared by many other efflux systems.[155] Knockout studies of *entS* and *tolC* have generated different phenotypes. Deletion of *entS* still results in some enterobactin excretion, while deletion of *tolC* completely abolishes enterobactin export. Thus, *E. coli* can likely compensate for loss of EntS through alternative means of enterobactin transport to the cytoplasm, but cannot excrete enterobactin from the periplasm to the environment by any other means than TolC.[155]

The secretion of the siderophore pyoverdine in *Pseudomonas aeruginosa* PAO1 is unique, owing to the fact that pyoverdine biosynthesis does not entirely take place in the cytoplasm. *P. aeruginosa* synthesizes the acylated pyoverdine precursor ferribactin, also known as PVDIq, in the cytoplasm via a series of NRPS enzymes.[156] PVDIq is transported into the periplasm by efflux pump PvdE,[157] whereupon several tailoring enzymes act on the precursor, cleaving the fatty acid tail and forming the mature chromophore through a series of enzymatic modifications.[158-159] Mature pyoverdine is then exported from the periplasm into the extracellular environment through the efflux pump system PvdRT-OpmQ.[160]

1.6.2. Uptake of Fe(III)-Siderophore Complexes and Release of Iron

Fe(III)-siderophore complexes are taken up by a bacterium through an outer membrane receptor (OMR) protein. Several OMR proteins have been characterized through X-ray crystallography, including FepA (enterobactin) and FhuA (ferrichrome/hydroxamates) in *E. coli*, FpvA (pyoverdine) and FptA (pyochelin) in *P. aeruginosa*.[161-164] All characterized siderophore receptor proteins consist of two domains: a β-barrel domain and a plug, or cork, domain (Figure 1.18). The elliptical β-barrel domain is embedded in the outer membrane, forming the channel for transport. The plug domain sits within the β-barrel domain, sealing off the channel when not active. Residues in both the β-barrel domain and plug domain interact with the corresponding Fe(III)-siderophore complex.[161-164] Several conformational changes in an OMR protein are triggered upon ligand binding, which seal off the Fe(III)-siderophore complex from the extracellular environment and allow a specific seven residue sequence in the plug domain, termed the TonB box, to interact with the protein TonB. TonB, together with the cytoplasmic membrane proteins ExbB and ExbD, channels the proton motive force of the cytoplasmic membrane, driving the transport of the Fe(III)-siderophore complex through the OMR channel and into the periplasm.[165-166]

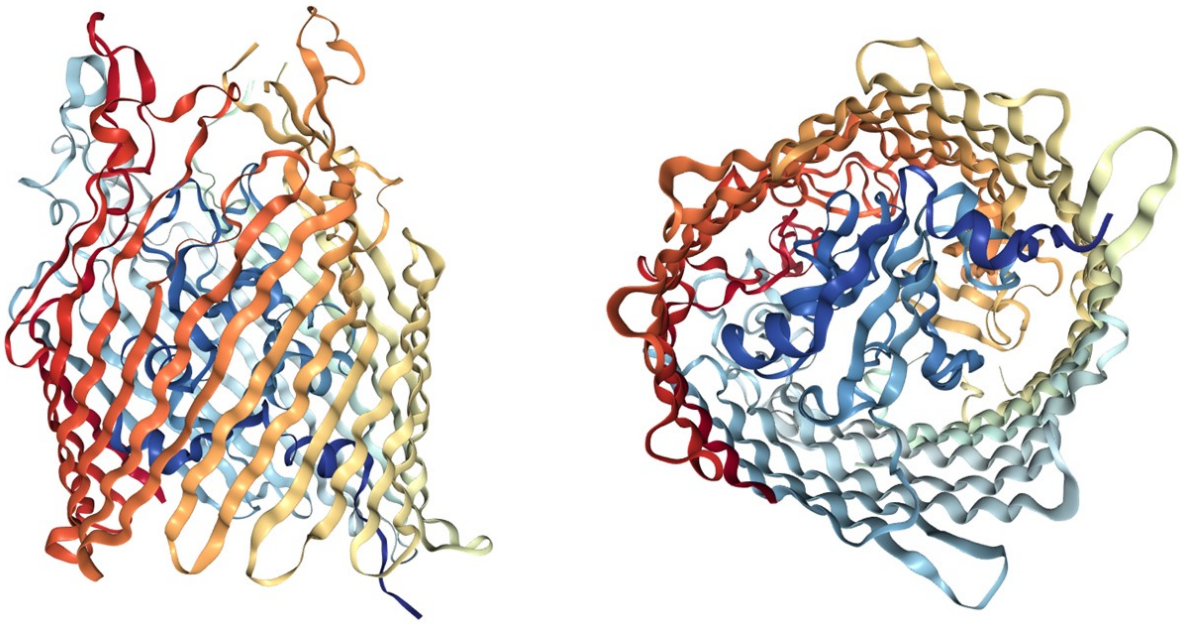

Figure 1.18. Crystal structure of ferric enterobactin OMR protein FepA. Left, view of β-barrel domain; Right, view down the β-barrel domain with the plug domain (blue) seated in the central channel (PDB code 1FEP).[161]

OMR proteins are generally specific to only one Fe(III)-siderophore complex, or a set of closely related siderophores. This selectivity is in some cases even stereospecific. *Pseudomonas fluorescens* CHA0 has been found to produce the enantiomer of the siderophore pyochelin, deemed enantio-pyochelin.[167] Supplementation of *P. fluorescens* CHA0 cultures with pyochelin does not promote growth, while enantio-pyochelin supplementation does. The converse is true in cultures of *P. aeruginosa*, the natural producer of pyochelin.[167] Each species has been found to utilize a distinct OMR protein for Fe(III)-siderophore uptake. The pyochelin OMR protein of *P. aeruginosa* does not appreciably bind to Fe(III)-enantio-pyochelin, while the enantio-pyochelin OMR protein of *P. fluorescens* CHA0 does not appreciably bind to Fe(III)-pyochelin, specificities supported by crystallography of each receptor.[168-169] Additionally, the inner-membrane ABC transporter FetCDE responsible for Fe(III)-enantio-

pyochelin transport has been shown to enforce stereoselectivity by binding to Fe(III)-enantio-pyochelin but not Fe(III)-pyochelin.[170]

After transport into the periplasm by an OMR protein, an Fe(III)-siderophore complex is bound by a periplasmic binding protein (PBP), which transports the complex to the inner membrane. PBPs are notably less specific than OMR proteins. The PBP FhuD, found in many bacteria, can transport a wide variety of hydroxamate siderophores.[171] Upon reaching the inner membrane, the PBP will release the complex, allowing it to be taken up into the cytoplasm through an ATP-driven ABC transporter protein.[172]

Iron scavenged from the environment by siderophores must be released from the siderophore complex before utilization in cellular processes. Due to the faster ligand exchange kinetics of high spin Fe(II) versus high spin Fe(III),[173] and the lower affinity of siderophores for Fe(II), Fe(III) reduction is a common strategy for triggering iron release from a siderophore complex.[174-175] FhuF is a 2Fe-2S protein from *E. coli* responsible for reduction of hydroxamate siderophore-bound Fe(III), with the Fe(II)-Fe(III) state shown by Mössbauer spectroscopy to be responsible for direct reduction of ferrioxamine B-bound Fe(III).[176] To reduce siderophore-complexed Fe(III), the reduction potential of the complex must fall within the range of physiological reducing agents. The reduction potential of Fe(III)-enterobactin is -750 mV at pH 7, well outside this range.[177] Thus before reduction takes place, the trilactone backbone of Fe(III)-enterobactin (Figure 1.2) is completely hydrolyzed, yielding an Fe(III)-tris(2,3-DHB-L-Ser) complex with a reduction potential of -350 V.[177-178] The *E. coli* esterase Fes has been shown to catalyze this hydrolysis of Fe(III)-enterobactin.[179]

This enzymatic hydrolysis step can also exhibit stereoselectivity. Fe(III)-bacillibactin (Figure 1.2), when taken up by its producer *Bacillus subtilis*, is hydrolyzed prior to iron

reduction by esterase BesA, similar to Fe(III)-enterobactin.[180] *B. subtilis* can take up Fe(III)-bacillibactin, Fe(III)-enterobactin, and Fe(III)-SerGlyCam (synthetic analogue of bacillibactin utilizing L-Ser in place of L-Thr) and subsist on the iron released from these complexes. While *B. subtilis* can take up Fe(III)-D-enterobactin (containing D-Ser in the trilactone core) and Fe(III)-D-SerGlyCam (D-Ser variant of SerGlyCam), it cannot utilize the iron from these complexes. The BesA esterase enforces stereoselectivity, cleaving L-amino acid trilactone complexes but not the corresponding D-amino acid variants.[76] Fes appears even more specific than BesA: only L-Ser trilactone variants are hydrolyzed by Fes, while Fe(III)-bacillibactin is unaffected.[76]

Pyoverdine-mediated iron uptake in *P. aeruginosa* differs somewhat from the approach described above. While Fe(III)-pyoverdine is still taken up through an OMR protein into the periplasm, Fe(III) is reduced and released from pyoverdine by periplasmic reductase FpvG, without Fe(III)-pyoverdine ever entering the cytoplasm. FpvC then chelates the resultant Fe(II) and shuttles it to an inner membrane transporter for relocation to the cytoplasm.[181] The apo pyoverdine, remaining in the periplasm, can then be re-exported through the same export system utilized by newly synthesized pyoverdine, a siderophore recycling system that gives *P. aeruginosa* an advantage in energy efficiency over competing strains.[182-184]

1.7. Conclusions

The microbial requirement for iron and scarcity of soluble Fe(III) in most environments have driven bacteria to evolve multiple iron acquisition strategies, including the biosynthesis and uptake of siderophores. Many siderophores are synthesized by nonribosomal peptide synthetases, a family of highly conserved, multi-modular proteins that synthesize peptidic

natural products in an assembly line fashion. NRPS biosynthetic products are particularly amenable to discovery through genome mining. Newly isolated and characterized NRPS-related siderophores further inform how NRPS assemble their products. As our understanding of NRPS enzymology improves, better predictions of their substrate specificities and tailoring reactions can be made, thus leading to more siderophore structures discovered. The structural characterization of siderophores is critical to understanding and manipulating iron uptake systems in bacteria, whether for antibiotic development, or for understanding drivers of ecological community change.

Over the years an incredible diversity of siderophore structures have been identified, including many structures utilizing β-hydroxyaspartate as a binding site. Through bioinformatics analysis two distinct but related routes to Asp hydroxylation in siderophore biosynthesis are evident. Asp hydroxylation is predicted to be carried out by either discrete hydroxylase enzymes or by NRPS hydroxylase domains, both of which are homologous to Fe(III)-α-ketoglutarate-dependent dioxygenases. These putative hydroxylases have only been characterized by sequence homology. Functional characterization of both the external hydroxylating enzyme and NRPS hydroxylating domains in β-OHAsp siderophore biosynthetic pathways is still required. Aspartyl β-hydroxylation is not limited to siderophores, and characterization of these hydroxylases can improve structural predictions for all β-OHAsp natural products through genome mining, including novel antibiotics.

UV irradiation of Fe(III)-siderophore complexes with β-OHAsp leads to oxidative cleavage of the peptide backbone, while Fe(III) complexes of citrate siderophores exhibit photo-induced decarboxylation of the α-hydroxycarboxylate group, with no further breakdown of the ligand. Recent photochemical mechanistic investigations of synthetic Fe(III) α-

hydroxycarboxylate complexes help to explain this difference in reactivity. Photoproducts of a synthetic complex observed under aerobic and anaerobic conditions support a multistep reaction pathway, consisting of photo-induced oxidative decarboxylation, autoxidation of the resultant aldehyde moiety by O_2, and further decarboxylation for a total loss of two carbon centers.[89] The susceptibility of aldehydes to oxidation explains the extensive photochemical ligand breakdown observed in ferric β-OHAsp siderophore complexes, while the resistance of the keto/enol tautomer of citrate siderophore photoproducts to oxidation protects the initial decarboxylation photoproduct from further reaction.[89] Photoproducts are not reported for the Fe(III) complexes of most β-OHAsp siderophores, therefore photochemical investigations of more β-OHAsp siderophores may aid in further developing a mechanistic model for Fe(III)-siderophore photoreactivity.

1.8. References

1. Neilands, J. B., *Annu. Rev. Biochem* **1981,** *50* (1), 715-731.

2. Rue, E. L.; Bruland, K. W., *Mar. Chem.* **1995,** *50* (1), 117-138.

3. Wu, J.; Luther, G. W., *Geochim. Cosmochim. Acta* **1996,** *60* (15), 2729-2741.

4. Aguilar-Islas, A. M.; Hurst, M. P.; Buck, K. N.; Sohst, B.; Smith, G. J.; Lohan, M. C.; Bruland, K. W., *Prog. Oceanogr.* **2007,** *73* (2), 99-126.

5. Winkelmann, G., *Biochem. Soc. Trans.* **2002,** *30* (4), 691-696.

6. Boukhalfa, H.; Crumbliss, A. L., *BioMetals* **2002,** *15* (4), 325-339.

7. Sandy, M.; Butler, A., *Chem. Rev.* **2009,** *109* (10), 4580-4595.

8. Hider, R. C.; Kong, X., *Nat. Prod. Rep.* **2010,** *27* (5), 637-657.

9. Raymond, K. N.; Dertz, E. A.; Kim, S. S., *Proc. Natl. Acad. Sci. USA* **2003,** *100* (7), 3584.

10. Müller, S. I.; Valdebenito, M.; Hantke, K., *BioMetals* **2009,** *22* (4), 691-695.

11. Bister, B.; Bischoff, D.; Nicholson, G. J.; Valdebenito, M.; Schneider, K.; Winkelmann, G.; Hantke, K.; Süssmuth, R. D., *BioMetals* **2004,** *17* (4), 471-481.

12. Hantke, K.; Nicholson, G.; Rabsch, W.; Winkelmann, G., *Proc. Natl. Acad. Sci. USA* **2003,** *100* (7), 3677.

13. Abergel, R. J.; Moore, E. G.; Strong, R. K.; Raymond, K. N., *J. Am. Chem. Soc.* **2006,** *128* (34), 10998-10999.

14. Zawadzka, A. M.; Abergel, R. J.; Nichiporuk, R.; Andersen, U. N.; Raymond, K. N., *Biochemistry* **2009,** *48* (16), 3645-3657.

15. Zane, H. K.; Naka, H.; Rosconi, F.; Sandy, M.; Haygood, M. G.; Butler, A., *J. Am. Chem. Soc.* **2014,** *136* (15), 5615-5618.

16. Sandy, M.; Butler, A., *J. Nat. Prod.* **2011,** *74* (5), 1207-1212.

17. Sandy, M.; Han, A.; Blunt, J.; Munro, M.; Haygood, M.; Butler, A., *J. Nat. Prod.* **2010,** *73* (6), 1038-1043.

18. Han, A. W.; Sandy, M.; Fishman, B.; Trindade-Silva, A. E.; Soares, C. A. G.; Distel, D. L.; Butler, A.; Haygood, M. G., *PLoS One* **2013,** *8* (10), e76151.

19. Dertz, E. A.; Xu, J.; Stintzi, A.; Raymond, K. N., *J. Am. Chem. Soc.* **2006,** *128* (1), 22-23.

20. Wen, Y.; Wu, X.; Teng, Y.; Qian, C.; Zhan, Z.; Zhao, Y.; Li, O., *Environ. Microbiol.* **2011,** *13* (10), 2726-2737.

21. Patzer, S. I.; Braun, V., *J. Bacteriol.* **2010,** *192* (2), 426.

22. Bickel, H.; Gäumann, E.; Keller-Schierlein, W.; Prelog, V.; Vischer, E.; Wettstein, A.; Zähner, H., *Experientia* **1960,** *16* (4), 129-133.

23. Wöhler, F., The treatment of haemochromatosis with desferrioxamine. In *Iron Metabolism: An International Symposium*, Gross, F., Ed. Springer Berlin Heidelberg: Berlin, Heidelberg, 1964; pp 551-567.

24. Nishio, T.; Tanaka, N.; Hiratake, J.; Katsube, Y.; Ishida, Y.; Oda, J., *J. Am. Chem. Soc.* **1988,** *110* (26), 8733-8734.

25. Ledyard, K. M.; Butler, A., *J. Biol. Inorg. Chem.* **1997,** *2* (1), 93-97.

26. Feistner, G. J.; Stahl, D. C.; Gabrik, A. H., *Org. Mass Spectrom.* **1993,** *28* (3), 163-175.

27. Martinez, J. S.; Zhang, G. P.; Holt, P. D.; Jung, H. T.; Carrano, C. J.; Haygood, M. G.; Butler, A., *Science* **2000,** *287* (5456), 1245-1247.

28. Vraspir, J. M.; Holt, P. D.; Butler, A., *BioMetals* **2011,** *24* (1), 85-92.

29. Kem, M. P.; Zane, H. K.; Springer, S. D.; Gauglitz, J. M.; Butler, A., *Metallomics* **2014,** *6* (6), 1150-1155.

30. Johnston, C. W.; Wyatt, M. A.; Li, X.; Ibrahim, A.; Shuster, J.; Southam, G.; Magarvey, N. A., *Nat. Chem. Biol.* **2013,** *9*, 241-243.

31. Snow, G. A., *Biochem. J* **1965,** *97* (1), 166-175.

32. Hermenau, R.; Ishida, K.; Gama, S.; Hoffmann, B.; Pfeifer-Leeg, M.; Plass, W.; Mohr, J. F.; Wichard, T.; Saluz, H.-P.; Hertweck, C., *Nat. Chem. Biol.* **2018,** *14* (9), 841-843.

33. Hermenau, R.; Mehl, J. L.; Ishida, K.; Dose, B.; Pidot, S. J.; Stinear, T. P.; Hertweck, C., *Angew. Chem. Int. Ed.* **2019,** *58* (37), 13024-13029.

34. Gibson, F.; Magrath, D. I., *Biochim. Biophys. Acta* **1969,** *192* (2), 175-184.

35. Warner, P. J.; Williams, P. H.; Bindereif, A.; Neilands, J. B., *Infect. Immun.* **1981,** *33* (2), 540.

36. Nassif, X.; Sansonetti, P. J., *Infect. Immun.* **1986,** *54* (3), 603.

37. Lawlor, K. M.; Payne, S. M., *J. Bacteriol.* **1984,** *160* (1), 266.

38. Guerinot, M. L.; Meidl, E. J.; Plessner, O., *J. Bacteriol.* **1990,** *172* (6), 3298.

39. Yamamoto, S.; Okujo, N.; Yoshida, T.; Matsuura, S.; Shinoda, S., *J. Biochem.* **1994,** *115* (5), 868-874.

40. Teintze, M.; Hossain, M. B.; Barnes, C. L.; Leong, J.; Van der Helm, D., *Biochemistry* **1981,** *20* (22), 6446-6457.

41. Teintze, M.; Leong, J., *Biochemistry* **1981,** *20* (22), 6457-6462.

42. Reid, R. T.; Livet, D. H.; Faulkner, D. J.; Butler, A., *Nature* **1993,** *366*, 455.

43. Homann, V. V.; Sandy, M.; Tincu, J. A.; Templeton, A. S.; Tebo, B. M.; Butler, A., *J. Nat. Prod.* **2009,** *72* (5), 884-888.

44. Robertson, A. W.; McCarville, N. G.; MacIntyre, L. W.; Correa, H.; Haltli, B.; Marchbank, D. H.; Kerr, R. G., *J. Nat. Prod.* **2018**.

45. Matthijs, S.; Brandt, N.; Ongena, M.; Achouak, W.; Meyer, J.-M.; Budzikiewicz, H., *BioMetals* **2016,** *29* (3), 467-485.

46. Matthijs, S.; Budzikiewicz, H.; Schäfer, M.; Wathelet, B.; Cornelis, P., *Z. Naturforsch., C.: Biosci* **2008,** *63* (1-2), 8-12.

47. Risse, D.; Beiderbeck, H.; Taraz, K.; Budzikiewicz, H.; Gustine, D., *Z. Naturforsch., C.: Biosci* **1998,** *53* (5-6), 295-304.

48. Rosconi, F.; Davyt, D.; Martínez, V.; Martínez, M.; Abin-Carriquiry, J. A.; Zane, H.; Butler, A.; de Souza, E. M.; Fabiano, E., *Environ. Microbiol.* **2013,** *15* (3), 916-927.

49. Kurth, C.; Schieferdecker, S.; Athanasopoulou, K.; Seccareccia, I.; Nett, M., *J. Nat. Prod.* **2016,** *79* (4), 865-872.

50. Kreutzer, M. F.; Nett, M., *Org. Biomol. Chem.* **2012,** *10* (47), 9338-9343.

51. Baars, O.; Zhang, X.; Gibson, M. I.; Stone, A. T.; Morel, F. M. M.; Seyedsayamdost, M. R., *Angew. Chem.* **2017,** *130* (2), 545-550.

52. Johnston, C. W.; Skinnider, M. A.; Wyatt, M. A.; Li, X.; Ranieri, M. R. M.; Yang, L.; Zechel, D. L.; Ma, B.; Magarvey, N. A., *Nat. Commun.* **2015,** *6*, 8421.

53. Kreutzer, M. F.; Kage, H.; Nett, M., *J. Am. Chem. Soc.* **2012,** *134* (11), 5415-5422.

54. Serrano Figueroa, L. O.; Pitts, B.; Uchida, M.; Richards, A. M., *Can. J. Chem.* **2015,** *94* (1), 35-43.

55. Serrano Figueroa, L. O.; Schwarz, B.; Richards, A. M., *Extremophiles* **2015,** *19* (6), 1183-1192.

56. Richards, A. M. Identification and Structural Characterization of Siderophores Produced by Halophilic and Alkaliphilic Bacteria. Washington State University, 2007.

57. Vargas-Straube, M. J.; Cámara, B.; Tello, M.; Montero-Silva, F.; Cárdenas, F.; Seeger, M., *PLoS One* **2016,** *11* (3), e0151273.

58. Franke, J.; Ishida, K.; Hertweck, C., *Chem. Eur. J.* **2015,** *21* (22), 8010-8014.

59. Franke, J.; Ishida, K.; Ishida-Ito, M.; Hertweck, C., *Angew. Chem. Int. Ed.* **2013,** *52* (32), 8271-8275.

60. Kanoh, K.; Kamino, K.; Leleo, G.; Adachi, K.; Shizuri, Y., *J. Antibiot.* **2003,** *56*, 871-875.

61. Hancock, D. K.; Coxon, B.; Wang, S.-Y.; White V, E.; Reeder, D. J.; Bellama, J. M., *J. Chem. Soc., Chem. Commun.* **1993,** (5), 468-470.

62. Matthijs, S.; Laus, G.; Meyer, J.-M.; Abbaspour-Tehrani, K.; Schäfer, M.; Budzikiewicz, H.; Cornelis, P., *BioMetals* **2009,** *22* (6), 951.

63. Budzikiewicz, H.; Kilz, S.; Taraz, K.; Meyer, J. M., Identical Pyoverdines from *Pseudomonas fluorescens* 9AW and from *Pseudomonas putida* 9BW. In *Z. Naturforsch., C.: Biosci*, 1997; Vol. 52, p 721.

64. Chen, W.-J.; Kuo, T.-Y.; Hsieh, F.-C.; Chen, P.-Y.; Wang, C.-S.; Shih, Y.-L.; Lai, Y.-M.; Liu, J.-R.; Yang, Y.-L.; Shih, M.-C., *Sci. Rep.* **2016,** *6* (1), 32950.

65. Martinez, J. S.; Butler, A., *J. Inorg. Biochem.* **2007,** *101* (11), 1692-1698.

66. Meyer, J.-M.; Van Van, T.; Stintzi, A.; Berge, O.; Winkelmann, G., *BioMetals* **1995,** *8* (4), 309-317.

67. Stephan, H.; Freund, S.; Beck, W.; Jung, G.; Meyer, J.-M.; Winkelmann, G., *BioMetals* **1993,** *6* (2), 93-100.

68. Loomis, L. D.; Raymond, K. N., *Inorg. Chem.* **1991,** *30* (5), 906-911.

69. Lewis, B. L.; Holt, P. D.; Taylor, S. W.; Wilhelm, S. W.; Trick, C. G.; Butler, A.; Luther, G. W., *Mar. Chem.* **1995,** *50* (1), 179-188.

70. McQueen, C. F.; Groves, J. T., *J. Biol. Inorg. Chem.* **2018,** *23* (7), 995-1007.

71. Evers, A.; Hancock, R. D.; Martell, A. E.; Motekaitis, R. J., *Inorg. Chem.* **1989,** *28* (11), 2189-2195.

72. Zhang, G.; Amin, S. A.; Küpper, F. C.; Holt, P. D.; Carrano, C. J.; Butler, A., *Inorg. Chem.* **2009,** *48* (23), 11466-11473.

73. Smith, R. M.; Martell, A. E., *Critical stability constants: inorganic complexes*. Springer: 1976; Vol. 4.

74. Karpishin, T. B.; Raymond, K. N., *Angew. Chem. Int. Ed. Engl.* **1992,** *31* (4), 466-468.

75. Bluhm, M. E.; Kim, S. S.; Dertz, E. A.; Raymond, K. N., *J. Am. Chem. Soc.* **2002,** *124* (11), 2436-2437.

76. Abergel, R. J.; Zawadzka, A. M.; Hoette, T. M.; Raymond, K. N., *J. Am. Chem. Soc.* **2009,** *131* (35), 12682-12692.

77. Müller, G.; Isowa, Y.; Raymond, K. N., *J. Biol. Chem.* **1985,** *260* (26), 13921-13926.

78. Butler, A.; Theisen, R. M., *Coord. Chem. Rev.* **2010,** *254* (3), 288-296.

79. Fry, H. S.; Gerwe, E. G., *Ind. Eng. Chem.* **1928,** *20* (12), 1392-1394.

80. Abrahamson, H. B.; Rezvani, A. B.; Brushmiller, J. G., *Inorg. Chim. Acta* **1994,** *226* (1), 117-127.

81. Küpper, F. C.; Carrano, C. J.; Kuhn, J.-U.; Butler, A., *Inorg. Chem.* **2006,** *45* (15), 6028-6033.

82. Abergel, R. J.; Zawadzka, A. M.; Raymond, K. N., *J. Am. Chem. Soc.* **2008,** *130* (7), 2124-2125.

83. Hickford, S. J. H.; Küpper, F. C.; Zhang, G.; Carrano, C. J.; Blunt, J. W.; Butler, A., *J. Nat. Prod.* **2004,** *67* (11), 1897-1899.

84. Martin, J. D.; Ito, Y.; Homann, V. V.; Haygood, M. G.; Butler, A., *J. Biol. Inorg. Chem.* **2006,** *11* (5), 633-641.

85. Amin, S. A.; Green, D. H.; Küpper, F. C.; Carrano, C. J., *Inorg. Chem.* **2009,** *48* (23), 11451-11458.

86. Shweky, I.; Bino, A.; Goldberg, D. P.; Lippard, S. J., *Inorg. Chem.* **1994,** *33* (23), 5161-5162.

87. Barbeau, K.; Rue, E. L.; Bruland, K. W.; Butler, A., *Nature* **2001,** *413*, 409-413.

88. Sayre, H.; Milos, K.; Goldcamp, M. J.; Schroll, C. A.; Krause, J. A.; Baldwin, M. J., *Inorg. Chem.* **2010,** *49* (10), 4433-4439.

89. Grabo, J. E.; Chrisman, M. A.; Webb, L. M.; Baldwin, M. J., *Inorg. Chem.* **2014,** *53* (11), 5781-5787.

90. Vernia, J. E.; Warmin, M. R.; Krause, J. A.; Tierney, D. L.; Baldwin, M. J., *Inorg. Chem.* **2017,** *56* (21), 13029-13034.

91. Glebov, E. M.; Pozdnyakov, I. P.; Grivin, V. P.; Plyusnin, V. F.; Zhang, X.; Wu, F.; Deng, N., *Photochem. Photobiol. Sci.* **2011,** *10* (3), 425-430.

92. Grabo, J. E.; Trotta, S. M.; Baldwin, M. J., *Inorg. Chem. Commun.* **2017,** *84*, 204-206.

93. Barbeau, K., *Photochem. Photobiol.* **2006,** *82* (6), 1505-1516.

94. Barbeau, K.; Rue, E. L.; Trick, C. G.; Bruland, K. W.; Butler, A., *Limnol. Oceanogr.* **2003,** *48* (3), 1069-1078.

95. O'Sullivan, D. W.; Hanson, A. K.; Miller, W. L.; Kester, D. R., *Limnol. Oceanogr.* **1991,** *36* (8), 1727-1741.

96. Johnson, K. S.; Coale, K. H.; Elrod, V. A.; Tindale, N. W., *Mar. Chem.* **1994,** *46* (4), 319-334.

97. Waite, T. D.; Szymczak, R.; Espey, Q. I.; Furnas, M. J., *Mar. Chem.* **1995,** *50* (1), 79-91.

98. Gledhill, M.; van den Berg, C. M. G., *Mar. Chem.* **1994,** *47* (1), 41-54.

99. Gärdes, A.; Triana, C.; Amin, S. A.; Green, D. H.; Romano, A.; Trimble, L.; Carrano, C. J., *BioMetals* **2013,** *26* (3), 507-516.

100. Zawadzka, A. M.; Kim, Y.; Maltseva, N.; Nichiporuk, R.; Fan, Y.; Joachimiak, A.; Raymond, K. N., *Proc. Natl. Acad. Sci. USA* **2009,** *106* (51), 21854.

101. Anderson, M. A.; Morel, F. M. M., *Limnol. Oceanogr.* **1982,** *27* (5), 789-813.

102. Amin, S. A.; Green, D. H.; Hart, M. C.; Küpper, F. C.; Sunda, W. G.; Carrano, C. J., *Proc. Natl. Acad. Sci. USA* **2009,** *106* (40), 17071-17076.

103. Koglin, A.; Walsh, C. T., *Nat. Prod. Rep.* **2009,** *26* (8), 987-1000.

104. Crosa, J. H.; Walsh, C. T., *Microbiol. Mol. Biol. Rev.* **2002,** *66* (2), 223-249.

105. Sattely, E. S.; Fischbach, M. A.; Walsh, C. T., *Nat. Prod. Rep.* **2008,** *25* (4), 757-793.

106. Samel, S. A.; Marahiel, M. A.; Essen, L.-O., *Mol. Biosyst.* **2008,** *4* (5), 387-393.

107. Gehring, A. M.; Mori, I.; Walsh, C. T., *Biochemistry* **1998,** *37* (8), 2648-2659.

108. Reitz, Z. L.; Sandy, M.; Butler, A., *Metallomics* **2017,** *9* (7), 824-839.

109. Shen, B., *Curr. Opin. Chem. Biol.* **2003,** *7* (2), 285-295.

110. Staunton, J.; Weissman, K. J., *Nat. Prod. Rep.* **2001,** *18* (4), 380-416.

111. Du, L.; Sánchez, C.; Shen, B., *Metab. Eng.* **2001,** *3* (1), 78-95.

112. Quadri, L. E. N.; Sello, J.; Keating, T. A.; Weinreb, P. H.; Walsh, C. T., *Chem. Biol.* **1998,** *5* (11), 631-645.

113. Hashizume, H.; Hattori, S.; Igarashi, M.; Akamatsu, Y., *J. Antibiot.* **2004,** *57* (6), 394-399.

114. Maki, H.; Miura, K.; Yamano, Y., *Antimicrob. Agents Chemother.* **2001,** *45* (6), 1823-1827.

115. Naruse, N.; Tenmyo, O.; Tomita, K.; Konishi, M.; Miyaki, T.; Kawaguchi, H.; Fukase, K.; Wakamiya, T.; Shiba, T., *J. Antibiot.* **1989,** *42* (6), 837-845.

116. Scaloni, A.; Bachmann, R. C.; Takemoto, J. Y.; Barra, D.; Simmaco, M.; Ballio, A., *Nat. Prod. Lett.* **1994,** *4* (3), 159-164.

117. Fukuchi, N.; Isogai, A.; Nakayama, J.; Takayama, S.; Yamashita, S.; Suyama, K.; Takemoto, J. Y.; Suzuki, A., *J. Chem. Soc., Perkin Trans. 1* **1992,** *0* (9), 1149-1157.

118. Di Giorgio, D.; Camoni, L.; Marchiafava, C.; Ballio, A., *Phytochemistry* **1997,** *45* (7), 1385-1391.

119. Scaloni, A.; Dalla Serra, M.; Amodeo, P.; Mannina, L.; Vitale, R. M.; Segre, A. L.; Cruciani, O.; Lodovichetti, F.; Greco, M. L.; Fiore, A.; Gallo, M.; Ambrosio, C.; Coraiola, M.; Menestrina, G.; Graniti, A.; Fogliano, V., *Biochem. J* **2004,** *384* (1), 25-36.

120. Singh, G. M.; Fortin, P. D.; Koglin, A.; Walsh, C. T., *Biochemistry* **2008,** *47* (43), 11310-11320.

121. Eichhorn, E.; van der Ploeg, J. R.; Kertesz, M. A.; Leisinger, T., *J. Biol. Chem.* **1997,** *272* (37), 23031-23036.

122. Neidig, M. L.; Brown, C. D.; Light, K. M.; Fujimori, D. G.; Nolan, E. M.; Price, J. C.; Barr, E. W.; Bollinger, J. M.; Krebs, C.; Walsh, C. T.; Solomon, E. I., *J. Am. Chem. Soc.* **2007,** *129* (46), 14224-14231.

123. Koehntop, K. D.; Emerson, J. P.; Que, L., *J. Biol. Inorg. Chem.* **2005,** *10* (2), 87-93.

124. Bollinger, J. M.; Price John, C.; Hoffart Lee, M.; Barr Eric, W.; Krebs, C., *Eur. J. Inorg. Chem.* **2005,** *2005* (21), 4245-4254.

125. Price, J. C.; Barr, E. W.; Tirupati, B.; Bollinger, J. M.; Krebs, C., *Biochemistry* **2003,** *42* (24), 7497-7508.

126. Price, J. C.; Barr, E. W.; Glass, T. E.; Krebs, C.; Bollinger, J. M., *J. Am. Chem. Soc.* **2003,** *125* (43), 13008-13009.

127. Krebs, C.; Galonić Fujimori, D.; Walsh, C. T.; Bollinger, J. M., *Acc. Chem. Res.* **2007,** *40* (7), 484-492.

128. Krebs, C.; Price, J. C.; Baldwin, J.; Saleh, L.; Green, M. T.; Bollinger, J. M., *Inorg. Chem.* **2005,** *44* (4), 742-757.

129. Grzyska, P. K.; Appelman, E. H.; Hausinger, R. P.; Proshlyakov, D. A., *Proc. Natl. Acad. Sci. USA* **2010,** *107* (9), 3982-3987.

130. Mitchell, A. J.; Dunham, N. P.; Martinie, R. J.; Bergman, J. A.; Pollock, C. J.; Hu, K.; Allen, B. D.; Chang, W.-C.; Silakov, A.; Bollinger, J. M.; Krebs, C.; Boal, A. K., *J. Am. Chem. Soc.* **2017,** *139* (39), 13830-13836.

131. Bollinger, J. M.; Chang, W.; Matthews, M. L.; Martinie, R. J.; Boal, A. K.; Krebs, C., Mechanisms of 2-Oxoglutarate-Dependent Oxygenases: The Hydroxylation Paradigm and Beyond. In *2-Oxoglutarate-Dependent Oxygenases*, The Royal Society of Chemistry: London, 2015; pp 95-122.

132. Agnoli, K.; Lowe, C. A.; Farmer, K. L.; Husnain, S. I.; Thomas, M. S., *J. Bacteriol.* **2006,** *188* (10), 3631-3644.

133. Parker, D. L.; Lee, S.-W.; Geszvain, K.; Davis, R. E.; Gruffaz, C.; Meyer, J.-M.; Torpey, J. W.; Tebo, B. M., *Front Microbiol.* **2014,** *5* (202), 202.

134. Weber, T., *Int. J. Med. Microbiol.* **2014,** *304* (3), 230-235.

135. Medema, M. H.; Fischbach, M. A., *Nat. Chem. Biol.* **2015,** *11* (9), 639-648.

136. Ziemert, N.; Alanjary, M.; Weber, T., *Nat. Prod. Rep.* **2016,** *33* (8), 988-1005.

137. Stachelhaus, T.; Mootz, H. D.; Marahiel, M. A., *Chem. Biol.* **1999,** *6* (8), 493-505.

138. Minowa, Y.; Araki, M.; Kanehisa, M., *J. Mol. Biol.* **2007,** *368* (5), 1500-1517.

139. Chevrette, M. G.; Aicheler, F.; Kohlbacher, O.; Currie, C. R.; Medema, M. H., *Bioinformatics* **2017,** *33* (20), 3202-3210.

140. Blin, K.; Wolf, T.; Chevrette, M. G.; Lu, X.; Schwalen, C. J.; Kautsar, S. A.; Suarez Duran, H. G.; de los Santos, E. L. C.; Kim, H. U.; Nave, M.; Dickschat, J. S.; Mitchell, D. A.; Shelest, E.; Breitling, R.; Takano, E.; Lee, S. Y.; Weber, T.; Medema, M. H., *Nucleic Acids Res.* **2017,** *45* (W1), W36-W41.

141. Challis, G. L., *ChemBioChem* **2005,** *6* (4), 601-611.

142. Martínez, J. L.; Herrero, M.; de Lorenzo, V., *J. Mol. Biol.* **1994,** *238* (2), 288-293.

143. de Lorenzo, V.; Bindereif, A.; Paw, B. H.; Neilands, J. B., *J. Bacteriol.* **1986,** *165* (2), 570.

144. de Lorenzo, V.; Neilands, J. B., *J. Bacteriol.* **1986,** *167* (1), 350.

145. Oves-Costales, D.; Kadi, N.; Challis, G. L., *Chem. Commun.* **2009,** (43), 6530-6541.

146. Carroll, C. S.; Moore, M. M., *Crit. Rev. Biochem. Mol. Biol.* **2018,** *53* (4), 356-381.

147. Bergeron, R. J.; Huang, G.; Smith, R. E.; Bharti, N.; McManis, J. S.; Butler, A., *Tetrahedron* **2003,** *59* (11), 2007-2014.

148. Barbeau, K.; Zhang, G.; Live, D. H.; Butler, A., *J. Am. Chem. Soc.* **2002,** *124* (3), 378-379.

149. Koppisch, A. T.; Browder, C. C.; Moe, A. L.; Shelley, J. T.; Kinkel, B. A.; Hersman, L. E.; Iyer, S.; Ruggiero, C. E., *BioMetals* **2005,** *18* (6), 577-585.

150. Nusca, T. D.; Kim, Y.; Maltseva, N.; Lee, J. Y.; Eschenfeldt, W.; Stols, L.; Schofield, M. M.; Scaglione, J. B.; Dixon, S. D.; Oves-Costales, D.; Challis, G. L.; Hanna, P. C.; Pfleger, B. F.; Joachimiak, A.; Sherman, D. H., *J. Biol. Chem.* **2012,** *287* (19), 16058-16072.

151. Oves-Costales, D.; Kadi, N.; Fogg, M. J.; Song, L.; Wilson, K. S.; Challis, G. L., *Chem. Commun.* **2008,** (34), 4034-4036.

152. Oves-Costales, D.; Kadi, N.; Fogg, M. J.; Song, L.; Wilson, K. S.; Challis, G. L., *J. Am. Chem. Soc.* **2007,** *129* (27), 8416-8417.

153. Carmichael, J. R.; Zhou, H.; Butler, A., *J. Inorg. Biochem.* **2019,** *198*, 110736.

154. Furrer, J. L.; Sanders, D. N.; Hook-Barnard, I. G.; McIntosh, M. A., *Mol. Microbiol.* **2002,** *44* (5), 1225-1234.

155. Bleuel, C.; Große, C.; Taudte, N.; Scherer, J.; Wesenberg, D.; Krauß, G. J.; Nies, D. H.; Grass, G., *J. Bacteriol.* **2005,** *187* (19), 6701.

156. Visca, P.; Imperi, F.; Lamont, I. L., *Trends Microbiol.* **2007,** *15* (1), 22-30.

157. Yeterian, E.; Martin, L. W.; Guillon, L.; Journet, L.; Lamont, I. L.; Schalk, I. J., *Amino Acids* **2010,** *38* (5), 1447-1459.

158. Hannauer, M.; Schäfer, M.; Hoegy, F.; Gizzi, P.; Wehrung, P.; Mislin, G. L. A.; Budzikiewicz, H.; Schalk, I. J., *FEBS Lett.* **2012,** *586* (1), 96-101.

159. Ringel, M. T.; Dräger, G.; Brüser, T., *J. Biol. Chem.* **2016,** *291* (46), 23929-23938.

160. Hannauer, M.; Yeterian, E.; Martin, L. W.; Lamont, I. L.; Schalk, I. J., *FEBS Lett.* **2010,** *584* (23), 4751-4755.

161. Buchanan, S. K.; Smith, B. S.; Venkatramani, L.; Xia, D.; Esser, L.; Palnitkar, M.; Chakraborty, R.; van der Helm, D.; Deisenhofer, J., *Nat. Struct. Biol.* **1999,** *6* (1), 56-63.

162. Ferguson, A. D.; Hofmann, E.; Coulton, J. W.; Diederichs, K.; Welte, W., *Science* **1998,** *282* (5397), 2215.

163. Cobessi, D.; Celia, H.; Folschweiller, N.; Schalk, I. J.; Abdallah, M. A.; Pattus, F., *J. Mol. Biol.* **2005,** *347* (1), 121-134.

164. Cobessi, D.; Celia, H.; Pattus, F., *J. Mol. Biol.* **2005,** *352* (4), 893-904.

165. Bradbeer, C., *J. Bacteriol.* **1993,** *175* (10), 3146.

166. Krewulak, K. D.; Vogel, H. J., *Biochem. Cell Biol.* **2011,** *89* (2), 87-97.

167. Youard, Z. A.; Mislin, G. L. A.; Majcherczyk, P. A.; Schalk, I. J.; Reimmann, C., *J. Biol. Chem.* **2007,** *282* (49), 35546-35553.

168. Brillet, K.; Reimmann, C.; Mislin, G. L. A.; Noël, S.; Rognan, D.; Schalk, I. J.; Cobessi, D., *J. Am. Chem. Soc.* **2011,** *133* (41), 16503-16509.

169. Hoegy, F.; Lee, X.; Noel, S.; Rognan, D.; Mislin, G. L. A.; Reimmann, C.; Schalk, I. J., *J. Biol. Chem.* **2009,** *284* (22), 14949-14957.

170. Reimmann, C., *Microbiology* **2012,** *158* (5), 1317-1324.

171. Clarke, T. E.; Braun, V.; Winkelmann, G.; Tari, L. W.; Vogel, H. J., *J. Biol. Chem.* **2002,** *277* (16), 13966-13972.

172. Cuív, P. Ó.; Keogh, D.; Clarke, P.; O'Connell, M., *Mol. Microbiol.* **2008,** *70* (5), 1261-1273.

173. Wilkins, R. G., *Kinetics and mechanisms of reactions of transition metal complexes*. VCH Publishers: 1991.

174. Fontecave, M.; Covès, J.; Pierre, J.-L., *BioMetals* **1994,** *7* (1), 3-8.

175. Schröder, I.; Johnson, E.; de Vries, S., *FEMS Microbiol. Rev.* **2003,** *27* (2-3), 427-447.

176. Matzanke, B. F.; Anemüller, S.; Schünemann, V.; Trautwein, A. X.; Hantke, K., *Biochemistry* **2004,** *43* (5), 1386-1392.

177. Cooper, S. R.; McArdle, J. V.; Raymond, K. N., *Proc. Natl. Acad. Sci. USA* **1978,** *75* (8), 3551.

178. O'Brien, I. G.; Cox, G. B.; Gibson, F., *Biochim. Biophys. Acta* **1971,** *237* (3), 537-549.

179. Lin, H.; Fischbach, M. A.; Liu, D. R.; Walsh, C. T., *J. Am. Chem. Soc.* **2005,** *127* (31), 11075-11084.

180. Miethke, M.; Klotz, O.; Linne, U.; May, J. J.; Beckering, C. L.; Marahiel, M. A., *Mol. Microbiol.* **2006,** *61* (6), 1413-1427.

181. Ganne, G.; Brillet, K.; Basta, B.; Roche, B.; Hoegy, F.; Gasser, V.; Schalk, I. J., *ACS Chem. Biol.* **2017,** *12* (4), 1056-1065.

182. Yeterian, E.; Martin, L. W.; Lamont, I. L.; Schalk, I. J., *Environ. Microbiol. Rep.* **2010,** *2* (3), 412-418.

183. Schalk, I. J.; Abdallah, M. A.; Pattus, F., *Biochemistry* **2002,** *41* (5), 1663-1671.

184. Imperi, F.; Tiburzi, F.; Visca, P., *Proc. Natl. Acad. Sci. USA* **2009,** *106* (48), 20440.

2. Characterization of the New Siderophore Pacifibactin and its Biosynthetic Gene Cluster in *Alcanivorax pacificus*

Sections of this chapter were published in: Hardy, C. D.; Butler, A. Ambiguity of NRPS Structure Predictions: Four Bidentate Chelating Groups in the Siderophore Pacifibactin. *J. Nat. Prod.* **2019**, 82, 990-997.

2.1. Introduction

Automated genome mining tools enable high-throughput scanning of bacterial genomes for gene clusters encoding biosynthetic machinery.[1-2] Natural products produced by non-ribosomal peptide synthetases are particularly amenable to discovery through bioinformatics approaches. The organization of a NRPS into distinct domains with predictable functions and amino acid substrates is a key feature driving software such as antiSMASH and PRISM, which utilize sequence analysis to identify NRPS-encoding gene clusters and predict their functionality.[3-4] Many siderophores are synthesized by NRPSs, and genome mining has enabled the prediction and discovery of many new siderophore structures.[5-9] NRPS-directed siderophore biosynthesis often employs extensive tailoring of both the amino acid substrates and the assembled product to yield Fe(III)-chelating functional groups. These tailoring reactions may be carried out by standalone proteins not accounted for in the commonly utilized NRPS analysis tools.

The genomes of many species within the obligate hydrocarbon-degrading microbial genus *Alcanivorax* have been sequenced, yet siderophore biosynthesis has only been identified in *Alcanivorax borkumensis*.[10] This abundance of sequenced *Alcanivorax* genomes enables a

genome mining approach for further characterization of siderophore production in the genus. To this end, fully sequenced genomes of *Alcanivorax* species not known to produce siderophores were screened for potential NRPS gene clusters encoding siderophore biosynthesis. Of the analyzed genomes, only *Alcanivorax pacificus* contains a candidate NRPS gene cluster for siderophore production.

We report herein that *Alcanivorax pacificus* contains a biosynthetic gene cluster that encodes the synthesis of the previously unknown siderophore pacifibactin. Structural characterization of pacifibactin reveals limitations of current automated genome mining approaches, highlighting several tailoring steps as yet undetectable through existing software. Structural variants of pacifibactin resulting from substrate selection promiscuity by an adenylation domain are also described. Pacifibactin is unique among siderophores in that it contains two hydroxamic acid and two β-hydroxyaspartic acid functional groups. Four potential bidentate Fe(III) binding groups are rarely observed in siderophore structures and were not predicted from the genome mining analysis. The coordination chemistry of Fe(III)-pacifibactin is reported as well as is the photoreactivity of the Fe(III)-siderophore complex due to coordination by β-hydroxyaspartic acid ligands,[11] and pacifibactin coordination chemistry with Ga(III) and Zr(IV).

2.2. Experimental

2.2.1. General Experimental Procedures

Optical rotation was measured on a Rudolph Autopol III polarimeter with a 50 mm microcell (1.2 mL). UV-visible absorbance was measured on an Agilent Cary 300 UV Vis spectrophotometer using 3 mL quartz cuvettes. NMR spectroscopy was carried out on 500 MHz (^{1}H, ^{13}C) and 600 MHz (COSY, HSQC, HMBC) Varian Unity Inova spectrometers.

Chemical shifts were referenced through residual solvent peaks [^{1}H (DMSO-d_6) 2.50 ppm, ^{13}C (DMSO-d_6) 39.51 ppm] or an external reference for samples dissolved in D_2O [^{1}H, ^{13}C (TMS) 0.0 ppm]. Mass spectrometry analysis was carried out on a Waters Xevo G2-XS QTof with positive mode electrospray ionization coupled to an ACQUITY UPLC H-Class system with a Waters BEH C18 column. Culture extracts were analyzed with a linear gradient of 0% to 30% CH_3CN (0.1% formic acid) in ddH_2O (0.1% formic acid) over 10 min, or for Zr(IV) competition experiments, a linear gradient of 0% to 60% CH_3CN (0.1% formic acid) in ddH_2O (0.1% formic acid) over 10 min. For MSMS analysis, a collision energy profile of 20, 25, 30 kEV was employed.

2.2.2. Genome Mining and Gene Cluster Annotation

The genome of *Alcanivorax pacificus* W11-5[12] was accessed through NCBI and analyzed with the NRPS cluster-predicting software PRISM and antiSMASH.[3-4] Genes within the pacifibactin cluster and their corresponding amino acid sequences were analyzed using BLAST and the PFAM database to predict function of proteins encoded by the cluster.

2.2.3. Bacterial Growth and Siderophore Isolation

Alcanivorax pacificus W11-5^{T}, obtained from Dr. Zongze Shao (Marine Culture Collection of China, Third Institute of State Oceanic Administration, P. R. China), was cultured on Difco 2216 Marine medium agar plates amended with sodium pyruvate. Single colonies were inoculated in a liquid low iron artificial seawater medium ASW+Py (10 g CAS amino acids L^{-1}, 1 g NH_4Cl L^{-1}, 1 g glycerol phosphate L^{-1}, 12.35 g $MgSO_4$ L^{-1}, 1.45 g $CaCl_2$ L^{-1}, 16.55 g NaCl L^{-1}, 0.75 g KCl L^{-1}, 5 g sodium pyruvate L^{-1} in ddH_2O, amended with 10 mL of 1.0 M HEPES L^{-1}, 2 mL of 1.0 M $NaHCO_3$ L^{-1}, and 6 mL of glycerol L^{-1}) or in a liquid single carbon source medium (24.6 g NaCl L^{-1}, 0.67 g KCl L^{-1}, 1.36 g $CaCl_2$ L^{-1}, 6.29 g $MgSO_4$ L^{-1}, 4.66 g

$MgCl_2$ L^{-1}, 0.18 g $NaHCO_3$ L^{-1}, 10.0 g sodium pyruvate L^{-1}, 2.0 g NH_4Cl L^{-1}, 0.2 g Na_2HPO_4 L^{-1}, 10 mM of Ser/Gly) for amino acid amendment, with microbial growth monitored by OD600. Cultures of 2 L and 500 mL (for amino acid amendment) volumes were grown at room temperature. Cultures were harvested in the late log phase of growth (5-7 days) by centrifugation (SLA-3000 rotor, ThermoScientific) at 6000 RPM for 30 min at 4 °C. Culture supernatants were decanted and shaken with 100 g/L culture XAD-2 polystyrene resin for 3 h at 4 °C to adsorb organics. The resin was filtered from the supernatant, washed with 250 mL of 90/10% ddH_2O/MeOH and eluted with 300 mL of 10/90% ddH_2O/MeOH. The eluent was concentrated under vacuum to 40 mL and stored at 4 °C for analysis. Eluent was further purified by semi-preparative HPLC on a YMC 20x250 mm C18-AQ column, with a linear gradient of 10% MeOH in ddH_2O (+0.1% trifluoroacetic acid) to 30% MeOH in ddH_2O (+0.1% trifluoroacetic acid) over 40 min, yielding pure product (30.02 mg from 2 L culture).

Pacifibactin: White solid; $[\alpha]^{18}_D$ -63 (c 0.100, MeOH); ^1H and ^{13}C NMR data, Table 1; HRESIMS *m/z* 923.4081 $[M+H]^+$ (calcd for $C_{34}H_{59}N_{12}O_{18}$, 923.4065).

2.2.4. Amino Acid Analysis

Purified apo pacifibactin (2 mg) was dissolved in 6 M HCl, sealed in an ampoule under argon, and heated at 80 °C for 8 h to hydrolyze the siderophore. The hydrolysis mixture was evaporated to dryness to remove HCl and re-dissolved in ddH_2O. After two additional cycles of evaporation and dissolution in ddH_2O, the hydrolysis mixture was derivatized with 1-fluoro-2-4-dinitrophenyl-5-L-alanine amide (Marfey's reagent) using standard procedures.[13] The hydrolysis procedure was also performed as described using 45% HI in place of 6M HCl to reduce any N5-acetyl-N5-hydroxyornithine and N5-hydroxyornithine to ornithine to aid in analysis. Derivatized hydrolysis products were separated by HPLC on a YMC 4.6x250mm

C18-AQ column with a gradient from 15% CH_3CN in ddH_2O (0.05% trifluoroacetic acid) to 50% CH_3CN in ddH_2O (0.05% trifluoroacetic acid) over 60 minutes. Derivatized hydrolysis products were co-injected with standards of Marfey's derivatized amino acids to determine the constituent amino acids of pacifibactin: D,L-*threo*-β-OHAsp (Sigma-Aldrich), L-Ser (Alfa-Aesar), D-Arg (Alfa-Aesar), D-Orn (Sigma-Aldrich), L-Orn (Sigma-Aldrich). D,L-*erythro*-β-OHAsp was synthesized through treatment of 2,3-*trans*-expoxysuccinic acid (50 mg) with 375 μL of concentrated aqueous NH_4OH (28%).[14] The reaction was sealed in a glass ampoule, and heated for 20 h at 50 °C. The crude mixture was dried, then dissolved in 1.5 mL of ddH_2O. The product was then derivatized with Marfey's reagent, and the formation of derivatized D,L-*erythro*-β-OHAsp as the dominant product was confirmed by UPLC-ESIMS, noting the mass of the derivatized amino acid and the difference in retention time in comparison to the D,L-*threo*-β-OHAsp derivatized standard.

2.2.5. Fe(III) Titration of Pacifibactin

A 2.12 mM stock solution of Fe(III) was prepared by diluting a 1 mg/mL $Fe(NO_3)_3$ atomic absorption standard solution with ddH_2O and standardized spectrophotometrically with 1,10-phenanthroline using established procedures.[15] A stock solution of apo pacifibactin was prepared by dissolving freeze dried siderophore in ddH_2O. To standardize the pacifibactin stock solution, a 400 μL aliquot of apo pacifibactin stock solution was lyophilized then dissolved with 2.77 mg of dried maleic acid in 700 μL of 99% $(CD_3)_2SO$. ^1H NMR peak integrations of pacifibactin and the maleic acid internal standard were then taken, establishing a stock concentration of 3.5 mM. A solution of apo pacifibactin (2 mL, 0.1 mM in ddH_2O buffered with 100 mM MOPS pH 7.1) was prepared in a 3 mL quartz cuvette and titrated with the standardized Fe(III) stock solution (2.14 mM in 40 mM HNO_3). After each aliquot of

Fe(III) was added, the solution was allowed to equilibrate for 24 h, a period determined by monitoring changes in the UV-vis absorption spectrum of the solution after Fe(III) addition. After equilibration, the UV-vis absorbance spectrum of the solution was measured.

2.2.6. Photolysis of Fe(III)-pacifibactin

Fe(III)-bound pacifibactin was prepared by adding Fe(III) stock solution to a solution of apo pacifibactin at a 1:1 ratio for a final concentration of 0.1 mM Fe(III)-pacifibactin in 100 mM MOPS pH 7.1 buffer (2 mL) in a 3 mL quartz cuvette. The solution was equilibrated for 24 h before photolysis. Solutions were photolyzed using a 450W mercury arc lamp (Ace Glass, 40-48% output in UV) as the light source, with cuvettes placed on a stand approximately 15 cm away from the lamp. UV-vis absorbance spectra of the solutions were measured at timed intervals. After photolysis, the reaction mixture was analyzed by UPLC-ESIMSMS to detect and characterize any photoproducts.

2.2.7. Preparation of Ga(III)-Pacifibactin

A stock solution of Ga(III) was prepared by dissolving a gallium metal ingot in boiling 30% HNO_3 for 24 h. The resultant $Ga(NO_3)_3$ stock solution was standardized by colorimetric titration with EDTA (pyrocatechol violet indicator).[16] Ga(III)-bound pacifibactin was prepared by adding Ga(III) stock solution to a solution of apo pacifibactin at a 4:3 molar ratio in ddH_2O (pH adjusted to 7.0 with NaOH addition) and equilibrating for 48 h. The solution was then purified by solid phase extraction using a Waters C18 SepPak to remove any excess Ga(III) and salts.

2.2.8. Exchange of Zr(IV) Between Pacifibactin and Desferrioxamine B

Desferrioxamine B mesylate was obtained from Sigma-Aldrich, and $Zr(acac)_2$ was obtained from Alfa-Aesar. To prepare Zr(IV)-pacifibactin, a 500 μL solution of 0.1 mM

pacifibactin and 0.1 mM $Zr(acac)_2$ in 100 mM MOPS pH 7 was prepared and allowed to equilibrate overnight. For competition studies with DFOB, a 500 µL solution of 0.1 mM Zr(IV)-pacifibactin and 0.1 mM DFOB in 100 mM MOPS pH 7 was prepared and allowed to equilibrate for one hour. Exchange of Zr(IV) between ligands was detected through UPLC-ESIMS, using the natural isotope signature of Zr as a diagnostic tool.

2.3. Results and Interpretation

2.3.1. Putative Siderophore Biosynthetic Gene Cluster Identified Through Genome Mining

The genomes of eight fully sequenced *Alcanivorax* species available through NCBI were analyzed using the bioinformatics software tools antiSMASH and PRISM,[3-4] which identify and annotate putative nonribosomal peptide synthetase (NRPS) genes. The genome of *Alcanivorax pacificus* W11-5T, a species isolated from a bacterial consortium found within seafloor sediment in the Pacific Ocean,[17] contains a putative siderophore biosynthetic gene cluster centered around three NRPS-encoding genes and one polyketide synthase (PKS)-encoding gene, identified by both antiSMASH and PRISM (Figure 2.1). Putative genes involved in siderophore transport, Fe(III)-siderophore reduction, and amino acid tailoring are also present within the cluster (full annotation, Table 2.1). A siderophore structure comprising L-Ser, malonic acid (PKS), L-Asp, D-Arg, D-Asp, L-Ser, L-OHOrn, and D-OHOrn is predicted from the adenylation domain specificity and the location of epimerization domains within the NPRS/PKS assembly line (Figure 1). The presence of genes predicted to encode a TonB-dependent receptor protein and siderophore-iron reductase (Table 2.1), and the incorporation of aspartic acid and ornithine which are commonly functionalized as Fe(III) binding groups, further supported siderophore production. Additionally, the genome of

Alcanivorax pacificus contains no other NRPS-encoding gene clusters, nor does it contain any biosynthetic gene clusters indicating currently known NRPS-independent siderophore.

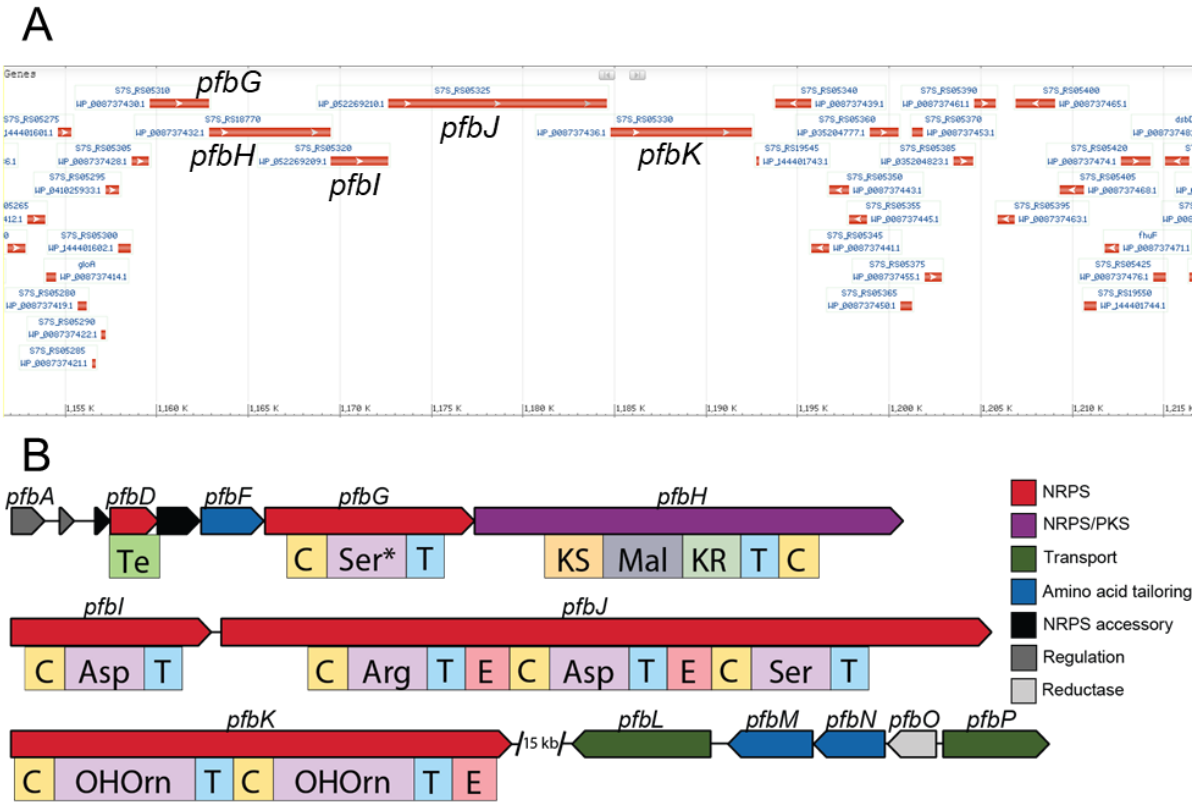

Figure 2.1. A) Graphical representation of *pfb* gene cluster within the *Alcanivorax pacificus* genome generated from the National Center for Biotechnology Information (NCBI) website. **B)** *pfb* biosynthetic gene cluster annotated with NRPS and PKS domains as identified by antiSMASH and PRISM. Adenylation domains (lavender boxes) are labeled with their substrate specificity prediction. The adenylation domain of PfbG is predicted to incorporate Ser, however structural characterization of pacifibactin establishes the presence of Ala. Te – thioesterase domain, C – condensation domain, T – thiolation domain, KS – ketosynthase domain, Mal – malonic acid (substrate specificity), KR – ketoreductase domain, E – epimerization domain.

Table 2.1. Full annotation of the *pfb* gene cluster.

Gene name	Gene/protein accession number	Predicted protein function
pfbA	S7S_RS05280/WP_008737419.1	Sigma factor
pfbB	S7S_RS05285/WP_008737421.1	DUF4880 family (unknown function)
pfbC	S7S_RS05290/WP_008737422.1	MbtH-like protein
pfbD	S7S_RS05295/WP_041025933.1	Thioesterase
pfbE	S7S_RS05300/WP_035204760.1	4'-phosphopantetheinyl transferase
pfbF	S7S_RS05305/WP_008737428.1	TauD-like dioxygenase
pfbG	S7S_RS05310/WP_008737430.1	Nonribosomal peptide synthetase
pfbH	S7S_RS18770/WP_008737432.1	Polyketide synthase/TauD-like dioxygenase
pfbI	S7S_RS05320/WP_052269209.1	Nonribosomal peptide synthetase
pfbJ	S7S_RS05325/WP_052269210.1	Nonribosomal peptide synthetase
pfbK	S7S_RS05330/WP_008737436.1	Nonribosomal peptide synthetase
pfbL	S7S_RS05400/WP_008737465.1	TonB dependent receptor
pfbM	S7S_RS05405/WP_008737468.1	L-Orn N5-monooxygenase
pfbN	S7S_RS05410/WP_008737468.1	N5-hydroxyornithine acetyl transferase
pfbO	S7S_RS50415/WP_008737471.1	Siderophore-Iron reductase FhuF
pfbP	S7S_RS05420/WP_008737474.1	Peptide ABC transporter

2.3.2. Isolation and Structural Characterization of Pacifibactin

To induce siderophore production, *Alcanivorax pacificus* was grown in an iron-deficient artificial seawater medium. *A. pacificus* grows readily under iron-starvation conditions, and aliquots of the culture tested positive in the liquid chrome azurol S (CAS) assay for strong Fe(III)-binding ligands.[18] UPLC-ESI-MS analysis of the supernatant extract revealed a candidate compound with protonated molecule masses of *m/z* 923.41 $[M+H]^+$ and *m/z* 462.20 $[M+2H]^{2+}$. The putative siderophore, named herein as pacifibactin, was purified by semi-preparative RP-HPLC. HR-ESI-MS of purified pacifibactin detects a protonated molecule of *m/z* 923.4081 (Figure 2.2). MSMS peptide b/y fragmentation reveals the constituent amino acids of pacifibactin (Figure 2.3, Figure 2.4), with an amino acid sequence from the carboxylate terminus of cyclized N5-OHOrn, N5-acetyl-N5-OHOrn, Ser, β-OHAsp, Arg, and β-OHAsp. The two β-OHAsp residues, N5-acetyl-N5-OH-Orn residue, and cyclized N5-

OHOrn residue yield in total four bidentate metal binding sites. The presence of four sites stands in contrast to almost all known siderophores, which generally contain no more than three bidentate metal binding sites.

MSMS fragmentation suggested a mass for the N-terminal amino acid that did not match any amino acid previously found in peptidic siderophores. Analysis of the NRPS domains within the gene cluster suggested that Ser and malonic acid (presumably incorporated by the PKS enzyme PfbH) should be incorporated at the N-terminus of pacifibactin. Mixed NRPS-PKS siderophore biosyntheses involve a decarboxylative Claisen condensation between the carboxylate functional groups of a NRPS-recruited amino acid and a PKS-recruited substrate,[8, 19] and indeed the mass of the N-terminal pacifibactin amino acid determined by MSMS fractionation is consistent with a decarboxylative Claisen condensation of Ser and malonate followed by stepwise reduction of the β-keto group to an alkyl moiety.

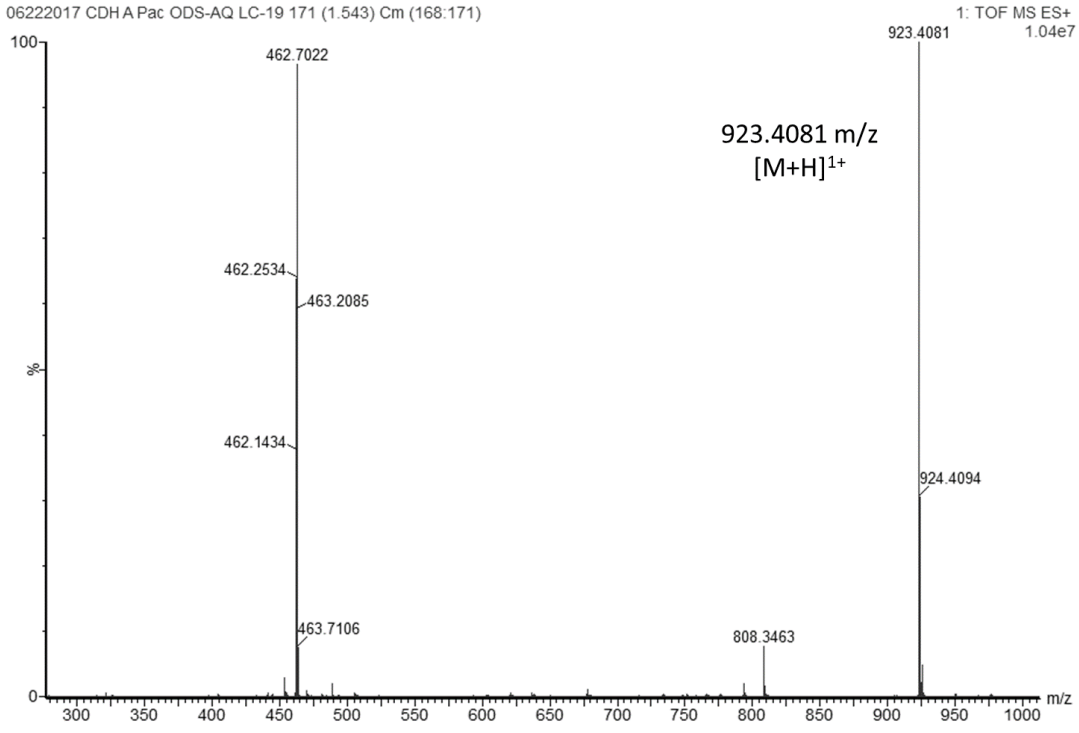

Figure 2.2. HR-ESI-MS spectrum of pacifibactin, m/z 923.4081 $[M+H]^{1+}$. Calculated exact mass for pacifibactin $[M+H]^{1+}$ is m/z 923.4065 ($C_{34}H_{59}N_{12}O_{18}$).

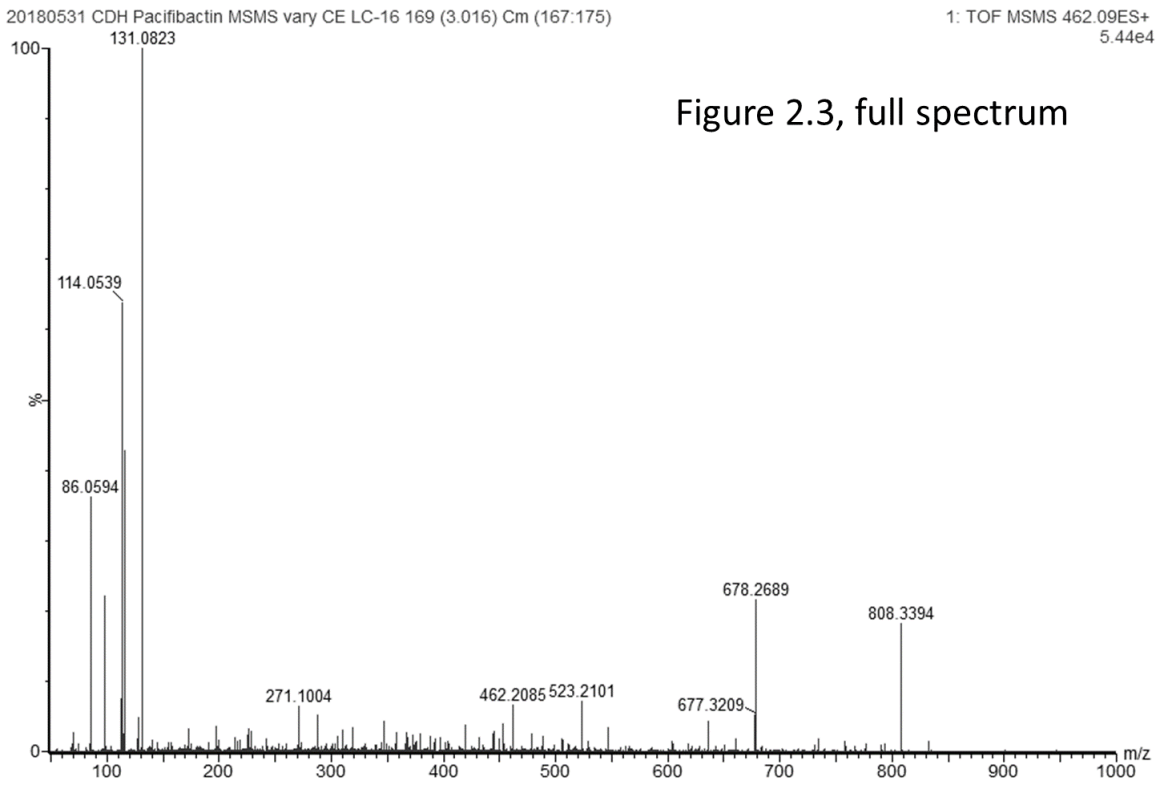

Figure 2.3, full spectrum

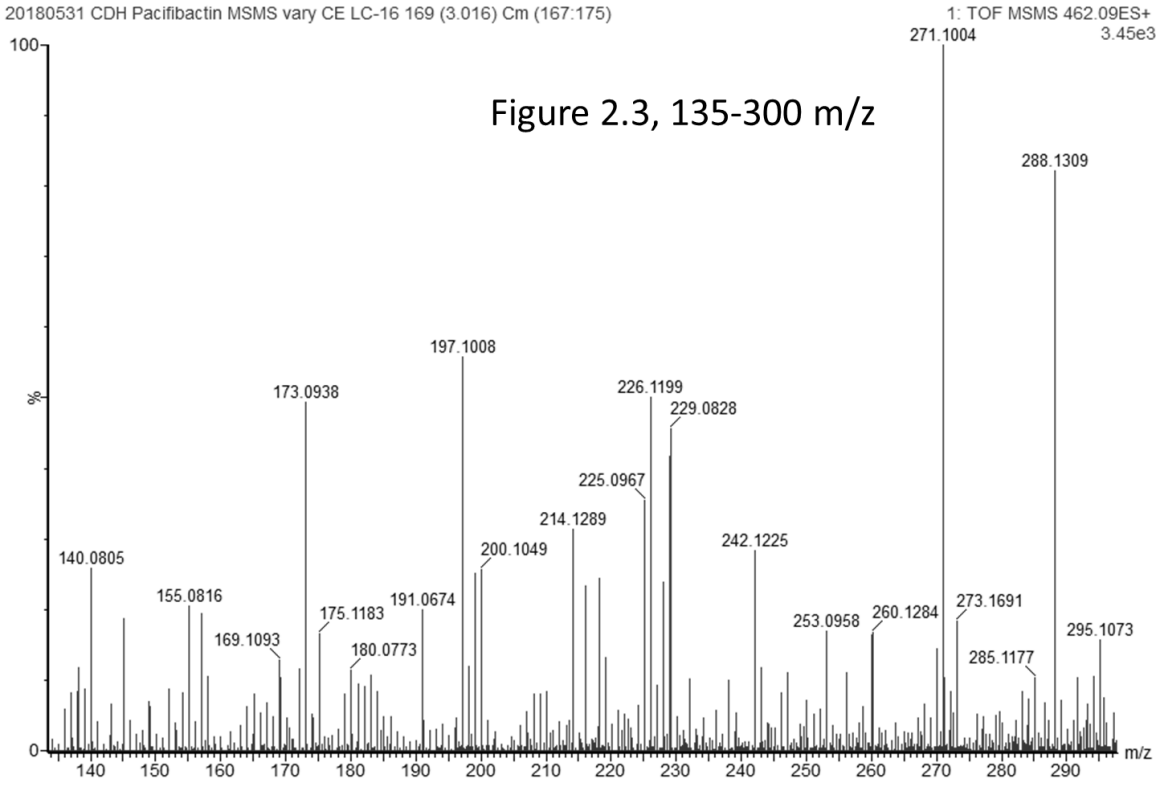

Figure 2.3, 135-300 m/z

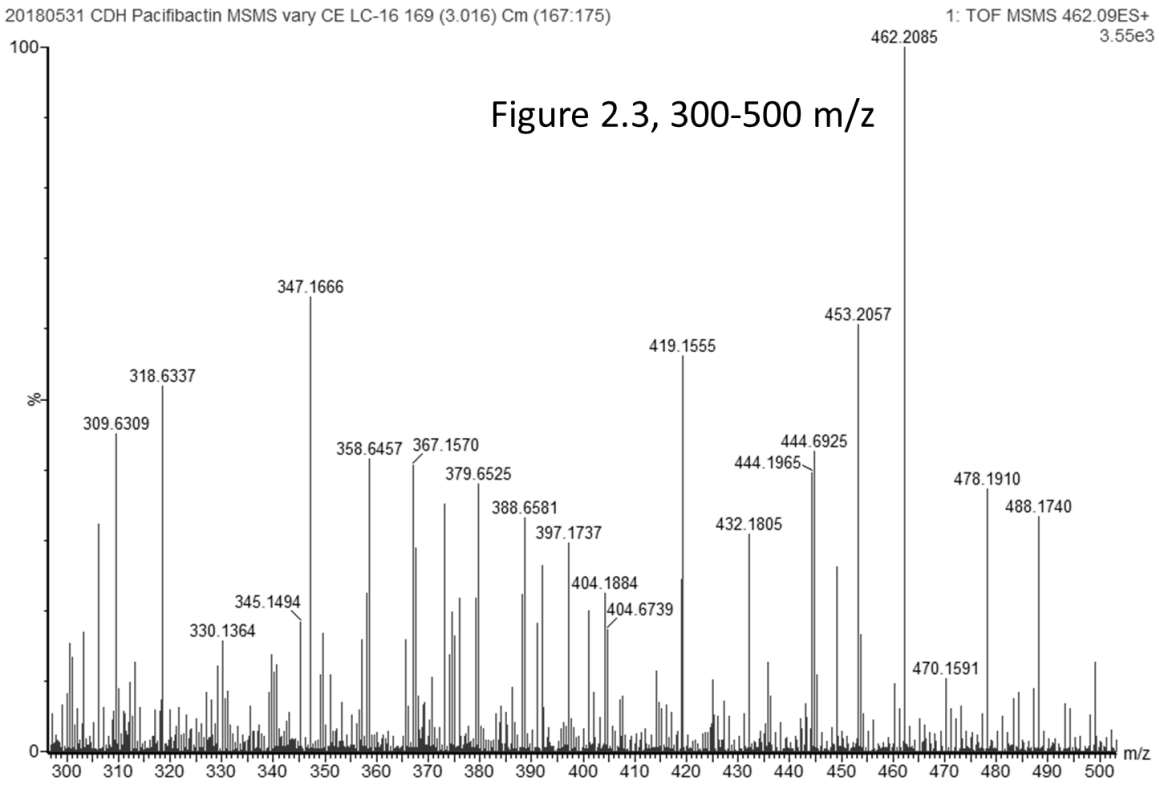

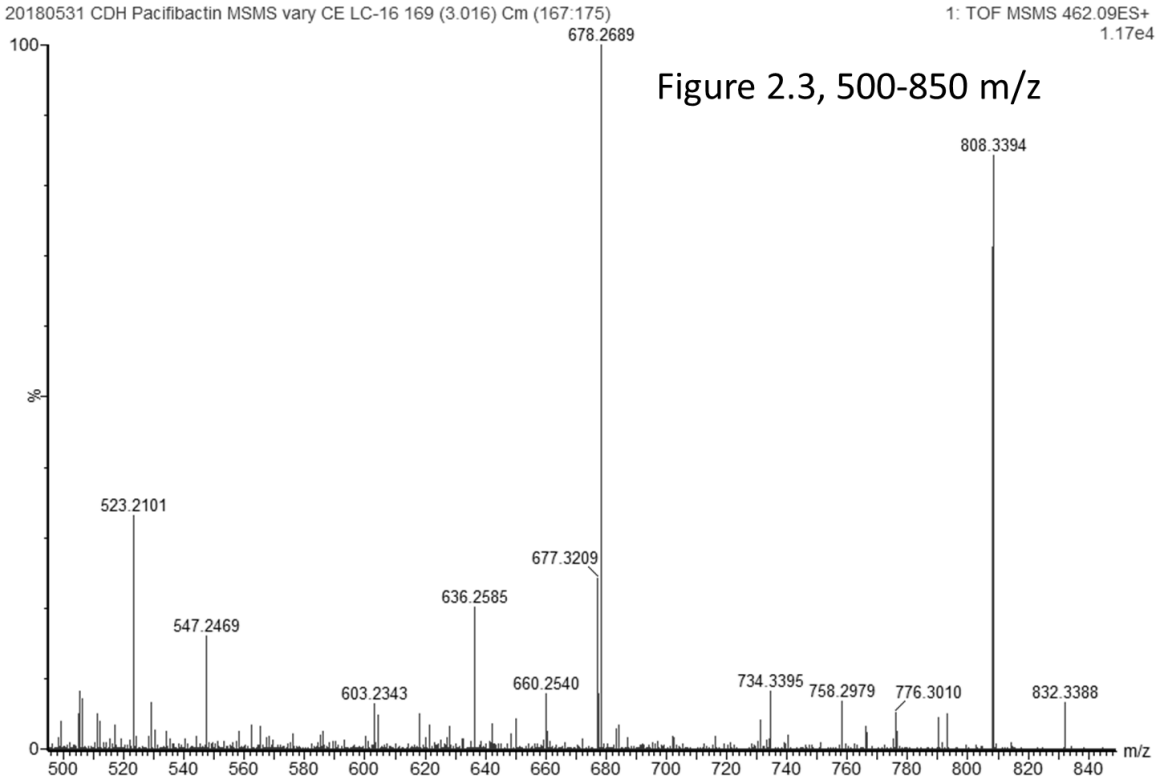

Figure 2.3. ESI-MSMS spectrum of pacifibactin (m/z = 462.2, z = 2), with selected regions zoomed in for clarity. Collision energy profile of 20, 25, and 30 kEV employed for optimal fragmentation.

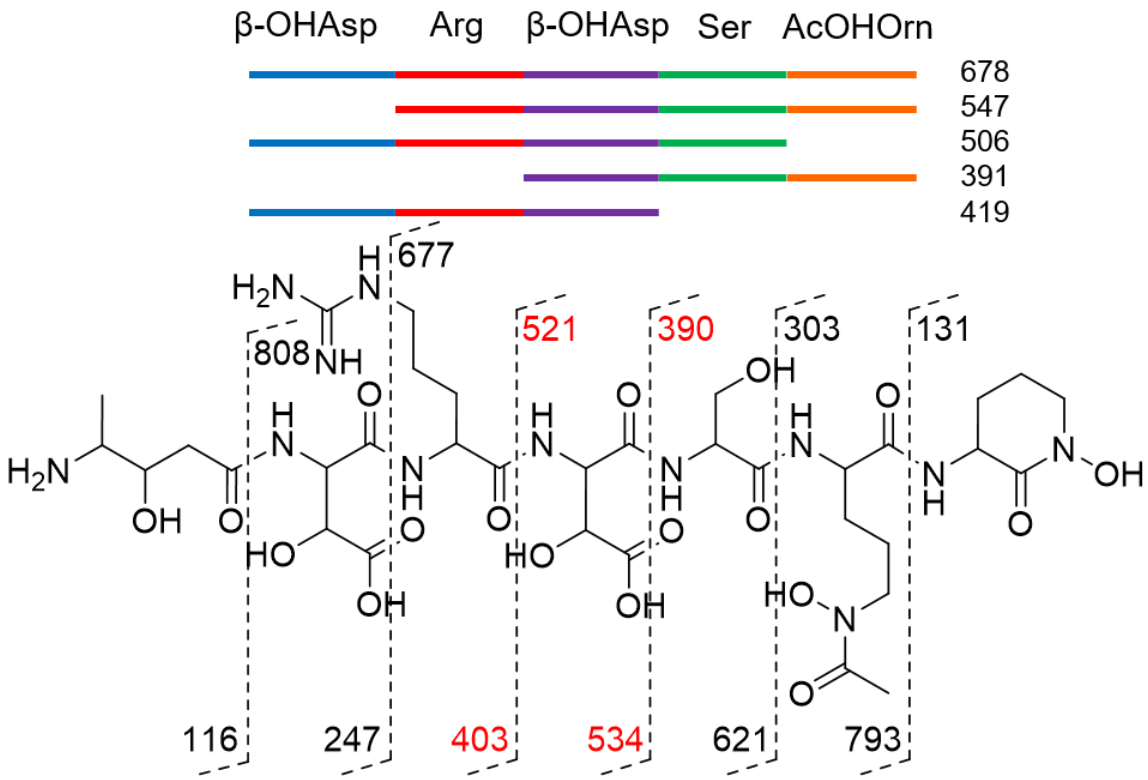

Figure 2.4. Structure of pacifibactin, with b/y peptide fragment masses (fragments with *m/z* in red were not observed). Observed internal fragments are shown above the structure.

Complete assignment of each ^{1}H and ^{13}C chemical shift of pacifibactin was accomplished through COSY, HSQC, and HMBC NMR techniques (Figures 2.5-2.10, Table 2.2). The NMR-supported structure of pacifibactin predicts an exact mass of *m/z* 923.4065 $[C_{34}H_{59}N_{12}O_{18}]^{+}$, which is within 2 ppm of the measured mass of *m/z* 923.4081 (Figure 2.2). NMR analysis unambiguously assigns the N-terminal amino acid as a γ-amino acid methylated at the γ-carbon and hydroxylated at the β-carbon. This unusual amino acid is consistent with a Claisen condensation between Ala (presumably incorporated by PfbG) and malonate (presumably incorporated by PfbH) followed by reduction of the β-keto to a hydroxy group, instead of the predicted condensation of Ser and malonate. Analysis of the PKS-encoding gene identifies a ketoreductase domain that could carry out this reduction to a hydroxyl functionality (Figure 2.1).

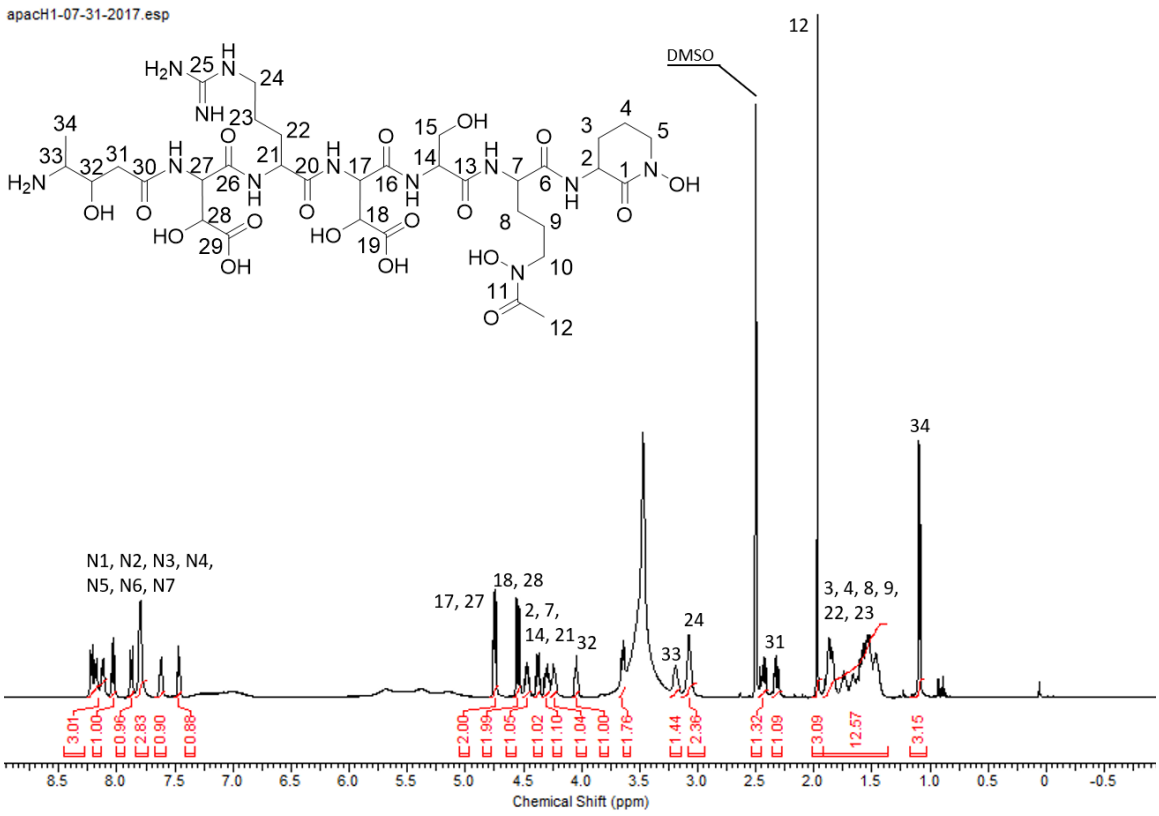

Figure 2.5. ^{1}H (500 MHz) NMR spectrum of pacifibactin (20 mg) in $(CD_3)_2SO$.

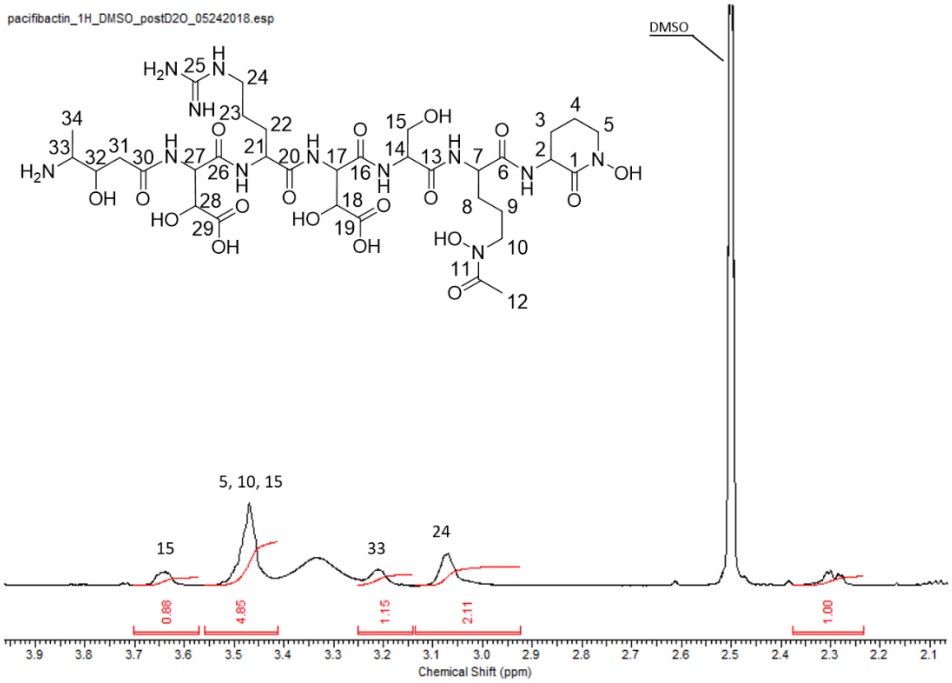

Figure 2.6. ^{1}H (500 MHz) NMR spectrum of pacifibactin (10 mg) in $(CD_3)_2SO$ previously dissolved in D_2O to eliminate signals from exchangeable protons, allowing for identification of resonances from 3.0-3.7 ppm.

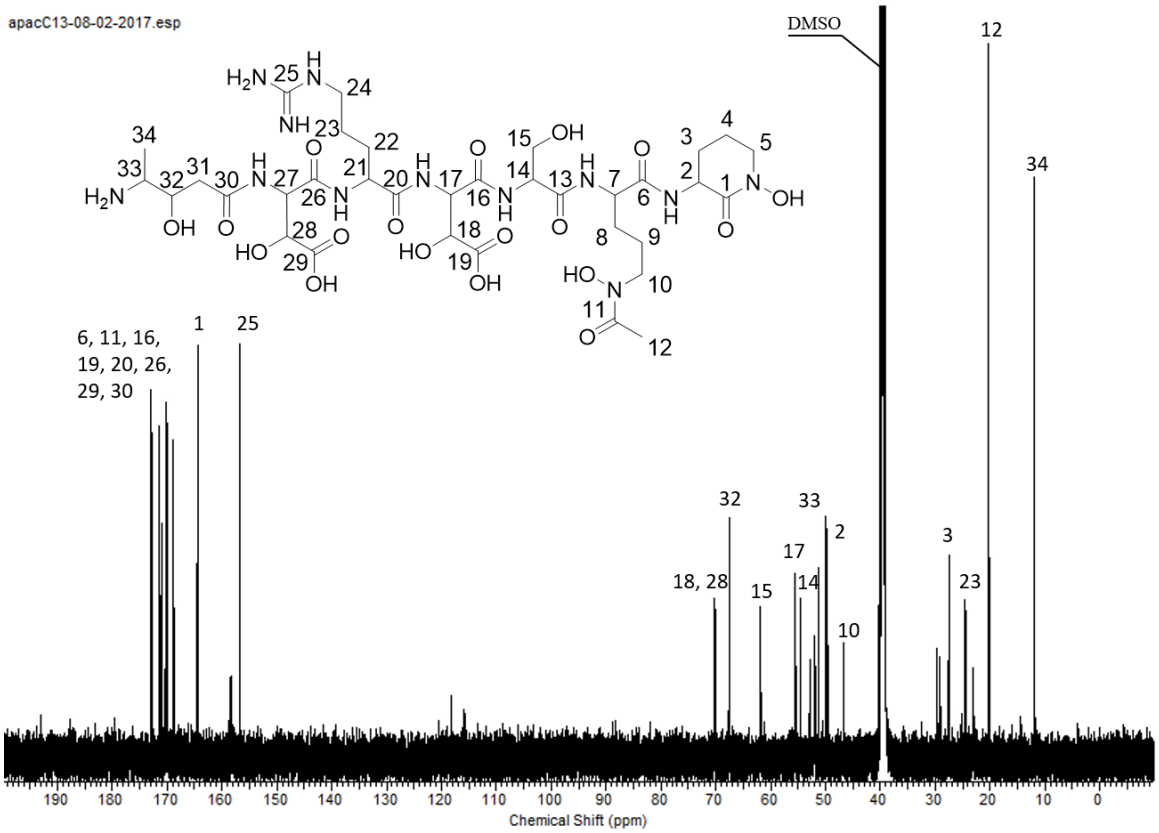

Figure 2.7. ^{13}C (125 MHz) NMR spectrum of pacifibactin (20 mg) in $(CD_3)_2SO$.

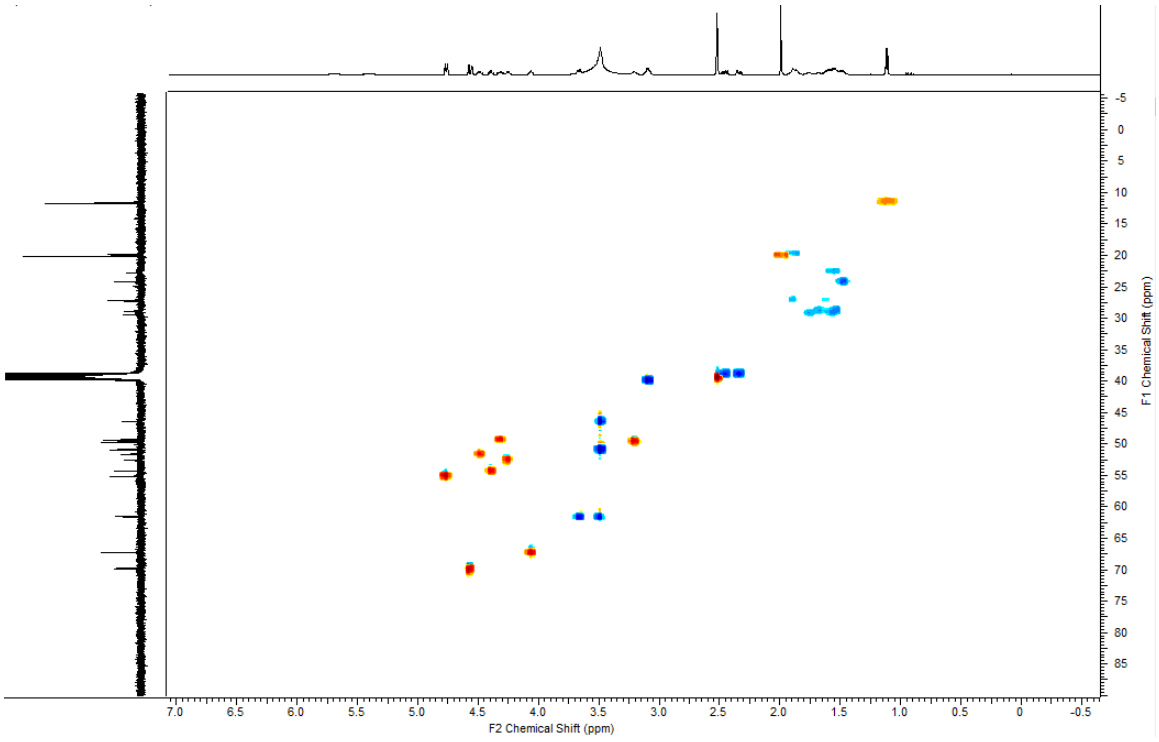

Figure 2.8. ^{1}H-^{13}C HSQC (600 MHz) NMR spectrum of pacifibactin (20 mg) in $(CD_3)_2SO$.

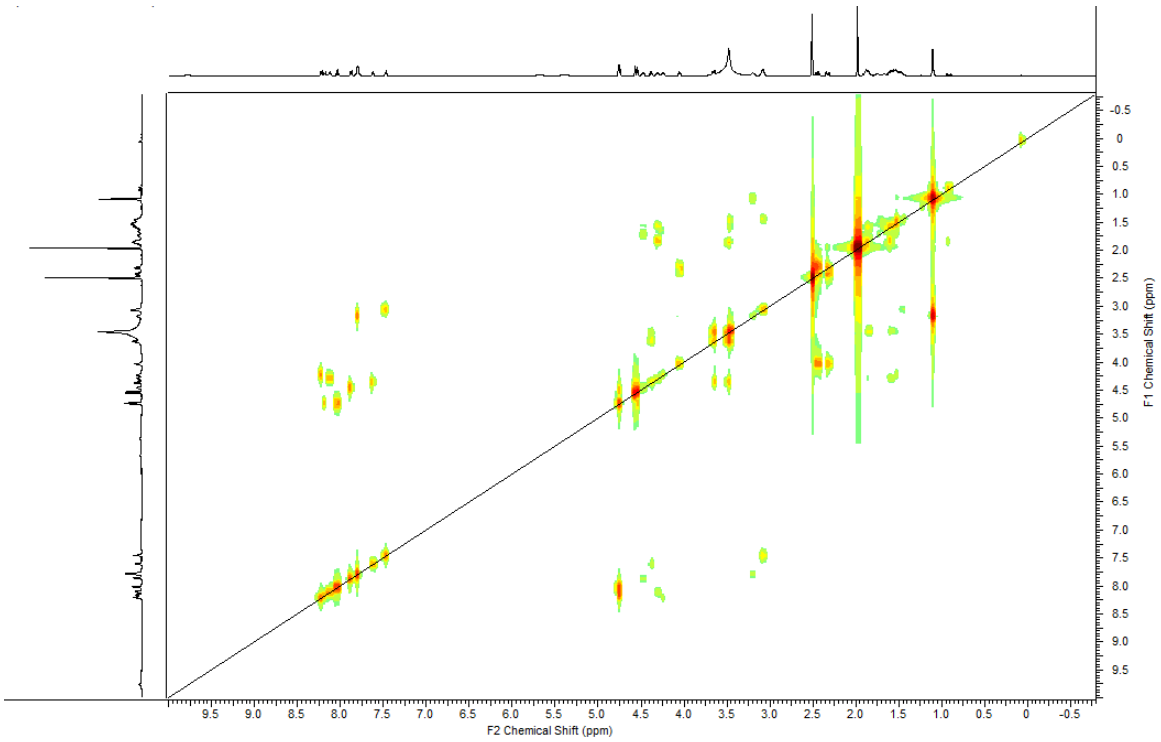

Figure 2.9. ^{1}H-^{1}H COSY (600 MHz) NMR spectrum of pacifibactin (20 mg) in $(CD_3)_2SO$.

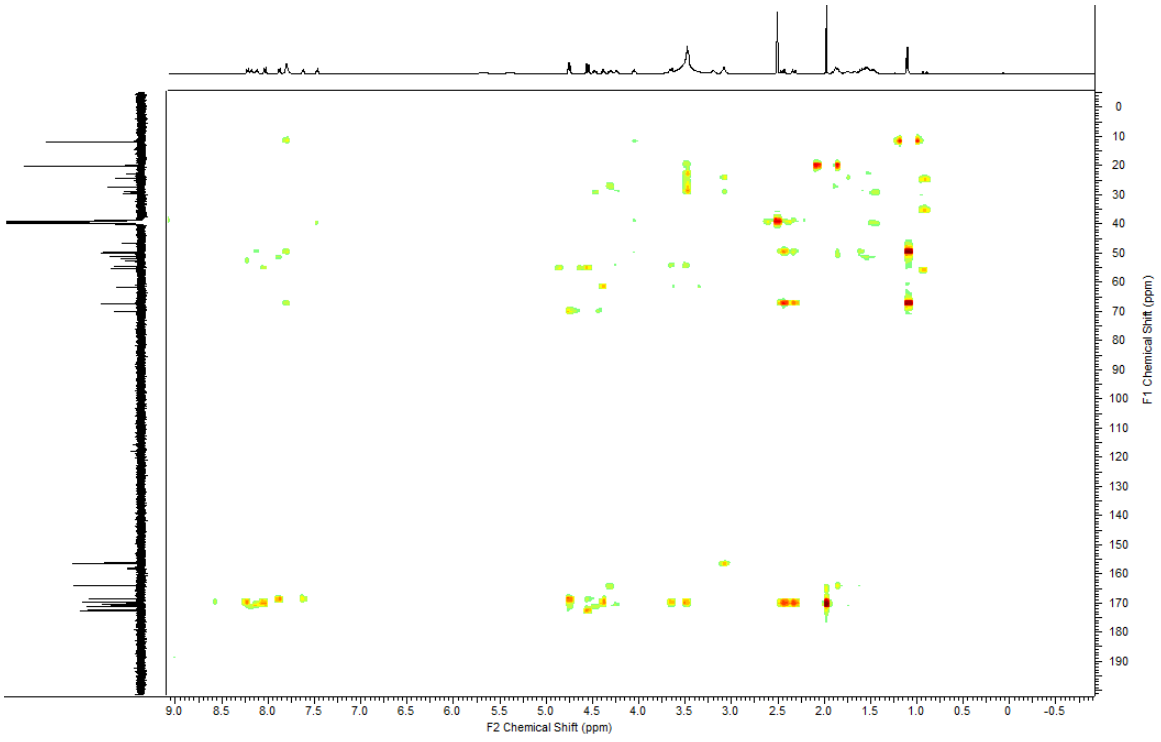

Figure 2.10. ^{1}H-^{13}C HMBC (600 MHz) NMR spectrum of pacifibactin (20 mg) in $(CD_3)_2SO$.

Table 2.2. NMR spectroscopic data (500 MHz, $(CD_3)_2SO$) for pacifibactin (20 mg).

	δ_c, type	δ_H (*J* in Hz)	COSY	HMBC
1	164.5, C			
2	49.6, CH	4.30, m	3, N1	1, 3, 6
3	20.1, CH_2	1.85, m; 1.59, m	2, 4	2
4	27.5, CH_2	1.88, m	3, 5	2, 3, 5
5	51.2, CH_2	3.48, m	4	3, 4
N1		8.12, d (8.0)	2	2, 6
6	171.0, C			
7	52.9, CH	4.24, m	8, 9, N2	6, 8
8	29.1, CH_2	1.52, m	7, 9	7, 9, 10
9	23.0, CH_2	1.57, m	8, 10	8, 10
10	46.7, CH_2	3.46, m	9	8, 11
11	170.3, C			
12	20.4, CH_3	1.97, s		11
N2		8.22, d (7.5)	7	7, 13
13	170.0, C			14, 15
14	54.6, CH	4.38, m	15, N3	13, 15, 16
15	61.9, CH_2	3.48, m; 3.65, m	14	13, 14
N3		7.62, d (7.5)	14	14, 16
16	168.9, C			
17	55.5, CH	4.76, t (2.6)	18, N4	16, 18, 19, 20
18	70.3, CH	4.56, d (2.5)	17	16, 17, 19
19	173.0, C			17, 18
N4		8.18, d (8.8)	17	20
20	171.4, C			
21	51.9, CH	4.47, m	22, N6	20, 22
22	29.6, CH_2	1.74, m; 1.55, m	21	20, 21, 23
23	24.5, CH_2	1.44, m; 1.48, m	24	21, 22, 24
24	40.3, CH_2	3.07, m	23, N5	22, 23
N5		7.47, t (5.6)	24	24, 25
25	156.7, C			
N6		7.87, d (8.0)	21	21, 26
26	168.8, C			
27	55.5, CH	4.74, t (2.6)	28, N7	26, 28, 29, 30
28	70.1, CH	4.54, d (2.5)	27	26, 27, 29
29	172.8, C			
N7		8.03, d (9.0)	27	27, 30
30	170.2, C			
31	38.9, CH_2	2.32, dd (14.27, 5.49) 2.43, dd (14.33, 8.35)	32	30, 32, 33
32	67.6, CH	4.04, m	31, 33	31, 33, 34
33	50.0, CH	3.19, m	32, 34	34
34	11.9, CH_3	1.09, d	33	32, 33

Comparison of the structure of pacifibactin to the bioinformatic prediction reveals several surprises. The adenylation domain of PfbG is predicted by both antiSMASH and PRISM to incorporate Ser, yet Ala appears to be incorporated into pacifibactin at the N-terminus instead. The ensemble algorithm SANDPUMA, which applies several different adenylation domain

specificity predictors and has outperformed any individual method in accuracy,[20] also predicts Ser incorporation by PfbG. The incorporation of Ala highlights the need for continuous refinement of adenylation domain predictor tools as more experimental data is generated.

The *pfb* gene cluster (Figure 2.1) contains three epimerization domains within the NRPS assembly line. Given the placement of the epimerization domains, incorporation of (starting from the N-terminus) L-Ala, L-β-OHAsp, D-Arg, D-β-OHAsp, L-Ser, L-N5-acetyl-N5-OHOrn, and D-N5-OHOrn is expected. Hydrolysis of pacifibactin with HCl or HI (for reductive hydrolysis to yield un-functionalized ornithine) and derivatization of the resultant hydrolysates with Marfey's reagent (1-fluoro-2-4-dinitrophenyl-5-L-alanine amide, FDAA) identifies L-*threo*-β-OHAsp, D-Arg, D-*threo*-β-OHAsp, L-Ser, L-Orn, and D-Orn in the hydrolysate through co-injections with the corresponding derivatized amino acid standards (Figure 2.11, 2.12). The identified amino acids are consistent with the bioinformatic prediction. Co-injections with D,L-*threo*-β-OHAsp confirmed the presence of the *threo* diastereomers in pacifibactin. Moreover, co-injections with a D,L-*erythro*-β-OHAsp establish that pacifibactin does not incorporate the *erythro* diastereomers (Figure 2.11). The incorporation of L-Ala was not confirmed as the PKS-governed reaction forms a carbon-carbon bond between Ala and malonate that is not broken under the hydrolytic conditions.

Blue traces– pacifibactin hydrolysate
Red traces– hydrolysate co-injected with respective derivatized amino acid standard

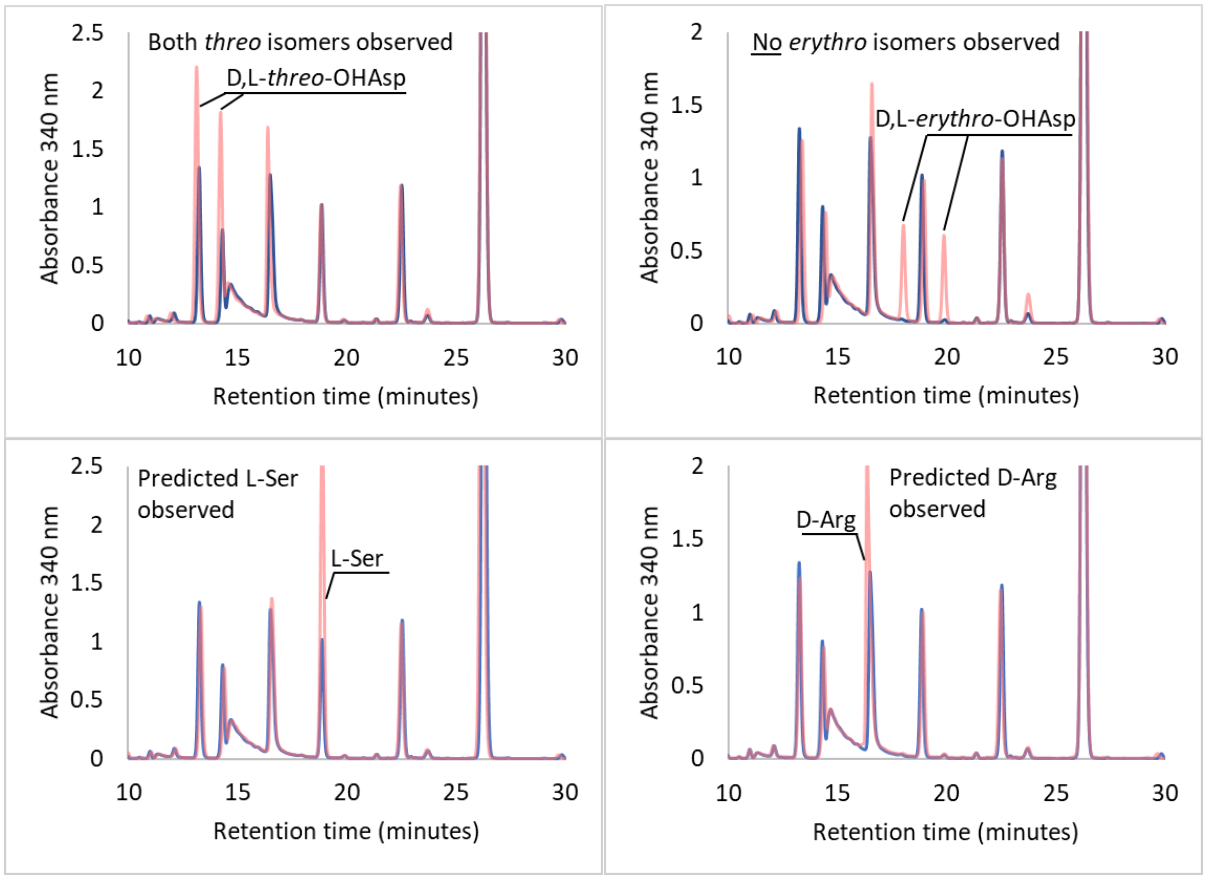

Figure 2.11. HPLC chromatograms of FDAA-derivatized pacifibactin hydrolysate (blue traces) and FDAA-derivatized pacifibactin hydrolysate co-injected with FDAA-derivatized amino acid standards (red traces). D,L-*threo*-β-OHAsp, D,L-*erythro*-β-OHAsp, L-Ser, and D-Arg standards were co-injected. Co-injection with D,L-*erythro*-β-OHAsp confirms that pacifibactin incorporates only *threo* stereoisomers.

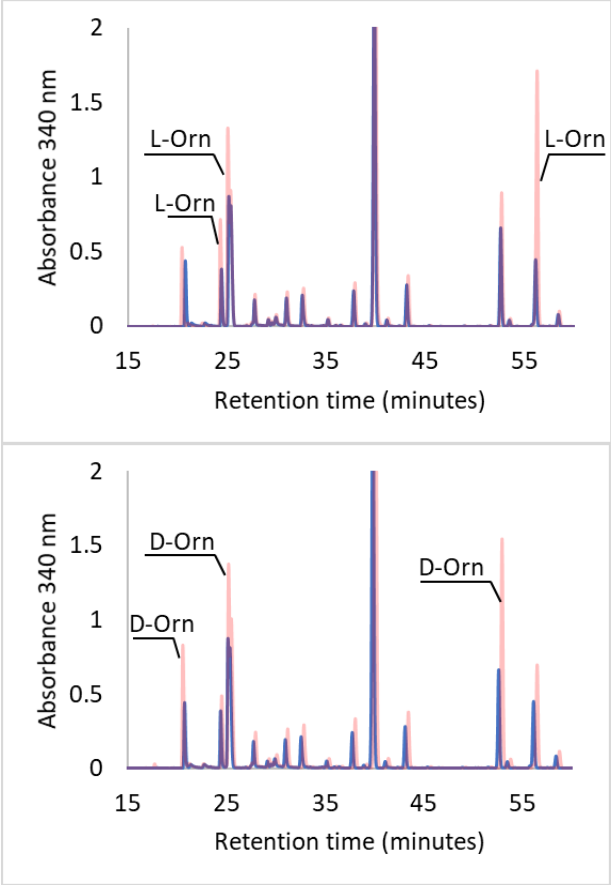

Figure 2.12. HPLC chromatograms of FDAA-derivatized pacifibactin hydrolysate from reductive hydrolysis with HI co-injected with FDAA-derivatized L-Orn and D-Orn standards. The three peaks resulting from FDAA derivatization of Orn represent derivatization at the α-amine, derivatization at the δ-amine, and derivatization at both amines.

2.3.3. Characterization of Structural Variants of Pacifibactin

The unexpected incorporation of Ala into pacifibactin at the N-terminal position, despite a consensus bioinformatic prediction of Ser incorporation, calls into question the substrate specificity of the corresponding adenylation domain. To probe whether L-Ser could be incorporated into pacifibactin in place of L-Ala, *A. pacificus* was cultured in media supplemented with L-Ser. ESI-MS analysis of the resultant culture extracts identified a co-eluting compound of *m/z* 470.2 (z = 2), 16 Da higher than the mass of pacifibactin. This mass increase matches the expected mass increase of Ser incorporation over Ala incorporation

(Figure 2.14). The fragmentation pattern observed by ESI-MSMS (Figure 2.15) confirms that this mass corresponds to a variant of pacifibactin, with the mass increase localized to the N-terminal amino acid (Figure 2.13).

To further test substrate variation at the pacifibactin N-terminus, *A. pacificus* was cultured with supplements of Gly, L-Thr, and L-Val. While no incorporation of L-Thr or L-Val was observed, *A. pacificus* produced a compound of *m/z* 455.2 (z = 2) when supplemented with Gly, 14 amu lower than the mass of pacifibactin (Figure 2.14). The difference is again localized to the N-terminal amino acid, based on MSMS fragmentation (Figure 2.13, Figure 2.16).

The interchange between incorporation of L-Ala, L-Ser, and Gly in pacifibactin biosynthesis is reminiscent of the moanachelin siderophores produced by *Vibrio sp.* NT1 which incorporate either Ala or Gly as the third amino acid residue.[21] The N-terminus of pacifibactin is presumably biosynthesized by PfbG based on bioinformatics analysis, thus further investigation into structural differences between the adenylation domain of PfbG and known Ser-incorporating domains could deepen the understanding of adenylation domain selectivity.

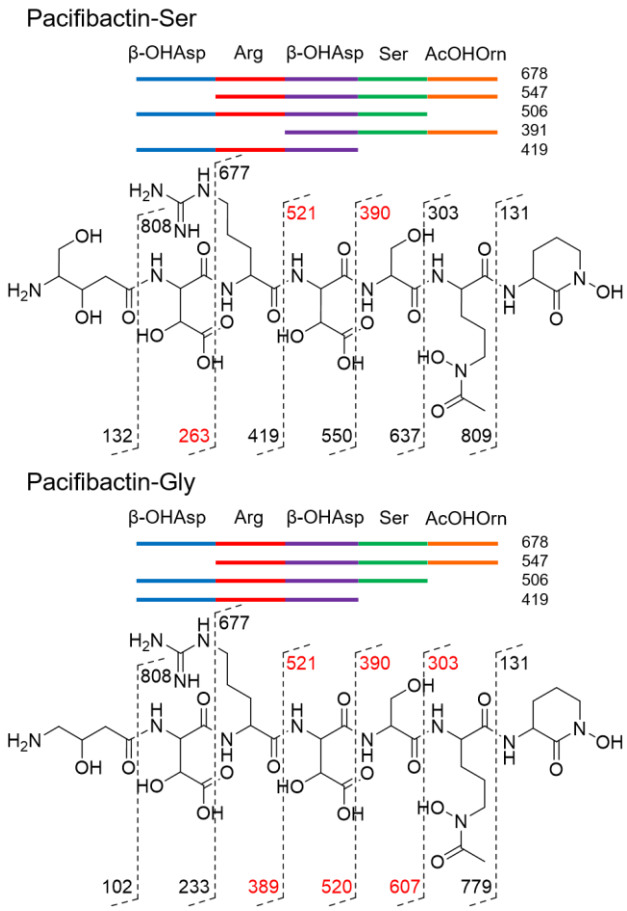

Figure 2.13. MSMS b/y fragmentation patterns for pacifibactin Ser (470.2 *m/z* $[M+2H]^{2+}$) and Gly (455.2 *m/z* $[M+2H]^{2+}$) variants (fragments with *m/z* in red were not observed). Observed internal fragments are shown above the structure.

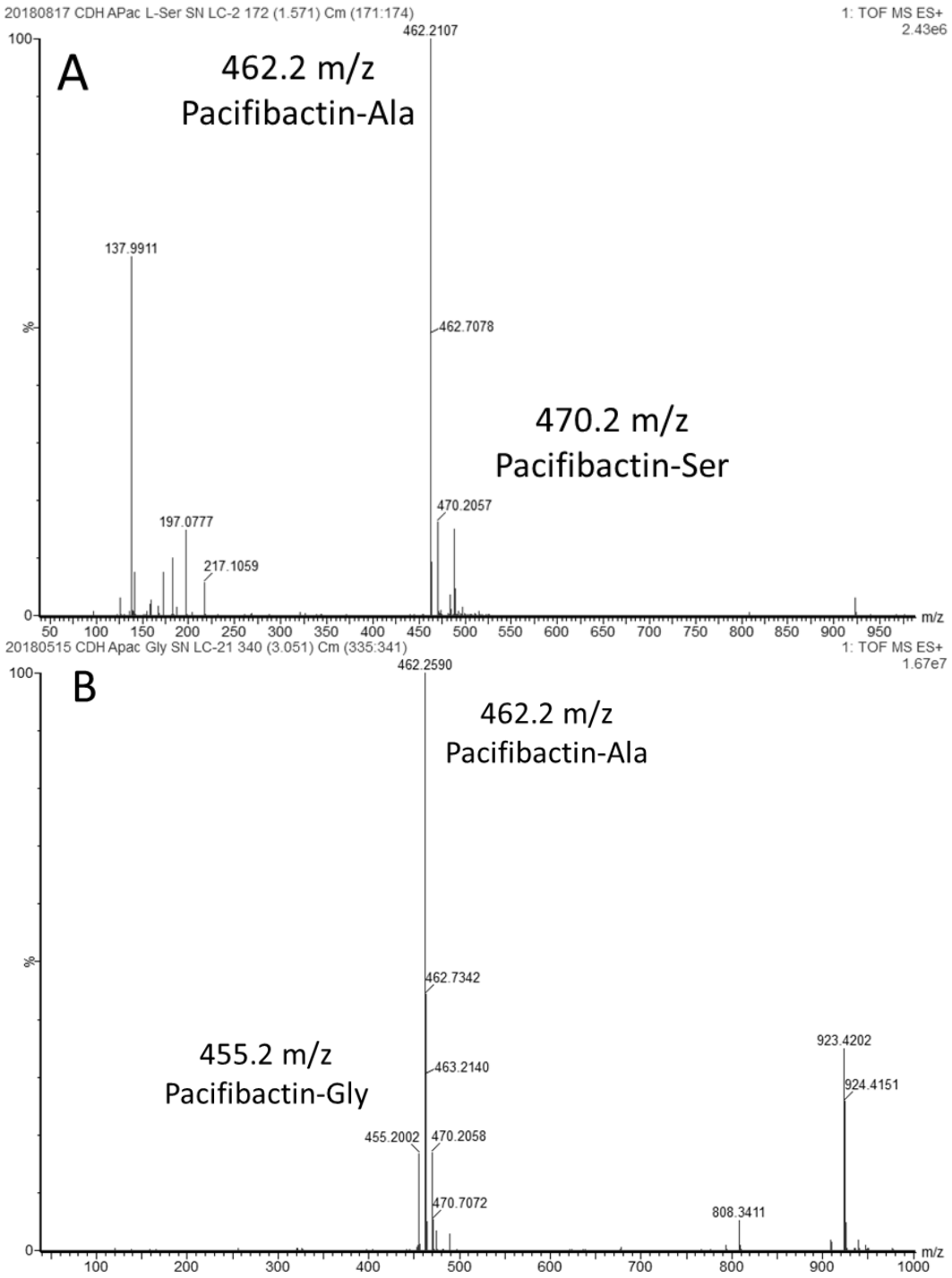

Figure 2.14. A) ESI-MS spectrum of pacifibactin variants from an L-Ser-amended culture of *A. pacificus*, Ala and Ser variants co-elute. **B)** ESI-MS spectrum of pacifibactin variants from a Gly-amended culture of *A. pacificus*, Ala and Gly variants co-elute.

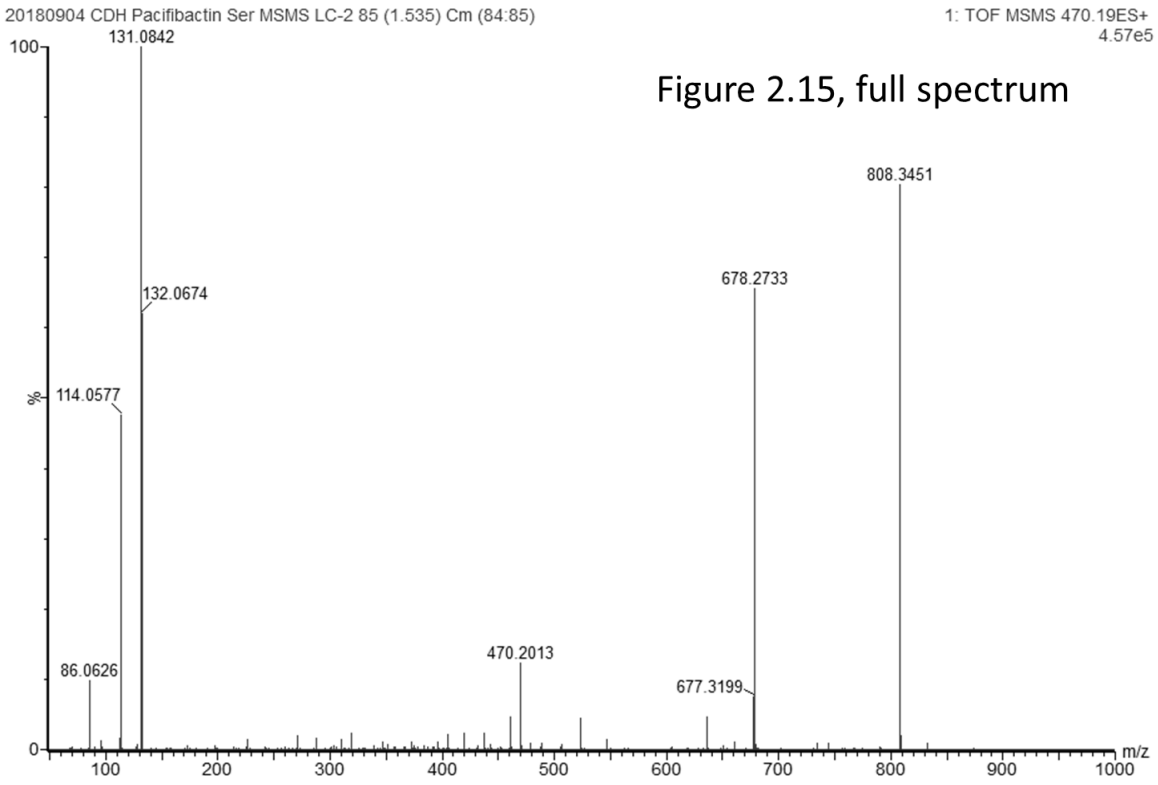

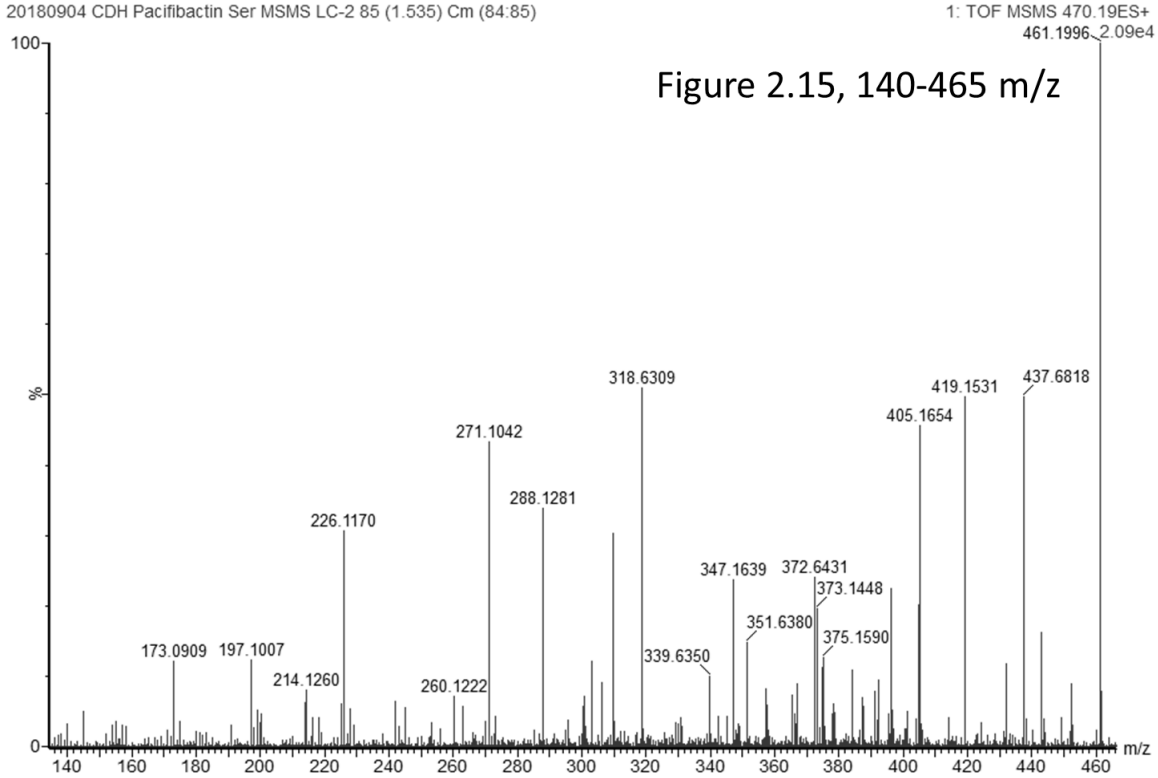

Figure 2.15. ESI-MSMS spectrum of pacifibactin-Ser (m/z = 470.2, z = 2), with selected region zoomed in for clarity. Collision energy profile of 20, 25, and 30 kEV employed.

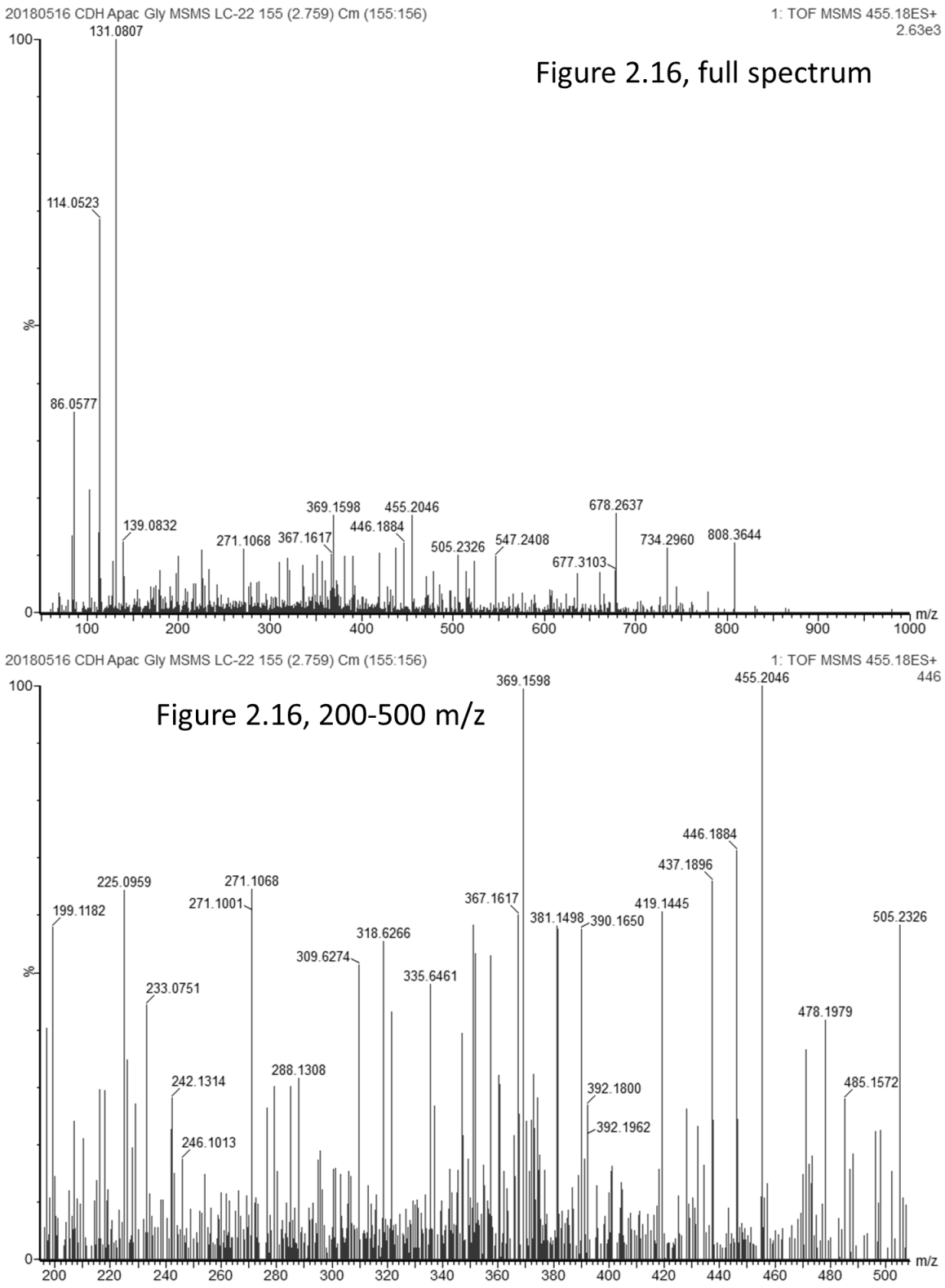

Figure 2.16. ESI-MSMS spectrum of pacifibactin-Gly (m/z = 455.2, z = 2), with selected region zoomed in for clarity. Collision energy profile of 20, 25, and 30 kEV employed.

2.3.4. Fe(III) Titration of Pacifibactin

The structure of pacifibactin contains four bidentate metal binding sites, an unusual feature for siderophores only observed among some desferrioxamines and malleobactin D.[22-23] The presence of four bidentate ligands in the structure of pacifibactin calls into question which groups coordinate Fe(III). Titrating a buffered solution of apo pacifibactin with Fe(III) under neutral pH conditions indicates that despite the extra binding group, pacifibactin coordinates Fe(III) in a 1:1 ratio, as observed for hexadentate siderophores (Figure 2.17). The UV-visible absorption spectrum of Fe(III)-pacifibactin features a peak at 305 nm characteristic of Fe(III)-α-hydroxycarboxylate ligand-to-metal charge transfer (LMCT), and a broad shoulder at 400 nm indicative of Fe(III)-hydroxamate LMCT (Figure 2.17). The spectrum resembles that of Fe(III)-serobactin, a siderophore with two β-OHAsp residues and one cyclized N5-OHOrn residue for Fe(III) coordination.[5] This resemblance suggests that pacifibactin coordinates one Fe(III) through both β-OHAsp residues and either the cyclized N5-OHOrn or the N5-acetyl-N5-OHOrn residue.

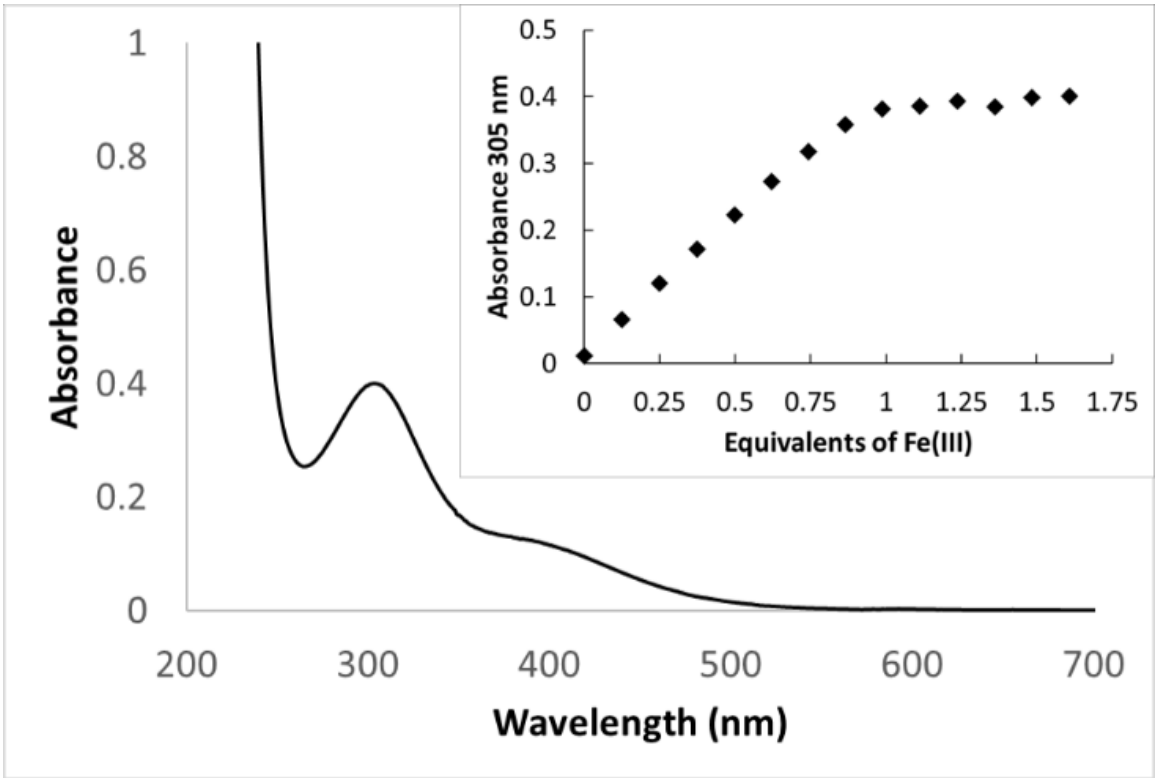

Figure 2.17. UV-visible absorption spectrum of 0.1 mM Fe(III)-pacifibactin in 100 mM MOPS buffer pH 7.1. Insert: spectrophotometric titration of apo pacifibactin (0.1 mM, in 100 mM MOPS pH 7.1) with Fe(III) (2.14 mM in 40 mM HNO_3). A break point in absorbance is observed at 0.9 equivalents Fe(III), suggesting a 1:1 coordination mode.

2.3.5. Photolysis of Fe(III)-Pacifibactin

Fe(III) complexes of α-hydroxycarboxylate siderophores, including β-OHAsp siderophores, are photoreactive.[8, 11, 14, 24-28] To probe photoreactivity, Fe(III)-pacifibactin was photolyzed with a 450W mercury-arc lamp and monitored by UV-visible spectrophotometry. Through 8 h of continuous photolysis, clear shifts in the UV-visible spectrum are observable (Figure 2.18). Upon photolysis, the Fe(III)-hydroxamate absorbance band around 400 nm nearly doubles in intensity and red shifts slightly while two near-isosbestic points are present, suggesting photolysis of Fe(III)-pacifibactin initially yields one Fe(III)-coordinating photoproduct. Continued photolysis after 8 h leads to a loss of isosbestic points, and eventual elimination of the Fe(III)-α-hydroxycarboxylate charge transfer band around 300 nm (Figure

S21). After photolysis, UPLC-ESIMSMS analysis of the reaction mixture identifies a photoproduct resulting from photooxidative cleavage of the peptide backbone at the C-16 to C-19 β-OHAsp residue (Figure 2.18), consistent with photoproducts of other β-OHAsp siderophores.[8, 11, 27]

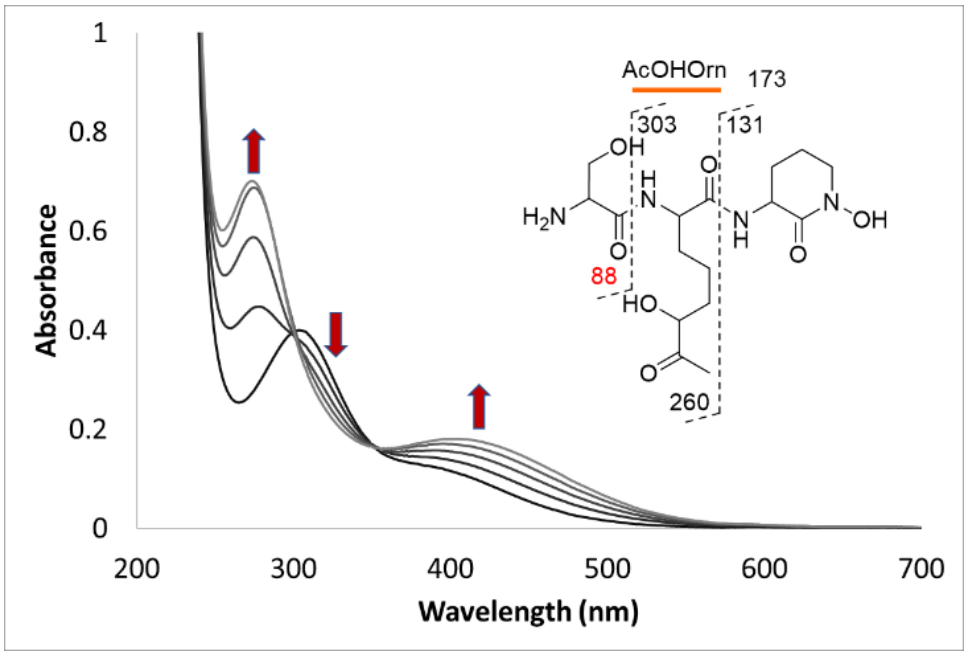

Figure 2.18. UV-visible absorbance spectra of 0.1 mM Fe(III)-pacifibactin in 100 mM MOPS buffer pH 7.1 subjected to 8 h of continuous photolysis with 450W UV mercury-arc lamp, collected from 220-700 nm. Scans are taken at 2 h time points, and lighter grey represents increased time. Arrows indicate increases and decreases in absorbance over time. Inset: structure of photoproduct detected by UPLC-ESI-MSMS (390.2 *m/z*, z = 1), with MSMS b/y fragmentation pattern.

2.3.6. Characterization of Ga(III)-Pacifibactin

To identify the binding groups involved in Fe(III) coordination in pacifibactin, the Ga(III)-pacifibactin complex was prepared as an NMR-compatible mimic to Fe(III)-pacifibactin. After Ga(III) complexation, ^{13}C chemical shifts in both β-OHAsp residues and the N5-acetyl-N5-OHOrn residue showed significant changes relative to apo pacifibactin, while no significant differences were observed in the ^{13}C chemical shifts of the cyclized N5-hydroxyornithine

residue (Table 2.3, Figures 2.18-2.23). The observed chemical shifts indicate that Ga(III) likely coordinates to pacifibactin through both β-OHAsp residues and N5-acetyl-N5-OHOrn, but not the cyclized N5-OHOrn residue.

Table 2.3. ^{13}C Chemical shifts of Ga(III)-pacifibactin (in D_2O) compared to apo pacifibactin.

		CO (ppm)	Cα (ppm)	Cβ (ppm)	Cγ (ppm)	Cδ (ppm)	C acetyl (ppm)
CyOHOrn	Apo	166.41	50.32	26.56	19.93	51.57	
	Ga(III)	166.18	49.97	26.83	19.83	51.65	
AcOHOrn	Apo	173.49	53.62	27.91	22.36	**47.20**	**173.84**
	Ga(III)	173.78	54.28	26.11	22.99	**49.87**	**164.61**
βOHAsp	Apo	**170.37**	**55.76**	**70.27**	**174.21**		
(C#16-19)	Ga(III)	**175.94**	**61.23**	**73.18**	**182.65**		
βOHAsp	Apo	**171.56**	**55.66**	**70.07**	**174.09**		
(C#26-29)	Ga(III)	**173.16**	**59.09**	**74.10**	**180.05**		

Bolded resonances indicate a significant change in the ^{13}C chemical shift after Ga(III) coordination.

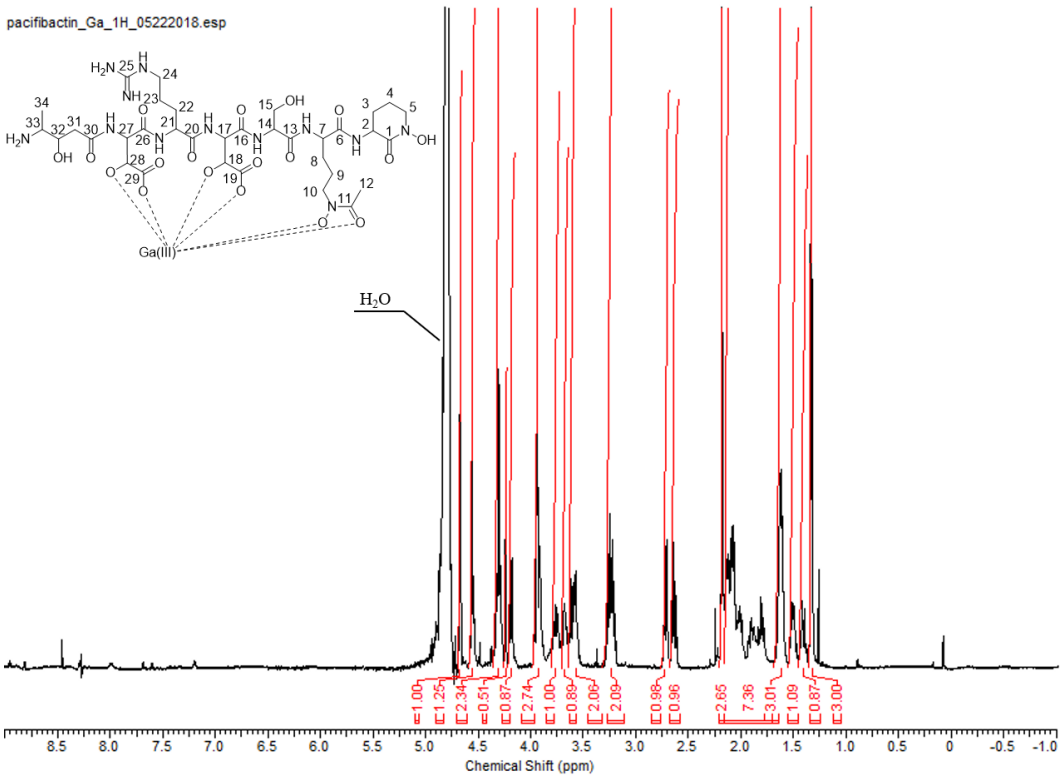

Figure 2.19. ^{1}H (500 MHz) NMR spectrum of Ga(III)-pacifibactin (10 mg) in D_2O.

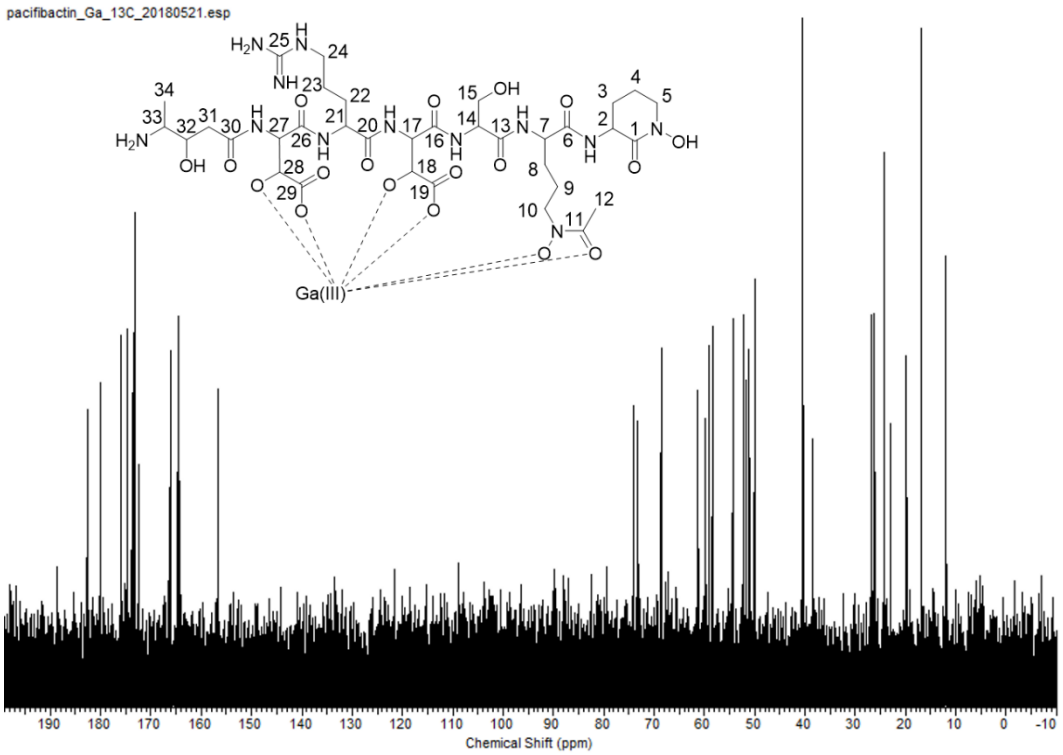

Figure 2.20. ^{13}C (125 MHz) NMR spectrum of Ga(III)-pacifibactin (10 mg) in D_2O.

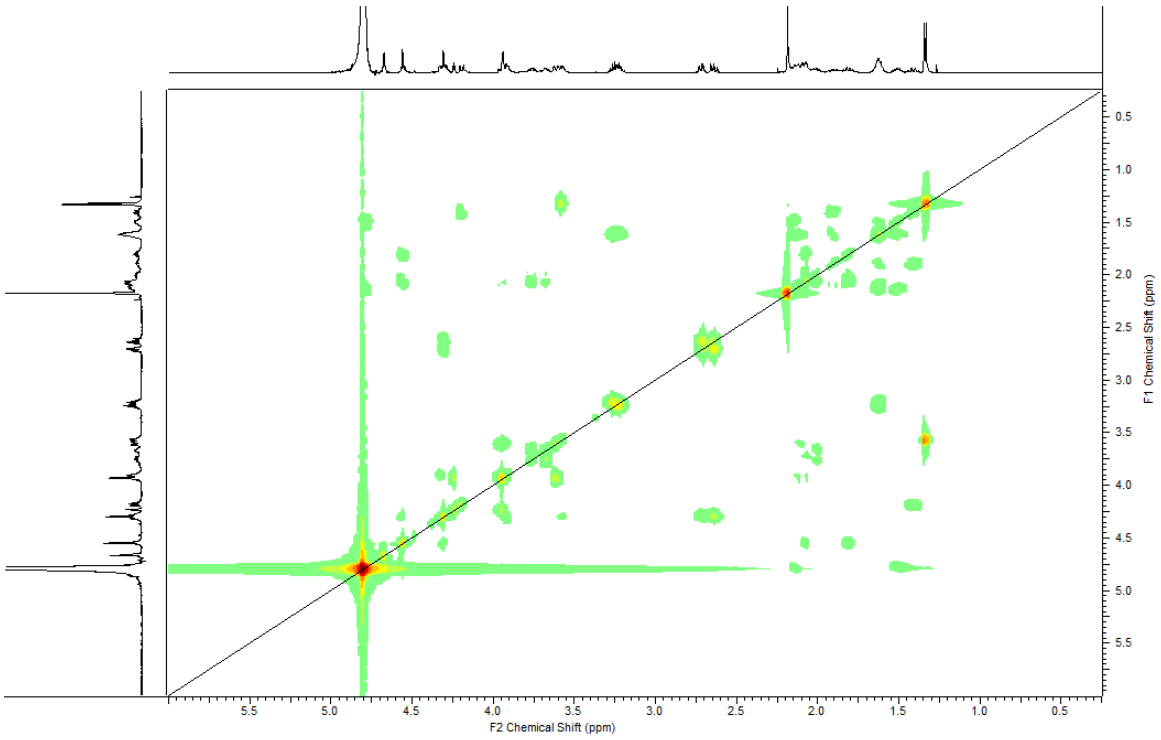

Figure 2.21. ^{1}H-^{1}H COSY (600 MHz) NMR spectrum of Ga(III)-pacifibactin (10 mg) in D_2O.

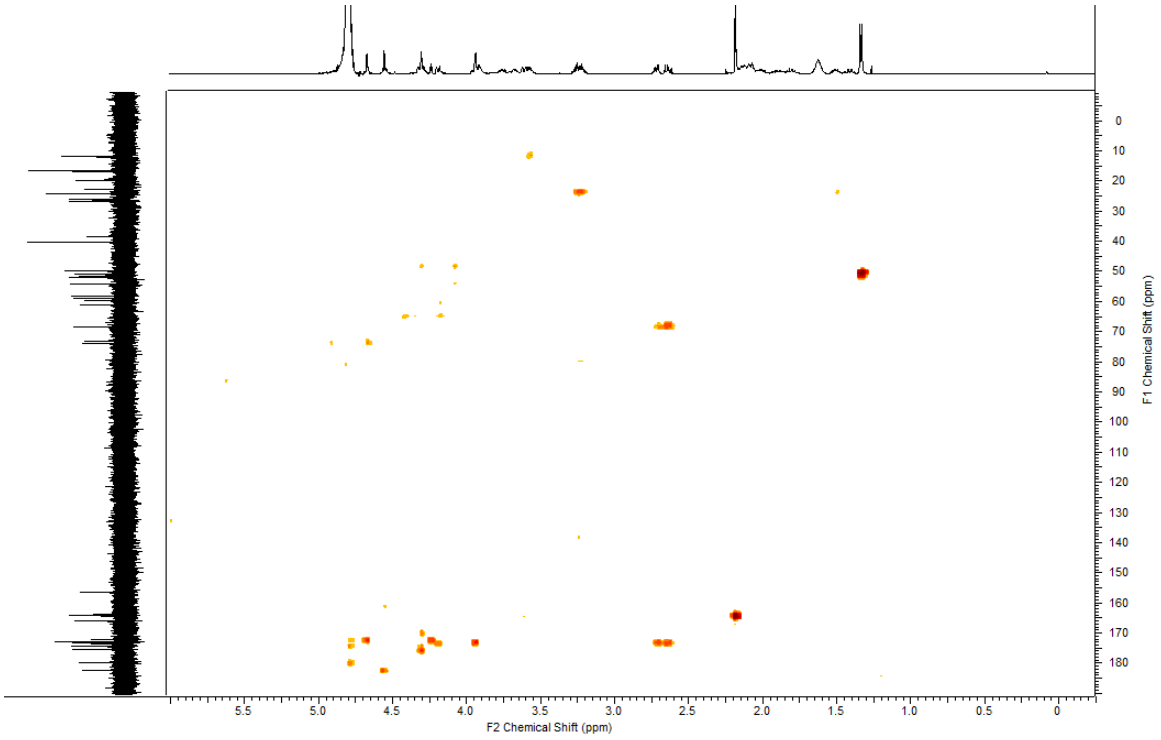

Figure 2.22. ^{1}H-^{13}C HMBC (600 MHz) NMR spectrum of Ga(III)-pacifibactin (10 mg) in D_2O.

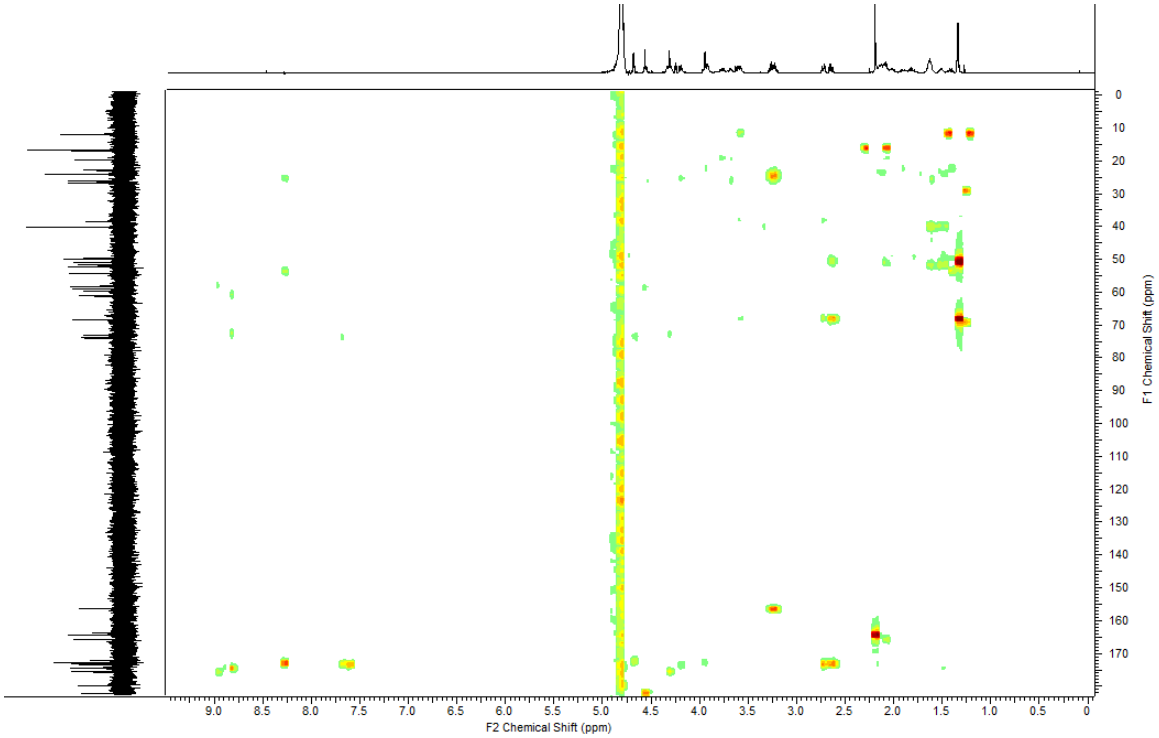

Figure 2.23. ^{1}H-^{13}C HMBC (600 MHz) NMR spectrum of Ga(III)-pacifibactin (10 mg) in 10% D_2O. As a separate ^{1}H NMR spectrum of Ga(III)-pacifibactin in 10% D_2O was not taken, the spectrum is enclosed in the ^{1}H NMR spectrum of Ga(III)-pacifibactin in 99% D_2O.

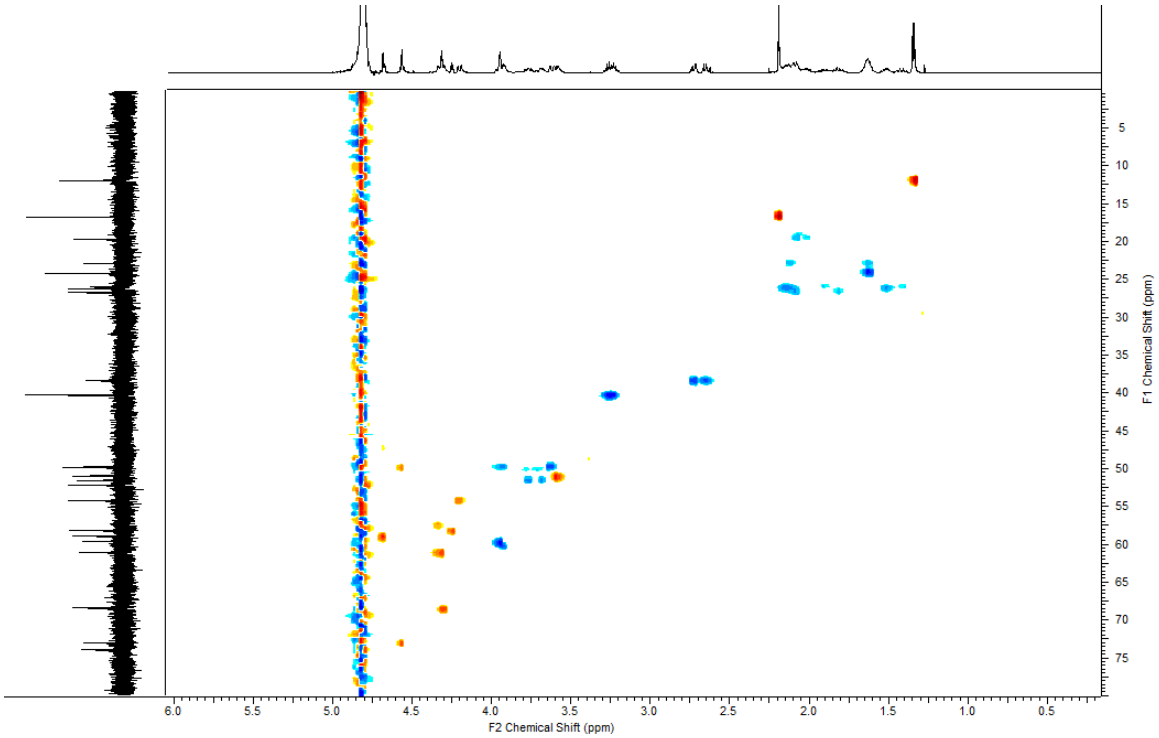

Figure 2.24. ^{1}H-^{13}C HSQC (600 MHz) NMR spectrum of Ga(III)-pacifibactin (10 mg) in 10% D_2O.

2.3.7. Zr(IV) Exchange Between Pacifibactin and Desferrioxamine B

Zirconium(IV)-89 is a radiometal of increasing usage in immunological positron emission tomography imaging.[29] The desferrioxamine siderophores have been used as a template for both synthetic[30] and engineered biosynthetic[31] assemblies of octadentate, water soluble Zr(IV) chelators. At first glance, pacifibactin appears capable of providing octadentate coordination through its four bidentate binding groups, and the charged Arg residue enhances the water solubility of the ligand. Thus, the coordination chemistry of pacifibactin to Zr(IV) was explored, including its competitiveness in Zr(IV) complexation against the hexadentate siderophore desferrioxamine B (DFOB).

UPLC-ESIMS analysis following overnight incubation of a solution of 0.1 mM apo pacifibactin and 0.1 mM $Zr(acac)_2$ in 100 mM MOPS (pH 7) indicates that nearly all pacifibactin in solution is chelating Zr(IV) (Figure 2.24). The mass spectrum of the Zr(IV)-pacifibactin complex peak is consistent with the isotopic natural abundance of zirconium (Figure 2.24). Zr(IV) complexation was not unexpected, as other hexadentate siderophores readily bind Zr(IV). To determine if the four bidentate binding groups of pacifibactin provide it with a competitive advantage over the hexadentate siderophore desferrioxamine B (DFOB), a siderophore already known to complex Zr(IV),[29] Zr(IV)-pacifibactin was incubated with apo DFOB. After one hour of incubation, the solution was analyzed by UPLC-ESIMS. After addition of apo DFOB a strong signal from apo pacifibactin is observable, as well as a clear signal for Zr(IV)-DFOB (Figure 2.25). These results indicate that pacifibactin does not outcompete hexadentate siderophores for complexation of Zr(IV).

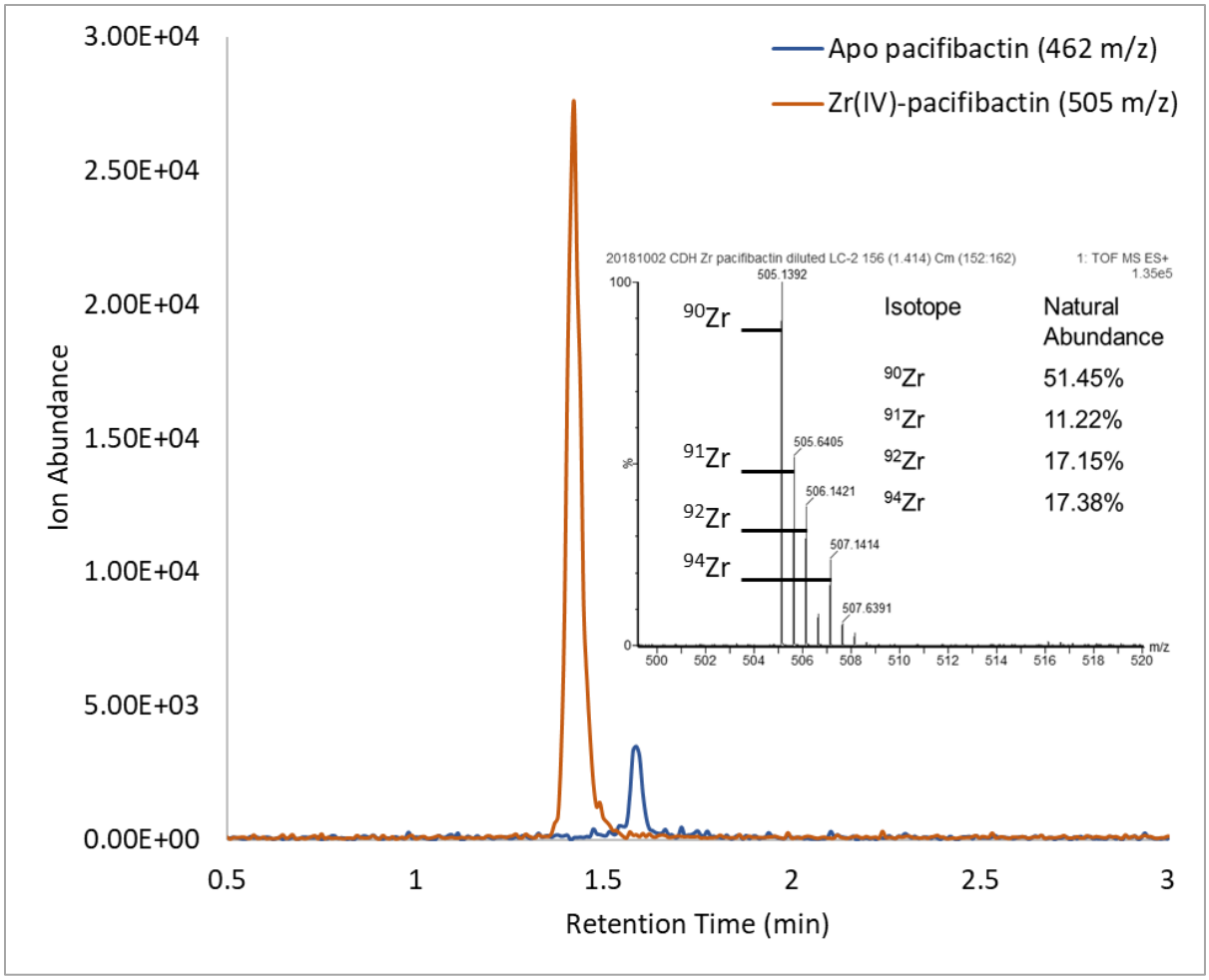

Figure 2.25. Extracted ion chromatograms of apo pacifibactin (blue, 462.2 ± 0.1 m/z) and Zr(IV)-pacifibactin (orange, 505.12-507.15 m/z) from a UPLC-ESIMS analysis of 0.1 mM pacifibactin and 0.1 mM $Zr(acac)_2$ after overnight incubation. A clear signal corresponding to Zr(IV)-pacifibactin is observed and much more abundant than apo pacifibactin signal. Inset: ESI-MS spectrum of Zr(IV)-pacifibactin, which is consistent with the natural isotope abundance of Zr.

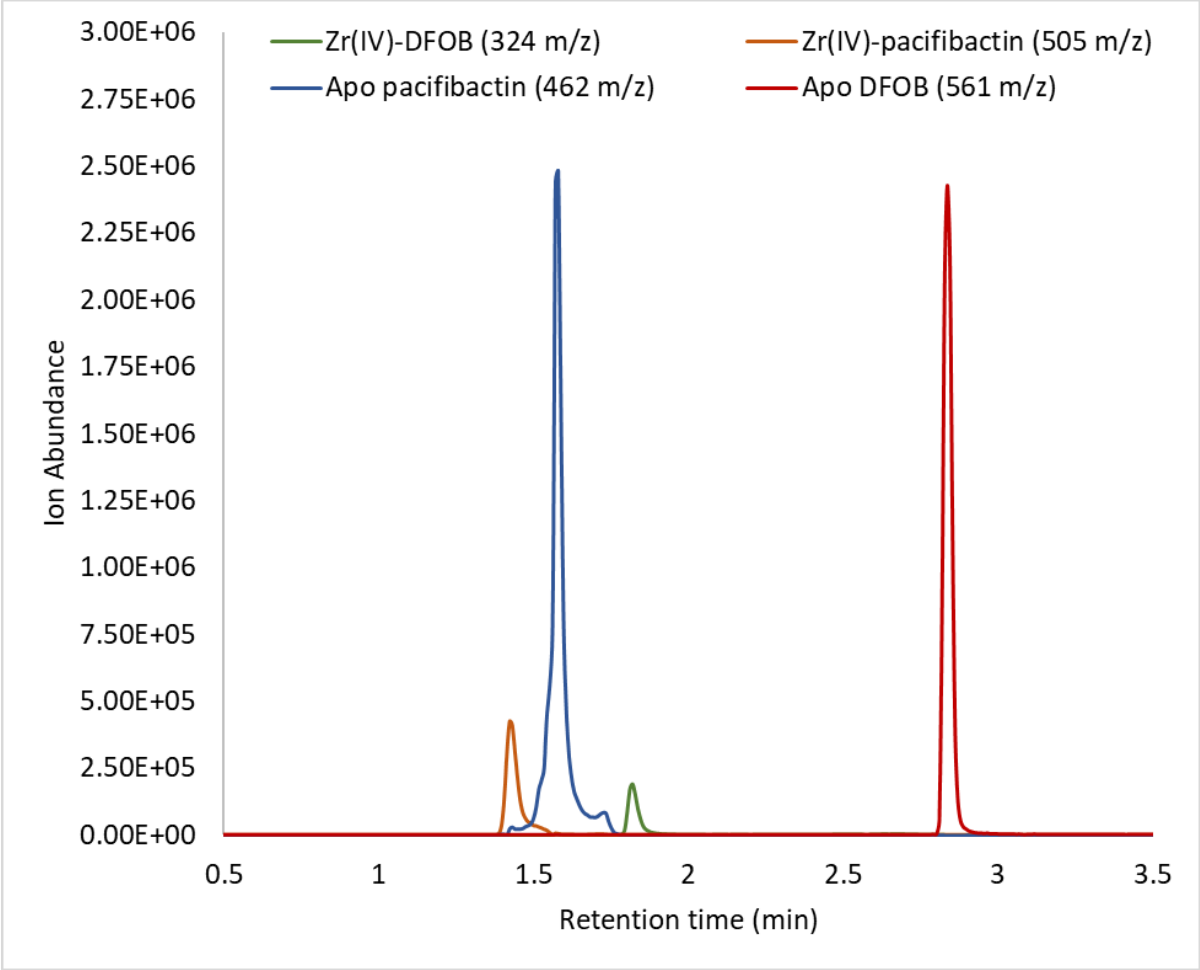

Figure 2.26. Extracted ion chromatograms of Zr(IV)-desferrioxamine B (green, 324.11-326.14 m/z), Zr(IV)-pacifibactin (orange, 505.12-507.15 m/z), apo desferrioxamine B (red, 561.36 ± 0.1 m/z and 281.18 ± 0.1 m/z), and apo pacifibactin (blue, 462.20 ± 0.1 m/z) from UPLC-ESIMS analysis of 0.1 mM Zr(IV)-pacifibactin incubated with 0.1 mM apo DFOB for one hour. The large increase in apo pacifibactin abundance relative to Zr(IV)-pacifibactin as well as the measurable Zr(IV)-DFOB signal indicate that DFOB is competitive with pacifibactin for chelation of Zr(IV).

2.4. Discussion

Perhaps the most intriguing aspect of pacifibactin is the presence of four bidentate binding groups in pacifibactin, as siderophores generally have three bidentate binding groups to satisfy hexadentate coordination to Fe(III). The bioinformatic analysis predicts incorporation of two Asp and two OHOrn by the NRPS assembly line, however neither Asp nor OHOrn act as bidentate metal chelators without further tailoring. While these residues were expected to

provide the metal chelation sites typical of siderophores, unmodified Asp and OHOrn residues have been identified in other siderophore structures,[22, 32-34] thus not all four residues were expected to be modified as bidentate metal chelators. An expanded manual analysis of the *pfb* gene cluster helps explain this unexpected result. The amino acid sequence of PfbN exhibits homology to N-acetyl transferases implicated in the acetylation of Lys and Orn in other siderophores.[35-36] N5-acetyl-N5-OHOrn is known to be synthesized prior to adenylation,[36] thus further development of predictor tools is needed to distinguish this substrate from OHOrn. The mechanism of N5-OHOrn cyclization is as yet unknown, however in consideration of the mechanism of NRPS peptide bond formation cyclization must occur after incorporation of OHOrn, making prediction through bioinformatics tools difficult.

Both Asp residues in pacifibactin are hydroxylated at the β-carbon to form β-OHAsp. Accordingly PfbF exhibits homology to the Fe(II)/α-ketoglutarate dependent Asp β-hydroxylase SyrP of *Pseudomonas syringae.*[37] Additionally, a domain exhibiting homology with SyrP is found in the PKS protein PfbH. Notably, neither antiSMASH nor PRISM picked up this domain as an Asp β-hydroxylase. Putative Asp β-hydroxylating domains have been observed in other siderophore gene clusters.[5, 8, 27, 34] In the biosynthetic gene clusters of serobactin and cupriachelin, both Asp β-hydroxylating NRPS domains and discrete Asp β-hydroxylating enzymes have been identified.[5, 27] Each of these siderophores, like pacifibactin, contain two β-OHAsp residues. β-Hydroxylation of Asp occurs after tethering to the assembly line, thus adenylation domain analysis alone is insufficient to predict incorporation of β-OHAsp residues in a NRPS product. However, development of future bioinformatics tools that pair adenylation domain analysis with identification of these putative β-hydroxylases could successfully predict incorporation of β-OHAsp.

The structure of pacifibactin highlights several limitations to existing NRPS cluster analysis programs. While programs such as antiSMASH identify and annotate NRPS domains within a gene cluster, both non-canonical NRPS domains and tailoring enzymes acting externally from the NRPS proteins elude identification. The characterization of pacifibactin makes clear that automated tools such as antiSMASH remain limited in their ability to generate accurate structure predictions of NRPS-synthesized siderophores, yet also details a path to improving these predictions. While antiSMASH by design takes a conservative approach to the chemistry prediction of NRPS and PKS products,[3] we propose that the identification of tailoring enzymes and domains associated with siderophore production could be incorporated into automated genome mining tools. The accurate prediction of OHOrn tailoring enzymes and Asp β-hydroxylases within NRPS gene clusters could not only improve the accuracy of structure predictions but also aid in distinguishing NRPS clusters as siderophore producers.

2.5. References

1. Jensen, P. R., *Trends Microbiol.* **2016,** *24* (12), 968-977.

2. Ziemert, N.; Alanjary, M.; Weber, T., *Nat. Prod. Rep.* **2016,** *33* (8), 988-1005.

3. Blin, K.; Wolf, T.; Chevrette, M. G.; Lu, X.; Schwalen, C. J.; Kautsar, S. A.; Suarez Duran, H. G.; de los Santos, E. L. C.; Kim, H. U.; Nave, M.; Dickschat, J. S.; Mitchell, D. A.; Shelest, E.; Breitling, R.; Takano, E.; Lee, S. Y.; Weber, T.; Medema, M. H., *Nucleic Acids Res.* **2017,** *45* (W1), W36-W41.

4. Skinnider, M. A.; Dejong, C. A.; Rees, P. N.; Johnston, C. W.; Li, H.; Webster, Andrew L. H.; Wyatt, M. A.; Magarvey, N. A., *Nucleic Acids Res.* **2015,** *43* (20), 9645-9662.

5. Rosconi, F.; Davyt, D.; Martínez, V.; Martínez, M.; Abin-Carriquiry, J. A.; Zane, H.; Butler, A.; de Souza, E. M.; Fabiano, E., *Environ. Microbiol.* **2013,** *15* (3), 916-927.

6. Bosello, M.; Zeyadi, M.; Kraas, F. I.; Linne, U.; Xie, X.; Marahiel, M. A., *J. Nat. Prod.* **2013,** *76* (12), 2282-2290.

7. Zane, H. K.; Naka, H.; Rosconi, F.; Sandy, M.; Haygood, M. G.; Butler, A., *J. Am. Chem. Soc.* **2014,** *136* (15), 5615-5618.

8. Kurth, C.; Schieferdecker, S.; Athanasopoulou, K.; Seccareccia, I.; Nett, M., *J. Nat. Prod.* **2016,** *79* (4), 865-872.

9. Hermenau, R.; Ishida, K.; Gama, S.; Hoffmann, B.; Pfeifer-Leeg, M.; Plass, W.; Mohr, J. F.; Wichard, T.; Saluz, H.-P.; Hertweck, C., *Nat. Chem. Biol.* **2018,** *14* (9), 841-843.

10. Kem, M. P.; Zane, H. K.; Springer, S. D.; Gauglitz, J. M.; Butler, A., *Metallomics* **2014,** *6* (6), 1150-1155.

11. Barbeau, K.; Rue, E. L.; Bruland, K. W.; Butler, A., *Nature* **2001,** *413*, 409-413.

12. Lai, Q.; Shao, Z., *J. Bacteriol.* **2012,** *194* (24), 6936.

13. Marfey, P., *Carlsberg Res. Commun.* **1984,** *49* (6), 591.

14. Robertson, A. W.; McCarville, N. G.; MacIntyre, L. W.; Correa, H.; Haltli, B.; Marchbank, D. H.; Kerr, R. G., *J. Nat. Prod.* **2018**.

15. Fortune, W. B.; Mellon, M. G., *Ind. Eng. Chem., Anal. Ed.* **1938,** *10*, 60-64.

16. Loomis, L. D.; Raymond, K. N., *J. Coord. Chem.* **1991,** *23* (1-4), 361-387.

17. Lai, Q.; Wang, L.; Liu, Y.; Fu, Y.; Zhong, H.; Wang, B.; Chen, L.; Wang, J.; Sun, F.; Shao, Z., *Int. J. Syst. Evol. Microbiol.* **2011,** *61* (6), 1370-1374.

18. Schwyn, B.; Neilands, J. B., *Anal. Biochem.* **1987,** *160* (1), 47-56.

19. Quadri, L. E. N.; Sello, J.; Keating, T. A.; Weinreb, P. H.; Walsh, C. T., *Chem. Biol.* **1998,** *5* (11), 631-645.

20. Chevrette, M. G.; Aicheler, F.; Kohlbacher, O.; Currie, C. R.; Medema, M. H., *Bioinformatics* **2017,** *33* (20), 3202-3210.

21. Gauglitz, J. M.; Butler, A., *J. Biol. Inorg. Chem.* **2013,** *18* (5), 489-497.

22. Franke, J.; Ishida, K.; Hertweck, C., *Chem. Eur. J.* **2015,** *21* (22), 8010-8014.

23. Feistner, G. J.; Stahl, D. C.; Gabrik, A. H., *Org. Mass Spectrom.* **1993,** *28* (3), 163-175.

24. Küpper, F. C.; Carrano, C. J.; Kuhn, J.-U.; Butler, A., *Inorg. Chem.* **2006,** *45* (15), 6028-6033.

25. Amin, S. A.; Green, D. H.; Küpper, F. C.; Carrano, C. J., *Inorg. Chem.* **2009,** *48* (23), 11451-11458.

26. Butler, A.; Theisen, R. M., *Coord. Chem. Rev.* **2010,** *254* (3), 288-296.

27. Kreutzer, M. F.; Kage, H.; Nett, M., *J. Am. Chem. Soc.* **2012,** *134* (11), 5415-5422.

28. Hardy, C. D.; Butler, A., *JBIC Journal of Biological Inorganic Chemistry* **2018**.

29. Deri, M. A.; Zeglis, B. M.; Francesconi, L. C.; Lewis, J. S., *Nucl. Med. Biol.* **2013,** *40* (1), 3-14.

30. Tieu, W.; Lifa, T.; Katsifis, A.; Codd, R., *Inorg. Chem.* **2017,** *56* (6), 3719-3728.

31. Richardson-Sanchez, T.; Tieu, W.; Gotsbacher, M. P.; Telfer, T. J.; Codd, R., *Org. Biomol. Chem.* **2017,** *15* (27), 5719-5730.

32. Franke, J.; Ishida, K.; Ishida-Ito, M.; Hertweck, C., *Angew. Chem. Int. Ed.* **2013,** *52* (32), 8271-8275.

33. Johnston, C. W.; Skinnider, M. A.; Wyatt, M. A.; Li, X.; Ranieri, M. R. M.; Yang, L.; Zechel, D. L.; Ma, B.; Magarvey, N. A., *Nat. Commun.* **2015,** *6*, 8421.

34. Kreutzer, M. F.; Nett, M., *Org. Biomol. Chem.* **2012,** *10* (47), 9338-9343.

35. Heydel, P.; Plattner, H.; Diekmann, H., *FEMS Microbiol. Lett.* **1987,** *40* (2-3), 305-309.

36. Robbel, L.; Helmetag, V.; Knappe, T. A.; Marahiel, M. A., *Biochemistry* **2011,** *50* (27), 6073-6080.

37. Singh, G. M.; Fortin, P. D.; Koglin, A.; Walsh, C. T., *Biochemistry* **2008,** *47* (43), 11310-11320.

3. Stereochemical Characterization of β-Hydroxyaspartate Siderophores

Sections of this chapter were published in: Reitz, Z. L.; Hardy, C. D.; Suk, J.; Bouvet, J.; Butler, A. Genomic analysis of siderophore β-hydroxylases reveals divergent stereocontrol and expands the condensation domain family. *Proc. Nat. Acad. Sci. USA* **2019**, *116*, 19805-19814

3.1. Introduction

Many siderophores synthesized by non-ribosomal peptide synthetases (NRPSs) incorporate β-hydroxyaspartic acid, which functions as a bidentate coordination site for Fe(III).[1] As discussed in detail in Chapter 1, NRPS gene clusters related to β-OHAsp siderophore production encode putative aspartyl β-hydroxylases, either as discrete enzymes or as domains within an NRPS enzyme.[2-12] In recent work, *Reitz et al* have analyzed biosynthetic gene clusters corresponding to structurally characterized β-OHAsp siderophores, revealing structural and functional patterns of their putative aspartyl β-hydroxylases that align with a corresponding phylogenetic analysis.[13] The hydroxylases form two distinct clades, termed "interface-associated" Asp β-hydroxylases ($I\beta H_{Asp}$) and "T_E-associated" aspartyl β-hydroxylases ($T\beta H_{Asp}$) (Figure 3.1).

$I\beta H_{Asp}$ hydroxylases are NRPS domains with homology to aspartyl β-hydroxylases. These hydroxylases seem to only function when the module that loads Asp for incorporation into the NRPS product also contains a distinct domain, termed the interface domain. This domain is homologous to condensation domains, but lacks key catalytic residues,[13] and is hypothesized to facilitate interaction between the hydroxylase domain and the NRPS-tethered Asp substrate.

IβH$_{Asp}$ hydroxylases are associated with siderophores containing L-*threo* β-OHAsp (2S, 3S) residues.

TβH$_{Asp}$ hydroxylases are discrete enzymes encoded by a separate gene, associated with hydroxylation of Asp residues tethered by a T$_E$ domain, a subset of thiolation domains that are generally followed by an epimerization domain. The siderophore products associated with TβH$_{Asp}$ hydroxylases almost all feature a 3R stereocenter in the β-OHAsp residue that corresponds to putative hydroxylation by a TβH$_{Asp}$ hydroxylase (Figure 3.1). These residues are all D-*threo* β-OHAsp residues (2R, 3R).

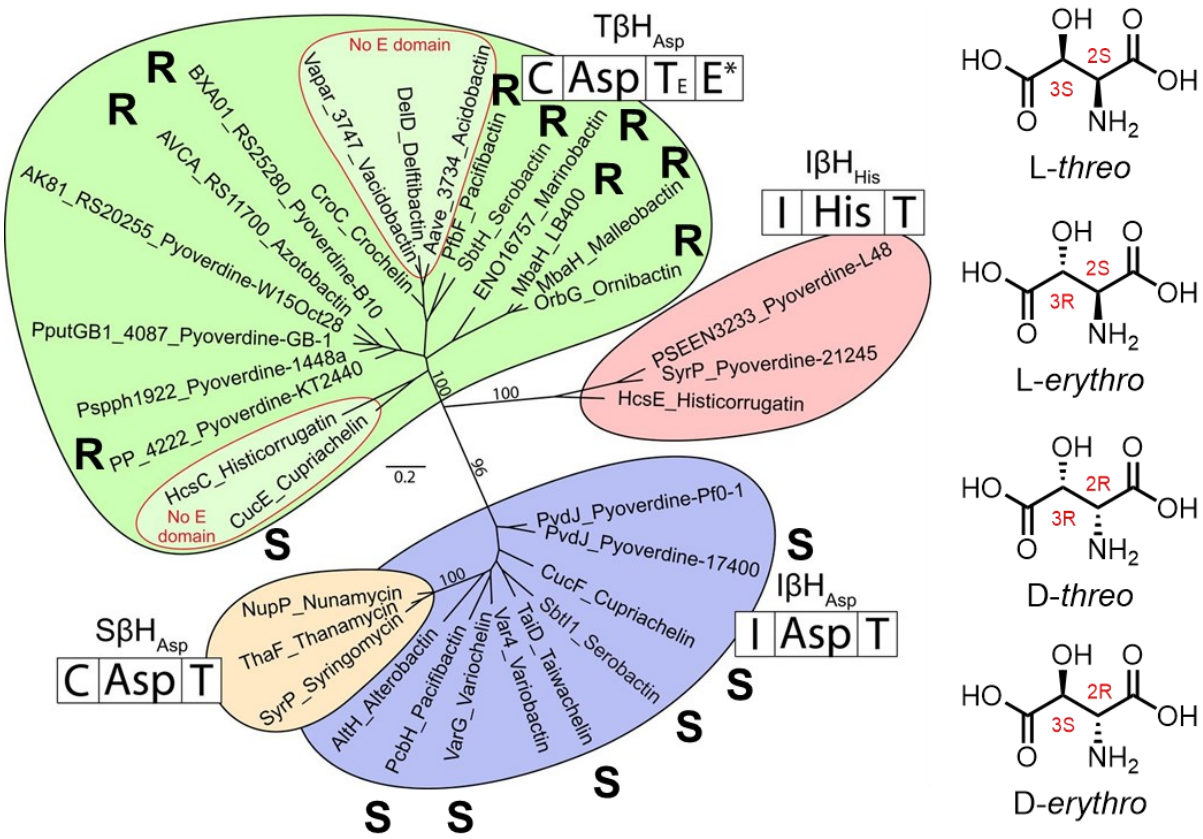

Figure 3.1. Phylogenetic tree of putative NRPS-associated β-hydroxylase-encoding genes. For genes that are associated with a stereochemically-characterized product, the stereochemistry at the 3 position of the β-OHAsp residue is shown alongside the gene name. The four β-OHAsp stereoisomers are displayed on right, with chirality at the 2 and 3 carbons noted.

The findings presented in this chapter support and expand on these functional subtypes of aspartyl β-hydroxylases, through the isolation and stereochemical characterization of several β-OHAsp siderophores. The siderophore alterobactin A has been isolated from *Pseudoalteromonas luteoviolacea* DSM 6061, thus correlating production of this stereochemically characterized siderophore with a putative gene cluster for the first time. Three siderophores incorporating β-OHAsp residues that lack stereochemical characterization, delftibactin of *Delftia acidovorans* DSM 39, pyoverdine GB-1 of *Pseudomonas putida* GB-1, and histicorrugatin of *Pseudomonas thivervalensis* DSM 13194 have been isolated and subjected to chiral amino acid analysis to determine the stereochemistry of their component amino acids.

3.2. Experimental

3.2.1. Bacterial Strains and Growth

Pseudoalteromonas luteoviolacea DSM 6061, *Pseudomonas thivervalensis* DSM 13194, and *Delftia acidovorans* DSM 39 were obtained from the German Collection of Microorganisms and Cell Cultures (Deutsche Sammlung von Mikroorganismen und Zellkulturen), and *Pseudomonas putida* GB-1 was obtained from B. Tebo (Oregon Health and Science University, Portland, OR). Each was maintained on LB agar plates. For siderophore isolation, *P. luteoviolacea* DSM 6061 was cultured in 1 L of artificial seawater medium (consisting of 30 $g \cdot L^{-1}$ NaCl, 24 $g \cdot L^{-1}$ $MgSO_4$, 6 $g \cdot L^{-1}$ $CaCl_2$, 3 $g \cdot L^{-1}$ KCl, 2 $g \cdot L^{-1}$ NH_4Cl, 0.2 $g \cdot L^{-1}$ glycerol phosphate, and 6 $g \cdot L^{-1}$ casamino acids) for 48 h at 23°C, shaken at 120 RPM. *D. acidovorans* DSM 39 was cultured in 1 L of acidovorax complex medium (consisting of 0.5 g·L−1 chelex-treated yeast extract, 1.0 g·L−1 chelex-treated casamino acids, 2.0 g·L−1 succinic acid, 2.0 g·L−1 L-glutamic acid, 0.3 g·L−1 KH2PO4, and 2.0 g·L−1 MOPS buffer,

pH adjusted to 7.2) for 48 h at 30 °C, shaken at 160 rpm. *P. thivervalensis* DSM 13194 was cultured in 1 L of casamino acids minimal medium (consisting of 5 $g \cdot L^{-1}$ chelex-treated casamino acids, 1.18 $g \cdot L^{-1}$ K_2HPO_4, and 0.25 $g \cdot L^{-1}$ $MgSO_4 \cdot 7H_2O$) for 144 h at 30 °C, shaken at 160 rpm. *P. putida* GB-1 was cultured in 1 L of casamino acids minimal medium for 67 h at 30 °C, shaken at 160 rpm.

3.2.2. Siderophore Isolation

Each culture was pelleted by centrifugation (SLA-3000 rotor, ThermoScientific) at 6000 RPM for 30 min at 4 °C. The resultant supernatant was decanted into a clean 1-L flask, to which 100 g of water-washed Amberlite XAD-4 resin was added. The supernatant was shaken with the resin for 3 to 4 h at 4 °C, 150 rpm. The resin was then filtered from the supernatant and eluted with 75% methanol in ultrapure water (*P. putida*) or 90% methanol in ultrapure water (*P. luteoviolacea* DSM 6061, *D. acidovorans* DSM 39*, and P. thivervalensis* DSM 13194). The eluent was concentrated *in vacuo* and analyzed by positive ion mode ESI-MS on a Waters Xevo G2-XS QTof coupled to an ACQUITY UPLC H-Class system, with a linear gradient of 0% to 60% CH_3CN (0.1% formic acid) in ddH_2O (0.1% formic acid) over 10 min for the presence of siderophore. MSMS analysis was conducted with a collision energy ramp of CE 25-35. To obtain pure siderophore, the concentrated eluent was separated by semipreparative reverse-phase high-performance liquid chromatography (RP-HPLC) (250 × 20-mm YMC C18-AQ column, 7 mL/min flow rate), employing a gradient of methanol in ultrapure water (+0.05% trifluoroacetic acid): 10 to 35% MeOH over 25 min (alterobactin, delftibactin), 10 to 40% MeOH over 30 min (histicorrugatin), or 5 to 30% MeOH over 25 min (pyoverdine GB-1). *Pseudoalteromonas luteoviolacea* DSM 6061yielded ~5 mg of alterobactin A per liter of culture, *Delftia acidovorans* DSM 39 yielded ~10 mg delftibactin

per liter of culture, *Pseudomonas thivervalensis* DSM 13194 yielded ~1 mg histicorrugatin per liter of culture, and *Pseudomonas putida* GB-1 yielded ~15 mg pyoverdine GB-1 per liter of culture.

3.2.3. Amino Acid Analysis

For each siderophore, ~1 mg was dissolved in 200 µL of ultrapure water. To the siderophore solution was added either 200 µL of 12 M HCl, 200 µL of 20% DCl in D_2O, or 200 µL of 55% HI. Each acidified solution was then transferred to a glass ampoule, blanketed with Ar, and sealed. For HCl hydrolyses, ampoules were heated for 4 h at 100 °C. For DCl hydrolyses, ampoules were heated for 6 h at 100 °C. For HI hydrolyses, ampoules were heated for 22 h at 100 °C. After heating, ampoules were opened, and crude hydrolysates were transferred to microcentrifuge tubes. Hydrolysates were evaporated and re-dissolved in ~700 µL of ultrapure water 3 times to remove any acid, and then brought to a final volume of 100 µL. Hydrolysates were reacted with FDAA (Marfey's reagent) following standard conditions.[14]

Derivatized hydrolysates were analyzed by RP-HPLC monitoring at 340 nm on a 250 × 4.6-mm YMC C18-AQ column, employing gradient elutions of either 15 to 50% acetonitrile (+0.05 trifluoroacetic acid) in ultrapure water (+0.05 trifluoroacetic acid) over 50 min, 1 mL/min flow rate (alterobactin, delftibactin, pyoverdine GB-1 hydrolysates); or 15 to 50% acetonitrile (no additives) in 50 mM triethylamine phosphate (pH 3.0) over 50 min, 1 mL/min flow rate (histicorrugatin hydrolysate). Derivatized hydrolysates were also analyzed by UPLC-ESIMS. A Waters BEH C18 column was used with a linear gradient of 15 to 50% CH_3CN (0.1% formic acid) in ddH_2O (0.1% formic acid) over 10 min (alterobactin, delftibactin,

histicorrugatin hydrolysates) or a linear gradient of 10 to 30% CH_3CN (0.1% formic acid) in ddH_2O (0.1% formic acid) over 10 min (pyoverdine GB-1 hydrolysate).

3.3. Results and Interpretation

3.3.1. Isolation and Characterization of Alterobactin A From P. luteoviolacea DSM-6061

The free-floating marine bacterium *Pseudoalteromonas luteoviolacea* S2 (formerly *Alteromonas luteoviolacea* S2) is known to produce the siderophores alterobactin A and B under low-iron conditions.[15] However, to date the biosynthesis of the alterobactins has not been explored, as the genome of *P. luteoviolacea* S2 is not sequenced. The strain *P. luteoviolacea* DSM 6061, on the other hand, has a fully sequenced and published genome. The genome contains a putative nonribosomal peptide synthetase (NRPS) gene cluster predicted to encode the biosynthetic machinery of alterobactin. To confirm production of alterobactin, *P. luteoviolacea* DSM 6061 was obtained and cultured, and the culture supernatant was extracted with XAD-4 resin.

UPLC-ESI-MS analysis of the *P. luteoviolacea* DSM 6061 supernatant extract identified a compound with m/z 464.6872 (z = 2), compared to the calculated exact mass of alterobactin A (m/z 464.6858, z = 2) (Figure 3.2). MSMS fragmentation of this compound identified several characteristic fragments of alterobactin A (Figure 3.3). Amino acid analysis of the FDAA-derivatized alterobactin hydrolysate and co-injection with a D,L-*threo* β-OHAsp standard confirmed that the L-*threo* stereochemistry of β-OHAsp in the isolated alterobactin A is conserved between strains S2 and DSM 6061 (Figure 3.4). This work thus correlates, for the first time, alterobactin production with a putative biosynthetic gene cluster.

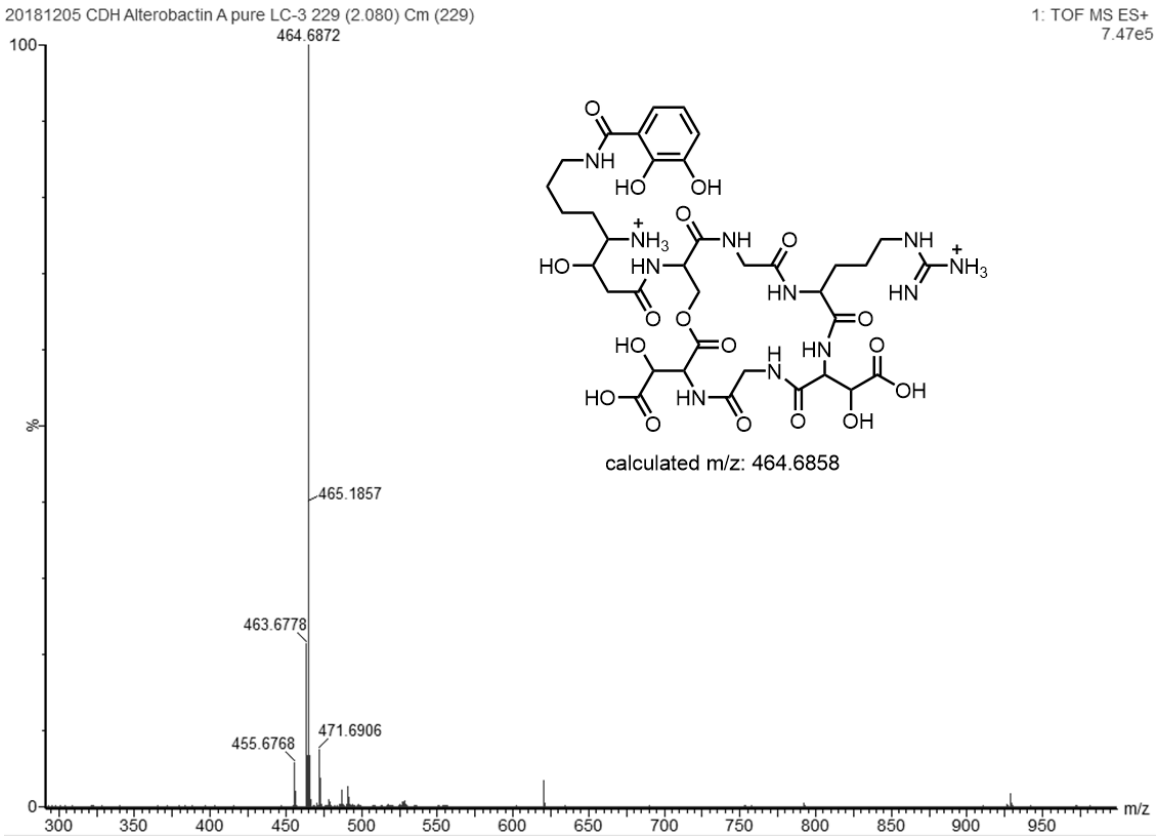

Figure 3.2. Positive-ion mode ESI-MS spectrum of alterobactin A from *P. luteoviolacea* DSM 6061.

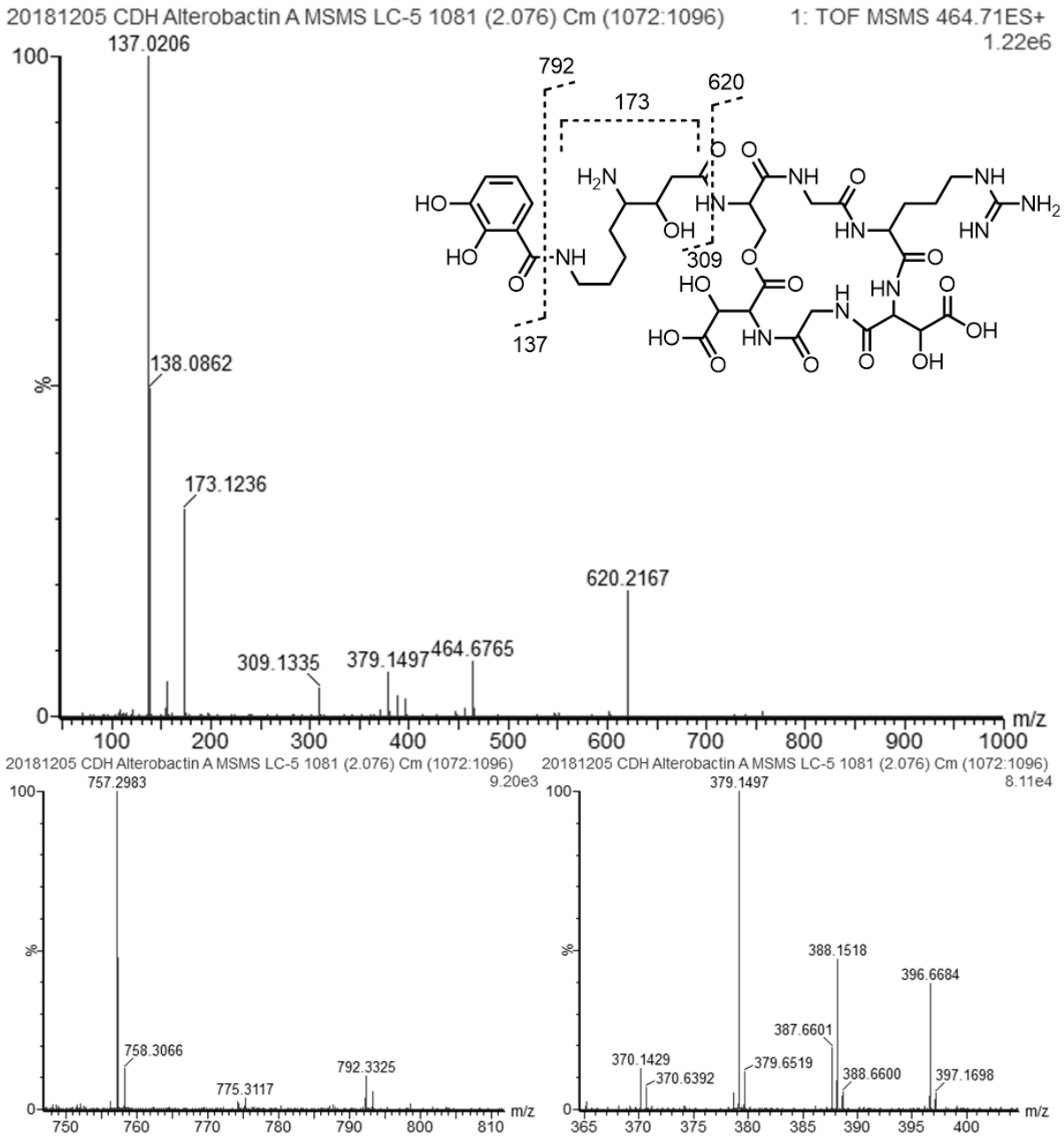

Figure 3.3. ESI-MSMS spectrum of alterobactin A. Fragments observed are delineated in the structure. Magnified regions of the spectrum are provided to clarify all fragments. The fragment of m/z 396.66 is the doubly charged ion of the 792.33 m/z fragment.

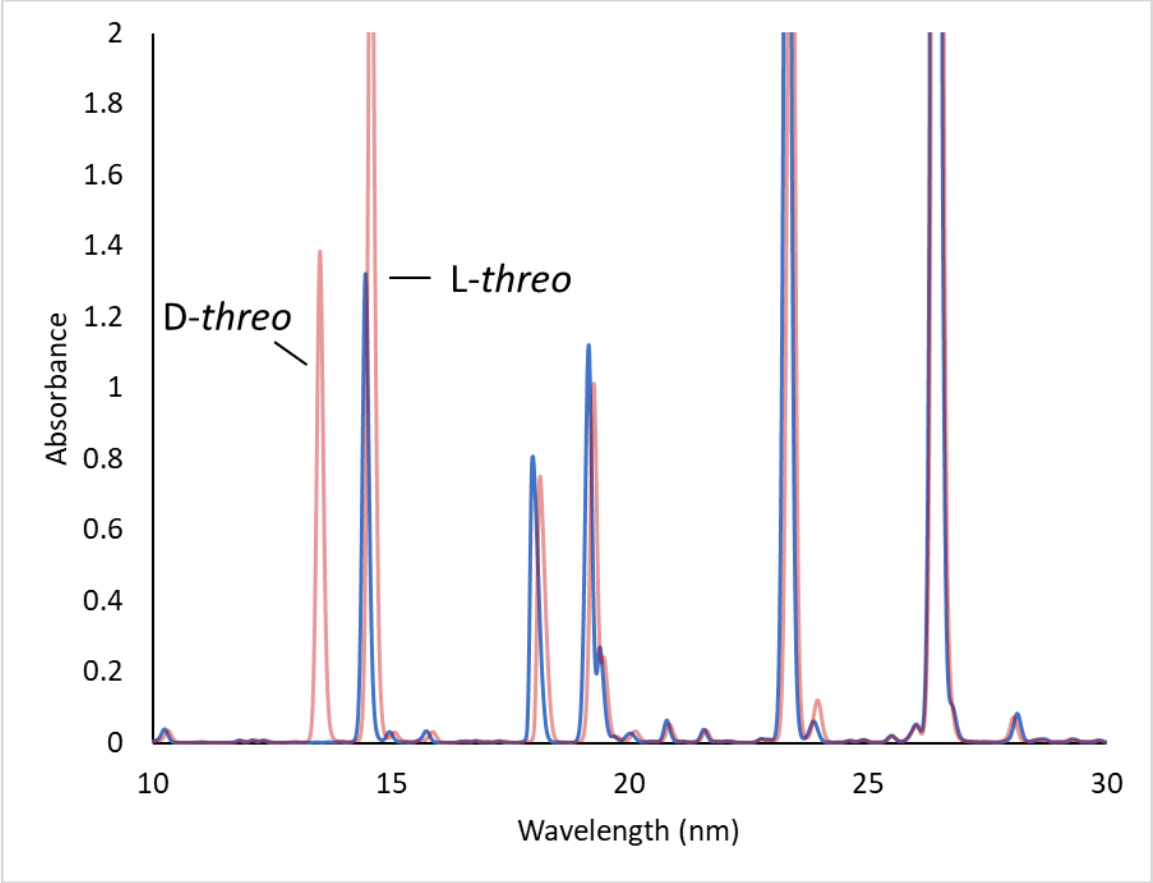

Figure 3.4. HPLC co-injection of FDAA-derivatized D,L-*threo*-β-OHAsp standard with derivatized alterobactin hydrolysate. Red trace represents co-injection, blue trace represents hydrolysate alone.

3.3.2. Isolation and Stereochemical Characterization of Delftibactin

The biosynthetic gene cluster of the NRPS siderophore delftibactin,[16] produced by *Delftia acidovorans* DSM 39, encodes the putative aspartyl β-hydroxylase DelD. Sequence homology places DelD in the $T\beta H_{Asp}$ clade. All β-OHAsp siderophores associated with a $T\beta H_{Asp}$ hydroxylase incorporate a D-*threo*-β-OHAsp (2R, 3R) residue. Distinguishing delftibactin from these stereochemically characterized siderophores is the lack of an epimerization functionality in the Asp-loading module. Presuming DelD exhibits the same stereospecificity as the rest of its clade, delftibactin should incorporate an L-*erythro*-β-OHAsp (2S, 3R) residue. The structure of delftibactin has been reported, but the stereochemistry of its constituent amino acids has yet to be characterized.[16] Thus, *D. acidovorans* DSM 39 was cultured, and delftibactin was extracted from the culture and identified by ESI-MS (Figure 3.5).

Hydrolysis of delftibactin and FDAA-derivatization of the hydrolysate allowed an assignment of the stereochemistry of its component amino acids (Figure 3.6, Figure 3.7). Delftibactin incorporates L-*erythro*-β-OHAsp exclusively, as predicted from the sequence homology of DelD. Delftibactin is thus only the second siderophore found to incorporate L-*erythro*-β-OHAsp, alongside imaqobactin of the unsequenced bacterium *Variovorax* sp. RKJM285.[17] The stereochemistry of the other amino acids comprising delftibactin is consistent with the domains encoded by the biosynthetic gene cluster—modules responsible for loading Ser, Arg, and one of two OHOrn residues contain dual E/C domains. Dual E/C domains are condensation domains that also function as epimerization domains, resulting in incorporation of a D-amino acid substrate in an identical functionality to discrete condensation and epimerization domains.[18-19] Accordingly, D-Ser, D-Arg, and D-Orn were identified from the amino acid analysis (Figure 3.7).

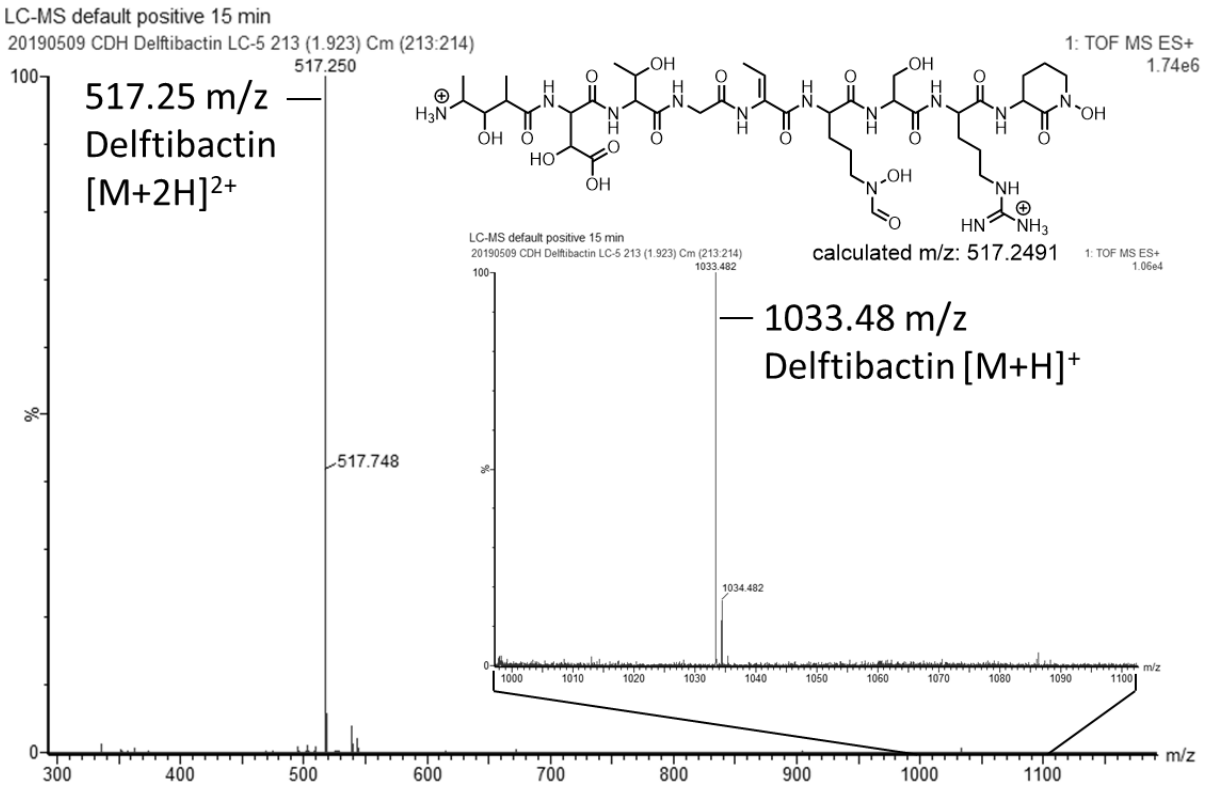

Figure 3.5. Positive-ion mode ESI-MS spectrum of delftibactin isolated from *Delftia acidovorans* DSM 39.

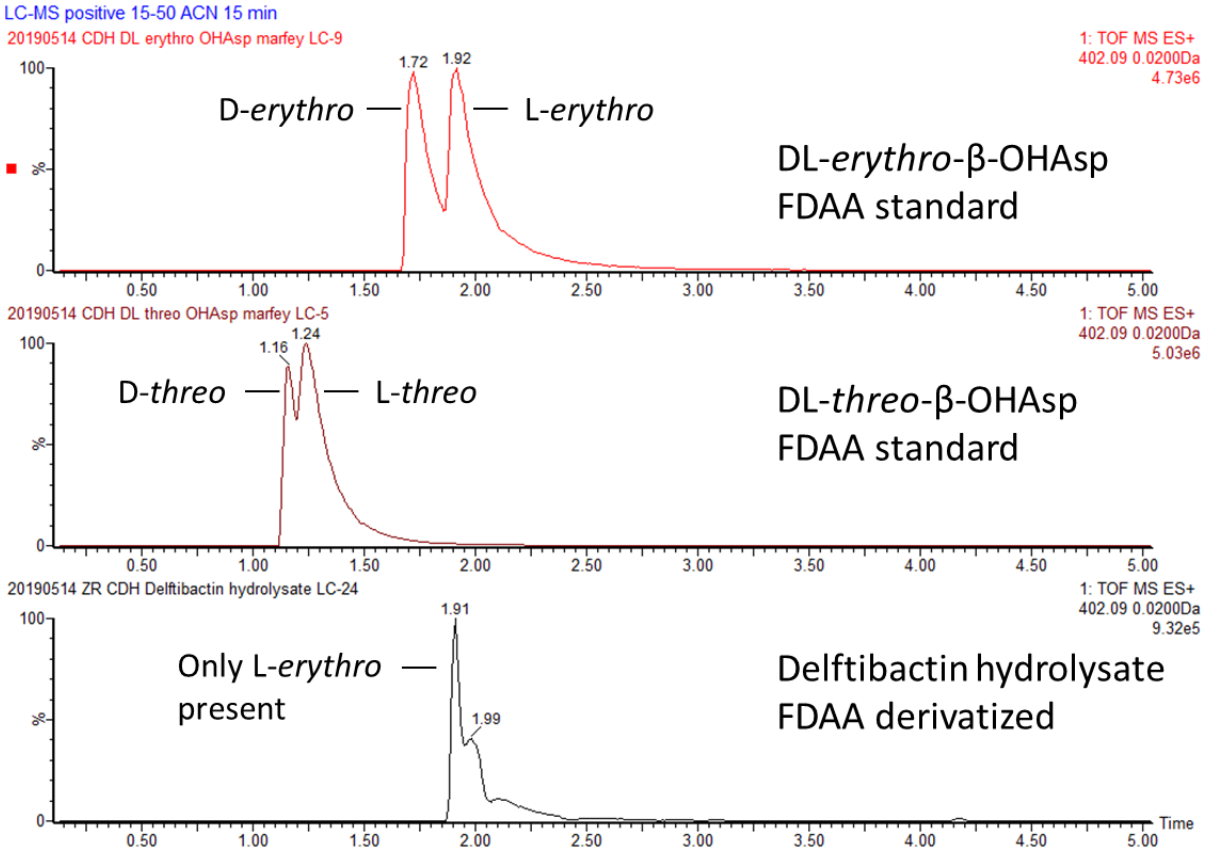

Figure 3.6. Extracted ion chromatograms of the FDAA-β-OHAsp molecular ion (402 m/z $[M+H]^+$) from UPLC-ESIMS analysis of FDAA-derivatized DL-*erythro*-β-OHAsp, DL-*threo*-β-OHAsp and delftibactin hydrolysate (HCl hydrolysis). Delftibactin contains only L-*erythro*-β-OHAsp. The relative positions of D and L stereoisomers are assigned based on literature precedent of elution order under RP-LC conditions.[17]

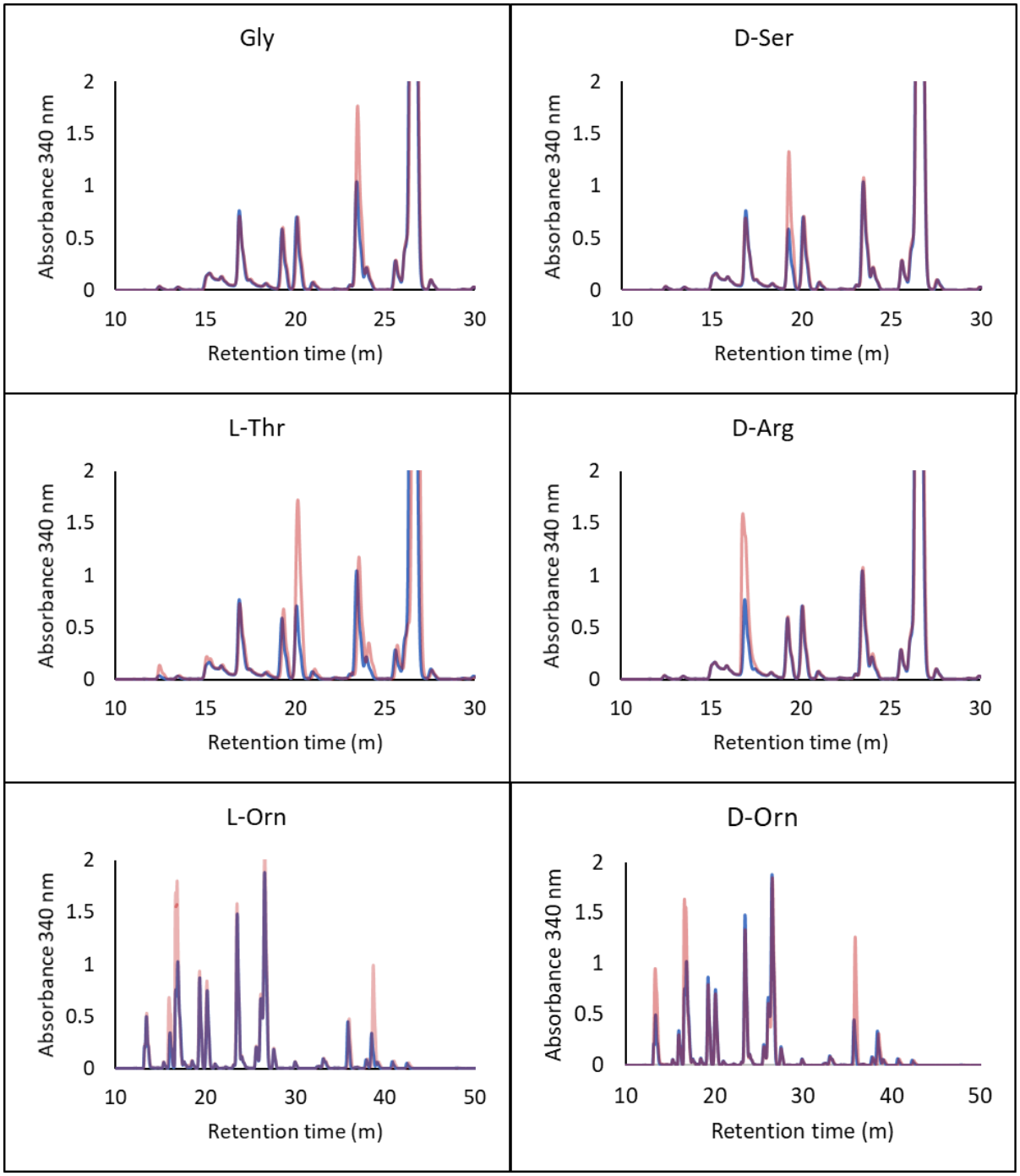

Figure 3.7. HPLC co-injections of FDAA-derivatized amino acid standards with delftibactin hydrolysate. Gly, Ser, Thr, Arg were co-injected with HCl hydrolysate, while Orn was co-injected with HI hydrolysate. Red lines represent co-injections, while blue lines represent hydrolysate alone.

3.3.3. Isolation and Stereochemical Characterization of Pyoverdine GB-1

Pseudomonas putida GB-1 produces a pyoverdine variant, termed pyoverdine GB-1, that has not been stereochemically characterized.[9] The gene cluster putatively responsible for biosynthesis of pyoverdine GB-1 encodes putative aspartyl β-hydroxylase PputGB1_4087, which falls within the $T\beta H_{Asp}$ clade. The Asp-loading NRPS module in the cluster contains an epimerization domain, thus pyoverdine GB-1 is expected to incorporate D-*threo*-β-OHAsp. Growth of *P. putida* GB-1 under iron-limited conditions led to production of pyoverdine GB-1, detected by ESI-MS (Figure 3.8). Amino acid analysis of pyoverdine GB-1 FDAA-derivatized hydrolysate enabled stereochemical assignment of its constituent amino acids (Figure 3.9, Figure 3.10). As expected, pyoverdine GB-1 contains only the D-*threo*-β-OHAsp stereoisomer, further solidifying the functionality of the $T\beta H_{Asp}$ clade as catalyzing 3R β-hydroxylation of Asp in a stereospecific manner. The only other D-amino acid identified from the hydrolysate was D-*allo*-Thr, consistent with the number and placement of epimerization domains in the NRPS architecture.[9] Thr, like β-OHAsp, contains a chiral center at the β-carbon, and thus can exist as four possible stereoisomers. D-*allo*-Thr (2R, 3R) is the expected product of epimerization of an NRPS-loaded L-Thr (2S, 3R) residue.

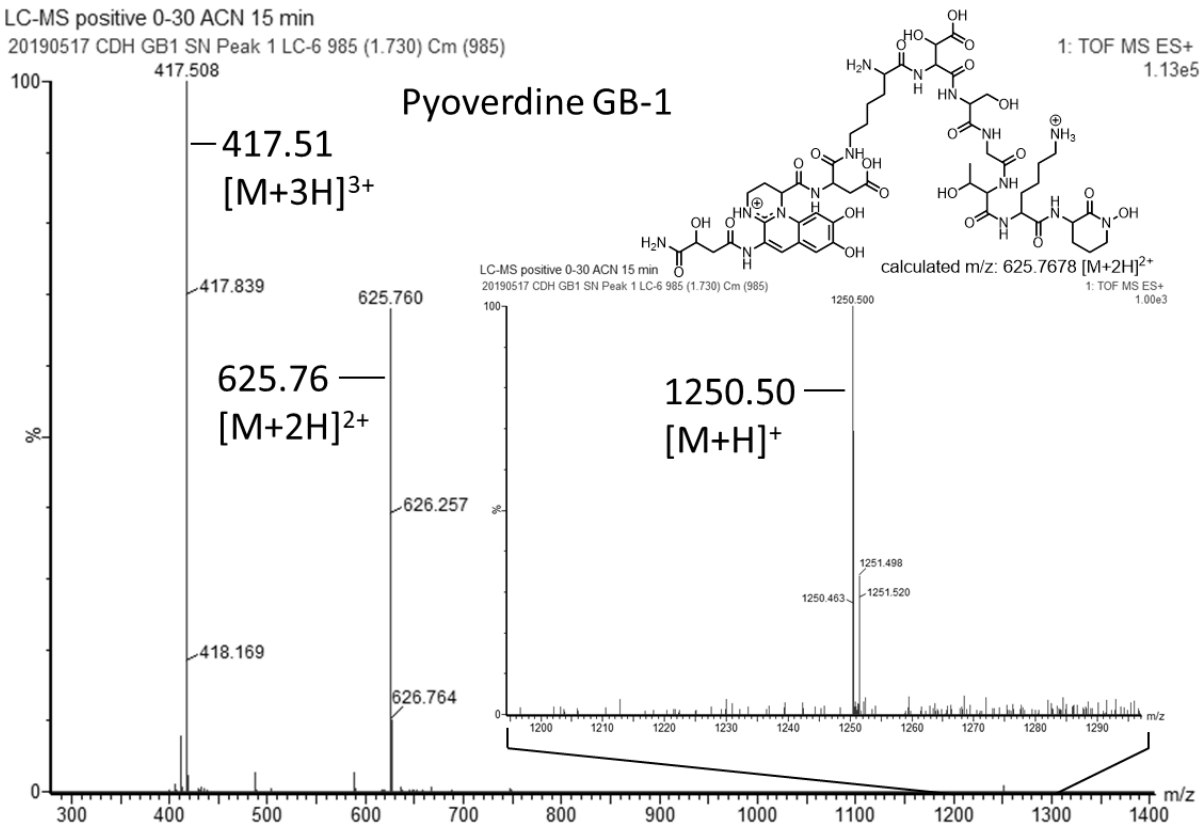

Figure 3.8. Positive-ion mode ESI-MS spectrum of pyoverdine GB-1 isolated from *Pseudomonas putida* GB-1.

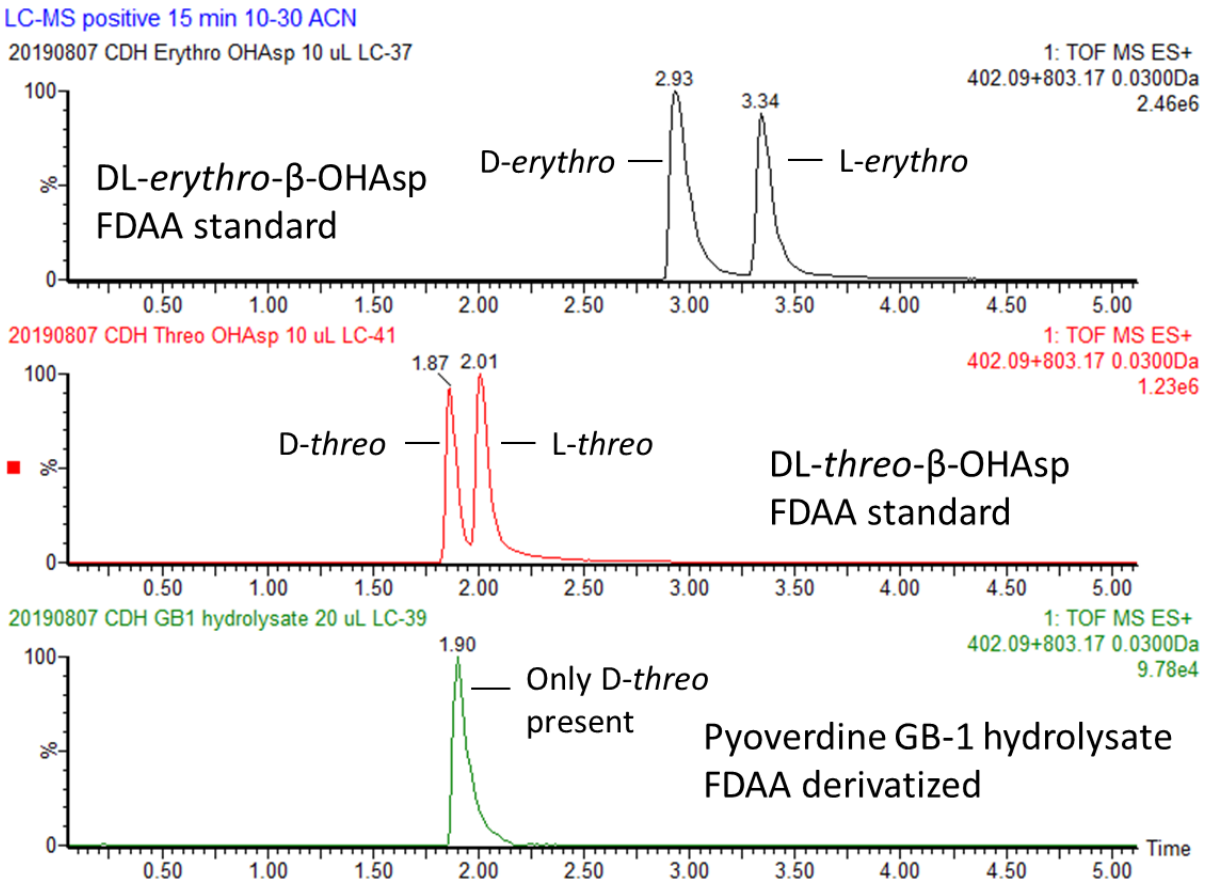

Figure 3.9. Extracted ion chromatograms of the FDAA-β-OHAsp molecular ion (402 m/z $[M+H]^+$) from UPLC-ESIMS analysis of FDAA-derivatized DL-*erythro*-β-OHAsp, DL-*threo*-β-OHAsp and pyoverdine GB-1 hydrolysate (HCl hydrolysis). Pyoverdine GB-1 contains only D-*threo*-β-OHAsp.

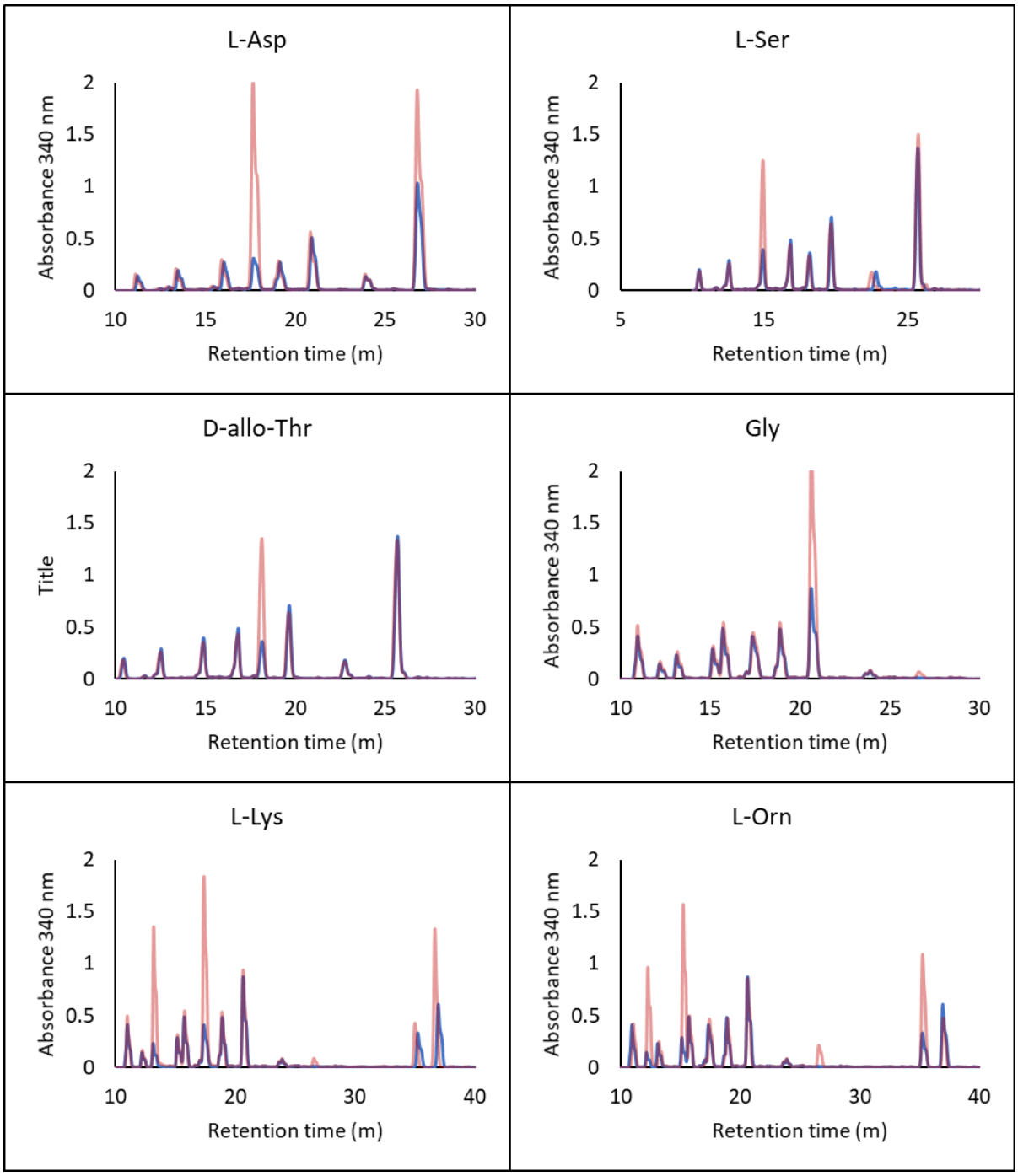

Figure 3.10. HPLC co-injections of FDAA-derivatized amino acid standards with pyoverdine GB-1 hydrolysate (HCl hydrolysis). Red lines represent co-injections, while blue lines represent hydrolysate alone.

3.3.4. Isolation and Stereochemical Characterization of Histicorrugatin

Histicorrugatin is an acyl peptidic siderophore produced by *Pseudomonas thivervalensis* DSM 13194.[20] Histicorrugatin, along with congeners corrugatin and ornicorrugatin, contain both β-OHAsp and β-OHHis functional groups utilized for Fe(III) coordination.[20-22] The histicorrugatin biosynthetic gene cluster encodes two putative β-hydroxylases: a hydroxylase domain within NRPS protein HcsE, with homology to putative histidine β-hydroxylases, and the β-hydroxylase enzyme HcsC, which clusters in the $T\beta H_{Asp}$ clade. Of all known putative aspartyl β-hydroxylases, HcsC is most closely related to CucE, encoded by the cupriachelin biosynthetic gene cluster of *Cupriavidus necator* H16.[3] While CucE falls within the $T\beta H_{Asp}$ clade based on sequence homology, cupriachelin is reported to contain two L-*threo*-β-OHAsp (2S, 3S) residues.[3] The cupriachelin cluster also encodes a putative $I\beta H_{Asp}$ domain within NRPS protein CucF, which is expected to generate L-*threo*-β-OHAsp. However, the cluster only contains one interface domain, thus the CucF hydroxylase is expected to only hydroxylate one of two residues, with CucE responsible for the second hydroxylation. As HcsC and CucE seem to form a distinct subclade (Figure 3.1), and the Asp-loading module in histicorrugatin biosynthesis lacks epimerization functionality, histicorrugatin was hypothesized to also incorporate L-*threo* β-OHAsp.

Histicorrugatin was extracted from a *P. thivervalensis* DSM 13194 culture, identified by ESI-MS (Figure 3.11), and purified for amino acid analysis. Hydrolysis of histicorrugatin and FDAA-derivatization of the hydrolysate allowed for stereochemical characterization (Figure 3.12, Figure 3.13). Histicorrugatin contains only L-*erythro*-β-OHAsp (Figure 3.12) in accordance with the stereoselectivity expected of the $T\beta H_{Asp}$ clade, but inconsistent with the reported stereochemistry in cupriachelin.[3] The stereochemistry of the other amino acids

(Figure 3.13) is again consistent with the number and placement of epimerization functionalities in the assembly line. The stereochemistry of the β-OHHis residues was not determined as appropriate standards were not obtained.

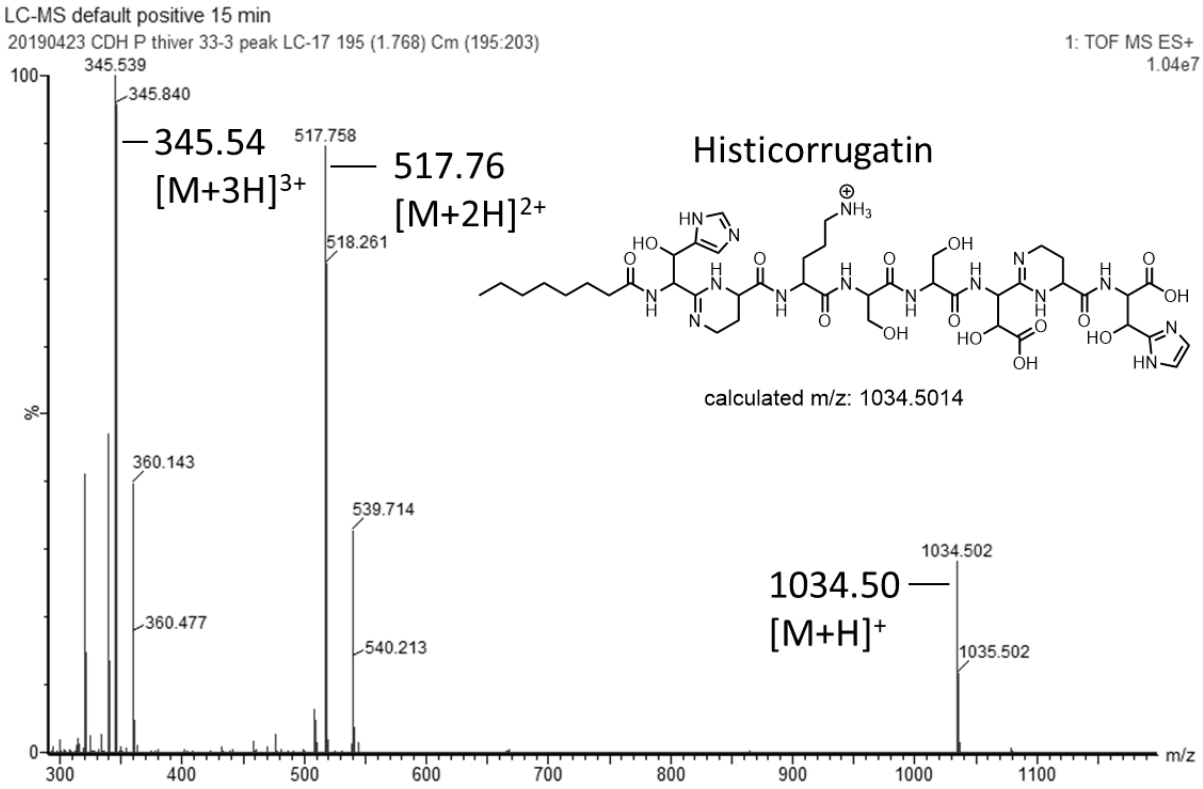

Figure 3.11. Positive-ion mode ESI-MS spectrum of histicorrugatin isolated from *P. thivervalensis* DSM 13194.

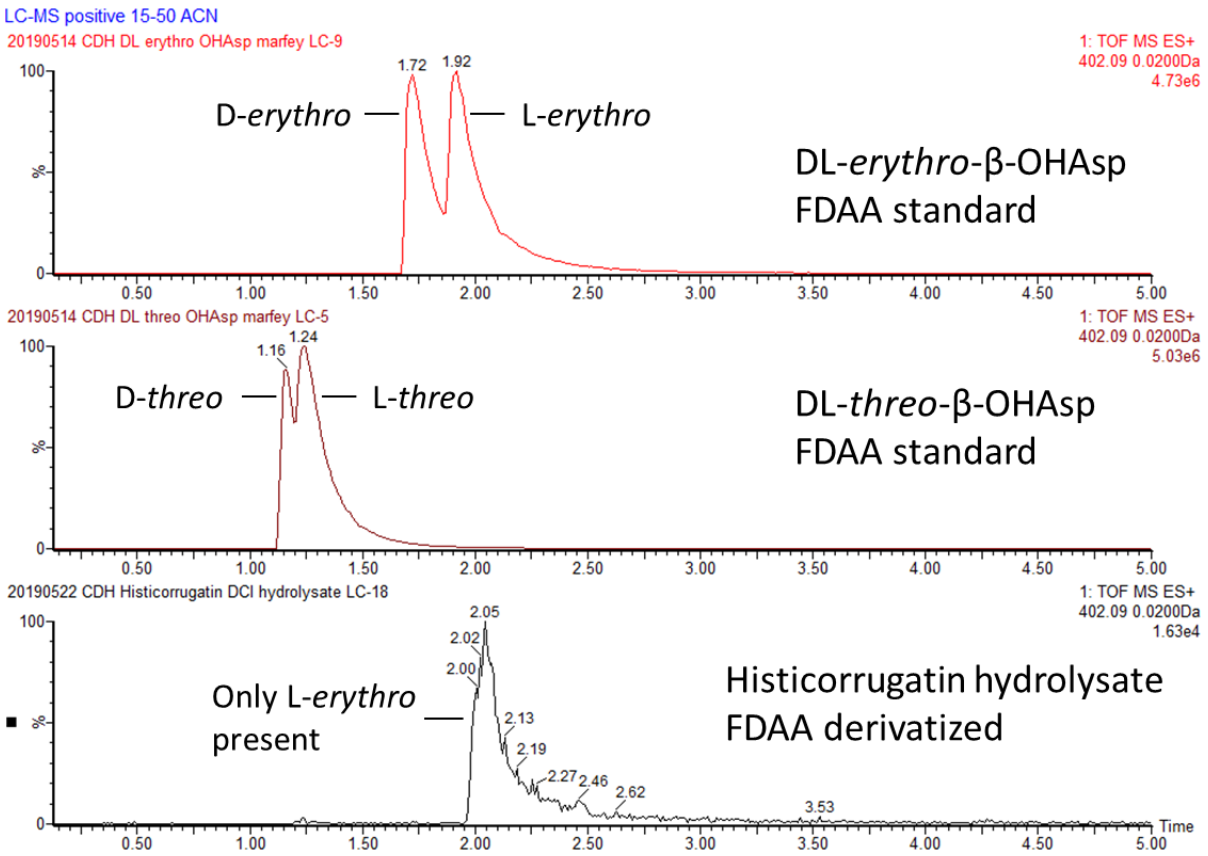

Figure 3.12. Extracted ion chromatograms of the FDAA-β-OHAsp molecular ion (402 m/z $[M+H]^+$) from UPLC-ESIMS analysis of FDAA-derivatized DL-*erythro*-β-OHAsp, DL-*threo*-β-OHAsp and histicorrugatin hydrolysate (DCl hydrolysis). Histicorrugatin only incorporates L-*erythro*-β-OHAsp. As HCl hydrolysis of histicorrugatin yielded a mixture of L-*erythro* and D-*threo*-β-OHAsp, DCl in D_2O was chosen as the acidifying agent to distinguish if one of the β-OHAsp stereoisomers resulted from epimerization under the hydrolytic conditions, which would yield a molecular ion of one mass unit higher in DCl/D_2O, as observed in the hydrolysis of the siderophore gramibactin.[23] Hydrolysis of histicorrugatin in DCl/D_2O yielded only L-*erythro*-β-OHAsp with the correct mass of 402 m/z

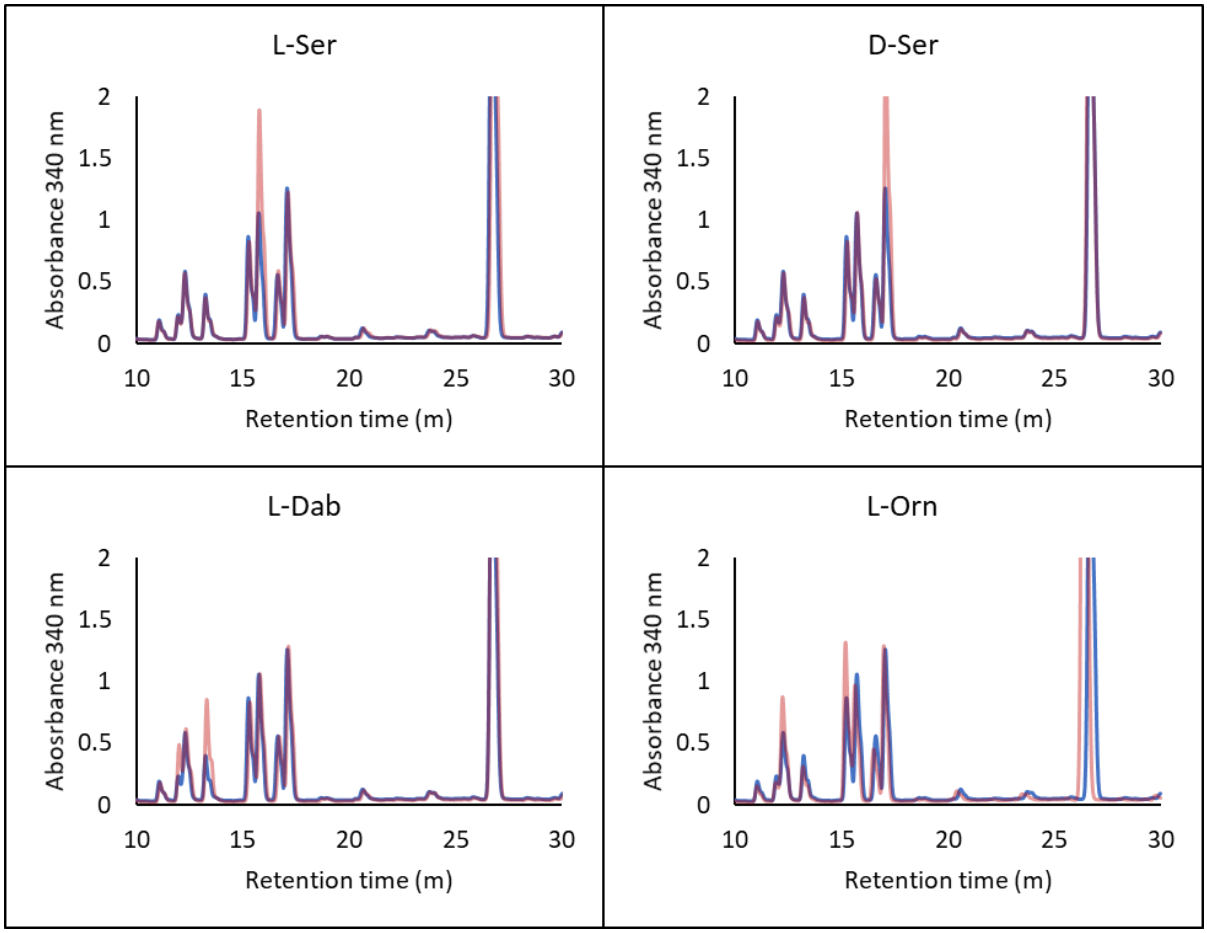

Figure 3.13. HPLC co-injections of FDAA-derivatized amino acid standards with histicorrugatin hydrolysate (HCl hydrolysis). Red lines represent co-injections, while blue lines represent hydrolysate alone.

3.4. Discussion

Stereochemical assignment of the β-OHAsp residues in delftibactin and pyoverdine GB-1 as L-*erythro* and D-*threo* β-OHAsp, respectively, further support the parallels observed between phylogeny, genomic organization, and stereoselectivity in siderophore aspartyl β-hydroxylases (Figure 3.14). While the prediction of α-carbon stereochemistry in NRPS amino acid residues through the presence or absence of an epimerization functionality is well established, this work provides the first *in silico* approach for prediction of β-carbon stereochemistry in β-OHAsp NRPS products.

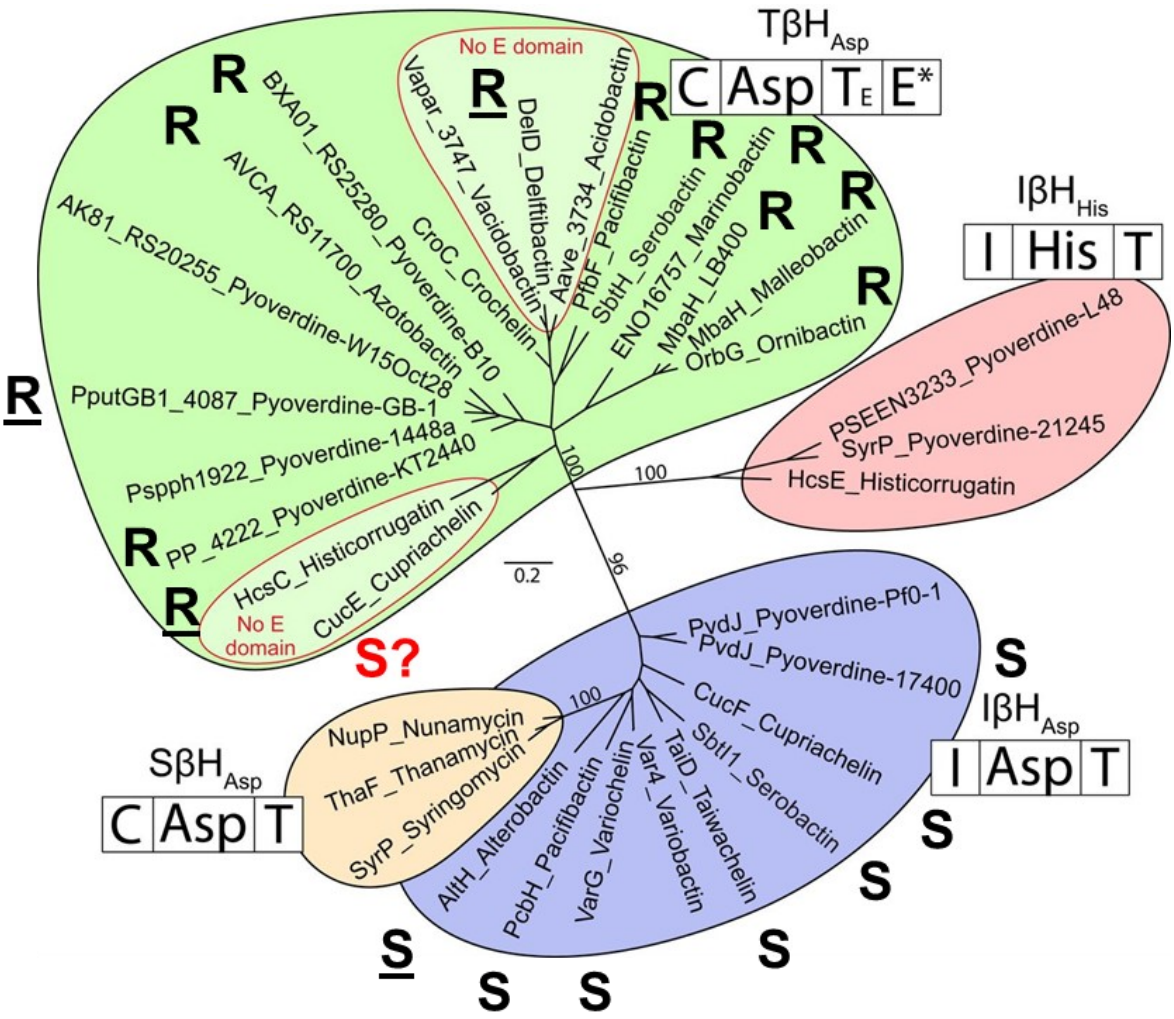

Figure 3.14. Phylogenetic tree of putative NRPS-associated β-hydroxylase-encoding genes labelled with the 3-carbon stereochemistry of the β-OHAsp residue associated with each hydroxylase. Associations determined from the work presented in this chapter are underlined (further associations are presented in chapter 4).

The L-*erythro* β-OHAsp stereochemistry of histicorrugatin does not support the hypothesis of a functional 3S subclade among the TβH$_{Asp}$ hydroxylases, suggesting that CucE is a sole exception for stereoselectivity among the known TβH$_{Asp}$ enzymes. Another possible explanation for this discrepancy is that CucE does not function as a hydroxylase in cupriachelin biosynthesis, and instead both β-OHAsp residues in cupriachelin are hydroxylated by the CucF IβH$_{Asp}$ domain. An example of this is found in the putative biosynthesis of alterobactin. The IβH$_{Asp}$ domain of NRPS protein AltH is the sole source of both β-hydroxylations in alterobactin

biosynthesis. However, the alterobactin biosynthetic gene cluster encodes two interface domains, presumably allowing the hydroxylase to function at both points in the assembly line.[13] As the cupriachelin gene cluster only encodes one interface domain, CucF is expected to function only on the Asp residue loaded by the interface domain-containing NRPS module. This hypothesis is supported by the biosynthetic gene cluster of taiwachelin, which encodes only one interface-associated hydroxylase and one interface domain, while loading two Asp residues during assembly. Accordingly, one Asp residue is hydroxylated, while the other Asp residue is unmodified.[4] Given the apparent stark exception of stereoselectivity in the $T\beta H_{Asp}$ clade presented by CucE, a re-evaluation of the cupriachelin amino acid stereochemistry was carried out, and the results are presented in chapter 4.

3.5. References

1. Hardy, C. D.; Butler, A., *J. Biol. Inorg. Chem.* **2018,** *23* (7), 957-967.

2. Agnoli, K.; Lowe, C. A.; Farmer, K. L.; Husnain, S. I.; Thomas, M. S., *J. Bacteriol.* **2006,** *188* (10), 3631-3644.

3. Kreutzer, M. F.; Kage, H.; Nett, M., *J. Am. Chem. Soc.* **2012,** *134* (11), 5415-5422.

4. Kreutzer, M. F.; Nett, M., *Org. Biomol. Chem.* **2012,** *10* (47), 9338-9343.

5. Rosconi, F.; Davyt, D.; Martínez, V.; Martínez, M.; Abin-Carriquiry, J. A.; Zane, H.; Butler, A.; de Souza, E. M.; Fabiano, E., *Environ. Microbiol.* **2013,** *15* (3), 916-927.

6. Vargas-Straube, M. J.; Cámara, B.; Tello, M.; Montero-Silva, F.; Cárdenas, F.; Seeger, M., *PLoS One* **2016,** *11* (3), e0151273.

7. Franke, J.; Ishida, K.; Hertweck, C., *Chem. Eur. J.* **2015,** *21* (22), 8010-8014.

8. Franke, J.; Ishida, K.; Ishida-Ito, M.; Hertweck, C., *Angew. Chem. Int. Ed.* **2013,** *52* (32), 8271-8275.

9. Parker, D. L.; Lee, S.-W.; Geszvain, K.; Davis, R. E.; Gruffaz, C.; Meyer, J.-M.; Torpey, J. W.; Tebo, B. M., *Front Microbiol.* **2014,** *5* (202), 202.

10. Matthijs, S.; Laus, G.; Meyer, J.-M.; Abbaspour-Tehrani, K.; Schäfer, M.; Budzikiewicz, H.; Cornelis, P., *BioMetals* **2009,** *22* (6), 951.

11. Kurth, C.; Schieferdecker, S.; Athanasopoulou, K.; Seccareccia, I.; Nett, M., *J. Nat. Prod.* **2016,** *79* (4), 865-872.

12. Hardy, C. D.; Butler, A., *J. Nat. Prod.* **2019,** *82* (4), 990-997.

13. Reitz, Z. L.; Hardy, C. D.; Suk, J.; Bouvet, J.; Butler, A., *Proc. Natl. Acad. Sci. USA* **2019,** *116* (40), 19805.

14. Marfey, P., *Carlsberg Res. Commun.* **1984,** *49* (6), 591.

15. Reid, R. T.; Livet, D. H.; Faulkner, D. J.; Butler, A., *Nature* **1993,** *366*, 455.

16. Johnston, C. W.; Wyatt, M. A.; Li, X.; Ibrahim, A.; Shuster, J.; Southam, G.; Magarvey, N. A., *Nat. Chem. Biol.* **2013,** *9*, 241-243.

17. Robertson, A. W.; McCarville, N. G.; MacIntyre, L. W.; Correa, H.; Haltli, B.; Marchbank, D. H.; Kerr, R. G., *J. Nat. Prod.* **2018**.

18. Balibar, C. J.; Vaillancourt, F. H.; Walsh, C. T., *Chem. Biol.* **2005,** *12* (11), 1189-1200.

19. Rausch, C.; Hoof, I.; Weber, T.; Wohlleben, W.; Huson, D. H., *BMC Evol. Biol.* **2007,** *7* (1), 78.

20. Matthijs, S.; Brandt, N.; Ongena, M.; Achouak, W.; Meyer, J.-M.; Budzikiewicz, H., *BioMetals* **2016,** *29* (3), 467-485.

21. Matthijs, S.; Budzikiewicz, H.; Schäfer, M.; Wathelet, B.; Cornelis, P., *Z. Naturforsch., C.: Biosci* **2008,** *63* (1-2), 8-12.

22. Risse, D.; Beiderbeck, H.; Taraz, K.; Budzikiewicz, H.; Gustine, D., *Z. Naturforsch., C.: Biosci* **1998,** *53* (5-6), 295-304.

23. Hermenau, R.; Ishida, K.; Gama, S.; Hoffmann, B.; Pfeifer-Leeg, M.; Plass, W.; Mohr, J. F.; Wichard, T.; Saluz, H.-P.; Hertweck, C., *Nat. Chem. Biol.* **2018,** *14* (9), 841-843.

4. Structural Revision of the Siderophore Cupriachelin, and Characterization of New Cupriachelin Variants

Sections of this chapter were published in: Reitz, Z. L.; Hardy, C. D.; Suk, J.; Bouvet, J.; Butler, A. Genomic analysis of siderophore β-hydroxylases reveals divergent stereocontrol and expands the condensation domain family. *Proc. Nat. Acad. Sci.* **2019**, *116*, 19805-19814

4.1. Introduction

Cupriachelin is a acylated peptidic siderophore produced by the freshwater bacterium *Cupriavidus necator* H16, synthesized by a set of non-ribosomal peptide synthetases (CucFGJH) working in an assembly line fashion.[1] Cupriachelin contains two β-hydroxyaspartate residues that function as Fe(III) ligands. These residues are both reported to exhibit L-*threo* (2S, 3S) stereochemistry.[1] The cupriachelin gene cluster encodes two putative aspartyl β-hydroxylases: an $I\beta H_{Asp}$ domain within NRPS enzyme CucF, and the $T\beta H_{Asp}$ hydroxylase enzyme CucE.[1-2] Only one Asp-loading NRPS module contains an interface domain (the module within CucF), while the other module (within CucG) contains a T_E domain. Thus, in accordance with the phylogenetic associations reported in Chapter 3, each hydroxylase is expected to be responsible for one of the two β-hydroxylations in cupriachelin biosynthesis. While a 3S β-OHAsp product of the CucF $I\beta H_{Asp}$ domain is in line with the stereochemistry of other $I\beta H_{Asp}$ domain products,[2] all other $T\beta H_{Asp}$ hydroxylases yield 3R β-OHAsp. The apparent exception in stereoselectivity posed by CucE gave reason to re-evaluate the amino acid stereochemistry of cupriachelin.

Reported herein is a structural revision of cupriachelin, reassigning the β-OHAsp stereochemistry as one L-*threo* and one L-*erythro* residue. This reassignment resolves the

remaining known exception of the stereoselectivity pattern observed among the $I\beta H_{Asp}$ and $T\beta H_{Asp}$ hydroxylases, further strengthening the predictive power of this phylogenetic and functional analysis. In addition, several new structural variants of cupriachelin produced by *C. necator* H16 are reported, with variants differing in the length of the fatty acid tail as well as differing in the C-terminal amino acid side chain composition.

4.2. Experimental

4.2.1. Culturing of Cupriavidus necator H16

Cupriavidus necator H16 was obtained from Professor Stanley Parsons (University of California, Santa Barbara, CA) and maintained on LB plates. For siderophore isolation, *C. necator* was cultured in 1 L of casamino acids minimal medium (consisting of 5 $g \cdot L^{-1}$ chelex-treated casamino acids, 1.18 $g \cdot L^{-1}$ K_2HPO_4, and 0.25 $g \cdot L^{-1}$ $MgSO_4 \cdot 7H_2O$) for 144 h at 30 °C, shaken at 160 rpm.

4.2.2. Isolation and Characterization of Cupriachelins

Cultures were pelleted by centrifugation (SLA-3000 rotor, ThermoScientific) at 6000 RPM for 30 min at 4 °C. The resultant supernatant was decanted into a clean 1-L flask, to which 100 g of water-washed Amberlite XAD-4 resin was added. The supernatant was shaken with the resin for 3 to 4 h at 4 °C, 150 rpm. The resin was then filtered from the supernatant and eluted with 90% methanol in ultrapure water. The eluent was concentrated *in vacuo* and analyzed by positive ion mode ESI-MS on a Waters Xevo G2-XS QTof coupled to an ACQUITY UPLC H-Class system, with a linear gradient of 0% to 100% CH_3CN (0.1% formic acid) in ddH_2O (0.1% formic acid) over 10 min for the presence of siderophore. Targeted UPLC-ESI-MSMS analysis of putative cupriachelin molecular ions was conducted with a collision energy ramp of CE 25-35. To obtain pure cupriachelin, the concentrated eluent was separated by

semipreparative reverse-phase HPLC (250 × 20-mm YMC C18-AQ column, 7 mL/min flow rate), employing a gradient of methanol (+0.05% trifluoroacetic acid) in ultrapure water (+0.05% trifluoroacetic acid) of 50% to 100% over 40 minutes, yielding ~3 mg cupriachelin per L of culture.

4.2.3. Amino Acid Analysis

Approximately 1 mg of cupriachelin C10 was dissolved in 200 µL of ultrapure water. To the siderophore solution was added 200 µL of 20% DCl in D_2O. The acidified solution was then transferred to a glass ampoule, blanketed with Ar, and sealed. The ampoule was heated for 6 h at 100 °C. After heating, the ampoule was opened, and crude hydrolysate was transferred to a microcentrifuge tube. Hydrolysate was evaporated and re-dissolved in ~700 µL of ultrapure water 3 times to remove any acid, and then brought to a final volume of 100 µL. Hydrolysate was reacted with FDAA (Marfey's reagent) following standard conditions.[3] Derivatized hydrolysate was analyzed by UPLC-ESIMS. A Waters BEH C18 column was used with a linear gradient of 10 to 30% CH_3CN (0.1% formic acid) in ddH_2O (0.1% formic acid) over 10 min.

4.3. Results and Interpretation

4.3.1. Isolation and Stereochemical Characterization of Cupriachelin

Cupriavidus necator H16 was cultured, cupriachelin was extracted from the culture supernatant, and was identified by ESI-MS and ESI-MSMS (Figure 4.1, Figure 4.2). Hydrolysis of cupriachelin and FDAA-derivatization of the hydrolysate enabled a rigorous re-examination of the stereochemistry of each β-OHAsp residue. UPLC-ESI-MS co-injections of cupriachelin derivatized hydrolysate with derivatized standards of D,L-*threo* β-OHAsp and D,L-*erythro* β-OHAsp unambiguously determine that cupriachelin incorporates both an L-

threo and an L-*erythro* β-OHAsp residue (Figure 4.3), as opposed to the assignment of two L-*threo* residues previously reported.[1] This reassignment is consistent with the stereoselectivity associated with both $I\beta H_{Asp}$ and $T\beta H_{Asp}$ hydroxylases, and resolves the only known exception of the pattern between stereoselectivity and phylogeny among siderophore aspartyl β-hydroxylases.

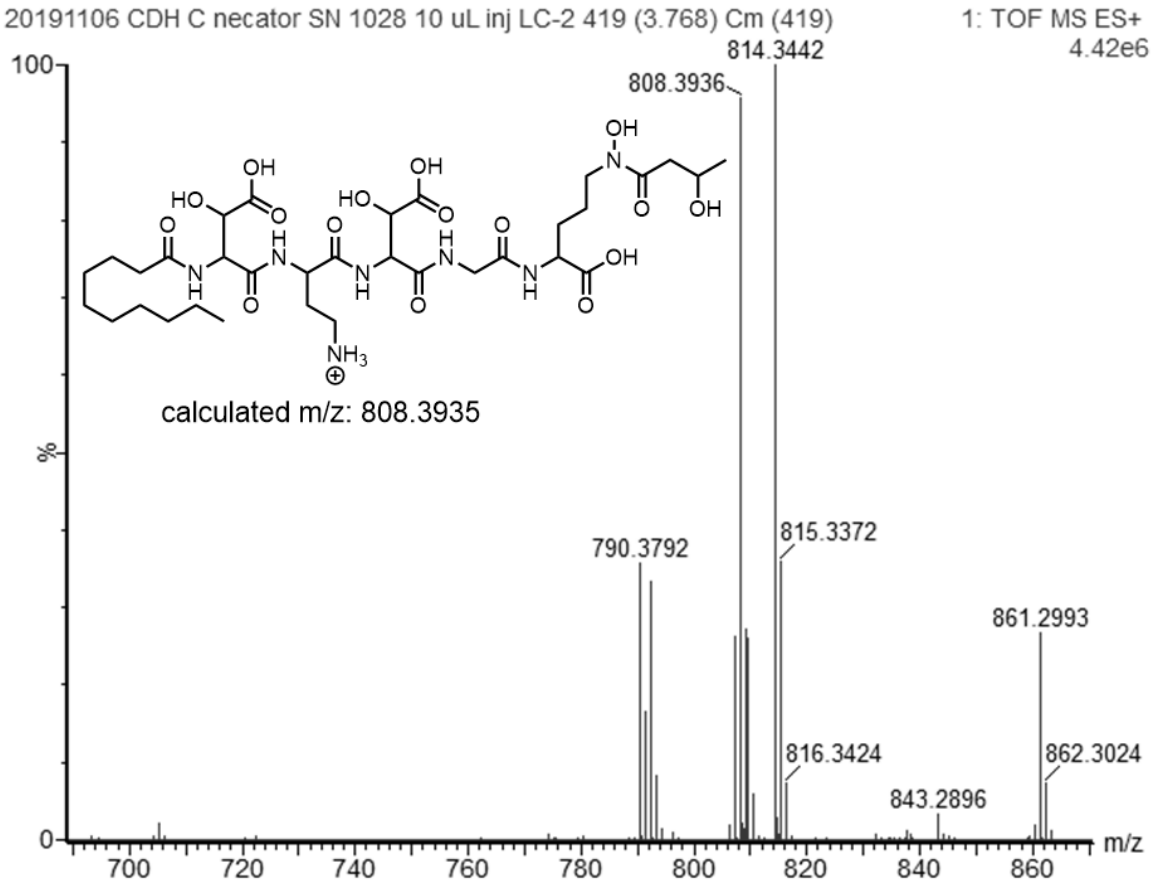

Figure 4.1. Positive-ion mode ESI-MS spectrum of cupriachelin isolated from *Cupriavidus necator* H16.

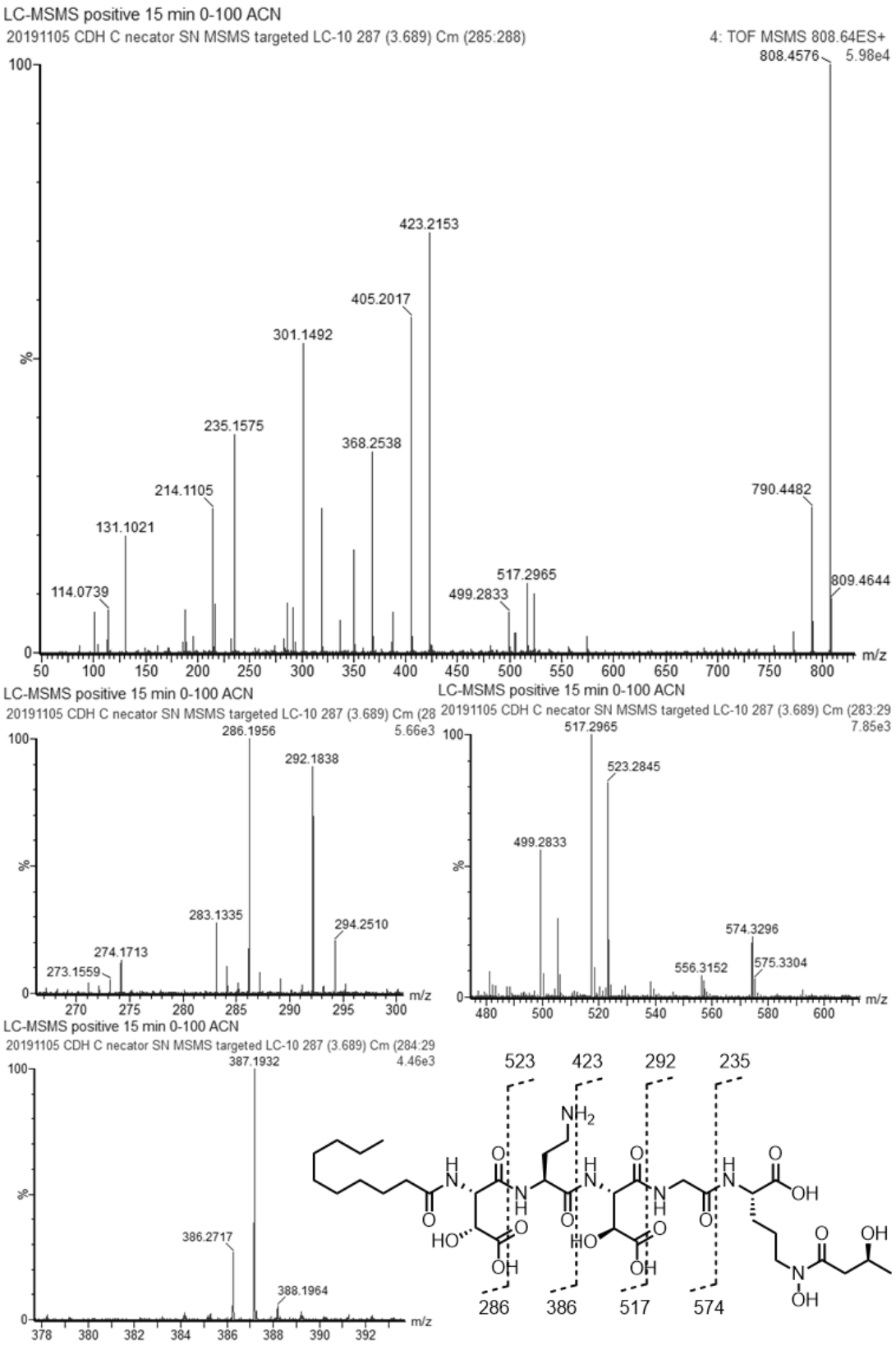

Figure 4.2. ESI-MSMS spectrum of cupriachelin. Fragments observed are delineated in the structure. Magnified regions of the spectrum are provided to clarify all fragments.

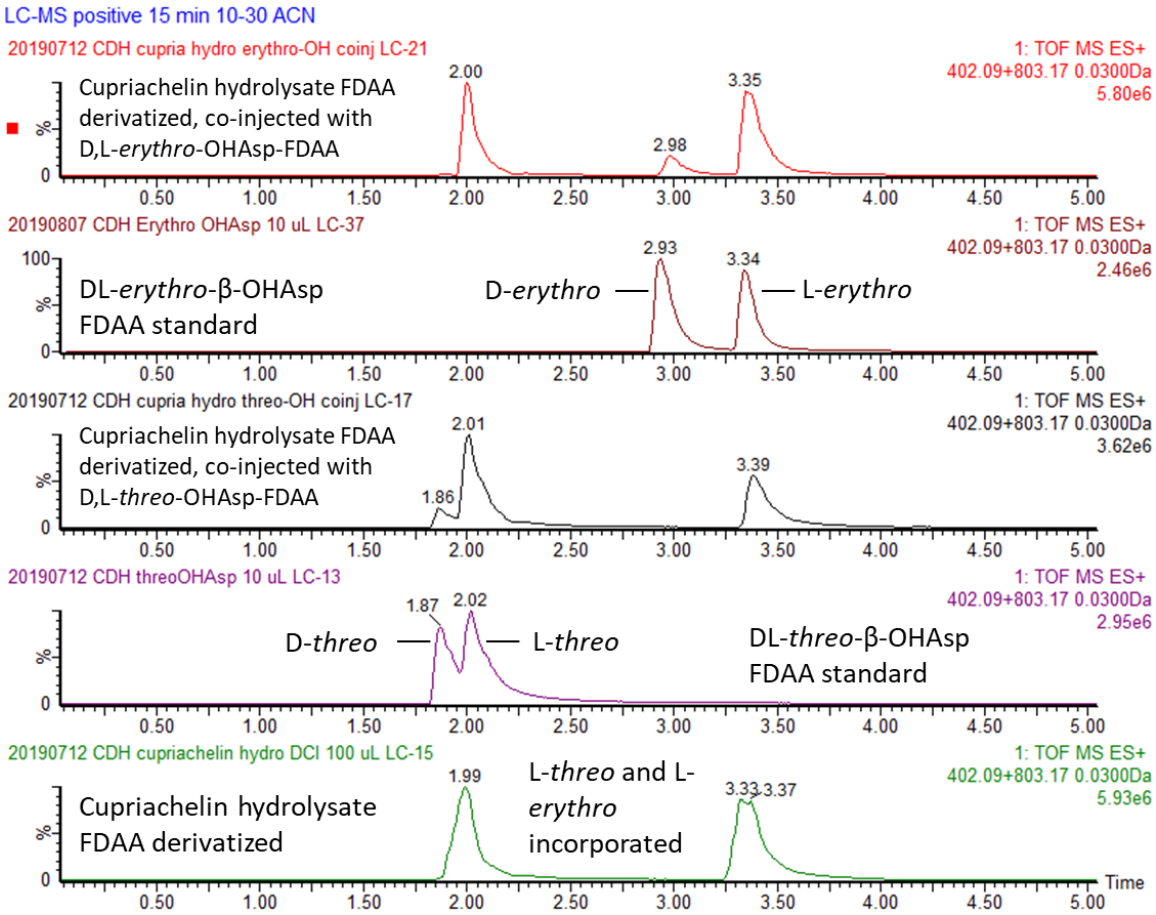

Figure 4.3. Extracted ion chromatograms of the FDAA-β-OHAsp molecular ions (402 m/z $[M+H]^+$, 803 m/z $[M+M+H]^+$) from UPLC-ESIMS analysis of FDAA-derivatized DL-*erythro*-β-OHAsp, DL-*threo*-β-OHAsp and cupriachelin hydrolysate (HCl hydrolysis), and co-injections of cupriachelin hydrolysate with each standard. Cupriachelin contains both L-*threo* and L-*erythro*-β-OHAsp.

4.3.2. Characterization of Cupriachelin Fatty Acid Variants

During UPLC-ESI-MS analysis of *C. necator* H16 culture extracts, several molecular ions of similar mass to, but distinct retention time from, cupriachelin were noted. Further interrogation of these molecular ions by MSMS fragmentation suggests that they are molecules structurally related to cupriachelin, composing a larger suite of siderophores. Cupriachelin, henceforth referred to as cupriachelin C10 to avoid confusion (referring to the number of carbon atoms in the fatty acid moiety), was originally reported to be produced alongside two congeners identified by ESI-MS, a C8 fatty acid variant and a C10 hydroxylated fatty acid variant.[1] This C10 hydroxylated fatty acid cupriachelin congener was not detected in this study, however the previously reported C8 fatty acid congener was detected by ESI-MS (Figure 4.4), and we report the first MSMS characterization of this compound (Figure 4.5).

In addition to the previously reported C8 and C10 variants, two more cupriachelin congeners differing in the composition of the fatty acid moiety were characterized by ESI-MS and MSMS fragmentation: a C12 fatty acid variant (Figure 4.6, Figure 4.7) and an unusual C11 fatty acid variant (Figure 4.8, Figure 4.9). MSMS fragmentation clearly establishes that the mass difference between each molecular ion is localized to the fatty acid tail, as each molecule shares the same peptide y fragments. The production of a suite of acylated peptidic siderophores, differing only by the composition of their fatty acid moiety, is a well-established and common motif among bacteria.[4] The production of a C11 cupriachelin variant is a less-expected result, as odd-chain fatty acids have been reported in few siderophore structures to date, of which only mycobactins are synthesized by NRPSs.[5-8] Odd chain fatty acids in siderophores can manifest as both straight chain and branched iso-fatty acids;[7-8] further

characterization through NMR or fatty acid methyl ester analysis is necessary to determine if cupriachelin C11 contains a straight chain or iso-fatty acid.

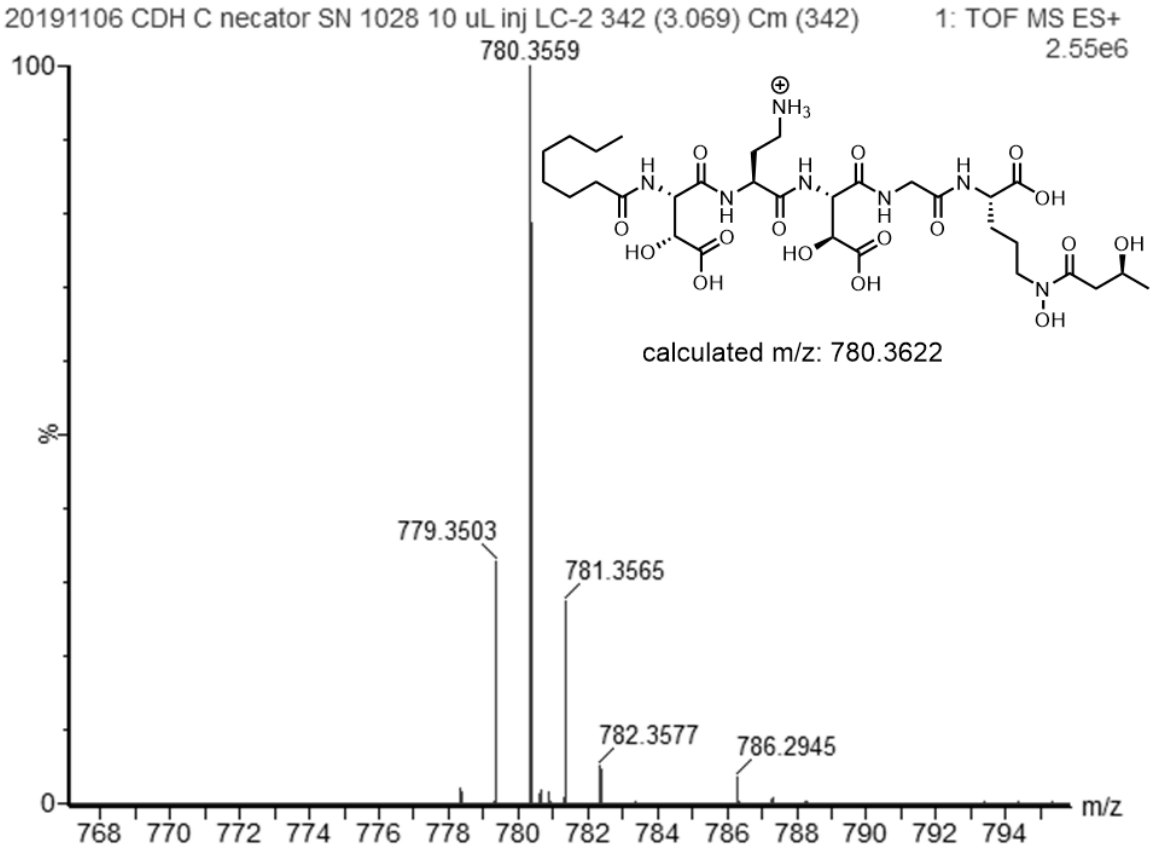

Figure 4.4. Positive-ion mode ESI-MS spectrum of cupriachelin C8.

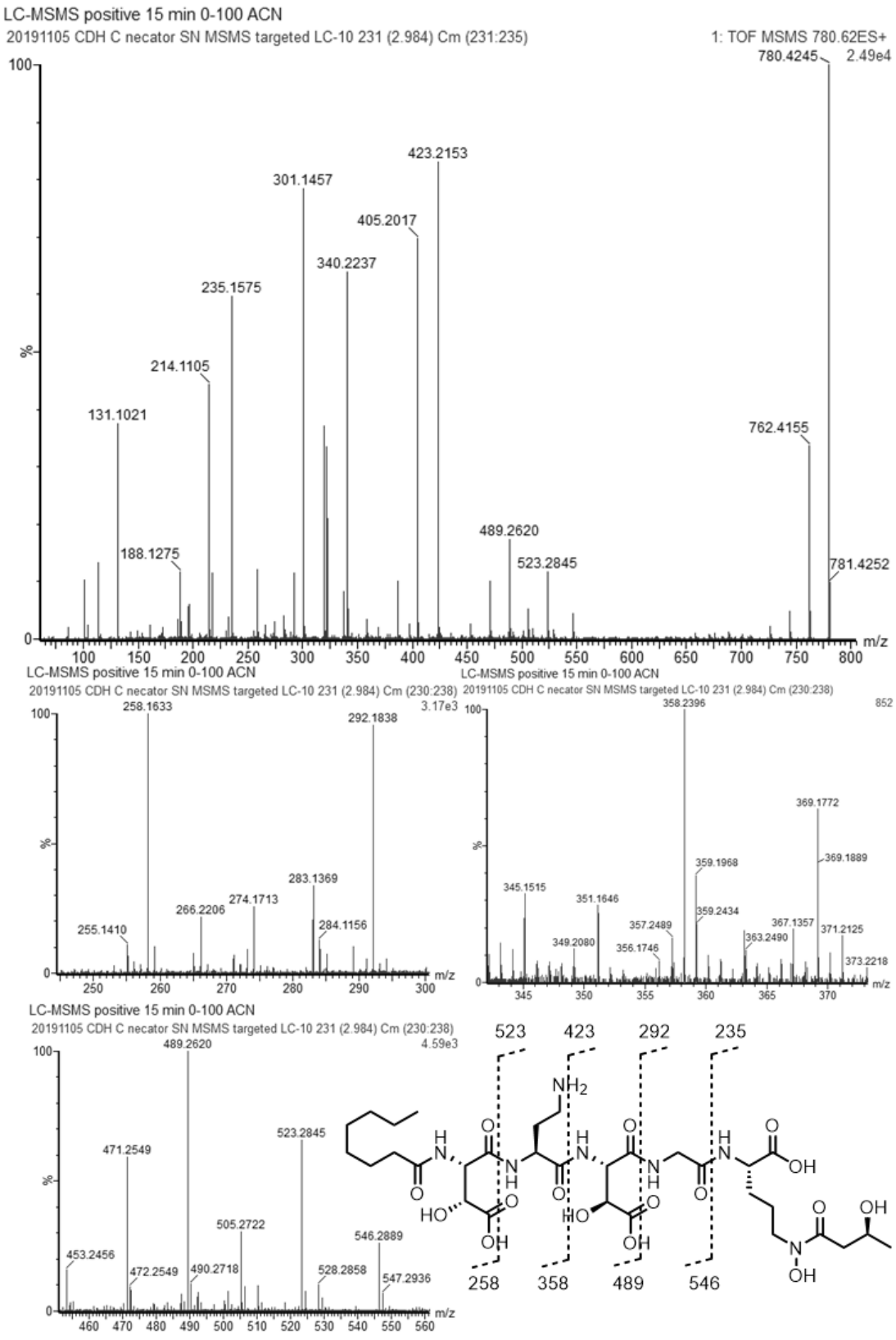

Figure 4.5. ESI-MSMS spectrum of cupriachelin C8. Fragments observed are delineated in the structure. Magnified regions of the spectrum are provided to clarify all fragments.

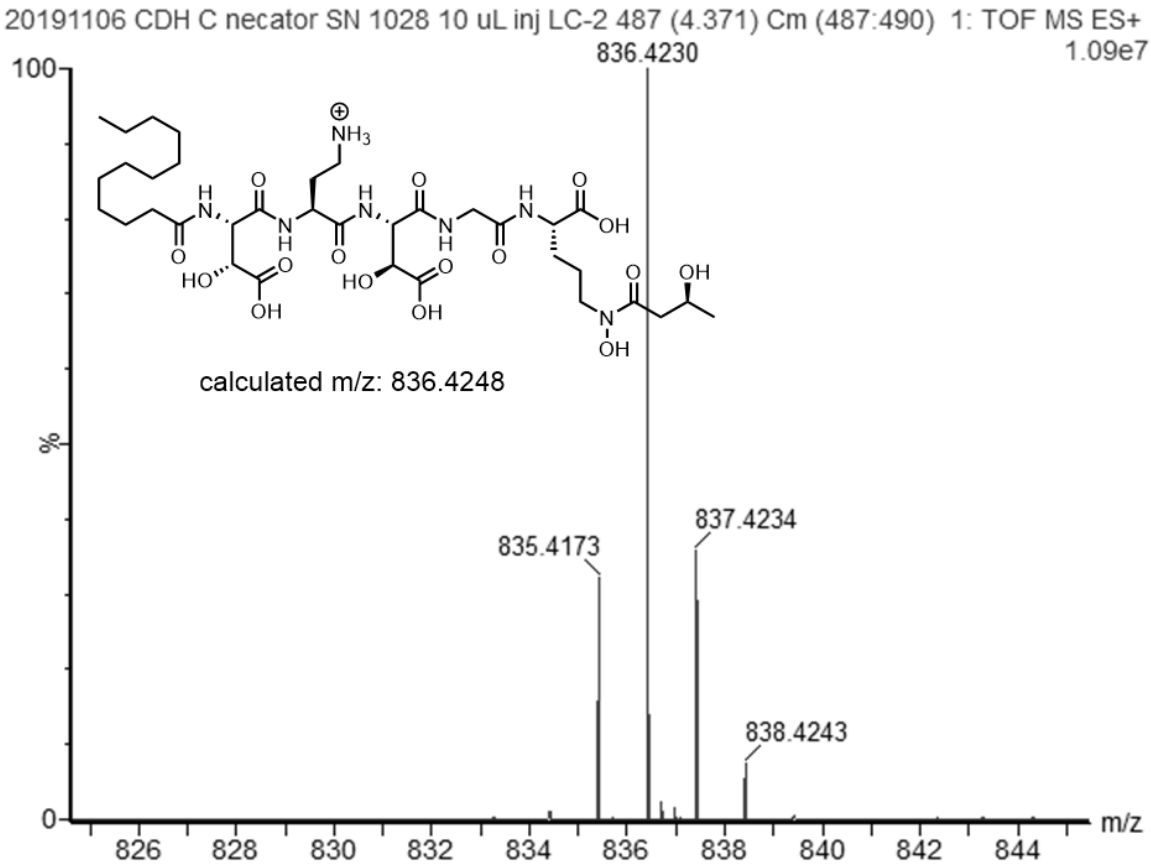

Figure 4.6. Positive-ion mode ESI-MS spectrum of cupriachelin C12.

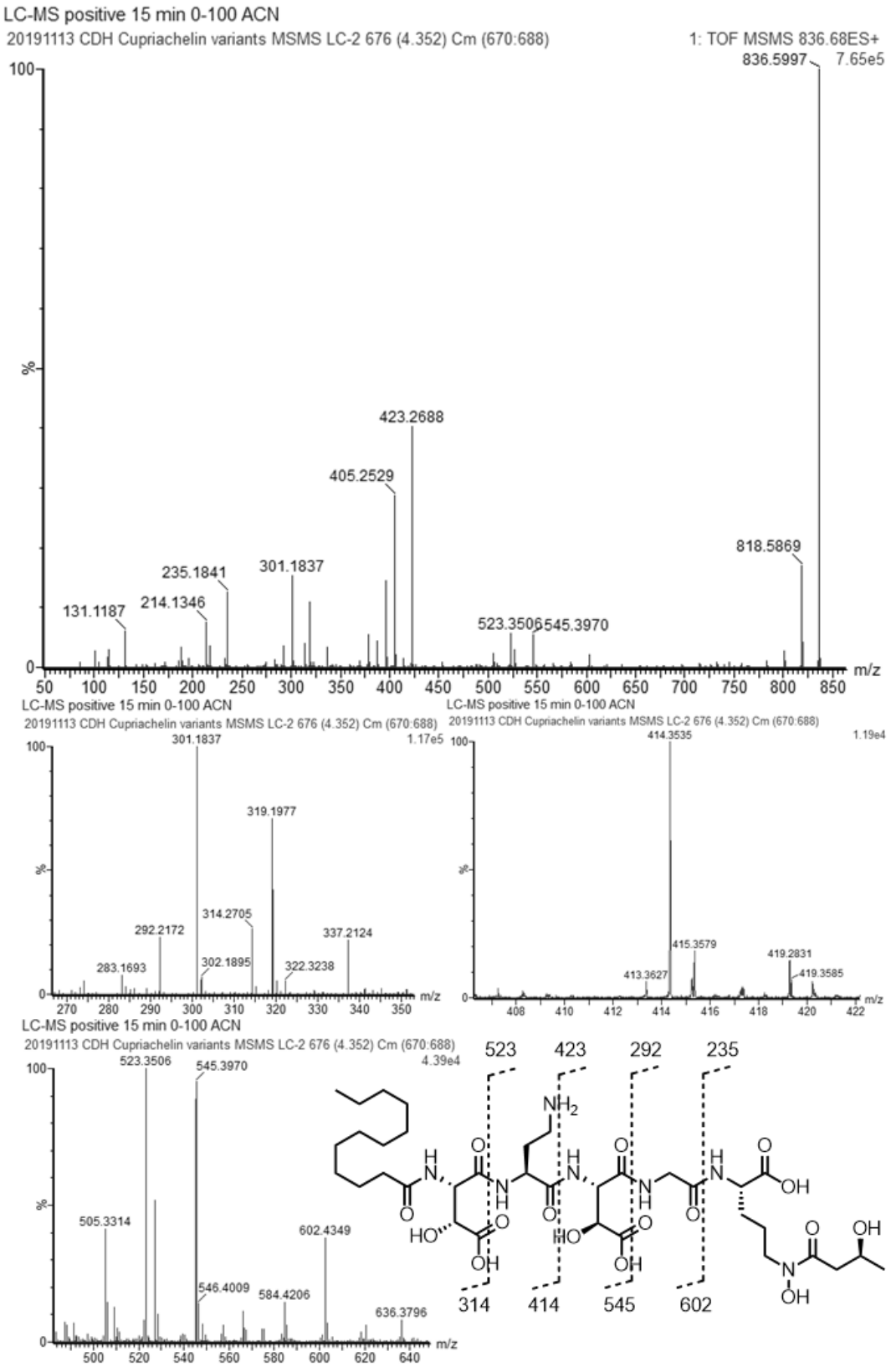

Figure 4.7. ESI-MSMS spectrum of cupriachelin C12. Fragments observed are delineated in the structure. Magnified regions of the spectrum are provided to clarify all fragments.

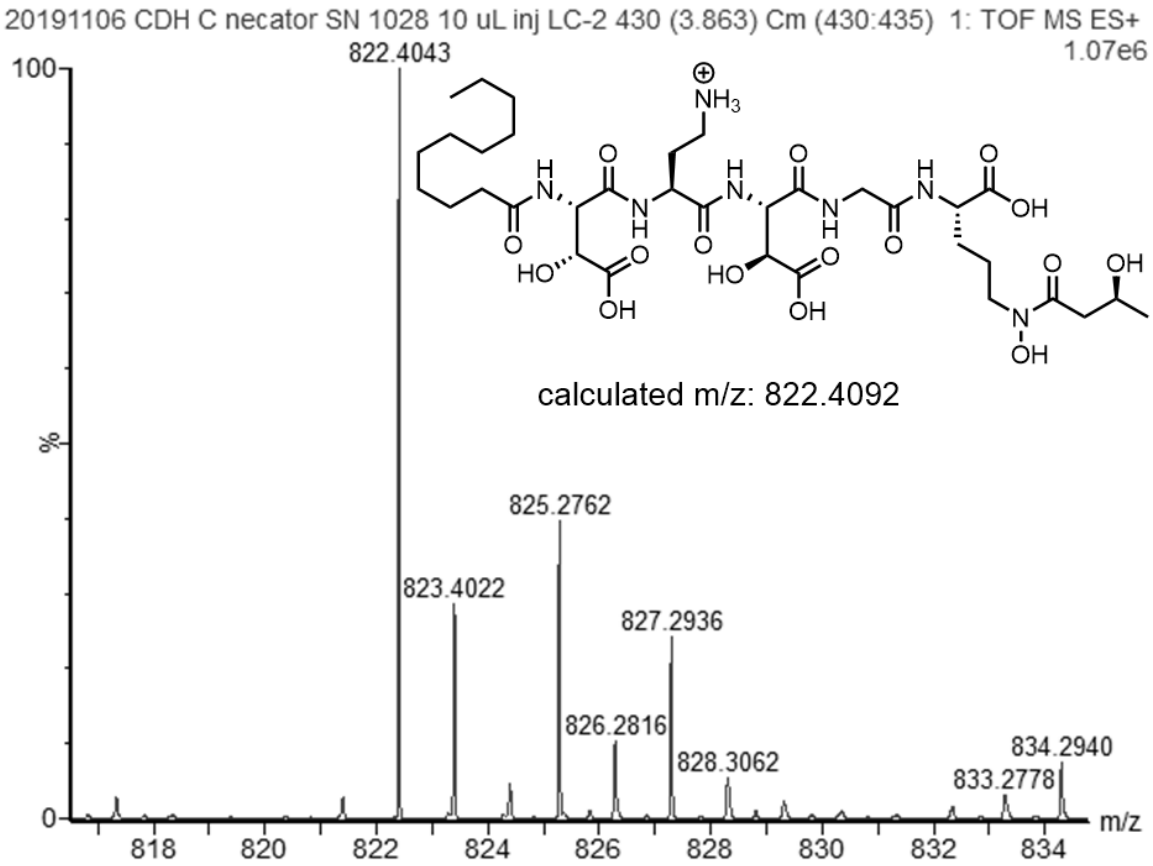

Figure 4.8. Positive-ion mode ESI-MS spectrum of cupriachelin C11.

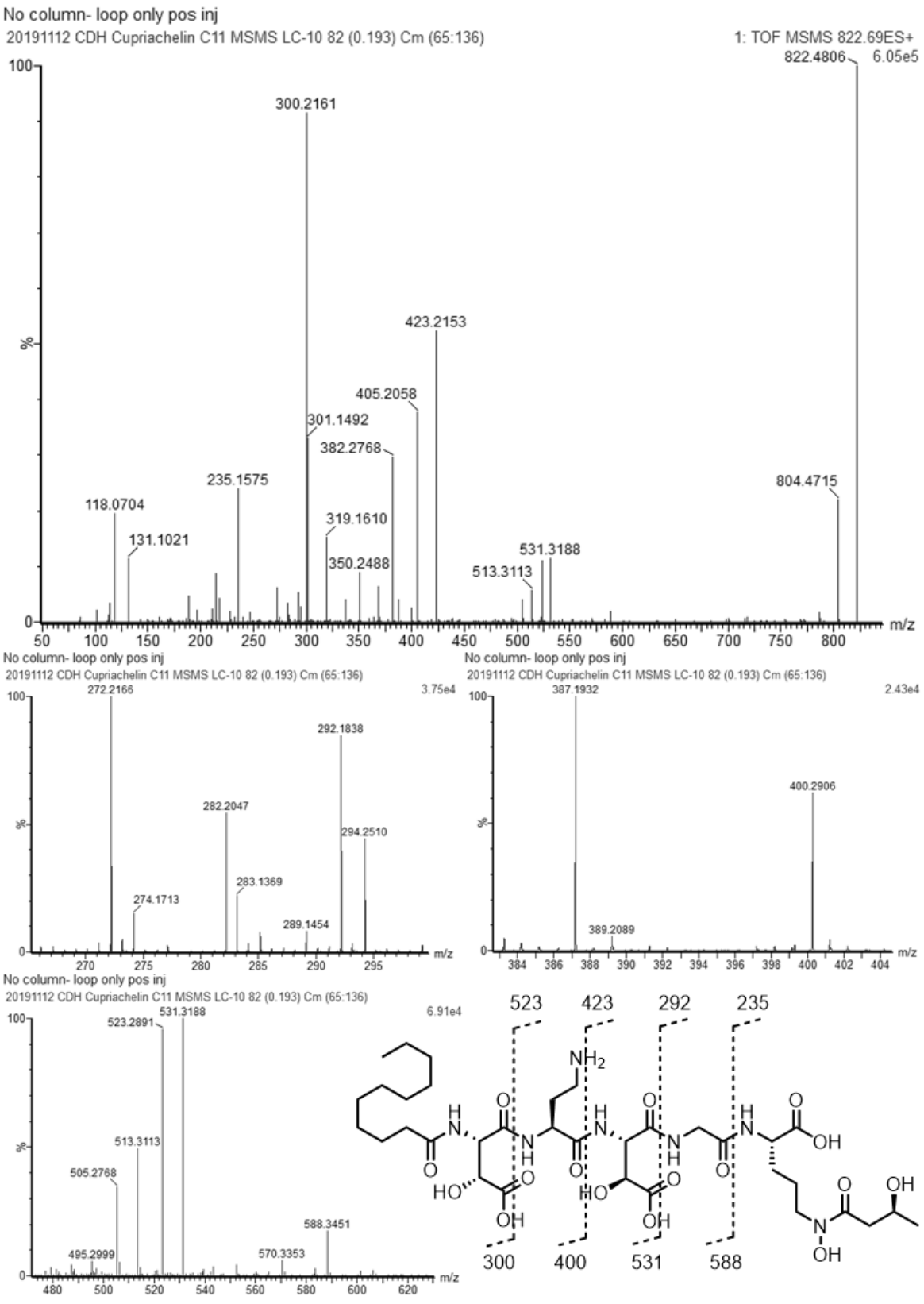

Figure 4.9. ESI-MSMS spectrum of cupriachelin C11. Fragments observed are delineated in the structure. Magnified regions of the spectrum are provided to clarify all fragments.

4.3.3. Characterization of Cupriachelin C-Terminal Residue Variants

In addition to the new cupriachelin congeners differing in the composition of the fatty acid tail, UPLC-ESI-MS analysis of *C. necator* H16 culture extracts detected two peaks of m/z 762 and m/z 790 that elute at comparable retention times to cupriachelin C8 and C10, respectively (Figure 4.10, Figure 4.11, Figure 4.12). Each molecular ion is a mass difference of 18 Da from cupriachelin C8 and C10, respectively, a mass difference inconsistent with typical modifications of a siderophore fatty acid moiety (hydroxylation, desaturation of an alkane to alkene). These molecular ions were further interrogated through ESI-MSMS to determine which residue differs in mass from the C8 and C10 cupriachelin variants. The resulting fragmentation patterns indicate that the 762 and 790 m/z molecular ions, deemed cupriachelin C8a and C10a respectively, share peptide b fragments with cupriachelin C8 and C10, but each y fragment differs by a mass of 18 (Figure 4.13, Figure 4.14), localizing the mass difference to the C-terminal N^5-OH-N^5(3-hydroxybutyrate)-Orn residue of cupriachelin. Determining the exact nature of the transformation leading to the loss of 18 Da in these variants will require further characterization through NMR, one possibility is a reductive dehydration of the 3-hydroxybutyrate moiety to an alkene (see proposed structure in Figures 4.11-4.14).

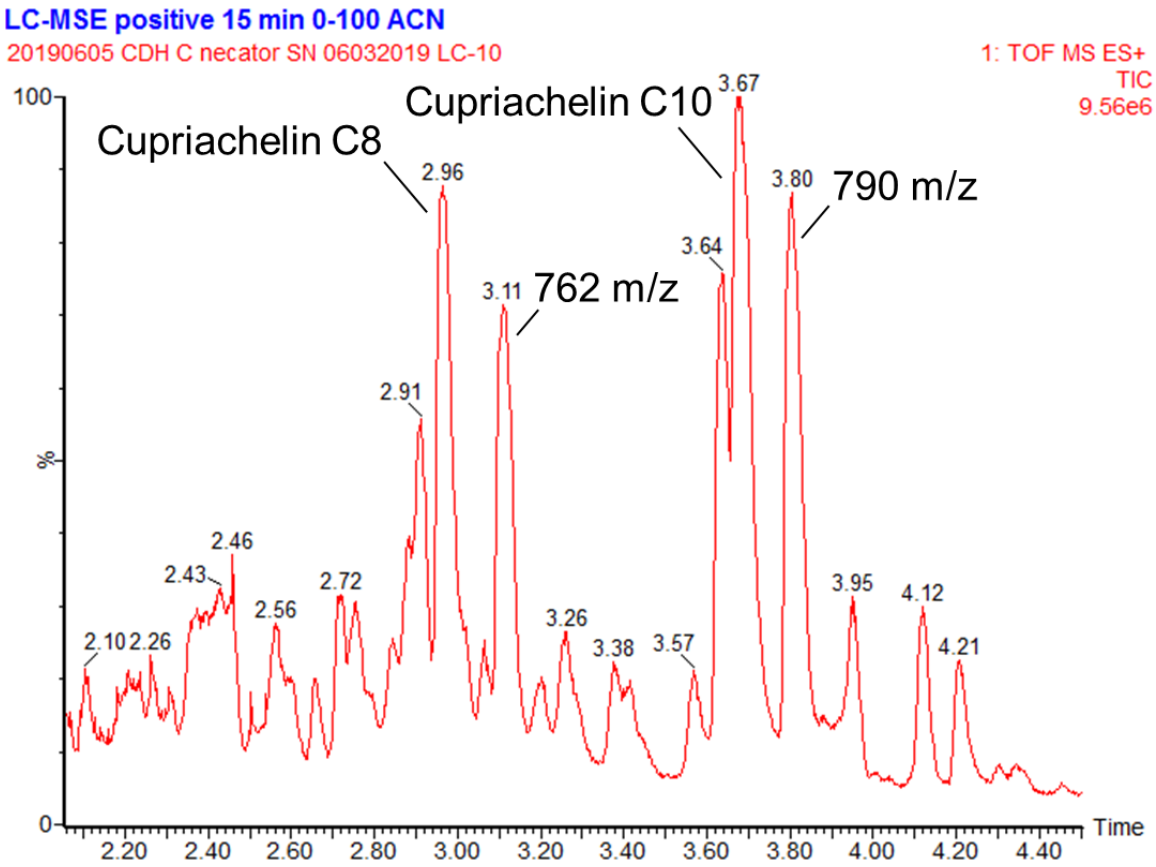

Figure 4.10. Total ion chromatogram of *C. necator* culture supernatant extract injection on UPLC-ESI-MS, highlighting the peaks of m/z 762 and 790 closely eluting to cupriachelins C8 and C10, respectively.

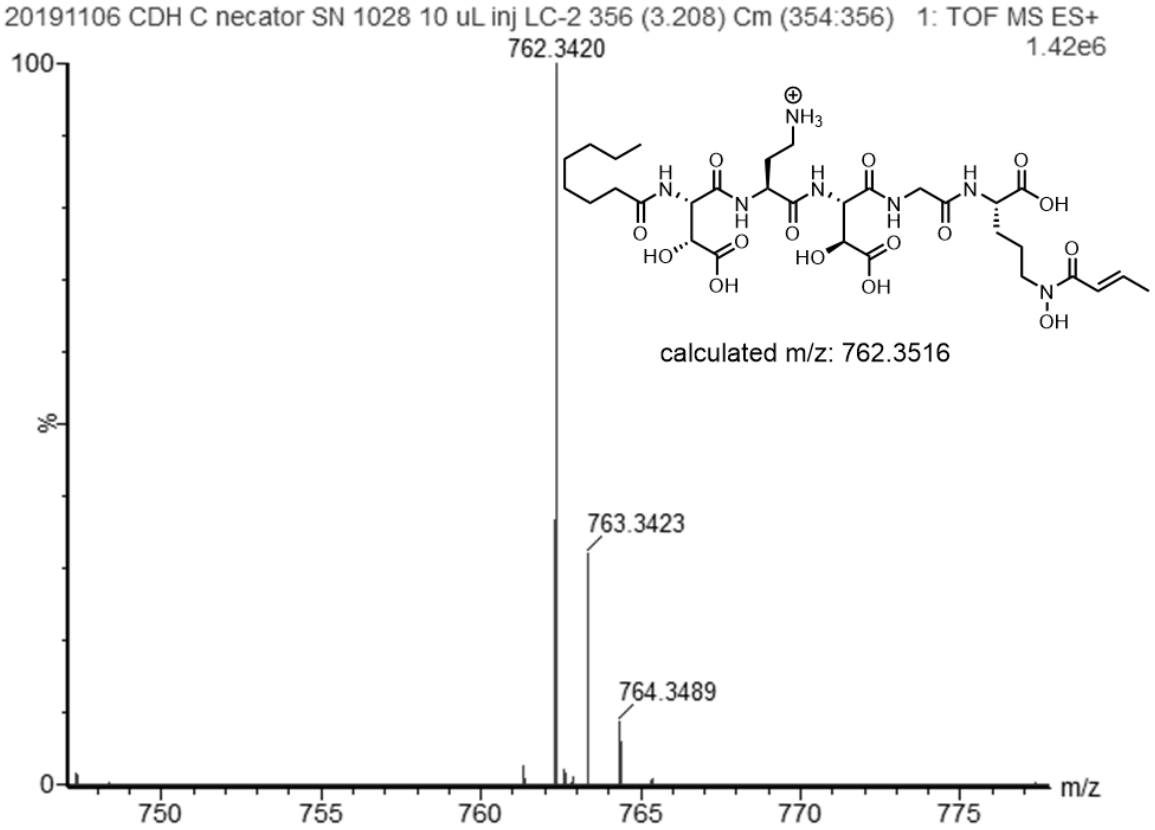

Figure 4.11. Positive-ion mode ESI-MS spectrum of cupriachelin C8a. The structure is depicted as a desaturation in the 3-hydroxybutyrate moiety, but this structure is speculative until further characterization is completed.

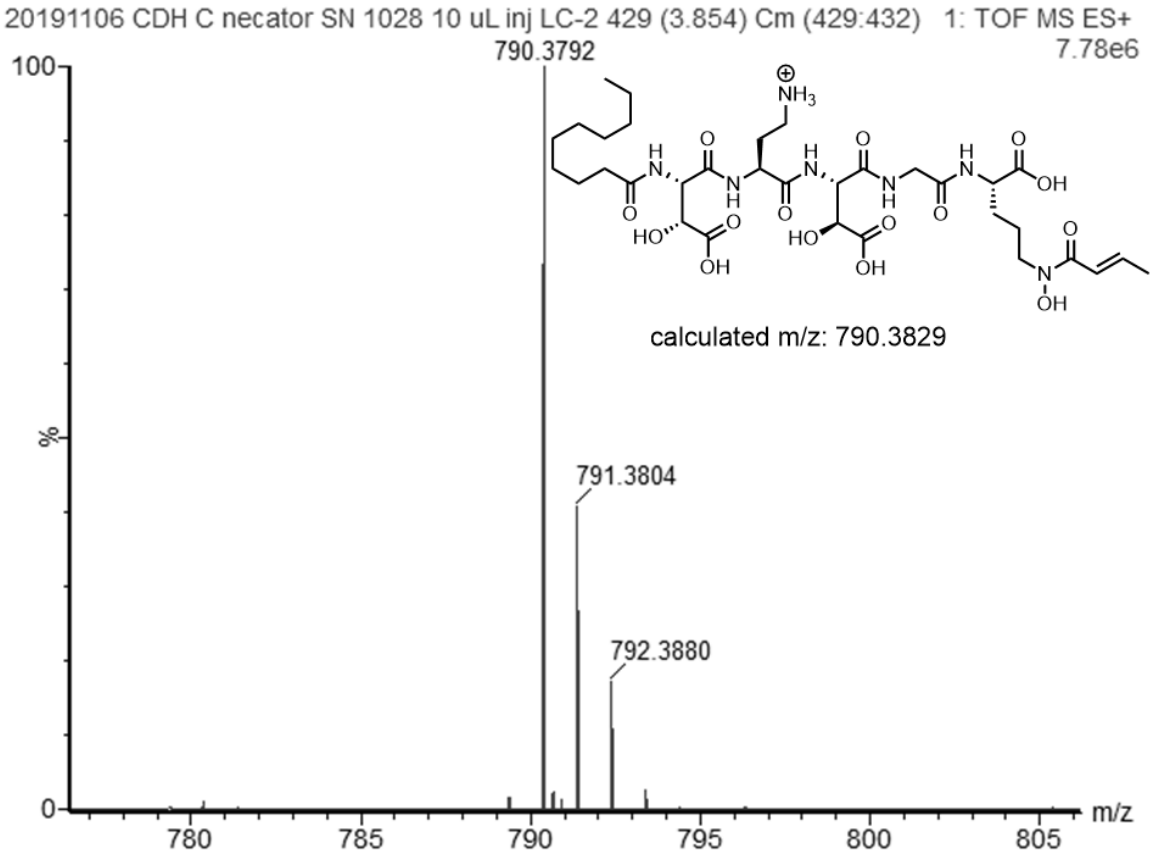

Figure 4.12. Positive-ion mode ESI-MS spectrum of cupriachelin C10a. The structure is depicted as a desaturation in the 3-hydroxybutyrate moiety, but this structure is speculative until further characterization is completed.

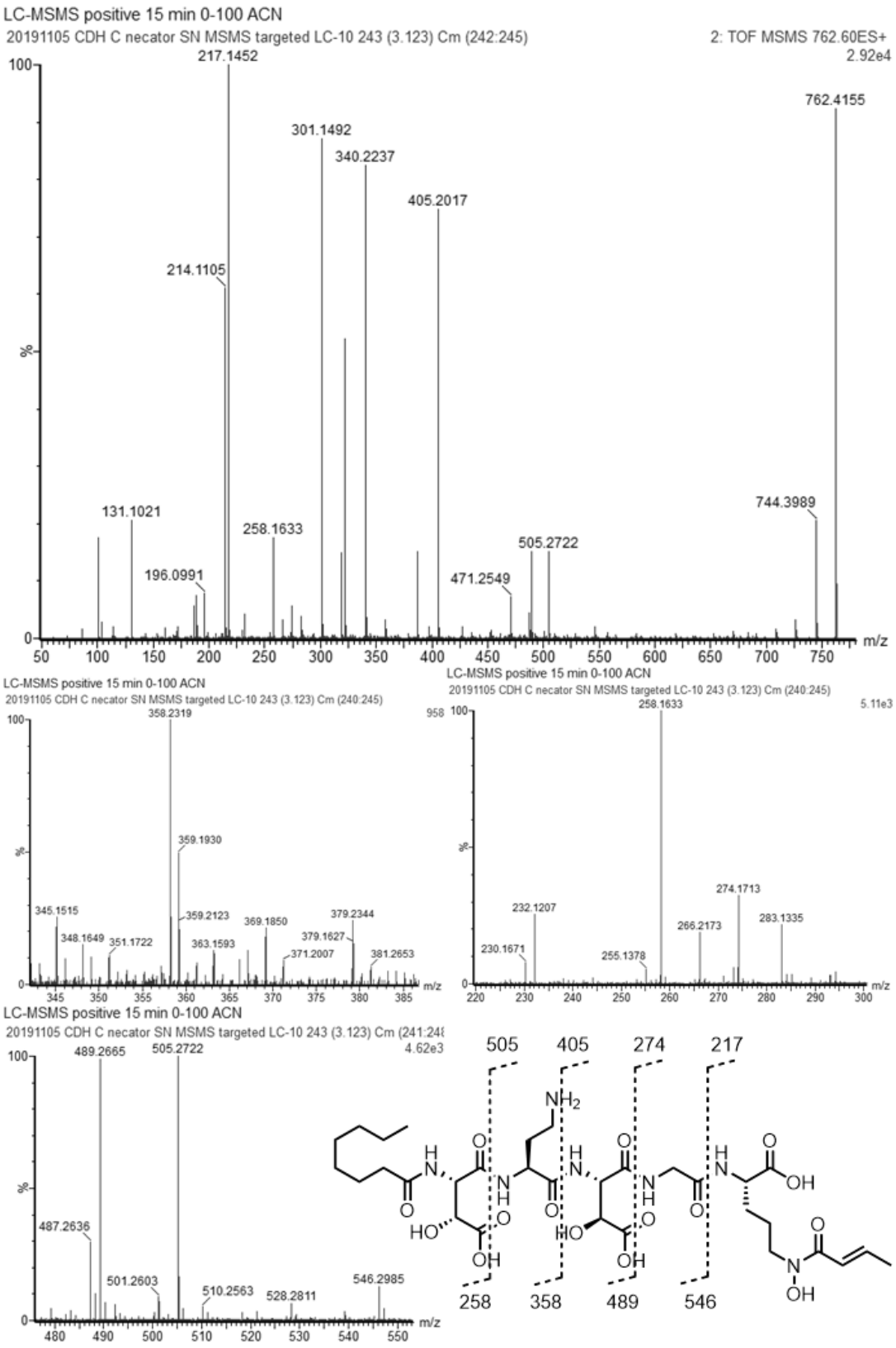

Figure 4.13. ESI-MSMS spectrum of cupriachelin C8a. Fragments observed are delineated in the structure. Magnified regions of the spectrum are provided to clarify all fragments.

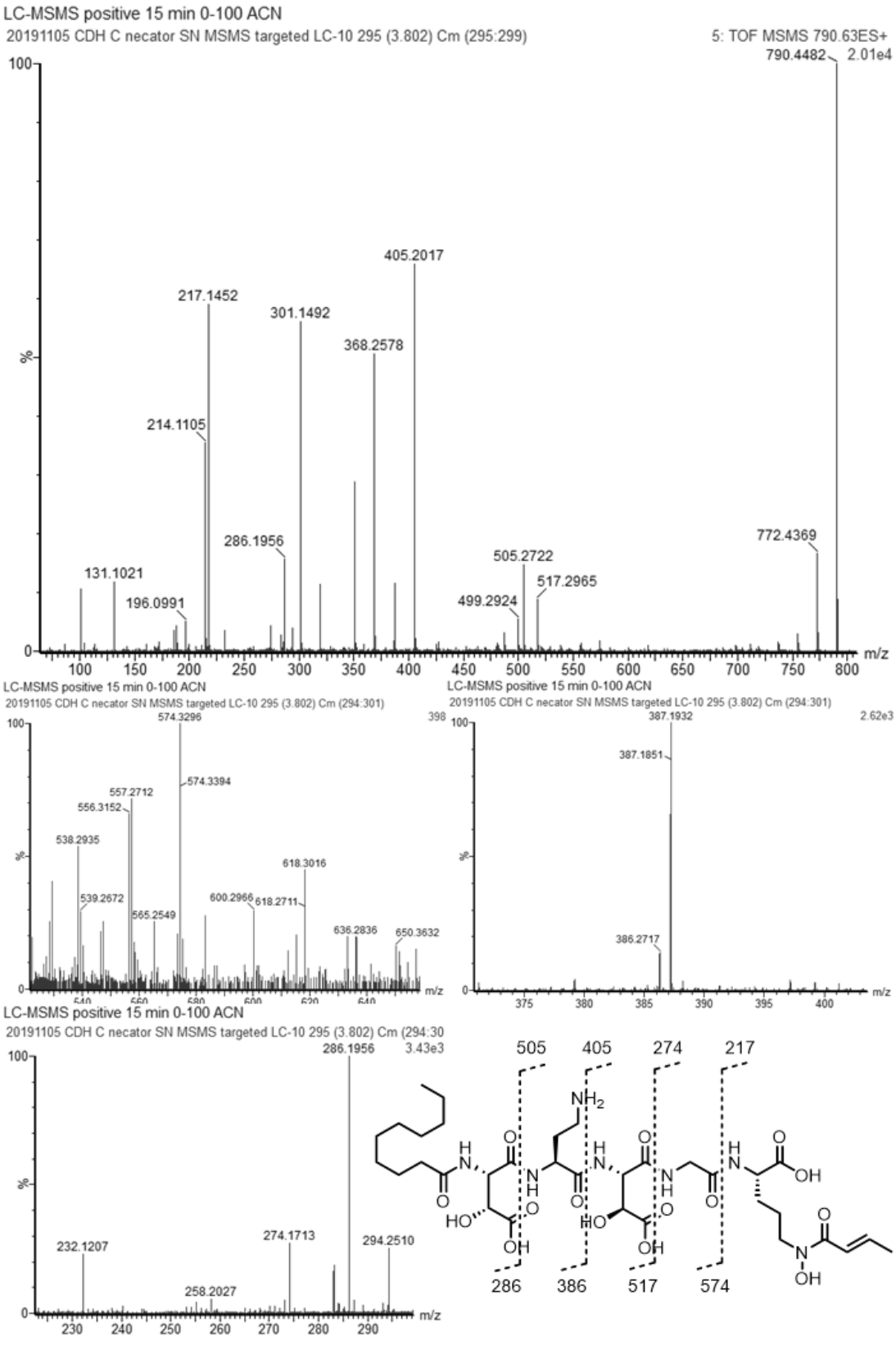

Figure 4.14. ESI-MSMS spectrum of cupriachelin C10a. Fragments observed are delineated in the structure. Magnified regions of the spectrum are provided to clarify all fragments.

4.4. Discussion

The re-assignment of cupriachelin β-OHAsp stereochemistry to L-*threo* and L-*erythro* eliminates an exception to stereoselectivity in the $T\beta H_{Asp}$ hydroxylase clade. Every stereochemically characterized β-OHAsp residue associated with a $T\beta H_{Asp}$ hydroxylase exhibits 3R stereochemistry, likewise every residue associated with an $I\beta H_{Asp}$ hydroxylase exhibits 3S stereochemistry (Figure 4.15). This now uniform association between stereoselectivity and phylogeny provides an opportunity to further improve bioinformatic structural predictions of β-OHAsp siderophores, as the reactivity of a putative siderophore aspartyl β-hydroxylase can now be predicted by its phylogeny. These results open a question regarding the structural basis of stereoselectivity differences between $I\beta H_{Asp}$ and $T\beta H_{Asp}$ hydroxylases. While no crystal structures of aspartyl β-hydroxylases are known, substrate-bound crystal structures of the *threo*-selective L-Asn β-hydroxylase AsnO and *erythro*-selective L-Arg β-hydroxylase VioC reveal that each enzyme holds its substrate in a different rotational conformation. AsnO holds L-Asn in a *trans* position, while VioC holds L-Arg in a strained *gauche* conformation.[9-10] These conformations admit only one β-hydrogen into the active site, either the *pro-threo* or *pro-erythro* hydrogen. It is expected that $I\beta H_{Asp}$ and $T\beta H_{Asp}$ hydroxylases would use a similar structural basis to enforce their stereoselectivity, and future *in vitro* and protein structure studies are necessary to further explore this possibility.

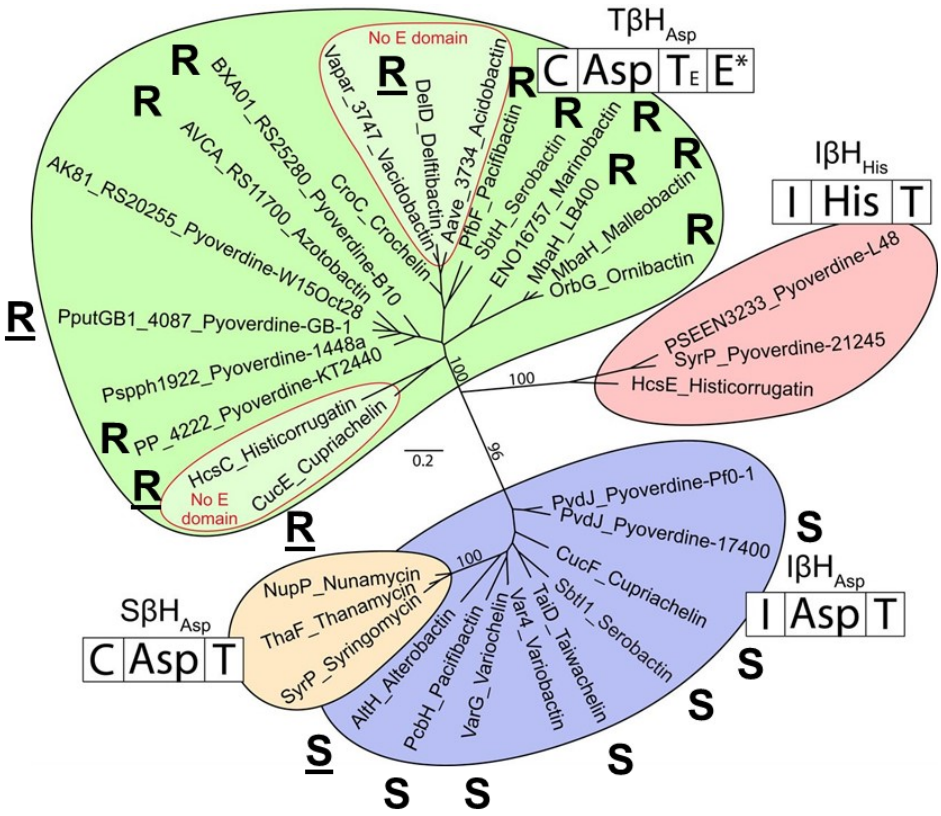

Figure 4.15. Phylogenetic tree of putative NRPS-associated β-hydroxylase-encoding genes labelled with the stereochemistry at the 3 carbon of the β-OHAsp residue associated with the hydroxylase. Associations determined from this work and that presented in Chapter 3 are underlined.

The discovery of new cupriachelin congeners differing in fatty acid composition is consistent with many other acylated peptidic siderophores, which consist of a suite of structures differing only by the length of the fatty acid tail.[4, 11-13] Molecular ions consistent with further fatty acid variants (including a C9 fatty acid tail variant) were detected by UPLC-ESIMS, however their abundances were too low to further probe by MSMS fragmentation. The cupriachelin variants C8a and C10a are perhaps even more intriguing, differing somehow in the composition of the C-terminal N^5-OH-N^5(3-Hbu)-Orn residue. This moiety has not been observed in any siderophore structure other than the cupriachelins, limiting our ability to hypothesize what transformations could account for a loss of 18 Da in the residue. The aforementioned reductive dehydration is a distinct possibility, but a cyclization of the amino

acid side chain onto the C-terminus of the peptide (analogous to the cyclization of C-terminal N^5-OHOrn residues observed in many siderophore structures) cannot be ruled out. Further structural characterization of cupriachelin C8a and C10a is underway to better understand how they differ structurally from the other cupriachelin congeners.

4.5. References

1. Kreutzer, M. F.; Kage, H.; Nett, M., *J. Am. Chem. Soc.* **2012,** *134* (11), 5415-5422.

2. Reitz, Z. L.; Hardy, C. D.; Suk, J.; Bouvet, J.; Butler, A., *Proc. Natl. Acad. Sci. USA* **2019,** *116* (40), 19805.

3. Marfey, P., *Carlsberg Res. Commun.* **1984,** *49* (6), 591.

4. Kem, M. P.; Butler, A., *BioMetals* **2015,** *28* (3), 445-459.

5. Snow, G. A., *Bacteriol Rev* **1970,** *34* (2), 99-125.

6. Lynch, D.; Brien, J.; Welch, T.; Clarke, P.; ÓCuív, P.; Crosa, J. H.; Connell, M., *J. Bacteriol.* **2001,** *183* (8), 2576.

7. Boiteau, R. M.; Repeta, D. J., *Metallomics* **2015,** *7* (5), 877-884.

8. Carmichael, J. R.; Zhou, H.; Butler, A., *J. Inorg. Biochem.* **2019,** *198*, 110736.

9. Strieker, M.; Kopp, F.; Mahlert, C.; Essen, L.-O.; Marahiel, M. A., *ACS Chem. Biol.* **2007,** *2* (3), 187-196.

10. Helmetag, V.; Samel, S. A.; Thomas, M. G.; Marahiel, M. A.; Essen, L.-O., *FEBS J.* **2009,** *276* (13), 3669-3682.

11. Martinez, J. S.; Zhang, G. P.; Holt, P. D.; Jung, H. T.; Carrano, C. J.; Haygood, M. G.; Butler, A., *Science* **2000,** *287* (5456), 1245-1247.

12. Vraspir, J. M.; Holt, P. D.; Butler, A., *BioMetals* **2011,** *24* (1), 85-92.

13. Martinez, J. S.; Carter-Franklin, J. N.; Mann, E. L.; Martin, J. D.; Haygood, M. G.; Butler, A., *Proc. Natl. Acad. Sci. USA* **2003,** *100* (7), 3754.

5. Characterizing and Modulating Photoreactivity of Fe(III)-β-Hydroxyaspartic Acid Siderophore Complexes

5.1. Introduction

Fe(III) complexes of α-hydroxycarboxylic acid siderophores are photochemically reactive.[1-2] Photon absorption into the ligand-metal charge transfer band (in the UV region, generally centered around 300 nm) of the Fe(III)-α-hydroxycarboxylate bond triggers photoreduction of Fe(III) to Fe(II), and oxidative breakdown of the ligand.[3] The products of several Fe(III)-siderophore complex photoreactions have been reported. Irradiation of siderophore complexes containing citrate results in oxidative loss of CO_2 at the α-hydroxycarboxylate site, yielding photoproducts with a ketone/enol tautomer, as illustrated in the photoreactions of Fe(III)-aerobactin (Figure 5.1a), Fe(III)-petrobactin, and Fe(III)-ochrobactin.[4-7] The characterized photoproducts of β-OHAsp siderophore Fe(III) complexes, in contrast, are much more varied in their structures. For the β-OHAsp siderophores aquachelin (Figure 5.1b), cupriachelin, and pacifibactin, the reported photoproducts are C-terminal fragments of the intact peptides, resulting from oxidative cleavage of the peptide backbone at β-OHAsp residue positions.[8-10] Two photoproducts are reported from irradiation of Fe(III)-variochelin, one an N-terminal fragment of the intact peptide, and the other a product resulting from oxidative decarboxylation of the β-OHAsp residue (analogous to the decarboxylation observed in citrate siderophores).[11] A photoproduct detected from irradiation of Fe(III)-imaqobactin contains an intact peptide backbone, but with loss of the entire β-OHAsp side chain, yielding a glycine residue.[12]

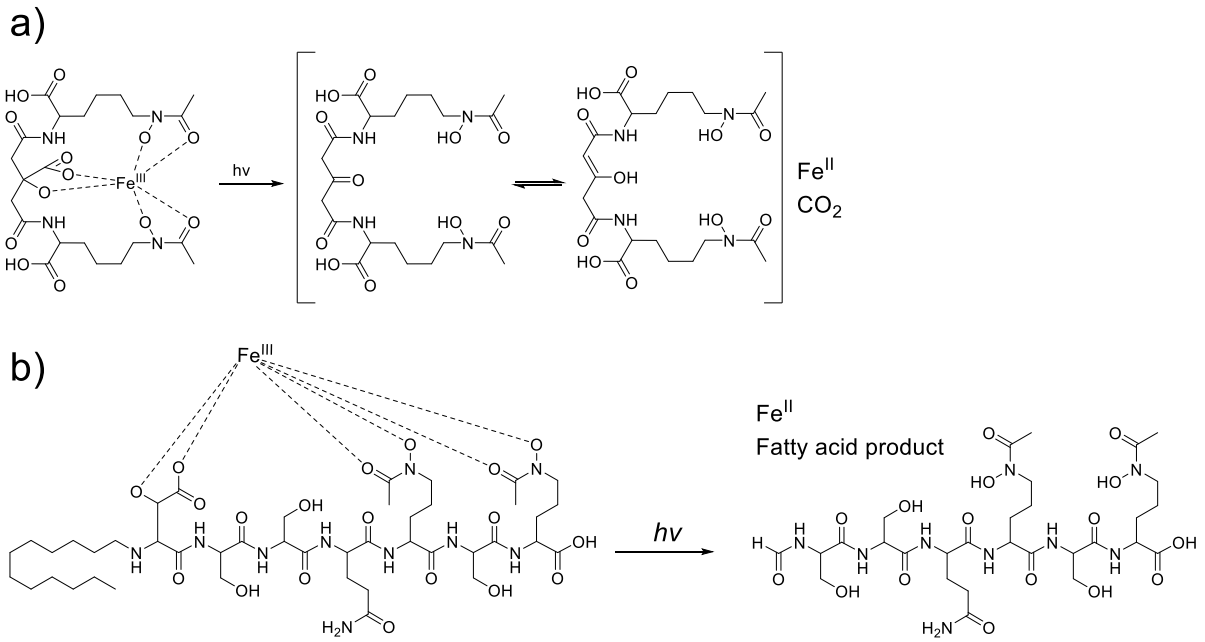

Figure 5.1. Photoreactions and known photoproducts of a) Fe(III)-aerobactin, which binds Fe(III) through a citrate functional group, and b) Fe(III)-aquachelin, which binds Fe(III) through a β-OHAsp functional group.

Recent investigations of synthetic Fe(III)-α-hydroxycarboxylate complex photoreactions reveal that photolysis under deoxygenated conditions results in oxidative decarboxylation of the ligand complex, forming an aldehyde moiety, with no further photoreactivity observed.[13] Under aerobic conditions, photolysis of the complex initially leads to oxidative decarboxylation, but further reactivity is observed. O_2-mediated oxidation of the resultant aldehyde functional group to a carboxylate functional group allows re-complexation of Fe(III) by the ligand, followed by further photolytic decarboxylation.[13] Phenanthroline is also reported to slow oxidation of the aldehyde-containing photoproduct, presumably through complexation of photo-generated Fe(II).[13] This sequential decarboxylation model of photoreactivity could explain the uniform photoreactivity of citrate siderophores, as decarboxylation yields an oxidation-resistant ketone-enolate moiety instead of an aldehyde.[13] Decarboxylation of a β-

OHAsp residue, on the other hand, would yield an aldehyde functional group, thus potentially explaining the further and varied reactivity observed in β-OHAsp siderophore photoreactions.

To test the applicability of this proposed pathway to Fe(III)-siderophore complex photoreactivity, we have carried out extensive mass spectrometry analysis of two β-OHAsp Fe(III)-siderophore complex photoreactions, those of pacifibactin and cupriachelin. Each siderophore contains two β-OHAsp residues of differing chirality (pacifibactin, L-*threo* and D-*threo* β-OHAsp; cupriachelin, L-*threo* and L-*erythro* β-OHAsp).[10, 14] Photoproducts corresponding to cleavage of the peptide backbone have been reported from previous studies of each siderophore.[9-10] We report herein the characterization of several new photoproducts of the Fe(III)-pacifibactin and Fe(III)-cupriachelin photoreactions, as well as measurements of how relative abundance of these products changes as a function of irradiation time. The structures of the photoproducts, and the patterns of their relative abundances over time, support the sequential decarboxylation model of β-OHAsp photoreactivity. We also report the shifts in observed photoproduct profiles when photolyzing Fe(III)-pacifibactin or Fe(III)-cupriachelin in the presence of phenanthroline.

5.2. Experimental

5.2.1. Isolation of Pacifibactin from Alcanivorax pacificus W11-5

Pacifibactin was isolated from cultures of *Alcanivorax pacificus* W11-5 following procedures outlined in chapter 2. Briefly, *A. pacificus* was cultured in 2L of ASW+Py low iron artificial seawater medium (10 g CAS amino acids L^{-1}, 1 g NH_4Cl L^{-1}, 1 g glycerol phosphate L^{-1}, 12.35 g $MgSO_4$ L^{-1}, 1.45 g $CaCl_2$ L^{-1}, 16.55 g NaCl L^{-1}, 0.75 g KCl L^{-1}, 5 g sodium pyruvate L^{-1} in ddH_2O, amended with 10 mL of 1.0 M HEPES L^{-1}, 2 mL of 1.0 M $NaHCO_3$ L^{-1}, and 6 mL of glycerol L^{-1}) at room temperature until late-log phase of growth (5-7 days). Cultures

were then pelleted by centrifugation (SLA-3000 rotor, ThermoScientific) at 6000 RPM for 30 min at 4 °C. Culture supernatants were decanted and shaken with 200 g Amberlite XAD-2 polystyrene resin for 3 h at 4 °C to adsorb organics. The resin was filtered from the supernatant, washed with 250 mL of 90/10% ddH_2O/MeOH and eluted with 300 mL of 10/90% ddH_2O/MeOH. The eluent was concentrated under vacuum and stored at 4 °C. Eluent was further purified by semi-preparative reverse-phase HPLC on a YMC 20x250 mm C18-AQ column, with a linear gradient of 10% MeOH in ddH_2O (+0.1% trifluoroacetic acid) to 30% MeOH in ddH_2O (+0.1% trifluoroacetic acid) over 40 min, yielding ~30 mg of pacifibactin per 2L culture.

5.2.2. Isolation of Cupriachelin from Cupriavidus necator H16

Cupriachelin (C10 variant) was isolated from cultures of *Cupriavidus necator* H16 following procedures outlined in chapter 4. Briefly, *C. necator* was cultured in 1 L of casamino acids minimal medium (consisting of 5 $g \cdot L^{-1}$ chelex-treated casamino acids, 1.18 $g \cdot L^{-1}$ K_2HPO_4, and 0.25 $g \cdot L^{-1}$ $MgSO_4 \cdot 7H_2O$) for 144 h at 30 °C. Cultures were pelleted by centrifugation (SLA-3000 rotor, ThermoScientific) at 6000 RPM for 30 min at 4 °C. The resultant supernatant was decanted into a clean 1-L flask, to which 100 g of Amberlite XAD-4 resin was added. The supernatant was shaken with the resin for 3 to 4 h at 4 °C, 150 rpm. The resin was then filtered from the supernatant and eluted with 90% methanol in ultrapure water, the eluent was concentrated under vacuum and stored at 4 °C. The concentrated eluent was separated by semi-preparative reverse-phase HPLC (250 × 20-mm YMC C18-AQ column, 7 mL/min flow rate), employing a gradient of methanol (+0.05% trifluoroacetic acid) in ultrapure water (+0.05% trifluoroacetic acid) of 50% to 100% over 40 minutes, yielding ~3 mg cupriachelin per L of culture.

5.2.3. Preparation of Fe(III)-Siderophore Reaction Mixtures

Fe(III)-siderophore solutions for photolysis were prepared with fresh 100 mM MOPS buffer pH adjusted to 7.2, siderophore stock solutions in ultrapure water (pacifibactin) or methanol (cupriachelin), standardized by Fe(III) titration, and 2.55 mM $Fe(NO_3)_3$ in dilute HNO_3 standardized spectrophotometrically with 1,10-phenanthroline using established procedures.[15] Fe(III)-pacifibactin solutions were prepared to final concentrations of 0.1 mM pacifibactin, 0.1 mM Fe(III) and 25 mM MOPS, diluted with ultrapure water. Fe(III)-cupriachelin solutions were prepared to final concentrations of 0.1 mM cupriachelin, 0.1 mM Fe(III) and 25 mM MOPS, diluted with ultrapure water and methanol for a final solvent ratio of 80% water and 20% methanol. Solutions were equilibrated for 24 h before photolysis. For photoreactions in the presence of 1,10-phenanthroline, aliquots of 10 mM 1,10-phenanthroline in MeOH were added to the 0.1 mM Fe(III)-siderophore solutions after the 24 h equilibration period. Solutions were prepared to final volumes of 2.5 mL (for analysis of photolysis at different time points) or 2.0 mL (for analysis of photolysis in the presence of phenanthroline).

5.2.4. Photolysis Conditions

Before photolysis, solutions were transferred to 3 mL quartz cuvettes (1 cm path length) with a stir bar and capped. Solutions were photolyzed with stirring using a 450W mercury arc lamp (Ace Glass, 40-48% output in UV) as the light source, with cuvettes placed on a stir plate at a consistent distance from the lamp. Progress of photolysis was monitored by UV-visible spectrophotometry on an Agilent Cary 300 UV Vis spectrophotometer scanning from 700-200 nm.

5.2.5. UPLC-ESIMS and ESIMS/MS Analysis of Photoreactions

Liquid chromatography-mass spectrometry analysis was carried out on a Waters Xevo G2-XS QTof with positive mode electrospray ionization coupled to an ACQUITY UPLC H-Class system with a Waters BEH C18 column. Fe(III)-pacifibactin photolysis samples were analyzed with a linear gradient of 0% to 30% CH_3CN (0.1% formic acid) in ddH_2O (0.1% formic acid) over 10 min, and Fe(III)-cupriachelin photolysis samples were analyzed with a linear gradient of 0% to 100% CH_3CN (0.1% formic acid) in ddH_2O (0.1% formic acid) over 10 min. ESIMS/MS analysis was carried out through data-independent targeted MS/MS methodology, specifying candidate molecular ions for MS/MS fragmentation. Molecular ions were fragmented with a collision energy ramp of 20-30 kEV (Fe(III)-pacifibactin photolysis samples) or 25-35 kEV (Fe(III)-cupriachelin photolysis samples).

5.3. Results and Interpretation

5.3.1. Characterization of New Pacifibactin Photoproducts

Buffered solutions of Fe(III)-pacifibactin (0.1 mM, 25 mM MOPS, pH 7.2) were photolyzed under continuous UV irradiation for 120 minutes, and aliquots were removed from the solution at various time points. Samples were then analyzed by UPLC-ESI-MS/MS to characterize putative photoproducts. Several molecular ions identified in the samples are consistent with sequential losses of CO_2 from the β-OHAsp residues of pacifibactin, further supported by MS/MS fragmentation patterns of the molecular ions. The molecular ion of 439 m/z (448 m/z, +H_2O adduct) is consistent with loss of one equivalent of CO_2 (**1,** Figures 5.2, 5.3, 5.4), and MS/MS fragments observed are consistent only with CO_2 loss localized to the L-*threo* β-OHAsp residue (N-terminal side) of pacifibactin. The molecular ion of 416 m/z (425

m/z, +H_2O adduct, 434 m/z, +2H_2O adduct) is consistent with loss of two equivalents of CO_2 (**2,** Figures 5.2, 5.3, 5.5). The molecular ion of 402 m/z (411 m/z, +H_2O adduct) is consistent with the loss of two equivalents of CO_2 and one equivalent of CO (**3,** Figures 5.2, 5.3, 5.6), and MS/MS fragmentation is only consistent with loss of CO at the position of the D-*threo* β-OHAsp residue (C-terminal side). The molecular ion of 388 m/z is consistent with loss of two equivalents of CO_2 and loss of two equivalents of CO (**4,** Figures 5.2, 5.7, 5.8).

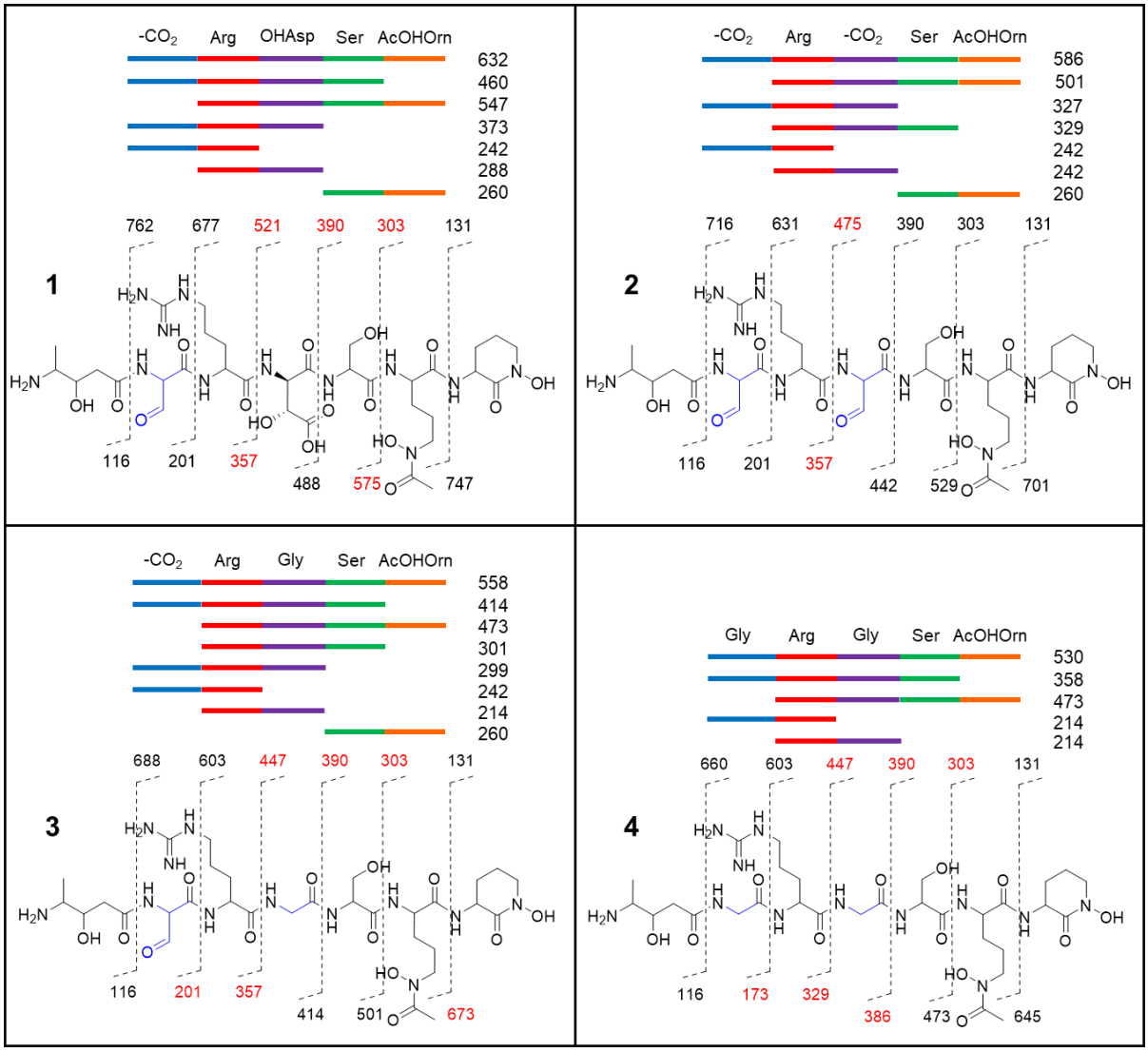

Figure 5.2. Pacifibactin photoproducts identified by ESI-MS/MS. Residues exhibiting photolytic decomposition are colored in blue. Peptide b/y fragmentation patterns are shown with each chemical structure, and the numbers listed represent the mass of each fragment (m/z values listed in red represent fragments not observed). The blocks above each chemical structure represent observed internal fragments. The propensity of pacifibactin to internally fragment has been observed previously.

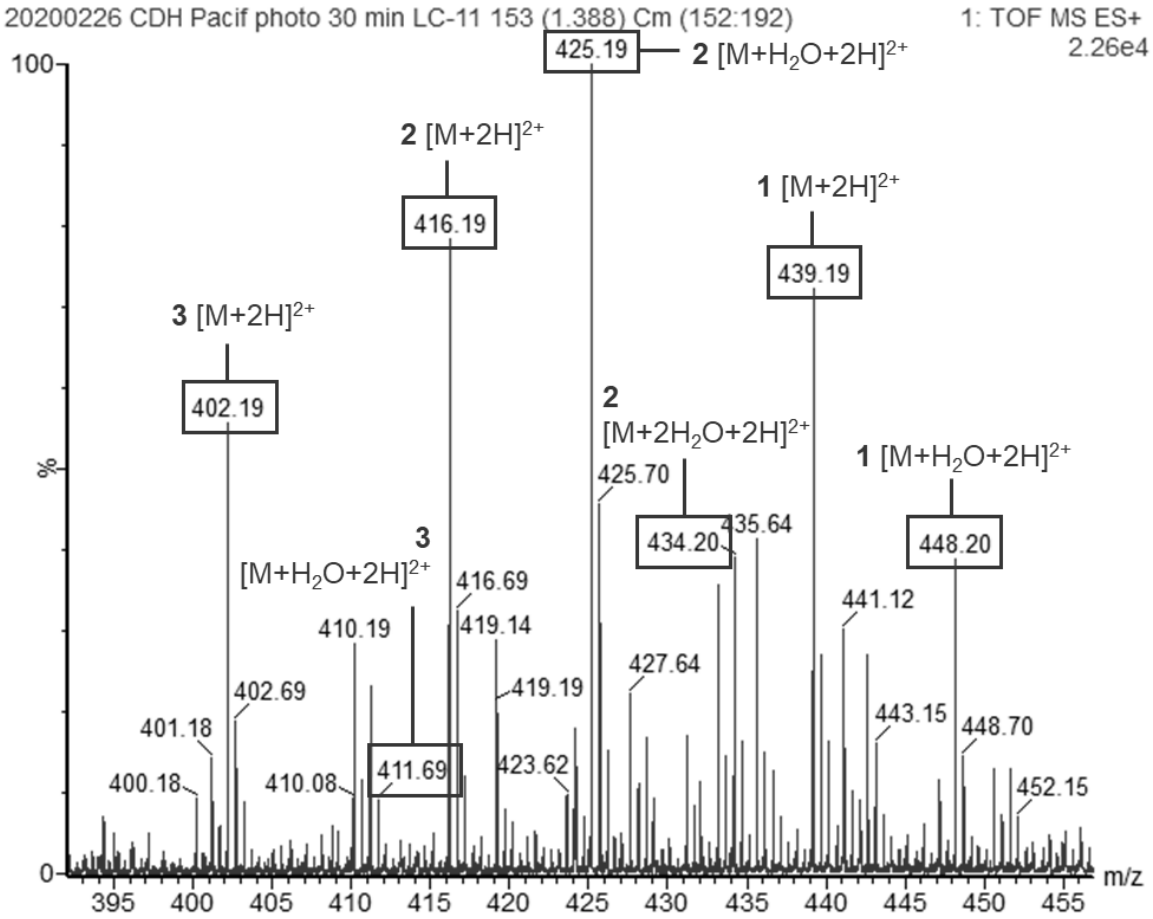

Figure 5.3. Positive-mode ESI-MS spectrum of pacifibactin photoproducts **1-3** molecular ions detected after 30 minutes of irradiation of 0.1 mM Fe(III)-pacifibactin in 25 mM MOPS buffer.

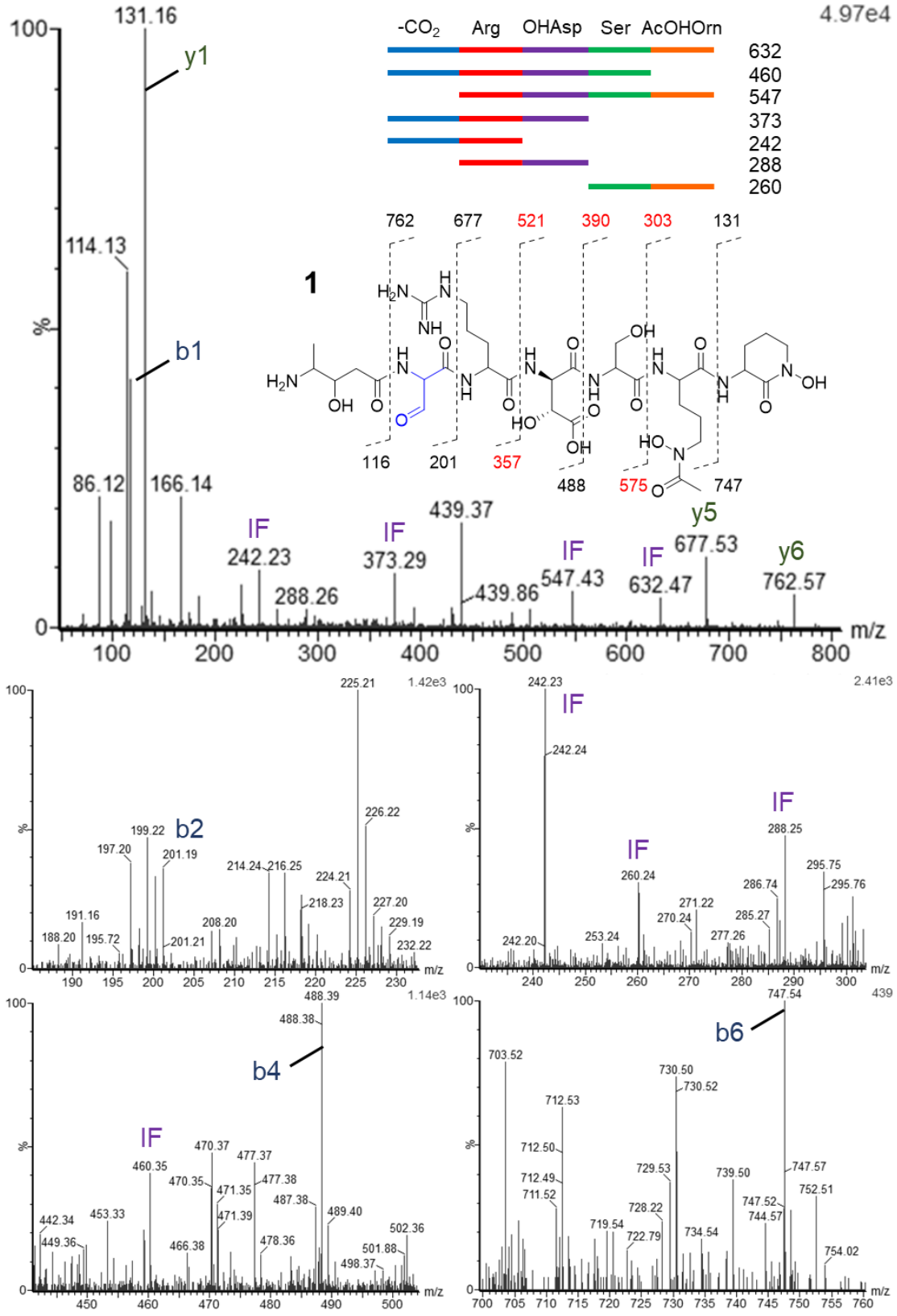

Figure 5.4. Positive mode ESI-MS/MS spectrum of pacifibactin photoproduct **1**: 439 m/z, $[M+2H]^{2+}$.

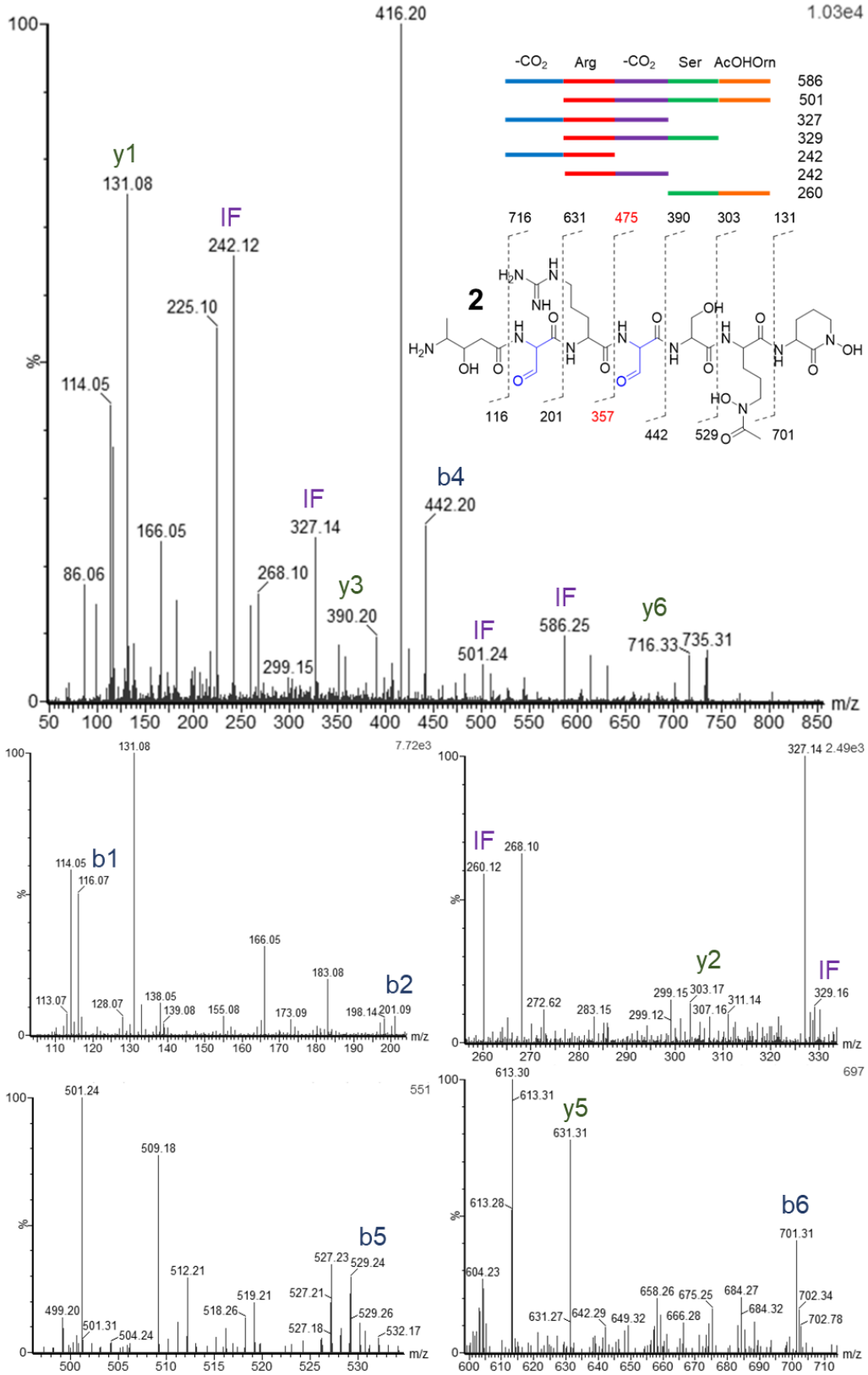

Figure 5.5. Positive mode ESI-MS/MS spectrum of pacifibactin photoproduct **2**: 416 m/z, $[M+2H]^{2+}$.

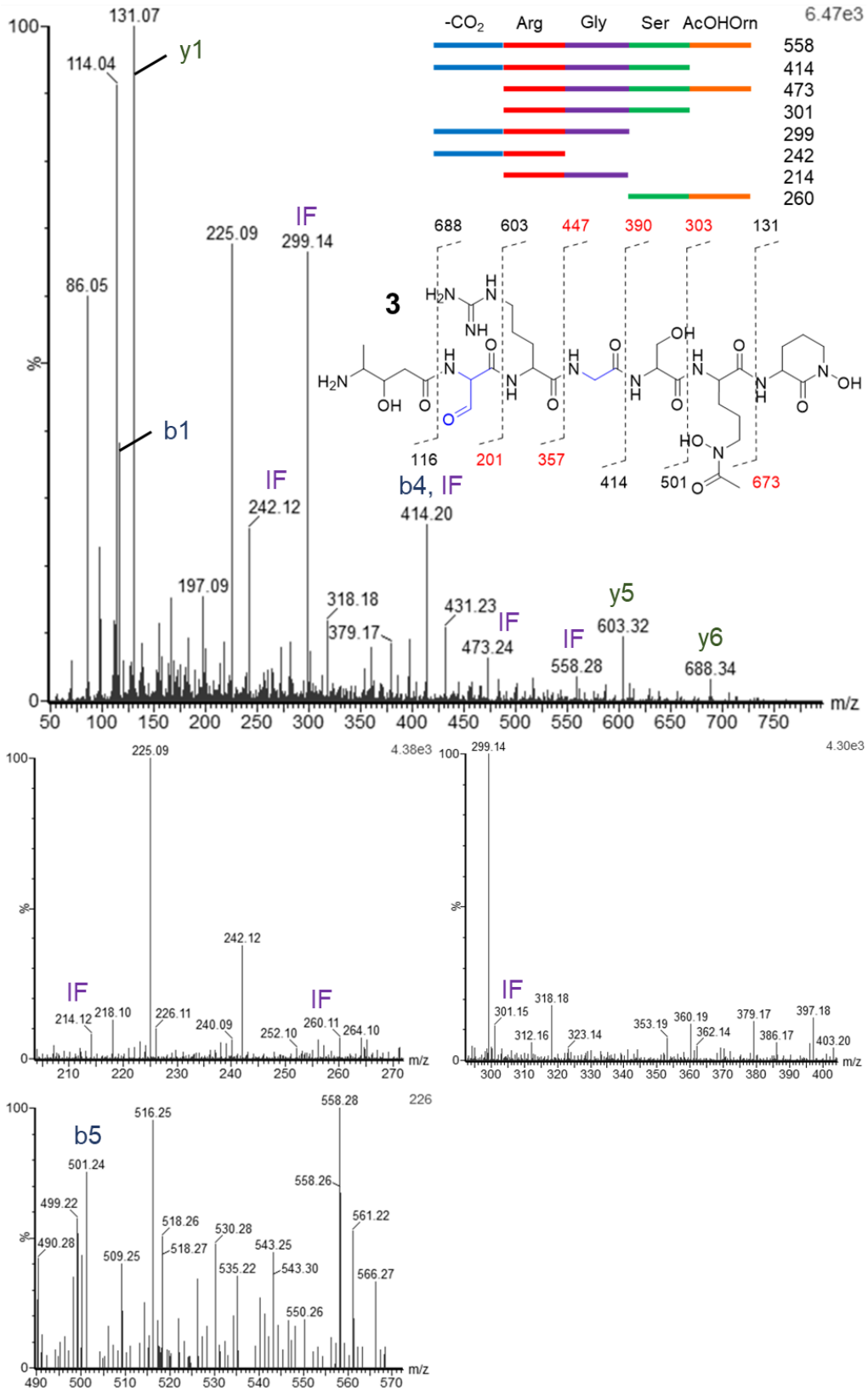

Figure 5.6. Positive mode ESI-MS/MS spectrum of pacifibactin photoproduct **3**: 402 m/z, $[M+2H]^{2+}$.

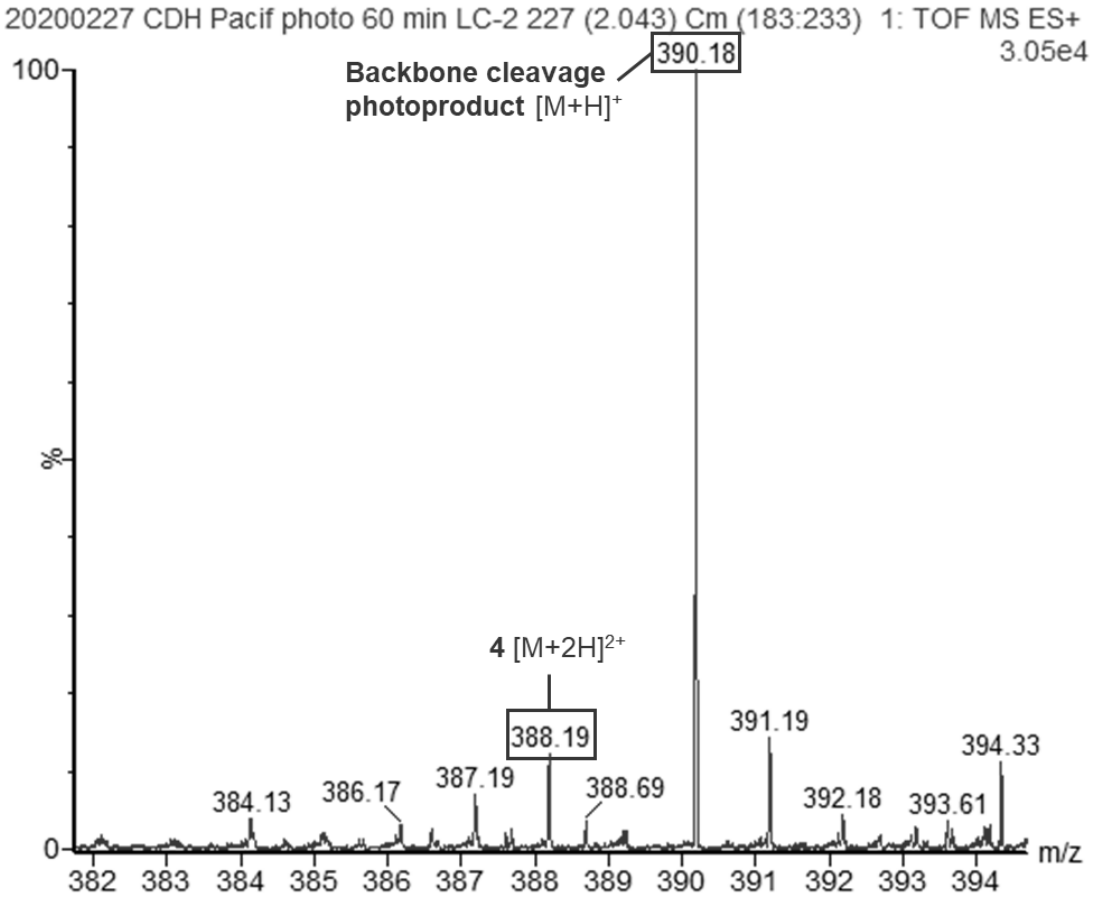

Figure 5.7. Positive-mode ESI-MS spectrum of pacifibactin photoproduct **4** and backbone cleavage photoproduct molecular ions detected after 30 minutes of irradiation of 0.1 mM Fe(III)-pacifibactin in 25 mM MOPS buffer.

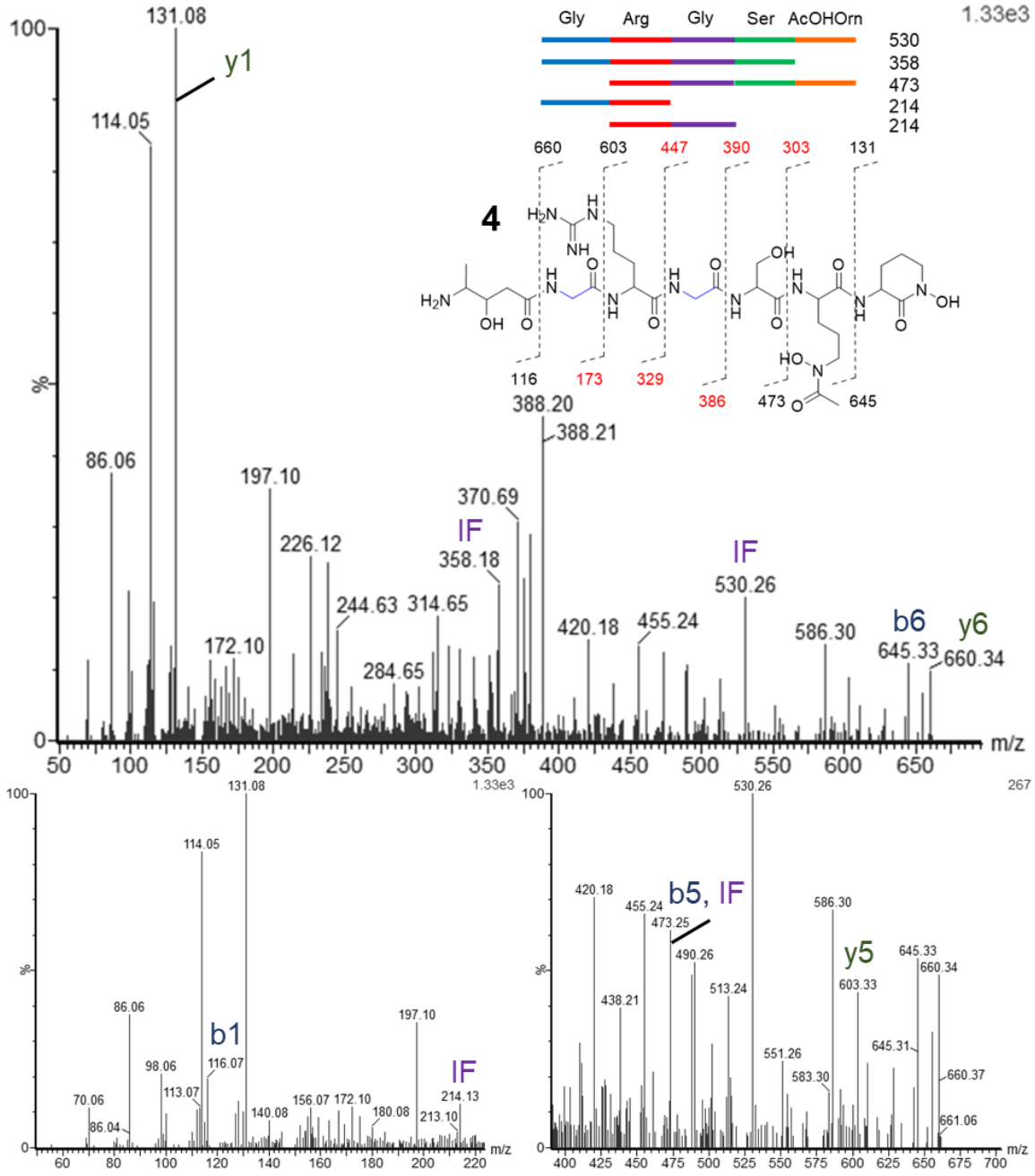

Figure 5.8. Positive mode ESI-MS/MS spectrum of pacifibactin photoproduct **8**: 388 m/z, $[M+2H]^{2+}$.

5.3.2. Characterization of New Cupriachelin Photoproducts

UPLC-ESI-MS/MS analysis of Fe(III)-cupriachelin samples (0.1 mM, 25 mM MOPS 7.2) revealed a set of photoproducts mirroring those observed in pacifibactin samples. The molecular ion of 762 m/z (780 m/z, $+H_2O$ adduct) is consistent with loss of one equivalent of CO_2 from cupriachelin at a β-OHAsp residue (**5** and **6,** Figures 5.9, 5.10, 5.11). MS/MS fragments consistent with loss of CO_2 at either the L-*erythro* (**5**) or L-*threo* (**6**) β-OHAsp residue are observed. The molecular ion of 716 m/z (734 m/z, $+H_2O$ adduct, 752 m/z, $+2H_2O$ adduct) is consistent with loss of two equivalents of CO_2 from cupriachelin, with the losses occurring at each β-OHAsp residue (**7,** Figures 5.9, 5.10, 5.12). The molecular ion of 688 m/z (706 m/z, $+H_2O$ adduct) is consistent with loss of two equivalents of CO_2 from β-OHAsp residues of cupriachelin and an additional loss of one equivalent of CO from one of the β-OHAsp residue positions (**8** and **9**, Figures 5.9, 5.10, 5.13). MS/MS fragmentation is consistent with loss of an additional equivalent of CO at either β-OHAsp residue position. The molecular ion of 660 m/z is consistent with loss of two equivalents of CO_2 and loss of two equivalents of CO (**10**, Figures 5.9, 5.10, 5.14), however the very low abundance of the product prevented quality MS/MS confirmation of the structure, with many expected b/y fragments not observed.

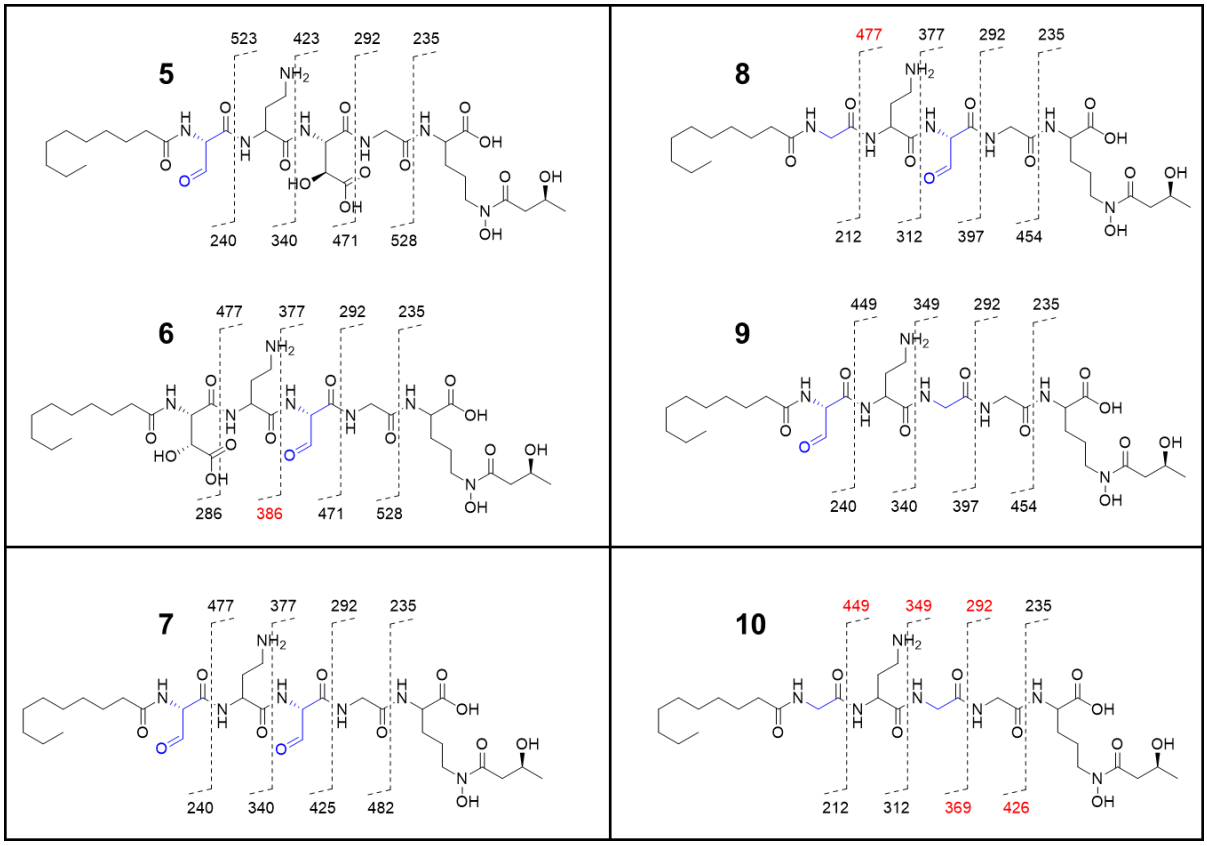

Figure 5.9. Cupriachelin photoproducts identified by ESI-MS/MS. Residues exhibiting photolytic decomposition are colored in blue. Peptide b/y fragmentation patterns are shown with each chemical structure, and the numbers listed represent the mass of each fragment (m/z values listed in red represent fragments not observed).

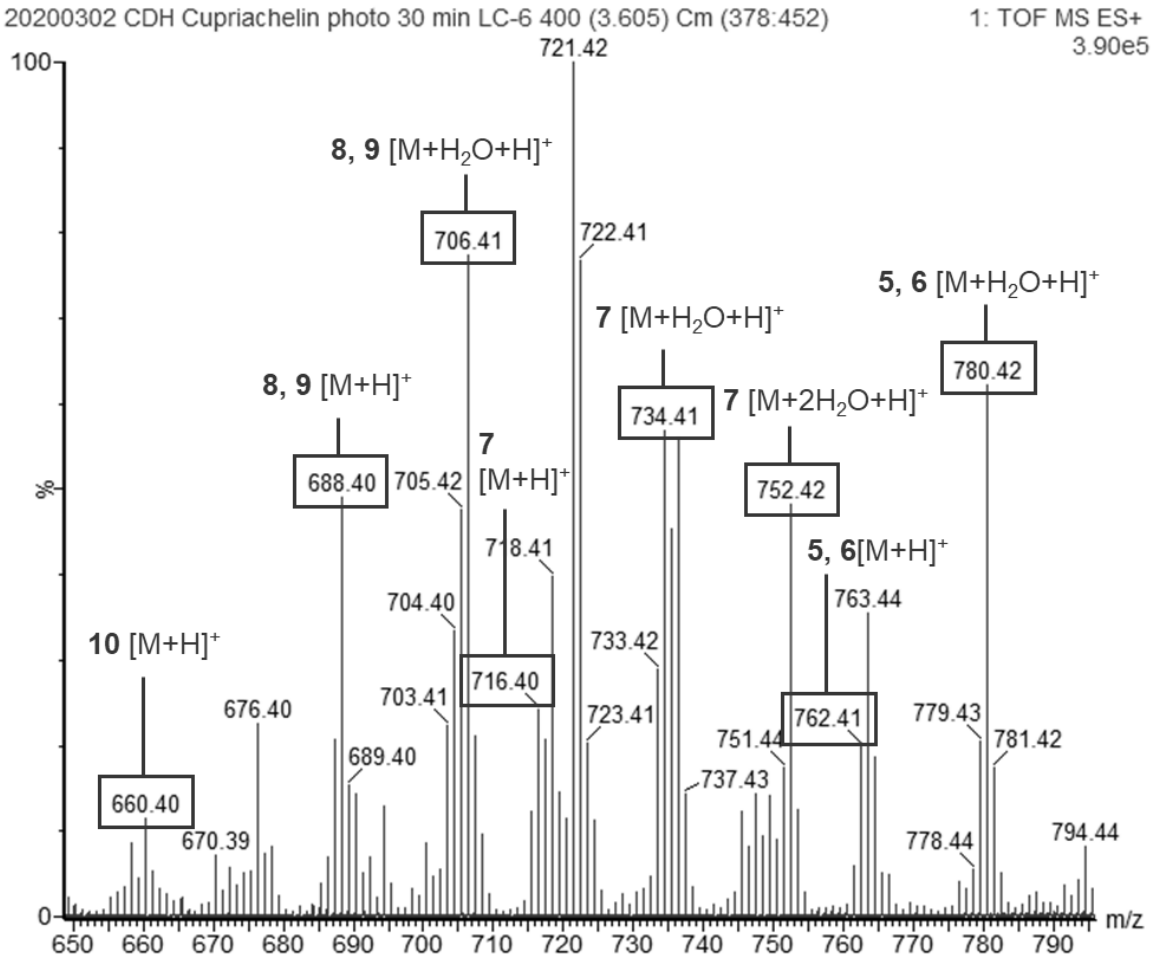

Figure 5.10. Positive-mode ESI-MS spectrum of cupriachelin photoproducts **5-10** molecular ions detected after 30 minutes of irradiation of 0.1 mM Fe(III)-cupriachelin in 25 mM MOPS buffer.

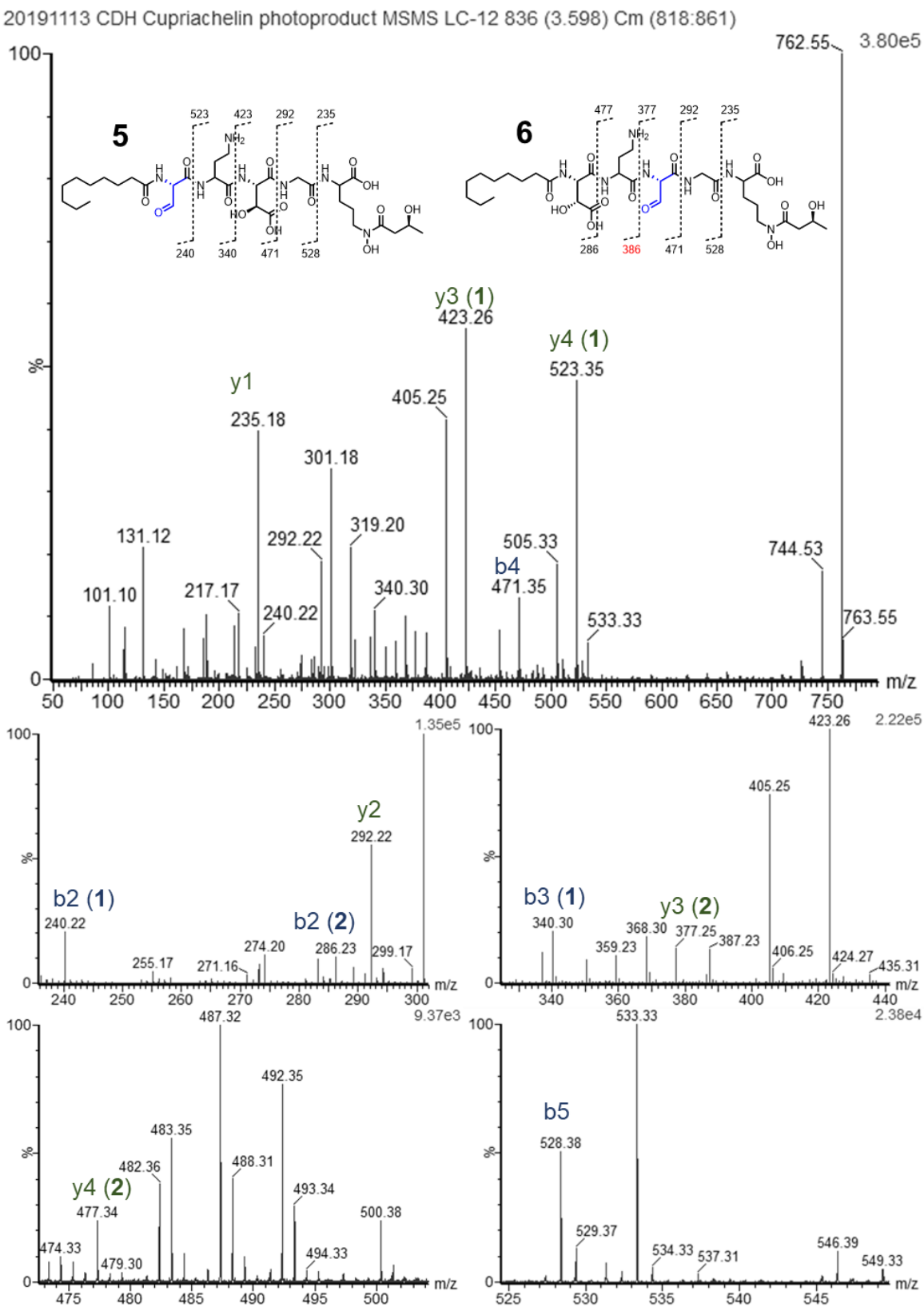

Figure 5.11. Positive mode ESI-MS/MS spectrum of cupriachelin photoproducts **5** and **6**: 762 m/z, $[M+H]^+$.

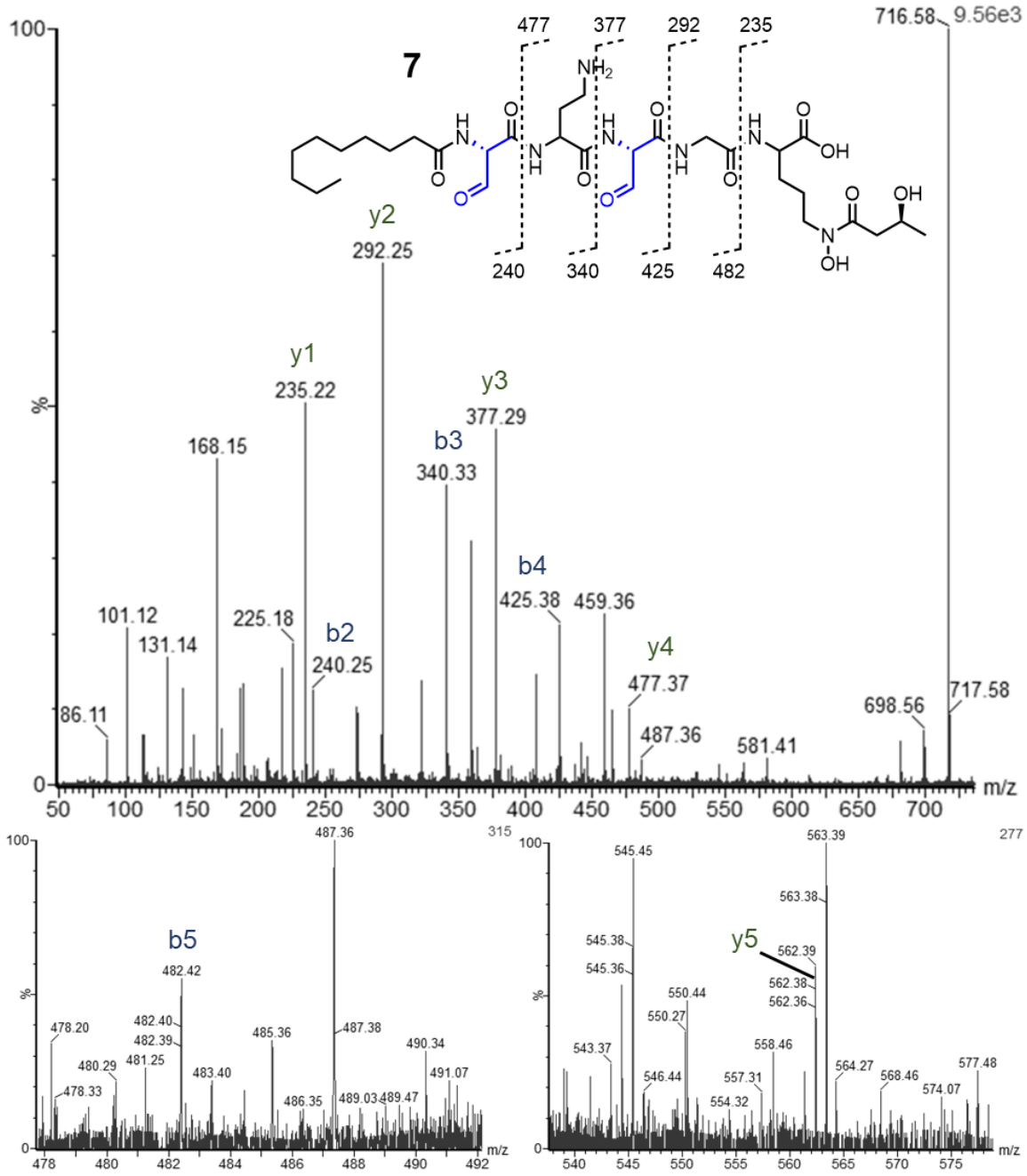

Figure 5.12. Positive mode ESI-MS/MS spectrum of cupriachelin photoproduct **7**: 716 m/z, $[M+H]^+$.

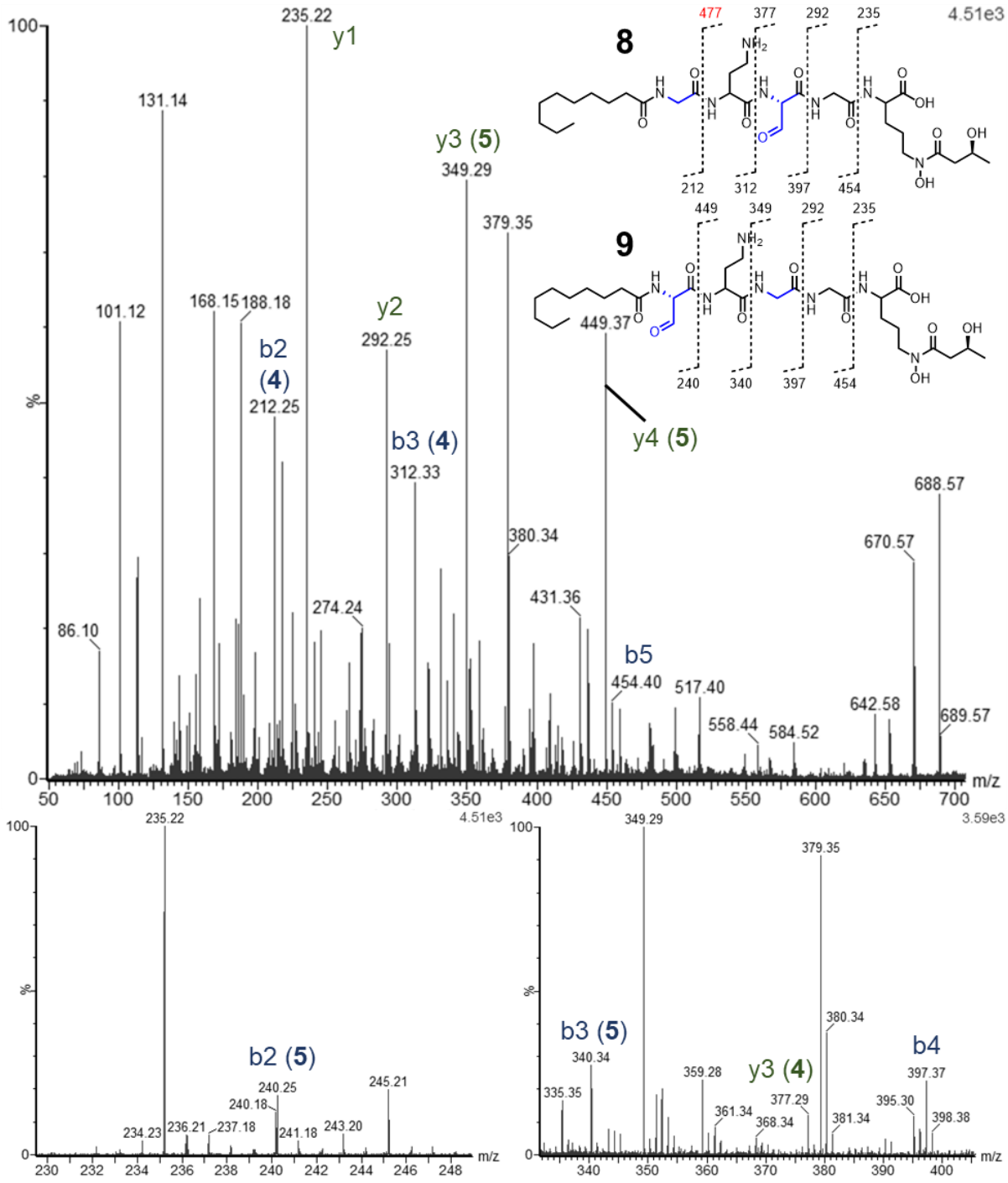

Figure 5.13. Positive mode ESI-MS/MS spectrum of cupriachelin photoproducts **8** and **9**: 688 m/z, $[M+H]^+$.

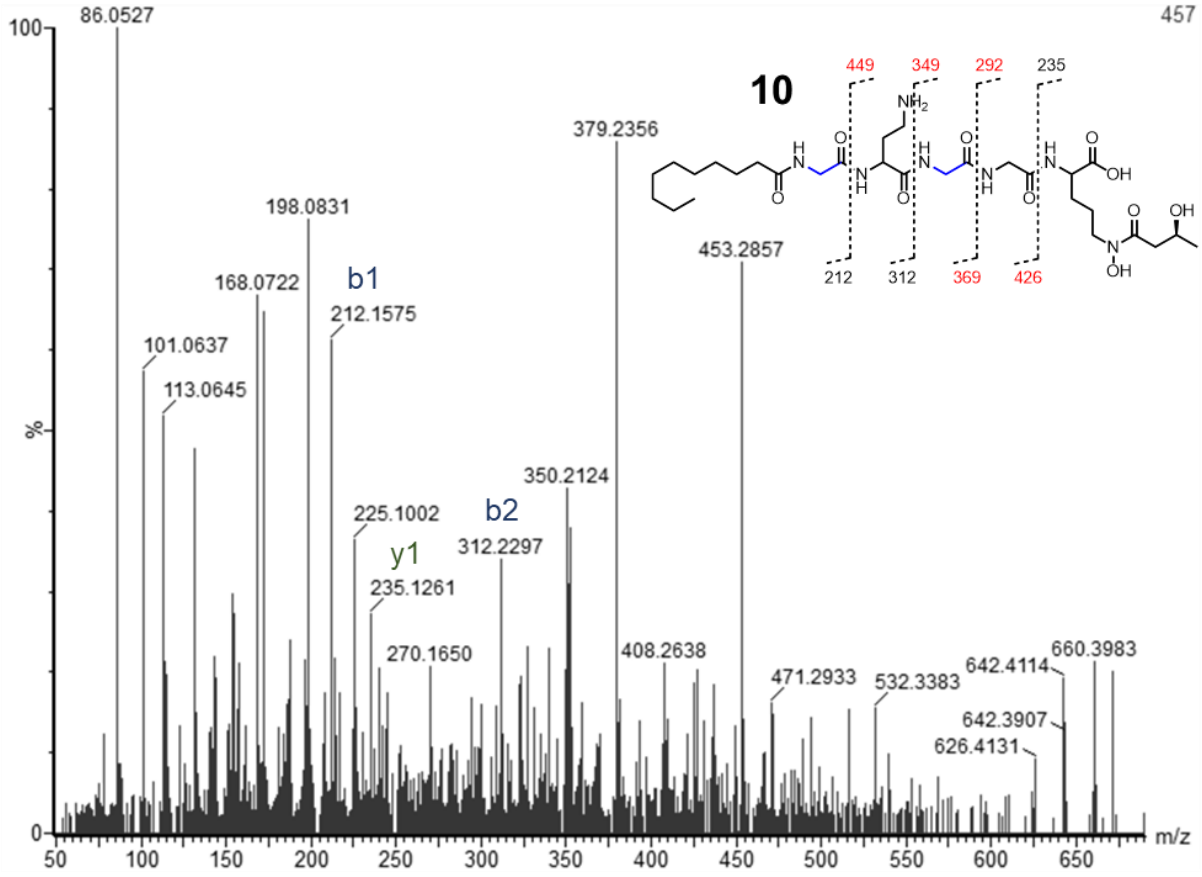

Figure 5.14. Positive mode ESI-MS/MS spectrum of cupriachelin photoproduct **10**: 688 m/z, $[M+H]^+$.

5.3.3. Shifts in Photoproduct Abundance Over Time

The identification of multiple new photoproducts of both Fe(III)-pacifibactin and Fe(III)-cupriachelin, as well as sampling the photoreactions at multiple irradiation time points, allowed for investigations into relative photoproduct abundance over time. Extracted ion chromatograms of each pacifibactin photoproduct identified in this study along with the peptide backbone cleavage photoproduct (390 m/z, Figure 5.6) previously described in chapter 2, from UPLC-ESIMS analysis of 0.1 mM Fe(III)-pacifibactin after 10, 20, 30, 60, and 120 minutes of irradiation, were plotted (Figure 5.15). At 10 minutes of irradiation, the abundance of **1** (corresponding to loss of one CO_2 equivalent from pacifibactin), as measured by ion count,

is greater than the other photoproducts. As irradiation time increases, the abundance of **1** decreases relative to **2** (-2CO_2) and **3** (-2CO_2, -1CO), and after 30 minutes of irradiation **2** is the predominant product, with significant amounts of **1** and **3** detected. After 60 minutes of irradiation, the predominant photoproduct is the backbone cleavage photoproduct, and after 120 minutes the backbone cleavage photoproduct is an order of magnitude more abundant than all other photoproducts. While **4** exhibited measurable abundance, peaking at 30 minutes of irradiation, its abundance remained far below all other measured photoproducts at every time point. From the aliquot analysis, two trends are readily apparent. **1** is the first photoproduct to arise, but steadily decreases in abundance as a function of irradiation time. Conversely, the backbone cleavage photoproduct initially exhibits low abundance relative to other photoproducts, but as irradiation time increases, it becomes the only detectable photoproduct in the reaction mixture. These results support a sequential photoreaction pathway model, where initial breakdown of the ligand manifests as loss of one or multiple equivalents of CO_2, with more extensive backbone cleavage only upon further irradiation.

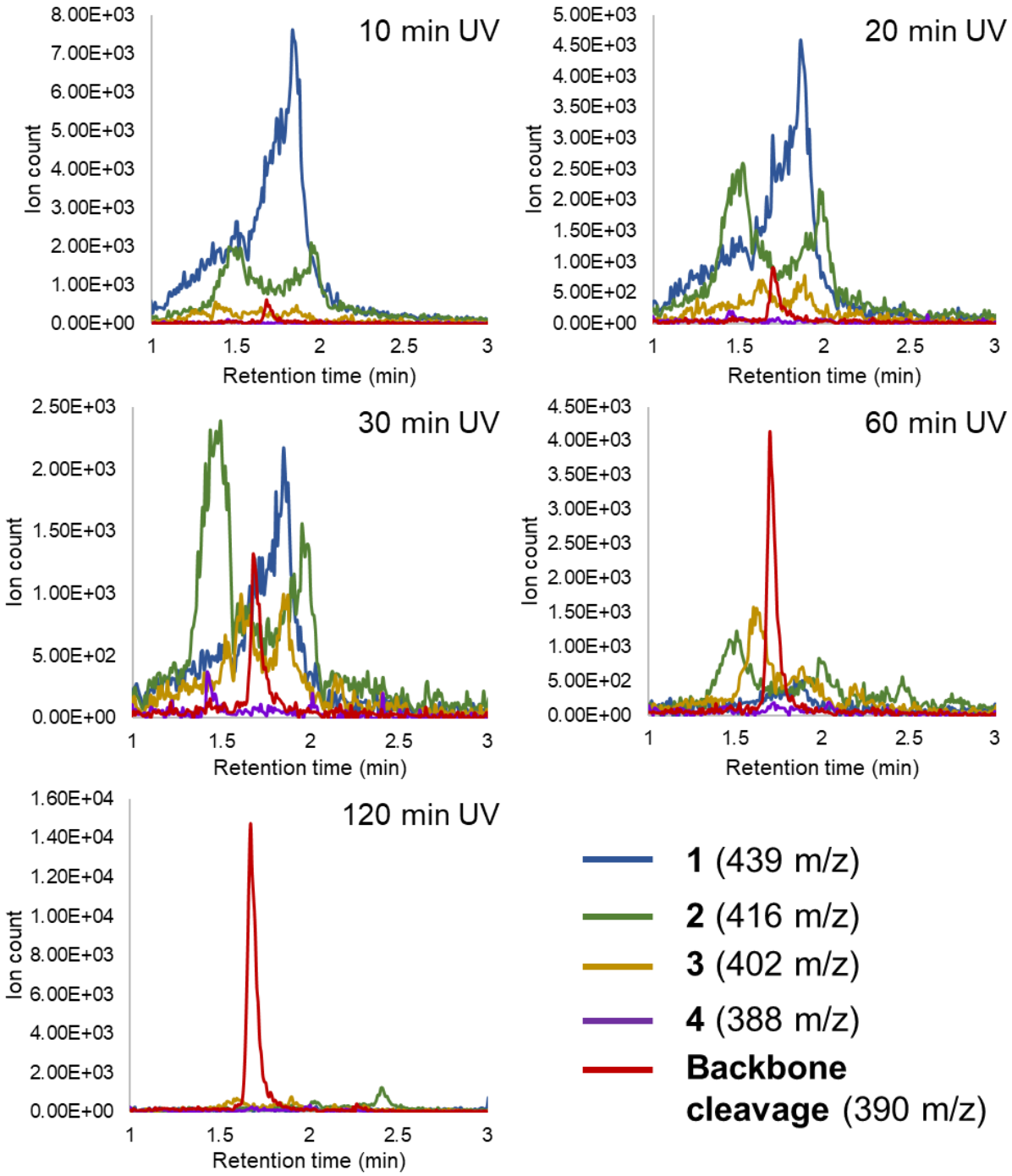

Figure 5.15. Extracted ion chromatograms of pacifibactin photoproducts **1-4** and backbone cleavage photoproduct from UPLC-ESIMS analysis of 0.1 mM Fe(III)-pacifibactin in 25 mM MOPS pH 7.2 after 10, 20, 30, 60, and 120 minutes of irradiation from a 450W UV lamp. In samples with less irradiation time, abundance of **1** predominates while in samples with greater length of irradiation time the backbone cleavage product predominates.

Photoproduct abundance in the Fe(III)-cupriachelin photoreaction was also measured by UPLC-ESIMS. However, the previously reported cupriachelin peptide backbone cleavage photoproduct at 320 m/z[9] was not detected at any time points. Several masses that could correspond to other peptide backbone cleavage photoproducts were detected, and candidate molecular ions were characterized by MS/MS. Two molecular ions at 403 m/z and 357 m/z are consistent with N-terminal cupriachelin backbone cleavage photoproducts (Figure 5.16). Several fragments were identified by MS/MS to further support the proposed structures, however the fragments observed mostly corresponded to b/y fragments with various losses of NH_3, H_2O and CO (Figures 5.17, 5.18), complicating structural assignment of the products.

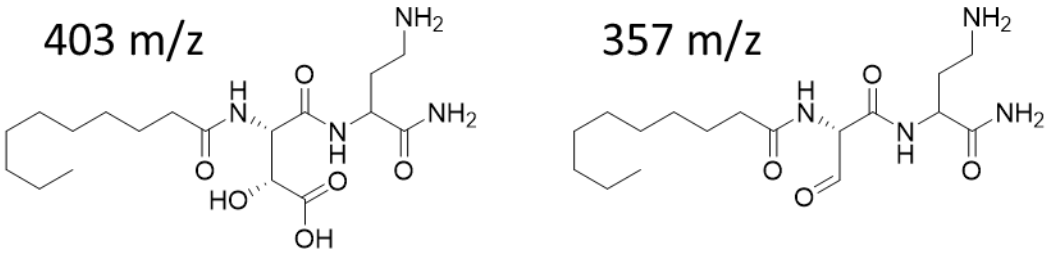

Figure 5.16. Putative N-terminal peptide backbone cleavage photoproducts identified from Fe(III)-cupriachelin photoreaction samples.

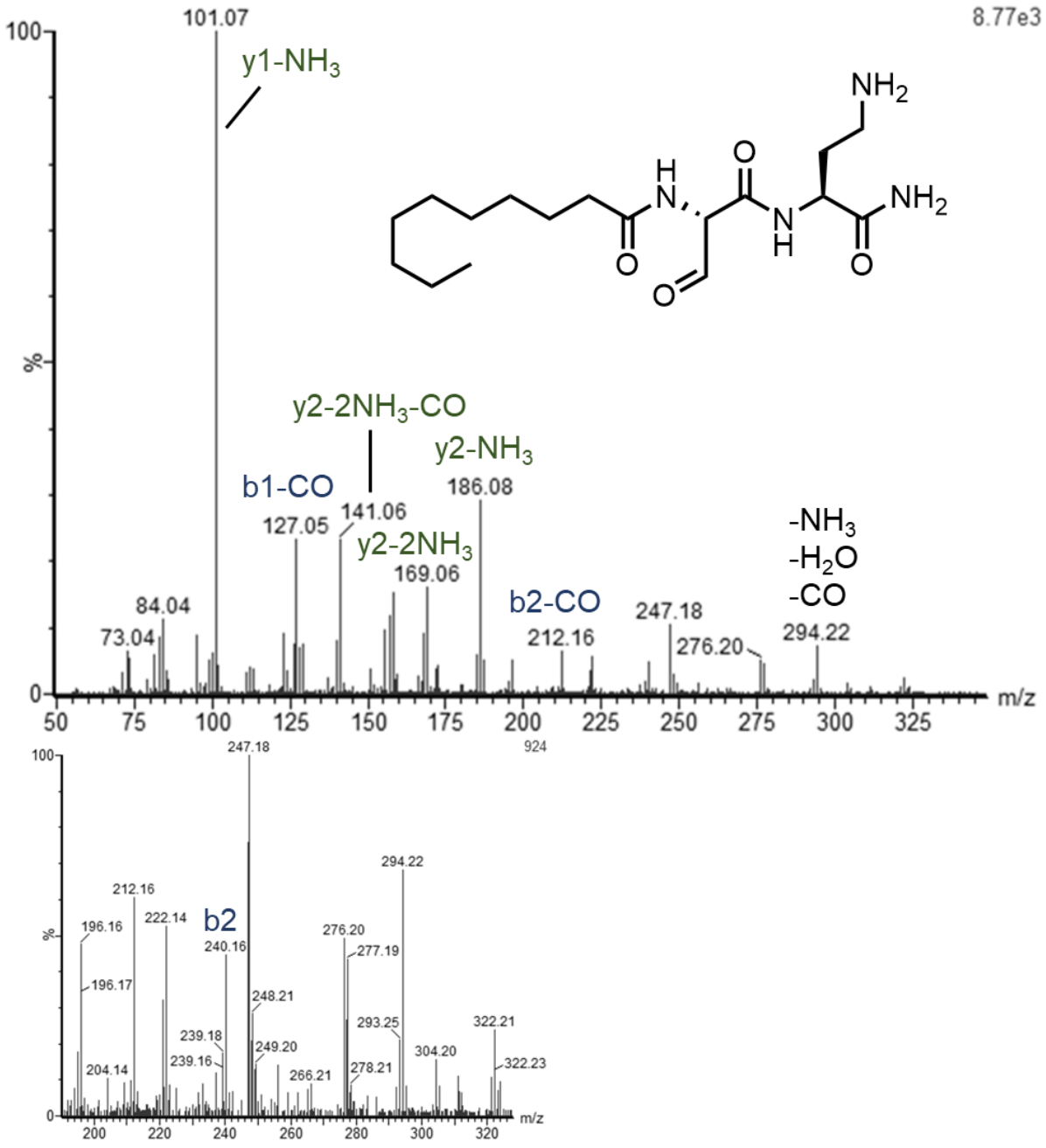

Figure 5.17. ESIMS/MS spectrum of 403 m/z molecular ion detected in Fe(III)-cupriachelin photoreactions. Fragmentation observed is consistent with a peptide backbone cleavage structure.

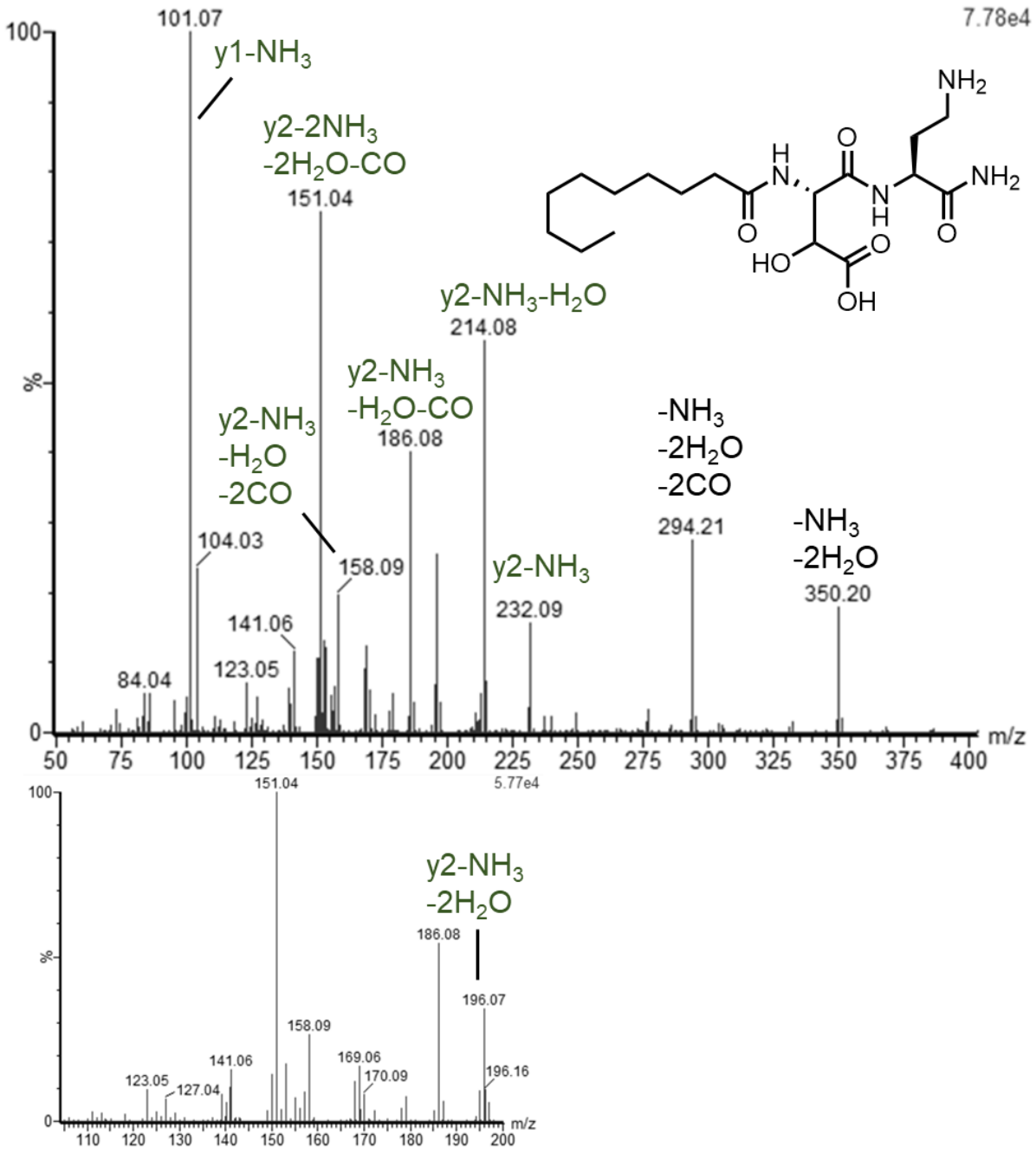

Figure 5.18. ESIMS/MS spectrum of 403 m/z molecular ion detected in Fe(III)-cupriachelin photoreactions. Fragmentation observed is consistent with a peptide backbone cleavage structure and loss of one equivalent of CO_2 from the β-OHAsp residue.

Extracted ion chromatograms of cupriachelin photoproduct molecular ions after 10, 20, 30, 60, and 120 minutes of irradiation were plotted (Figure 5.19). At 10 minutes of irradiation, **5** and **6** (-1CO_2) showed much higher abundance than **7-10**, like the observations from photolysis

of Fe(III)-pacifibactin. Relative abundances of photoproducts **5-10** closely track with the results from pacifibactin as irradiation time increases, as the **7** ($-2CO_2$), **8** and **9** ($-2CO_2$, -1CO) molecular ions outnumber those of **5** and **6** after 30 minutes of irradiation. Relative abundance of the peptide backbone photoproducts over time, however, differs from the pattern observed in Fe(III)-pacifibactin photolysis. At 10 minutes of irradiation, the abundance of the cupriachelin 403 m/z backbone cleavage photoproduct is greater than the abundance of any other photoproduct, including **5** and **6** (corresponding to loss of one CO_2). After 20 minutes of irradiation, both putative backbone cleavage photoproducts are higher in abundance than photoproducts **5-10**. As irradiation time increases, the abundance of 357 m/z first matches, then increases relative to that of 403 m/z. As the 357 m/z photoproduct corresponds with a loss of CO_2 from the 403 m/z product, this change in relative abundance could be triggered by photolysis of an Fe(III) complex of the 403 m/z photoproduct, which appears to contain an intact β-OHAsp ligand. The early and consistent relative abundance dominance of the cupriachelin backbone cleavage photoproducts is a stark contrast to the pattern observed in pacifibactin photoproduct abundance. This result calls into question whether decarboxylation always precedes photolytic peptide backbone cleavage, and potentially indicates variable reactivity among Fe(III) complexes of different β-OHAsp siderophores.

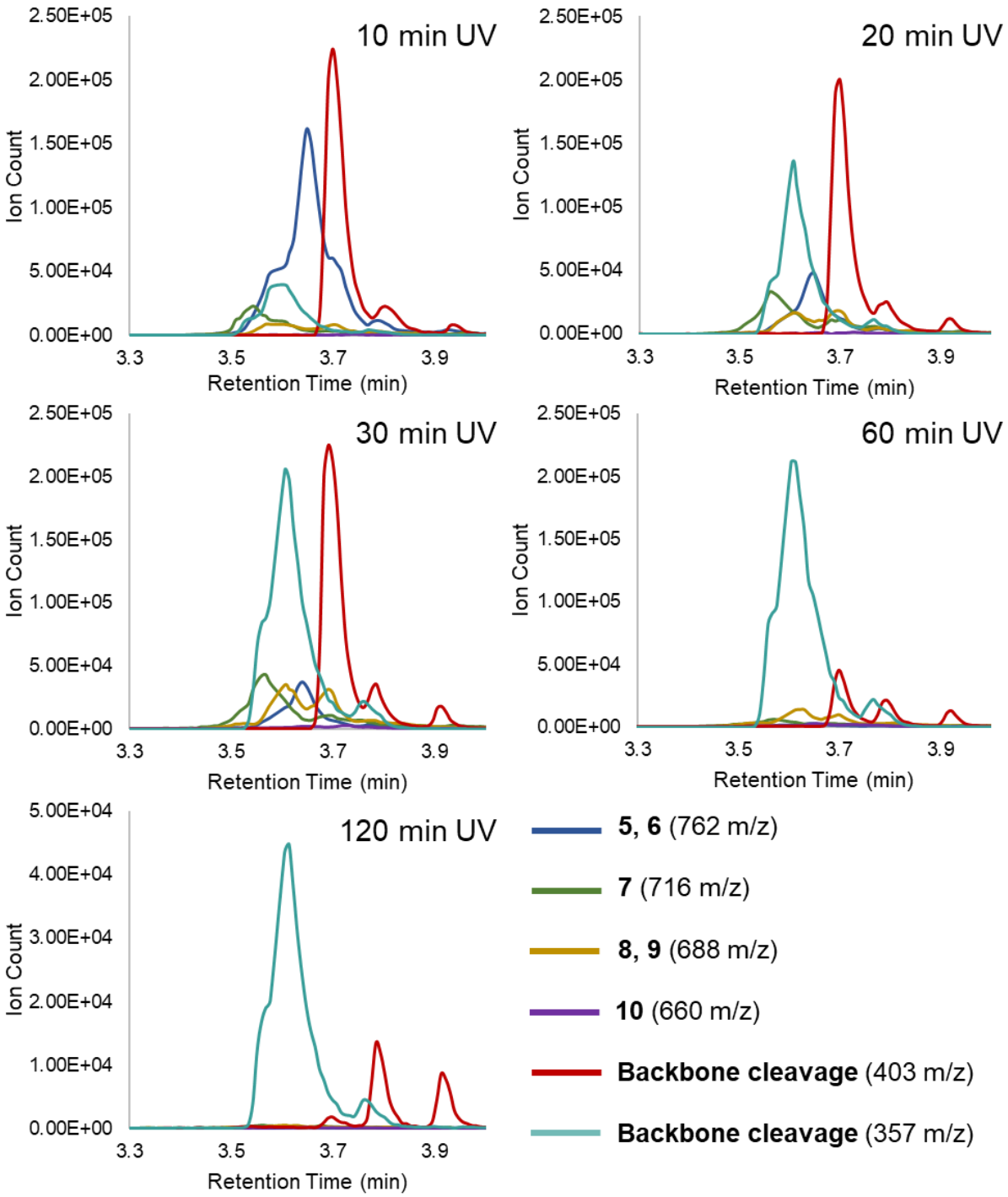

Figure 5.19. Extracted ion chromatograms of cupriachelin photoproducts **5-10** and putative backbone cleavage photoproducts from UPLC-ESIMS analysis of 0.1 mM Fe(III)-cupriachelin in 25 mM MOPS pH 7.2 after 10, 20, 30, 60, and 120 minutes of irradiation. Backbone cleavage photoproducts quickly outpace other photoproducts as irradiation time increases.

5.3.4. Changes in Photoproduct Abundance from Addition of Phenanthroline

To better understand how Fe(III)-cupriachelin and Fe(III)-pacifibactin photoreactions proceed, we searched for a way to modulate or control reaction conditions to selectively access the "initial" photoproducts of reach reaction. 1,10-Phenanthroline (phen) is a noted effective chelator of Fe(II), slowing the rate of Fe(II) oxidation in neutral, oxidative environments. *Grabo et al* determined that irradiation of a Fe(III)-α-hydroxycarboxylic acid complex in the presence of excess phen results in relatively less oxidative breakdown of the α-OH-carboxylic acid ligand.[13] To slow the rate of Fe(II) oxidation, and thus better observe the initial reaction products of Fe(III)-pacifibactin photolysis, a solution of Fe(III)-pacifibactin with excess phen (0.1 mM Fe(III)-siderophore, 0.6 mM phen, 25 mM MOPS pH 7.2) was prepared and irradiated for 3 h. Upon irradiation the solution turned a dark red color, indicative of complexation of Fe(II) by phenanthroline, and the UV-visible absorbance spectrum of the solution was consistent with the absorbance spectrum of $Fe^{II}(phen)_3$ (λ_{max} of 510 nm, Figure 5.20).

The irradiated sample was then analyzed by UPLC-ESIMS and extracted ion chromatograms of photoproduct molecular ions were plotted (Figure 5.21). After 3 h of irradiation in the presence of phen, the abundance of **1** (-1CO_2) far exceeds any other photoproduct, with ion counts several-fold higher than **2**, the photoproduct with the next largest abundance (Figure 5.21). The results suggest that upon photolysis of Fe(III)-pacifibactin, there is initial near-clean conversion of the intact ligand to **1**, further supporting a photolysis pathway for Fe(III)-pacifibactin that begins with decarboxylation.

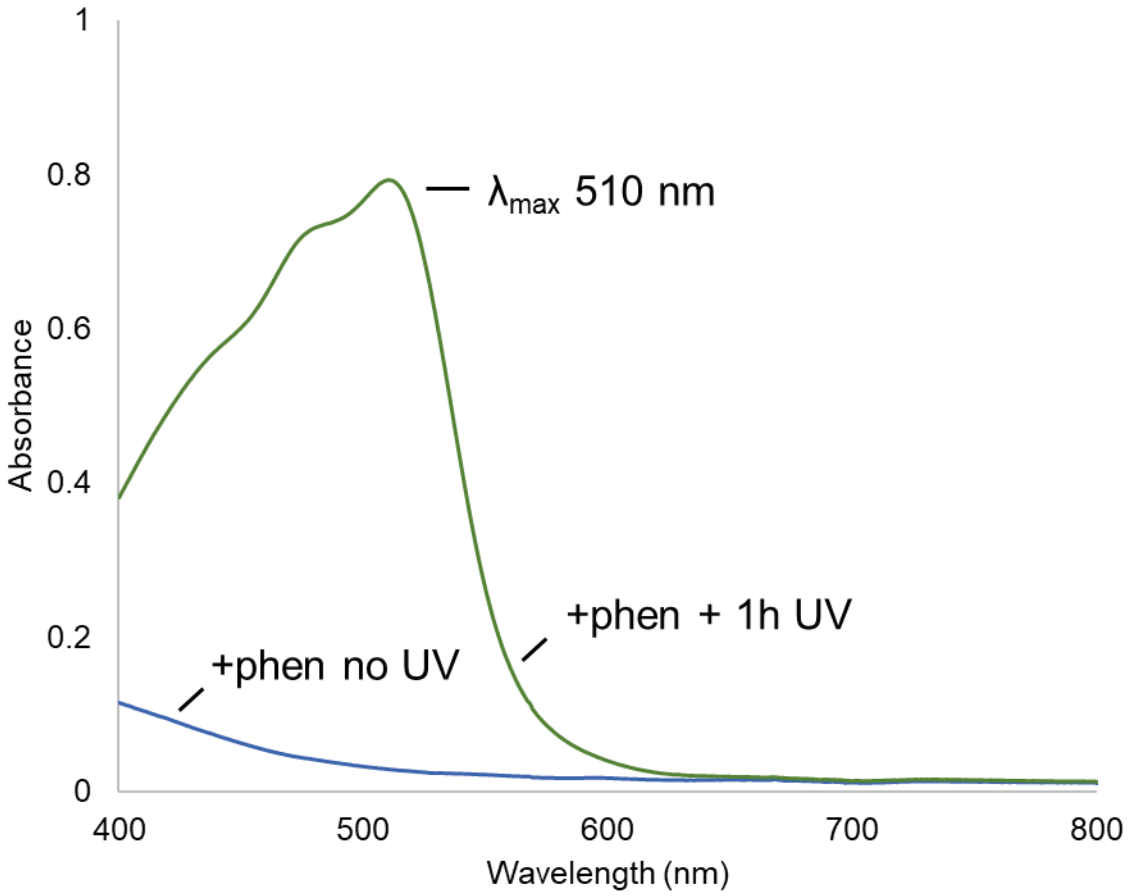

Figure 5.20. UV-visible absorbance spectrum of Fe(III)-cupriachelin (0.1 mM, 25 mM MOPS) in presence of 0.6 mM phenanthroline, before UV irradiation and after 1 h UV irradiation. After irradiation, a broad absorbance band with λ_{max} of 510 nm arises, characteristic of $Fe^{II}(phen)_3$ complex formation.

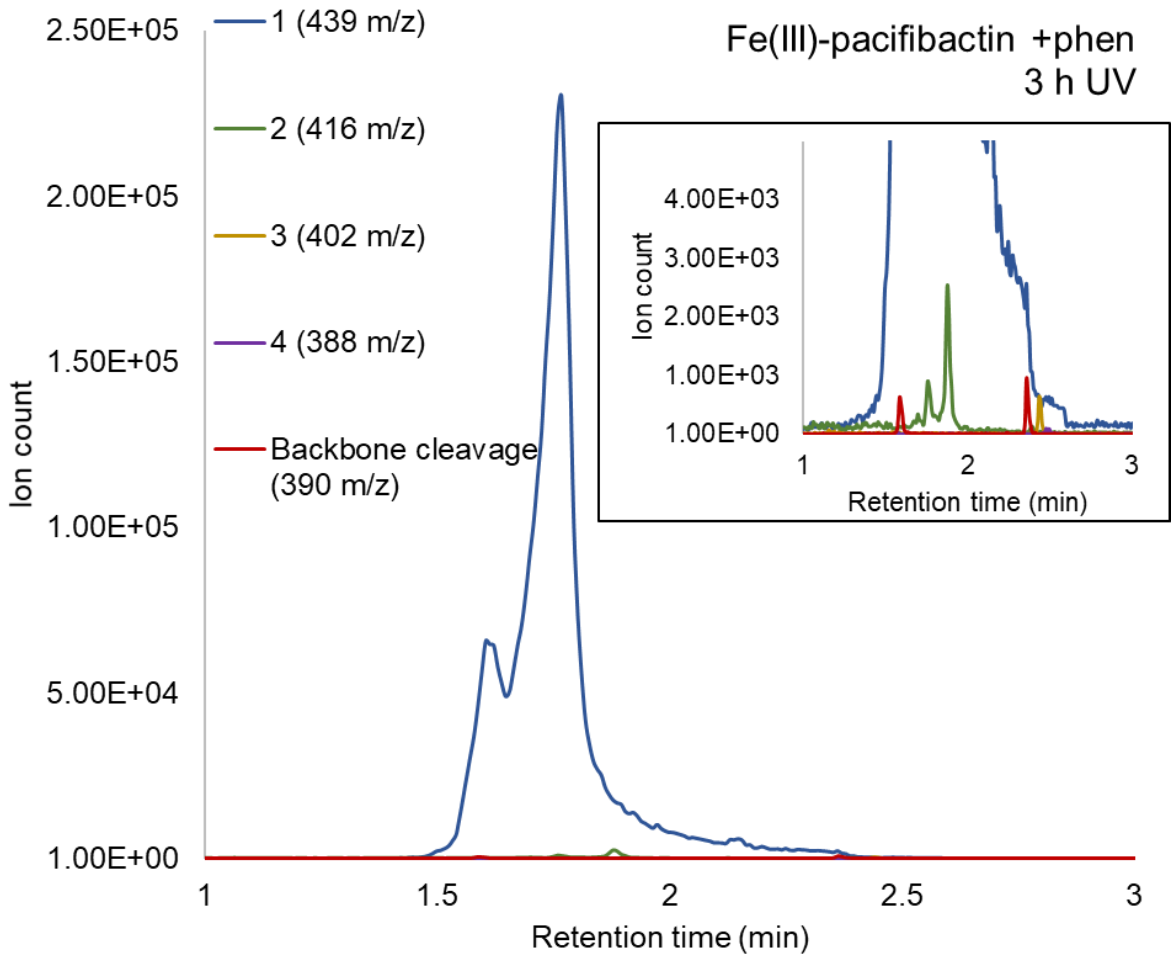

Figure 5.21. Extracted ion chromatograms of pacifibactin photoproducts **1-4** and backbone cleavage photoproduct from UPLC-ESIMS analysis of 0.1 mM Fe(III)-pacifibactin 0.6 mM phen after 3 h of irradiation. Abundance of **1** far exceeds abundance of all other photoproducts.

Photolysis of Fe(III)-cupriachelin in the presence of phen was then carried out under the same conditions (0.1 mM Fe(III)-cupriachelin, 0.6 mM phen, 25 mM MOPS pH 7.2, 3 h irradiation), and the resulting solution was analyzed by UPLC-ESIMS. As with Fe(III)-pacifibactin photolysis in the presence of phen, the abundance of **5** and **6** (-1CO_2) is greater than other photoproducts (Figure 5.22). However, a significant amount of the 403 m/z backbone cleavage product was also detected. While the possibility of direct conversion from intact cupriachelin to the backbone cleavage product cannot be ruled out given the significant abundance of the backbone cleavage product detected, the predominance of **5** and **6** supports

a photolysis pathway beginning with loss of CO_2 (as with pacifibactin), but followed by a very rapid peptide backbone cleavage reaction.

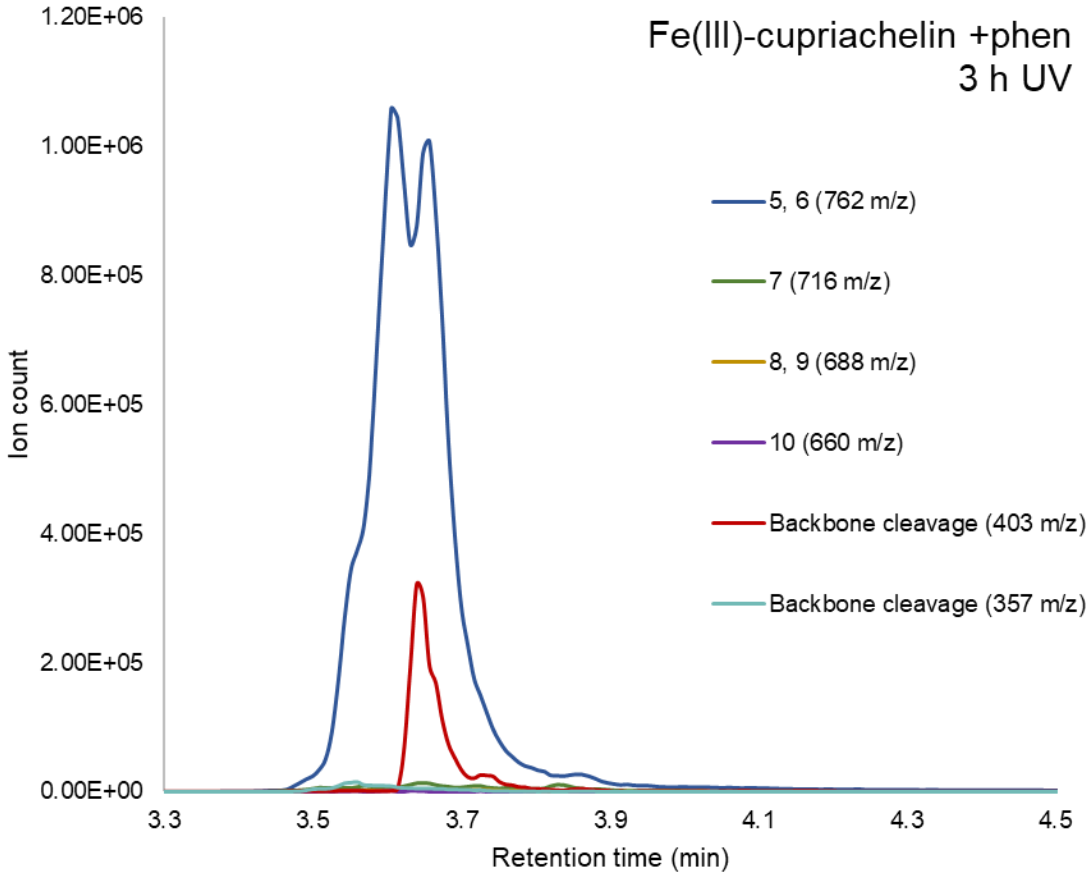

Figure 5.22. Extracted ion chromatograms of cupriachelin photoproducts **5-10** and backbone cleavage photoproducts from UPLC-ESIMS analysis of 0.1 mM Fe(III)-cupriachelin and 0.6 mM phen in 25 mM MOPS after 3 h of irradiation. Abundance of **5** exceeds abundance of other photoproducts, but a significant amount of the 403 m/z backbone cleavage product was also detected.

5.4. Discussion

This identification of several new photoproducts from the photoreactions of Fe(III)-pacifibactin and Fe(III)-cupriachelin is the first example of multiple photoproducts detected from single Fe(III)-siderophore photoreactions, other than the report of a backbone cleavage and decarboxylation photoproduct from the photolysis of Fe(III)-variochelin.[11] For both

Fe(III)-pacifibactin and Fe(III)-cupriachelin, the photoproducts reported in this study correspond to either loss of 1 equivalent of CO_2, 2 equivalents of CO_2, 2 equivalents of CO_2 and 1 equivalent of CO, or 2 equivalents of CO_2 and 2 equivalents of CO. These photoproducts are all consistent with the photolysis scheme of sequential decarboxylation proposed by *Grabo et al*.[13] The relative abundances of these characterized photoproducts as a function of irradiation time further support the proposed scheme. As irradiation time increases, products corresponding to multiple decarboxylation events increase in abundance, relative to products resulting from a single decarboxylation. The Fe(III)-siderophore complexes yielded no significant amount of the multiple-decarboxylation photoproducts when irradiated in the presence of the Fe(II) chelator phenanthroline, further supporting a hypothesis that multiple decarboxylation events can only occur through repeated cycles of Fe(II) oxidation, re-complexation, and photolysis.

Less clear is the mechanism and timing of photolytic peptide backbone cleavage relative to photolytic decarboxylation. In the photolysis of Fe(III)-pacifibactin, the peptide backbone cleavage photoproduct approached an abundance comparable to the decarboxylation photoproducts only in samples irradiated for 30 minutes or more. When Fe(III)-pacifibactin was photolyzed in the presence of excess phenanthroline, no backbone cleavage photoproduct was detected even after 3 hours of irradiation. Thus, the backbone cleavage photoproduct of Fe(III)-pacifibactin appears to only arise after initial photolytic decarboxylation of the intact ligand. Photolysis of Fe(III)-cupriachelin, on the other hand, leads to rapid formation of backbone cleavage photoproducts. After only 10 minutes of irradiation, these products exhibit comparable abundance to the decarboxylation photoproducts, and after 20 minutes of irradiation, backbone cleavage photoproducts are clearly dominant in abundance. Photolysis

of Fe(III)-cupriachelin in the presence of excess phenanthroline did yield primarily the single decarboxylation photoproduct, but in contrast to Fe(III)-pacifibactin photolysis, a significant amount of backbone cleavage photoproduct was still detected. These differing results suggest that the timing and relation between photolytic decarboxylation and photolytic peptide backbone cleavage in β-OHAsp Fe(III)-siderophore complexes varies significantly between different siderophores.

In a sequential decarboxylation model of β-OHAsp siderophore photolysis, each successive oxidative decarboxylation event would be coupled with a reduction of Fe(III) to Fe(II), enabling one siderophore ligand to generate multiple equivalents of Fe(II) photolytically. This potential of β-OHAsp siderophores has important implications in ecological iron availability. Fe(III) reduction in ocean environments is known to enhance iron uptake in phytoplankton, stimulating growth.[16-17] Photolysis of Fe(III)-vibrioferrin, a siderophore produced by alga-associated *Marinobacter* species containing citrate and α-ketoglutarate functional groups, promotes uptake of Fe(III) by the alga *Scrippsiella trochoida*.[18-19] Vibrioferrin binds and photochemically reduces Fe(III) unavailable to the alga, the Fe(II) then re-oxidizes under oceanic conditions into a highly-bioavailable form of iron.[18-19] The ability of a β-OHAsp siderophore to turn over multiple equivalents of Fe(III) photochemically could allow these ligands to function as bio-available iron "factories" for broader ecological communities. Future work to quantify Fe(II) generation in β-OHAsp siderophore photolysis is a critical next step in further exploring this possibility.

5.5. References

1. Hardy, C. D.; Butler, A., *J. Biol. Inorg. Chem.* **2018,** *23* (7), 957-967.

2. Butler, A.; Theisen, R. M., *Coord. Chem. Rev.* **2010,** *254* (3), 288-296.

3. Abrahamson, H. B.; Rezvani, A. B.; Brushmiller, J. G., *Inorg. Chim. Acta* **1994,** *226* (1), 117-127.

4. Küpper, F. C.; Carrano, C. J.; Kuhn, J.-U.; Butler, A., *Inorg. Chem.* **2006,** *45* (15), 6028-6033.

5. Abergel, R. J.; Zawadzka, A. M.; Raymond, K. N., *J. Am. Chem. Soc.* **2008,** *130* (7), 2124-2125.

6. Hickford, S. J. H.; Küpper, F. C.; Zhang, G.; Carrano, C. J.; Blunt, J. W.; Butler, A., *J. Nat. Prod.* **2004,** *67* (11), 1897-1899.

7. Martin, J. D.; Ito, Y.; Homann, V. V.; Haygood, M. G.; Butler, A., *J. Biol. Inorg. Chem.* **2006,** *11* (5), 633-641.

8. Barbeau, K.; Rue, E. L.; Bruland, K. W.; Butler, A., *Nature* **2001,** *413*, 409-413.

9. Kreutzer, M. F.; Kage, H.; Nett, M., *J. Am. Chem. Soc.* **2012,** *134* (11), 5415-5422.

10. Hardy, C. D.; Butler, A., *J. Nat. Prod.* **2019,** *82* (4), 990-997.

11. Kurth, C.; Schieferdecker, S.; Athanasopoulou, K.; Seccareccia, I.; Nett, M., *J. Nat. Prod.* **2016,** *79* (4), 865-872.

12. Robertson, A. W.; McCarville, N. G.; MacIntyre, L. W.; Correa, H.; Haltli, B.; Marchbank, D. H.; Kerr, R. G., *J. Nat. Prod.* **2018**.

13. Grabo, J. E.; Chrisman, M. A.; Webb, L. M.; Baldwin, M. J., *Inorg. Chem.* **2014,** *53* (11), 5781-5787.

14. Reitz, Z. L.; Hardy, C. D.; Suk, J.; Bouvet, J.; Butler, A., *Proc. Natl. Acad. Sci. USA* **2019,** *116* (40), 19805.

15. Fortune, W. B.; Mellon, M. G., *Ind. Eng. Chem., Anal. Ed.* **1938,** *10*, 60-64.

16. Anderson, M. A.; Morel, F. M. M., *Limnol. Oceanogr.* **1982,** *27* (5), 789-813.

17. Barbeau, K., *Photochem. Photobiol.* **2006,** *82* (6), 1505-1516.

18. Amin, S. A.; Green, D. H.; Hart, M. C.; Küpper, F. C.; Sunda, W. G.; Carrano, C. J., *Proc. Natl. Acad. Sci. USA* **2009,** *106* (40), 17071-17076.

19. Amin, S. A.; Green, D. H.; Küpper, F. C.; Carrano, C. J., *Inorg. Chem.* **2009,** *48* (23), 11451-11458.